Determination of Degradation Mechanisms During the Cyclic Ageing of Li-ion Batteries

Von der Fakultät Energie-, Verfahrens- und Biotechnik
der Universität Stuttgart
zur Erlangung der Würde eines Doktor-Ingenieur
(Dr.-Ing.) genehmigte Abhandlung

Vorgelegt von
M. Sc. Matthias Simolka
aus Rheinfelden (Baden)

Hauptberichter:	Prof. Dr. rer. nat. K. Andreas Friedrich
Mitberichter:	Prof. Dr. rer. nat. Helmut Ehrenberg

Tag der mündlichen Prüfung: 10.03.2021

Institut für Gebäudeenergetik, Thermotechnik und Energiespeicherung (IGTE)
der Universität Stuttgart

Erscheinungsjahr
2021

Danksagung

Diese Arbeit wäre ohne die Unterstützung einer Reihe von Personen gar nicht möglich gewesen. Ich möchte mich bei meinem Doktorvater Prof. Dr. K. Andreas Friedrich für die Betreuung der Arbeit und Unterstützung bedanken. Ebenso danke ich Prof. Dr. Helmut Ehrenberg für die Übernahme der Zweitprüfung.

An der Hochschule Esslingen wurde ich von Prof. Dr. Renate Hiesgen vom ersten Tag an und bis zu Ihrem Ableben gefördert und geleitet, dafür danke ich ihr von Herzen. Prof. Dr. Hanno Käß möchte ich für die gute Zusammenarbeit, das Vertrauen und die Übernahme der Betreuung an der Hochschule Esslingen am Ende der Arbeit danken. Bei den Arbeiten am REM unterstützte mich Dr. Jürgen Kraut, der auch die Laborräume mit mir teilte. Für die vertrauensvolle und kollegiale Zusammenarbeit dabei möchte ich mich bedanken. Dr. Jürgen Haiber und Bernd Jung möchte ich für die geduldige und freundliche Unterstützung bei der Herstellung von Messhilfen danken. Dem Rechenzentrum der Hochschule Esslingen möchte ich für die sicherlich nicht einfache Unterstützung aller meiner Vorhaben danken. Prof. Dr. Ferdinand Panik, Hannah Schmidt, Alexander Kohs und Praveen Kuppusamy möchte ich für die gute Zusammenarbeit in unserem gemeinsamen Forschungsprojekt danken.

Am Deutschen Zentrum für Luft- und Raumfahrt in Stuttgart möchte ich den Kollegen für die Unterstützung und Hilfestellungen bei der Bewältigung von Messungen und anderer Fragestellungen danken. Dr. Norbert Wagner danke ich für die fachlichen Diskussionen und die offene Tür. Christopher Heim und Dr. Miriam Steinhauer danke ich für Zusammenarbeit und Hilfestellungen bei jeglichen Fragen. Bei Brigitta Sievert möchte ich mich für die Unterstützung bei Fragen rund um Messaufbauten bedanken. Dr. Indro Biswas, Dr. Pawel Gazdzicki und Anke Lützner danke ich für die Übernahme und Auswertung der XPS Messungen und Unterstützung beim Korrekturlesen. Ich möchte mich auch bei allen anderen Doktoranden am DLR für die großartige Unterstützung und gegenseitige Förderung bei den Doktorandenseminaren bedanken.

Ein ganz besonderer Danke geht an meine direkten Kollegen an der Hochschule Esslingen. Tobias Morawietz, Michael Handl und Jan-Frederik Heger möchte ich für Ihre unglaubliche Hilfsbereitschaft bei fachlichen, sowie auch menschlichen Fragestellungen danken. Die gemeinsamen Erfahrungen, die ich mit euch in der Bürogemeinschaft gesammelt haben, werden mir ein Leben lang bleiben.

Meinen Eltern Marianne und Joachim danke ich von ganzem Herzen für die bedingungslose Unterstützung, die ich in meinem Leben erhalten habe und die vieles erst ermöglicht hat.
Meinen Kindern Joseph und Lise danke ich dafür, dass sie mir den Blick auf das Wesentliche erhalten. Et ma femme Viviane, je te remercie pour la sacrée patience et pour ton soutien qui a rendu tout cela possible.

Für Joseph und Lise, weil ihr das Leben mit Glück erfüllt

&

Pour Viviane, pour être ma boussole dans tous les conditions

Erklärung

Ich erkläre, dass ich diese Doktorarbeit selbstständig und ohne Benutzung anderer als der angegebenen Hilfsmittel angefertigt habe.

_____

Matthias Simolka

Berlin, den 11. März 2021

In Memory of

Prof. Dr. rer. nat. Renate Hiesgen

Mentor & Colleague

Table of content

List of figures

List of tables

I. Kurzfassung

Die Degradationsmechanismen von kommerziellen Li-Ionen Batterien (hier sind wieder aufladbare Sekundärzellen bzw. Akkumulatoren gemeint) wurden in den letzten Jahrzenten ausgiebig untersucht. Dennoch verbleiben einige offene Fragen in Bezug auf den Zusammenhang zwischen Veränderungen im Verhalten der Batteriezelle, welche auf Systemebene der Batteriezelle beobachtet werden, und Materialdegradation, welche innerhalb der Batteriezelle auftreten. Um das Verständnis über die Einflüsse der Materialdegradationen auf das Verhalten der Batteriezelle auf Systemebene zu verbessern, wurden verschiedene Analysemethoden angewendet und die Erkenntnisse kombiniert.

Eine für die Untersuchung von Relaxationsvorgängen angepasste Analysemethode der elektrochemischen Deformationsmikroskopie (Engl. electrochemical strain microscopy, ESM) wird vorgestellt, welche auf der Rasterkraftmikroskopie basiert. Diese Analysemethode wird auf labortechnisch hergestellte Silizium-Komposit-Anoden und kommerzielle $LiFePO_4$-Kathoden angewendet. Die Oberflächenausdehnung, hervorgerufen durch die Vegard Deformation, ist proportional zur ionischen Konzentrationsveränderung und der Aktivität von Li-ionen im angeregten Materialvolumen unterhalb der Messspitze. Das angeregte Materialvolumen ist nur wenige Nanometer tief. Die Ergebnisse zeigen eine Abhängigkeit von der Materialstruktur, wobei eine höhere Mobilität und Aktivität der Li-Ionen an Strukturgrenzen auftreten. Die Analysemethode liefert Zeitkonstanten und damit Diffusionskoeffizienten auf der Nanometer Skala. Die nach dieser Methode ermittelte elektrochemische Aktivität nimmt mit der Alterung ab.

Die Alterung von kommerziellen Batteriezellen wird auf Systemebene mit der inkrementellen Kapazitätsanalyse (Engl. incremental capacity analysis, ICA), der differenziellen Spannungsanalyse (Engl. differential voltage analysis, DVA) und der Ruhespannung (Engl. open circuit voltage, OCV) verfolgt. Die Alterung bei 50% Entladetiefe führt zu einem höheren Kapazitätsverlust während der Zyklisierung im Vergleich zur Zyklisierung über 100% der verfügbaren Kapazität. Insgesamt wurden 14 verschiedene Merkmale des Zellverhaltens mit verschiedenen Analysemethoden während des Alterungsprozesses verfolgt. Die Intensität des ersten ICA Scheitelpunktes korreliert in hohem Maße mit der Kapazitätsabnahme und wird darauf aufbauend verwendet, um die Restkapazität und Lebensdauer zu prognostizieren. Der Verlust von Lithium und Aktivmaterial, speziell an der Kathodenseite, sind die Hauptursachen für den Kapazitätsverlust. Die post-mortem Untersuchungen zeigen, dass es zur Bildung von

Lithiumfluorid-Kristallen an der Anodenoberfläche gekommen ist, welche bei 55°C gealtert wurde. Es wird gezeigt, dass die Eisenauflösung nicht nur temperaturabhängig ist, sondern ebenfalls von der Entladetiefe beeinflusst wird. Neben der Auflösung von Eisen aus der Elektrode in den Elektrolyten wird die Auflösung von Vanadium aus der Elektrode und in den Elektrolyten beobachtet. Mikrometer große Agglomerate zeigen sich an der Kathodenoberfläche, welche die Oberflächenleitfähigkeit reduzieren. Die Reduktion der Oberflächenleitfähigkeit korreliert allerdings nicht mit der Abnahme der Kapazität. Die Alterung bei -20°C führt zu einer stabilen Lithium Schicht, welche im Anschluss auch bei der Charakterisierung bei Raumtemperatur beobachtet wird.

II. Abstract

Degradation mechanisms in commercial Li-ion batteries have been extensively studied over the past decades. However, there are still open questions regarding the link between the observed changes on the system level of the battery with the actual degradation on the material level happening inside the battery. Therefore, different techniques are applied and findings combined to improve the understanding of material degradation influences on the system level behavior.

A tailored electrochemical strain microscopy (t-ESM) technique, which is based on atomic force microscopy, is presented. The technique is applied to laboratory made silicon composite anodes and commercial $LiFePO_4$ cathodes. The surface displacement induced by the Vegard strain is proportional to the ionic concentration change and activity of Li-ions within the probed volume under the tip. The probed volume spans only a few nanometers in depth inside the material. The results indicate a structural dependency, with higher mobility and activity at boundaries. The technique provides time constants and hence diffusion coefficients on the nano-scale. The electrochemical activity, which is analyzed with the t-ESM technique, is found to decrease due to ageing.

The ageing of commercial battery cells is monitored using system level methods such as incremental capacity analysis (ICA), differential voltage analysis (DVA) and tracking of the open-circuit voltage (OCV). Ageing at 50% depth of discharge (DOD) leads to higher capacity fading compared to cycling over 100% of the available capacity. In total, 14 different features of the cell behavior are tracked during the ageing process using various analysis techniques. The intensity of the first discharge peak of the ICA curves is found to correlate well with the capacity fading and is used to predict the remaining capacity and lifetime. The loss of lithium and the loss of active material, especially at the cathode, are the main factors leading to the observed capacity decay. The post-mortem analysis reveals the formation of lithium fluoride crystals on the anode surfaces, aged at 55°C. The iron dissolution (from the electrode into the electrolyte) is shown to be temperature dependent and in addition dependent on the depth of discharge. Next to iron dissolution, vanadium dissolution (from the electrode into the electrolyte) from the cathode is observed. Micrometer sized agglomerates (consisting out of nano particles from cathode active material) are observed on the cathode surface, which decrease the surface conductivity, but does not directly correlate with the capacity fading. Ageing at -20°C leads to the formation of stable Li plating, which is subsequently observed at room temperature cycling.

III. List of Abbreviations, Formulas and Symbols

Abbreviations

AFM	Atomic force microscopy
AP	Ageing profile
BMS	Battery management systems
BOL	Beginning of life
BSE	Back-scattered electrons
C_2H_2	Acetylene
$(CH_2O)_2CO$	Ethylene carbonate
DMC	Dimethyl carbonate
DMT	Derjaguin, Muller and Toporov model for the evaluation of the material stiffness
DOD	Depth of discharge
DST	Dynamic stress test
DVA	Differential voltage analysis
EC	Ethylene carbonate
EIS	Electrochemical impedance spectroscopy
EMF	Electromotive force
EOC	End of charge
EOD	End of discharge
EOL	End of life
EV	Electric vehicle
ICA	Incremental capacity analysis
ICE	Internal combustion engine
KOH	Potassium hydroxide
LAM_{NE}	Loss of active material at the negative electrode
LAM_{PE}	Loss of active material at the positive electrode
LFP	LiFePO4
Li_2CO_3	Lithium carbonate
$LiPF_6$	Lithium hexafluorophosphate
LLI	Loss of lithium inventory
nonequi-OCV	non-equilibrium OCV
OCV	Open circuit voltage

PE	Primary electrons
PHEV	Plug-In electric vehicles
RT	Room temperature
SE	Secondary electrons
SEI	Solid electrolyte interface
SEM	Scanning electron microscopy
SPI	Solid permeable interface
SPM	Scanning probe microscopy
STM	Scanning tunnelling microscopy
SOC	State of charge
SOH	State of health
TEM	Transmission electron microscopy
USABC	US American Battery Consortium
WLTP	Worldwide harmonized light vehicles test procedure

Formulas

A	Area
a_i	Activity of species *i*
a	Intercept of overpotential axis of Tafel plot
b	Slope of Tafel plot
C_{ox}^*	Bulk concentration of oxidized species
C_{ox}	Concentration of oxidized species
C_{red}^*	Bulk concentration of reduced species
C_{red}	Concentration of reduced species
c_i	Concentration of species *i*
D_i	Diffusion coefficient of species *i*
E	Applied potential
E^0	Standard potential
E_{cell}^0	Standard potential of electrochemical cell consisting of anode and cathode potential
E_{cell}	Full cell potential
E_{anode}^0	Standard potential of anode
E_A	Anode potential from full cell

$E^0_{cathode}$	Standard potential of cathode
E_C	Cathode potential from full cell
E_{OCV}	Open-circuit potential
e	Elementary charge
F	Faraday constant
G	Total sum of Gibbs free energy
G^0	Gibbs free energy
ΔG^0	Gibbs free energy at equilibrium
ΔG^0_{ox}	Gibbs free energy of oxidation at equilibrium
ΔG_{ox}	Gibbs free energy of oxidation out of equilibrium
ΔG^0_{red}	Gibbs free energy of reduction at equilibrium
ΔG_{red}	Gibbs free energy of reduction out of equilibrium
ΔG_r	Change of Gibbs free energy during reaction
ΔG^0_r	Change of Gibbs free energy during reaction using standard chemical potentials of species
ΔG^*_{ox}	Activation Gibbs free energy for the oxidation
ΔG^*_{red}	Activation Gibbs free energy for the reduction
G_m	Molar Gibbs energy
i	Current
i_0	Exchange current density
i_{anodic}	Anodic current density
$i_{cathodic}$	Cathodic current density
J_i	Ionic flux of species *i*
k	Reaction constant
k_{ox}	Reaction constant of oxidation
k^0_{ox}	Reaction constant of oxidation for Arrhenius' equation
k_{red}	Reaction constant of reduction
k^0_{red}	Reaction constant of reduction for Arrhenius' equation
k^0	Reaction rate using 0.5 for the symmetry factor
M_i	Mobility of species *i*
n	Number of electrons
n_i	Species *i*
p	Pressure

R	Gas constant
T	Temperature
t	Time
x_i	Mole fraction of species *i*

Greek symbols

α	Symmetry factor
μ_i	Chemical potential of species *i*
μ_i^0	Standard chemical potential of species *i*
$\tilde{\mu}_i$	Electrochemical potential of species *i*
$\tilde{\mu}_A$	Electrochemical potential of the anode
$\tilde{\mu}_C$	Electrochemical potential of the cathode
ν	Reaction rate
ν_{ox}	Reaction rate of oxidation
ν_{red}	Reaction rate of reduction
ν_i	Stoichiometric number of species *i*
ξ	Reaction coordinate
σ_h	Hydrostatic stress
σ_{ll}	Stress in direction *ll*
ϕ	Electrical potential
Ω_i	Molar volume of species *i*

1 Introduction

1.1 Relevance of Topic

Batteries play an important part in the transformation of the energy system from fossil energy to renewable energy resources. They are used on small scale for mobile energy storage power tools and communication devices, on big scale for mobile energy storage automotive systems and stationary systems like households and integration of renewable energies. Current battery technology is reaching the limit for further considerable improvements of the storage capacity and power density. Potential next generation cell chemistries like Lithium – Sulfur and Lithium – Air are promising candidates for a new jump in both storage capacity and power density, but both systems possess their own drawbacks that hinder a wide commercial application in the near future. Nevertheless, improvements in durability and further knowledge of the detrimental effects occurring inside the electrodes during their utilizations are still vital for the current battery technology. New methods and a closer link between cell level variations and material level degradations are necessary to analyses the aging of battery cells and to provide valuable information to material scientist and manufacturers for further development.

1.2 Aim of this Work

This work is separated into two sections. The first section is focused solely at the material level on nano-meter scale. The aim is the development of a method to visualize the ionic concentration change and its distribution in battery materials and follow the degradation of the materials using this method. In addition, relaxation times and hence diffusion coefficients are mapped next to the ionic concentration change and distribution. This serves on one hand as a tool for material experts, since they can learn about the behaviour of ions moving and distributing inside the material and on the other hand as a tool for experts in modelling of battery systems, due to the locally resolved diffusion coefficients and relaxation times, which are useful for their simulations.

The second section combines results of the material level with the cell level, to improve the understanding of the influence of material level changes on cell level behaviour. To accomplish this goal, different cell level analysis methods like differential voltage and incremental capacity

analysis, open-circuit potential tracking and electrochemical impedance spectroscopy are utilized to track the aging of cells and combined with post-mortem material analysis using scanning electron and atomic force microscopy, energy dispersive X-ray spectroscopy and X-ray photoelectron spectroscopy to connect the observed changes in the material with the behaviour on the cell level.

2 Fundamentals of Electrochemical Cells

2.1 Principle Set-Up of a Battery Cell

The set-up of a commercial battery has its origin in the idea of the galvanic cell. In principle, two electrodes of different material are immersed into an electrolyte and ions and electrons passing through the electrolyte and accordingly the outer electric circuit drive a redox reaction. The galvanic cell transforms chemical energy, which is stored in the materials of the electrodes, in electrical energy and for charging process vice versa. The electrode at which the oxidation takes place is called the anode, the electrode at which the reduction occurs the cathode. The designation anode/cathode depends on the direction of the flow of electrons and ions, therefore, in general electrochemistry, reversible reactions at one electrode can be anode or cathode depending on the direction of the reaction. However, the name convention in battery technology sets the electrode at which the oxidation takes place during discharge as the anode.

In the history of electrochemistry, there are numerous different examples for galvanic cells. The two most famous which are usually taught and given as examples are the Voltaic pile and the Daniell Element. The Voltaic pile consists of zinc and copper plates stacked on top of each other and separated by a cotton cloth soaked with an electrolyte, for example salt water. In the Daniell Element, copper as the cathode is immersed in a copper sulphate solution and zinc as the anode is immersed in zinc sulphate solution. Both compartments are connected with a salt bridge for the ion exchange. Reactions in the battery cell are linked to the available electrode surface and accompanied by solid-state mass diffusion inside the electrode material. This mass diffusion leads to a change in the chemical composition of the electrode and a volume expansion or shrinkage [1]. In the examples of the galvanic cell, the electrodes are metals, but in commercial systems, the cathodes are rather metallic oxides like $FePO_4$ and MnO_2. For the anodes, metals are occasionally used, but another practical choice are materials which serve as a host for the intercalation of ions such as carbon and graphite [2].

Another approach for anode materials is the formation of an alloy, for example using silicon. The disadvantage of the Li-alloying is the lithium driven volume expansion of up to 200% and more [3]. Three mechanisms for the storage of lithium ions into the materials are available, i) alloying which was already mentioned, examples are silicon, tin, antimony and other intermetallic alloys, ii) conversion reactions, for example Fe_2O_3, Co_3O_4 and NiP_2 and iii) intercalation reactions, for example carbon, graphene and titanium oxides [1,4,5].

The principle set-up of a battery cell is given in Figure 2-1. The cathode consists out of small particles with a size of roughly 50 nm to 1 µm in diameter which are embedded in a polymer binder to ensure the mechanical stability. To increase the electric conductivity of the overall electrode, the cathode particles are either mixed or coated with carbon. The cathode mixture is coated on aluminium foil as a current collector. The anode consists of the particles, which are either nanoparticles with roughly 50 nm diameter as it is used for silicon or up to a few micrometres, as it can be seen for graphite flakes. A polymer binder is used for the anode material to ensure the structural stability. The anode mixture is coated on copper foil. The electrodes are immersed in electrolyte, which is typically a non-aqueous liquid mixture of carbonates like ethylene carbonate and polyethylene carbonate with the addition of a salt, to increase the ionic conductivity. To avoid any short circuits in the case of a liquid electrolyte, a separation layer is inserted in-between the anode and cathode. This layer, called the separator, consist of an electric isolating polymer mesh, which is permeable for the ions in the electrolyte. However, the use of solid electrolytes is a promising technique to improve the safety, due to the hindered flammability of most ceramics, and increase of the storage capacity of the battery cell, since other materials, for example, lithium metal or high-voltage cathodes with a potential of 5 V and more versus the anode can be used. Materials for solid electrolytes are ceramics, such as the perovskite-type lithium lanthanum titanate (LLTO), lithium phosphorus oxynitride (LIPON) or $Li_{14}ZnGe_4O_{16}$ and related compositions (LISICON) [6–8].

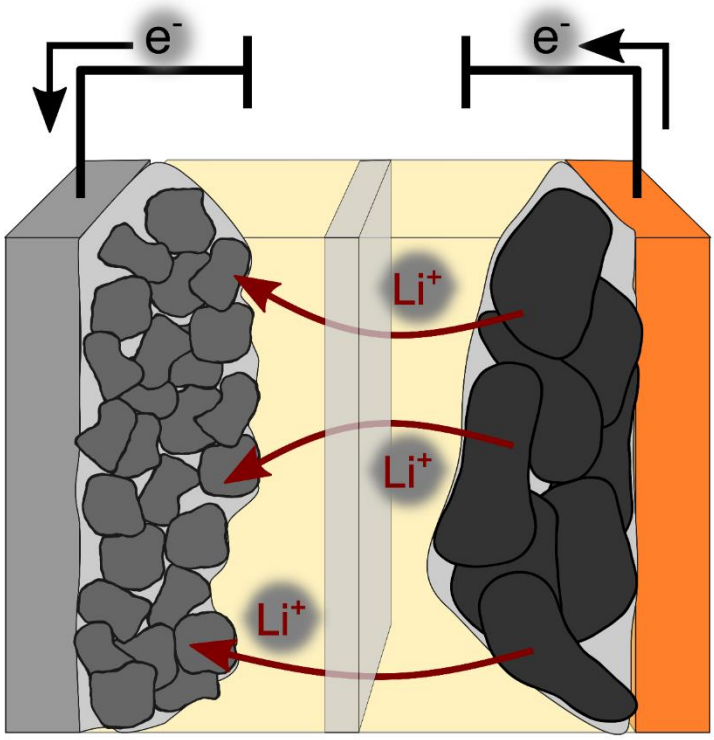

Figure 2-1: Principle set-up of a battery cell with cathode, anode and separator and electrolyte in between. During discharge, ions travel through the electrolyte and separator from the anode to the cathode. The electrons pass through the external circuit.

2.2 Intercalation Process of Li-ions into Host Electrodes

During the charging and discharging process in rechargeable batteries, Li-ions are reversibly inserted into and removed from a host lattice of the electrode via an intercalation process. The intercalation process is characterised by only small amount of structural changes in the host material by the incorporation of Li-ions, examples of intercalation type electrodes are graphite, $LiMn_2O_4$, $LiFePO_4$ and $LiCoO_2$. Another type of incorporation and removal process of Li-ions into an electrode material are conversion reactions, in which chemical bonds are broken up and created during a chemical transformation. One promising conversion process based candidate is sulphur for the cathode with a gravimetric capacity of 1672 mAh g^{-1} and silicon for the anode with a gravimetric capacity of 3579 mAh g^{-1} (assuming 3.75 transferred electrons for $Li_{15}S_4$).

The intercalation cathode materials have different structures, which affect the dimensionality of the Li-ion diffusion. $LiMnO_2$ for example exhibits a layer structure which overs a two dimensional Li-ion transport, $LiMn_2O_4$ on the other hand allows for a three dimensional Li-ion

transport, based on the spinel structure. The Li-ion transport within $LiFePO_4$ is limited to only one dimension, based on the olivine structure [9].

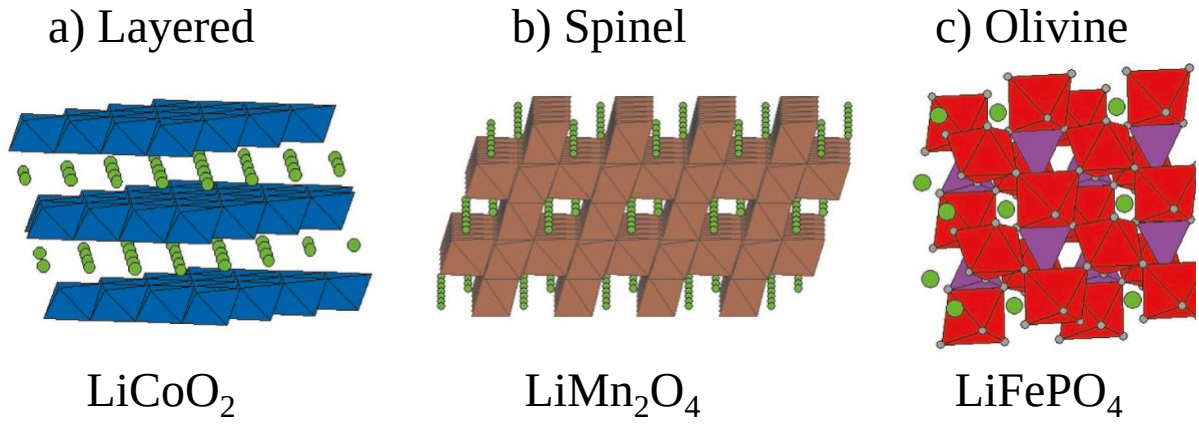

Figure 2-2: Crystal structures of currently used cathode electrodes (adapted from [9])

For the intercalation of Li-ions into the graphite negative electrode, the insertion is separated into up to five separate phases (including the 1d+4 phase), also referred to different stages of intercalation, which are the origin for the appearance of separated voltage plateaus during the discharging process [10]. In an idealistic consideration, the ions are inserted into specific layers until the entire layer is filled with Li-ions and only afterwards, a new layer is filled.

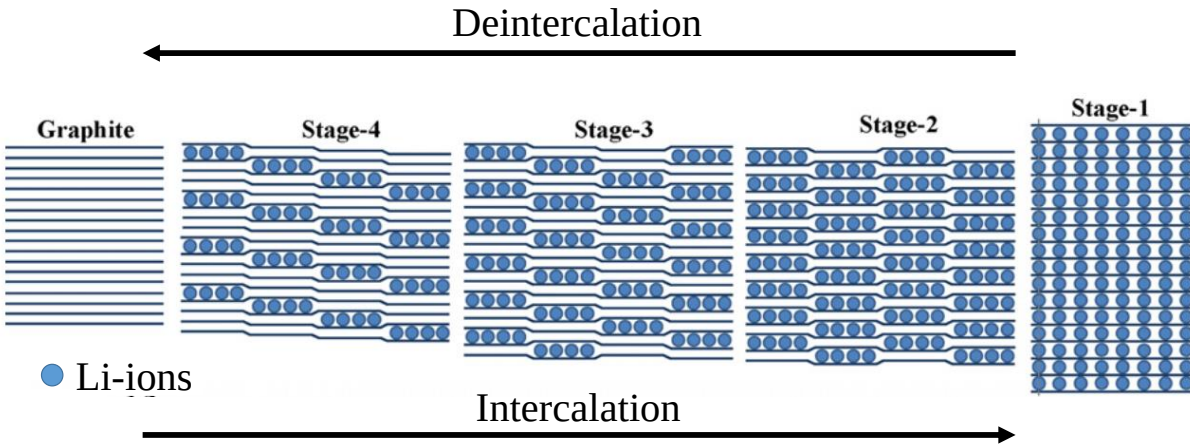

Figure 2-3: Staging process during intercalation and deintercalation into the graphite layers (adapted from [11])

2.3 Thermodynamic Principles Describing the Behaviour of Electrochemical Cells

The potential of the battery cell depends on the materials in the anode and cathode. It can either be calculated with the Gibbs free energy (G^0), using the electropotential series or by experiment. The relation between the standard potential E^0 (as well known as the electromotive force, "emf") and the change in Gibbs free energy ΔG^0 is expressed in the equation (2.1) with n being the number electrons transferred and F the Faraday constant (which is the product of the Avogadro constant and the elementary charge). By rearranging equation (2.1) and with the known change in Gibbs free energy, the standard potential can be calculated. The Gibbs free energy ΔG^0 represents the maximum amount of work the cell can deliver, but only if the process is thermodynamically reversible [12].

$$\Delta G^0 = -nFE^0 \tag{2.1}$$

The second way to calculate the standard voltage of the cell is to extract the standard electrode potentials of the materials used and by subtraction of the standard electrode potential of the anode of the standard electrode potential of the cathode, shown in (2.2):

$$E^0_{cell} = E^0_{cathode} - E^0_{anode} \tag{2.2}$$

The standard electrode potentials are measured against a known electrode material. Hydrogen gas flowing by a platinum electrode immersed in an acidic solution is chosen as the standard electrode versus which all other materials are referred and the standard potential of hydrogen is set as 0 V under standard conditions [1,2,13].

In the battery technology, the standard potential of the cell is ideally also the Open Circuit Voltage (OCV) if materials properties are ideal. The electrode potentials depend on the chemical potentials μ of the electrode materials, which is depending on the composition of the electrode. In a general view, the chemical potential reflects the ability or the potential of an element to undergo chemical changes in a system [1,12–14]. In a system with only one species, the chemical potential equals the molar Gibbs energy, so:

$$\mu = G_m \tag{2.3}$$

In a system with more than one species, the chemical potential of species A depends on the Gibbs energy and the amount of the species in the mixture

$$\mu_1 = \left(\frac{\partial G}{\partial n_1}\right)_{p,.T,n} \tag{2.4}$$

With μ_1 as the chemical potential of the species 1, n_1 the amount of species 1, p the pressure, T the temperature and n the total amount of all species in the mixture. The total amount of

Gibbs free energy is the sum of the products of the chemical potentials and the amount of the species (see (2.5)).

$$G = \sum_i \mu_i n_i \tag{2.5}$$

Being interested in small changes in the reaction and introducing the stoichiometric number υ_i of the species i, which indicates the ratio of species i in a reaction, and the reaction coordinate ξ, equation (2.5) takes the form:

$$dG = \sum_i \mu_i dn_i = \sum_i \mu_i \upsilon_i d\xi = d\xi \sum_i \mu_i \upsilon_i \tag{2.6}$$

The overall change in the reaction Gibbs energy ΔG_r is the derivative of equation (2.6) by the reaction coordinate ξ, which results in [12]:

$$\Delta G_r = \left(\frac{\partial G}{\partial \xi}\right)_{p,T} = \sum_i \mu_i \upsilon_i \tag{2.7}$$

In mixtures, the chemical potential consist of the standard chemical potential of a component 1 (μ_1^0) and the mixing term depending on the activity (a_1) or mole fraction of the component (x_1) [15]. For ideal solutions, the mole fraction is used. For deviations from ideal behaviour, the activity needs to be used with $a_1 = \gamma_1 x_1$, in which γ_1 represents the activity coefficient of species 1.

$$\mu_1 = \mu_1^0 + RT \ln a_1 = \mu_1^{0\prime} + RT \ln x_1 \tag{2.8}$$

with

$$\mu_1^{0\prime} = \mu_1^0 + RT \ln y_1 \tag{2.9}$$

If stresses in the material due to changes in the concentrations are included, the chemical potential is extended with a third term with Ω_1 as the molar volume of the species 1 and σ_h as the hydrostatic stress, which is defined as $\sigma_h = {}^1/_3 (\sigma_{11} + \sigma_{22} + \sigma_{33})$ [16,17].

$$\mu_1 = \mu_1^{0\prime} + RT \ln x_1 - \Omega_1 \sigma_h \tag{2.10}$$

Since the electrodes in batteries are charged, the formula for the chemical potential μ_1 is extended with an additional term taking into account the charge of the material in an electrical potential. This leads to the equation for the electrochemical potential $\tilde{\mu}_1$ for species 1:

$$\tilde{\mu}_1 = \mu_1 + zF\phi \tag{2.11}$$

In the equation (2.11) the second term represents the work needed to add a charged ion into a region with the electric potential ϕ. In case of a neutral ion ($z = 0$) the electrochemical potential

reduces to the chemical potential [12]. With the concept of the electrochemical potential being established, the potential at OCV can be computed:

$$E_{OCV} = \frac{\tilde{\mu}_C - \tilde{\mu}_A}{e} \tag{2.12}$$

With $\tilde{\mu}_C$ as the electrochemical potential of the cathode, $\tilde{\mu}_A$ the electrochemical potential of the anode and e the elementary charge [1,13,14]. Since equation (2.12) only holds for equilibrium conditions, it is not valid for changes in temperature and composition. To achieve this, the dependency of the Gibbs free energy on the temperature and the activity is introduced. Combining equation (2.7) and (2.8) describes the change in reaction Gibbs energy using the activities of the reactants and products involved.

$$\begin{aligned} \Delta G_r = \sum_i v_i(\mu_i^0 + RT \ln a_i) = \sum_i \mu_i^0 v_i + v_i RT \ln a_i \\ = \Delta G_r^0 + RT \ln a_i^{v_i} \end{aligned} \tag{2.13}$$

Using the already established relation between the Gibbs free energy and the electrode potential in (2.1), substituting equation (2.1) in (2.13) and rearrange it leads to the Nernst equation, which describes the behaviour of the cell potential depending on the temperature and activities or bulk concentration of the oxidized species C_{ox}^* and reduced species C_{red}^* [2,12,15]:

$$E = E^0 - \frac{RT}{zF} \ln a_i^{v_i} = E^{0\prime} - \frac{RT}{zF} \ln \frac{C_{ox}^*}{C_{red}^*} \tag{2.14}$$

with the activity coefficients of the oxidizes y_{ox} and reduced species y_{red}

$$E^{0\prime} = E^0 - \frac{RT}{zF} \ln \frac{y_{ox}}{y_{red}} \tag{2.15}$$

Unfortunately, there are several losses during normal battery utilization, which reduce the actual measured potential. These losses arise from i) the inner resistance of the battery cell itself (e.g. electric connections and material resistances), called the ohmic overpotential, ii) the energy needed to activate the reactions, called activation overpotential and iii) the concentration overpotential, since the applied load leads to a change in concentration at the electrode surfaces compared to the bulk, due to diffusion. Decreasing the current applied to the cell decreases as well the overpotential losses [2].

A simple relationship between the overpotential applied to a cell η and the resulting current i is given by the Tafel equation (2.16):

$$\eta = E - E^0 = a \pm b \log i \tag{2.16}$$

The variables a and b are constants which need to be determined experimentally. The Tafel equation is limited to high overpotentials and does not describe systems at equilibrium, therefore, a more precise way for the linkage between overpotential and current is necessary [2]. The differences of the Gibbs free energy and the electric potential are the driving forces for the cell reactions. Still, the rates of the cell reactions cannot be determined with the equations represented until here. For this, another variable is introduced. The magnitude of the current flowing due to an electrochemical reaction is governed by its reaction rate. Therefore, by determining the reaction rates of the oxidation and reduction, the resulting current can be described and vice versa. The reaction rate v of a reaction of interest is the product of the rate constant k and the concentration of the reactant. For the oxidation of species C_{ox} and reduction of species C_{red}, this results in:

$$v_{ox} = k_{ox} C_{ox} \tag{2.17}$$

$$v_{red} = k_{red} C_{red} \tag{2.18}$$

The cathodic and anodic current densities result from the reaction rate and the charge transferred per mol of the species, which is given by the Faraday constant, the number of electrons transferred during the redox reaction n and the area A of the electrodes. Since the reactions are taking place at the interfaces of electrode and electrolyte, the concentrations of interest are the ones at the interfaces, and not the bulk concentrations. For comparisons, it is convenient to relate the currents to the electrode areas.

$$i_{cathodic} = nFAk_{ox} C_{ox} = nFAv_{ox} \tag{2.19}$$

$$i_{anodic} = nFAk_{red} C_{red} = nFAv_{red} \tag{2.20}$$

In case the reactions are in equilibrium, the cathodic and anodic current has an equal magnitude and the net current is zero, if the reactions are not in equilibrium a net current i can be measured, as equation (2.21) indicates.

$$i = i_{cathodic} - i_{anodic} = nFA(k_{ox} C_{ox} - k_{red} C_{red}) \tag{2.21}$$

As mentioned before regarding the activation overpotential, the redox reactions need some activation energy to start the oxidation and reduction process. This necessity for the activation is physically included in the rate constant, coming from transition state theory and using an Arrhenius' equation like set-up, expressed in (2.22) and (2.23) [2,12].

$$k_{ox} = k_{ox}^0 \exp\left(\frac{-\Delta G_{ox}^*}{RT}\right) \tag{2.22}$$

$$k_{red} = k_{red}^0 \exp\left(\frac{-\Delta G_{red}^*}{RT}\right) \tag{2.23}$$

Here, ΔG_{ox}^{*} and ΔG_{red}^{*} are the activation Gibbs energies for the oxidation and reduction reaction and k_{ox}^{0} and k_{red}^{0} are constants with the same dimension as the reaction rate. Since the electrode potential has a strong influence on the reaction rate, the relationship between the reaction rate and the potential needs to be described. Figure 2-4a) shows the reaction free energy at constant pressure and temperature of a redox process. During equilibrium at E^0 oxidation and reduction have the same activation barrier ΔG_{ox}^{0} and ΔG_{red}^{0}. If the potential is shifted, in this example to a lower value than E^0, the reduction reaction is favoured since the barrier height changes for the oxidation and reduction. For the oxidation, the barrier height increases to ΔG_{ox} (with $\Delta G_{ox} > \Delta G_{ox}^{0}$) while for the reduction, the barrier height decreases to ΔG_{red} (with $\Delta G_{red} < \Delta G_{red}^{0}$). This change in barrier heights leads to the net flow of a cathodic current [15].

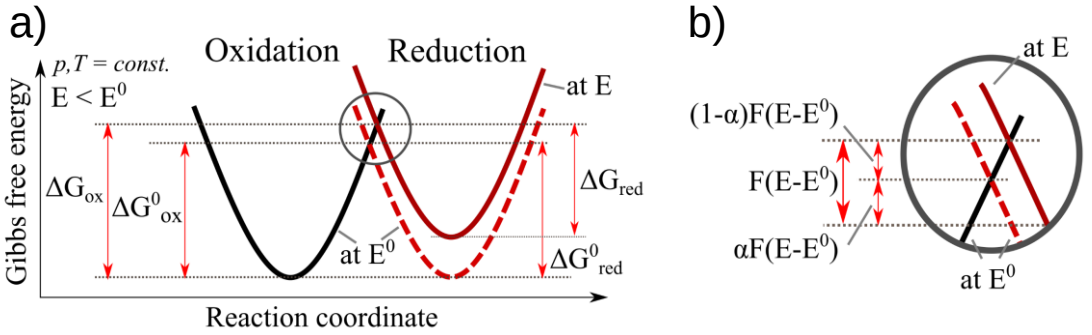

Figure 2-4: a) Influence of potential change on Gibbs free energy, b) zoom of a)

Figure 2-4 b) indicates, that ΔG_{ox} has increased by the amount of $(1-\alpha)F(E-E^0)$ and ΔG_{red} has decreased by $\alpha F(E-E^0)$ leading to equation (2.24) and (2.25):

$$\Delta G_{red} = \Delta G_{red}^{0} - \alpha F(E-E^0) \tag{2.24}$$

$$\Delta G_{ox} = \Delta G_{ox}^{0} + (1-\alpha)F(E-E^0) \tag{2.25}$$

The variable α is called the symmetry factor, since it is a measure for the balance between reduction and oxidation. Often it is set as 0.5 [2,15]. Combining equation (2.24) and (2.25) with (2.22) and (2.23) combines the effect of the potential shift on the reaction with the reaction rate of the half reactions. This leads to the following equations:

$$k_{red} = k_{red}^{0} \exp\left(\frac{\Delta G_{red}^{0}}{RT}\right) \exp\left(\frac{-\alpha F(E-E^0)}{RT}\right) \tag{2.26}$$

$$k_{ox} = k_{ox}^{0} \exp\left(\frac{\Delta G_{ox}^{0}}{RT}\right) \exp\left(\frac{(1-\alpha)F(E-E^0)}{RT}\right) \tag{2.27}$$

Since at equilibrium, the net current is zero, since the reduction and oxidation have the same rate constant, equation (2.26) and (2.27) can be simplified by using the standard rate constant of the equilibrium potential $k^{0.5}$. This is exactly the case for a symmetry factor α of 0.5. At equilibrium the barrier heights for the reduction and oxidation are the same, so they can be combined to the standard Gibbs free energy of activation ΔG^0. Including these simplifications in equation (2.26) and (2.27) leads to:

$$k_{red} = k^0 \exp\left(\frac{-\alpha F(E - E^0)}{RT}\right) \tag{2.28}$$

$$k_{ox} = k^0 \exp\left(\frac{(1-\alpha) F(E - E^0)}{RT}\right) \tag{2.29}$$

With

$$k^0 = k^{0.5} \exp\left(\frac{\Delta G^0}{RT}\right) \tag{2.30}$$

Now the final step is to combine equation (2.19), (2.20) and (2.21) with (2.28) and (2.29) which leads to the Butler-Volmer equation:

$$i_0 = nFAk^0 \left(C_{ox} \exp\left(\frac{(1-\alpha) F(E - E^0)}{RT}\right) - C_{red} \exp\left(\frac{-\alpha F(E - E^0)}{RT}\right)\right) \tag{2.31}$$

Equation (2.31) describes the link between the applied potential, the surface concentrations and the resulting current at the interface [2,12,18]. The Butler-Volmer equation is used to model the intercalation and deintercalation of Li-ions from the electrolyte into the host material. For the further transport of the ions inside the solids, other equations are necessary, which are described in the following. The flux of the ions J_1 inside the solid is driven by the difference in electrochemical potential $\nabla \mu_1$ and dependent on the mobility of the ions M_1 and the ionic concentration c_1. The relationship is expressed in equation (2.32) [16,19–21]:

$$J_1 = -M_1 c_1 \nabla \tilde{\mu}_1 \tag{2.32}$$

For the difference in electrochemical potential, we combine equation (2.10) and (2.11) which leads to:

$$\tilde{\mu}_1 = \mu_1^{0\prime} + RT \ln x_1 - \Omega_1 \sigma_h + zF\phi \tag{2.33}$$

Applying the Nabla operator to equation (2.33) and noting that $\nabla(RT \ln x_1) = RT \frac{\nabla x_1}{x_1} = RT \frac{\nabla c_i}{c_i}$ gives [16]:

$$\nabla\tilde{\mu}_1 = RT\frac{\nabla c_i}{c_i} - \Omega_1\nabla\sigma_h + zF\nabla\phi \tag{2.34}$$

Since the system is isolated and enclosed, conservation of mass applies:

$$\frac{\partial c_i}{\partial t} - \nabla J_1 = 0 \tag{2.35}$$

Now combining equation (2.32), (2.34) and (2.35) and noting that $M_i = \frac{n\,F\,D_i}{R\,T}$ leads to the change of ionic concentration due to concentration gradient, the presence of an electrical field and stresses inside the solid:

$$\frac{\partial c_i}{\partial t} = -\frac{nFD_i}{RT}(RT\nabla^2 c_i - \Omega_i\nabla c_i\nabla\sigma_h - \Omega_i c_i\nabla^2\sigma_h - z_i c_i F\nabla^2\phi) \tag{2.36}$$

2.4 Electrochemical Reactions Inside the Cell

The principle of a battery cell is the transformation from chemical energy, which is stored in the material, into electrical energy and vice versa. The transformation of energy is achieved by coupled oxidation and reduction reactions, which are taking place at the electrodes of the battery. All the reactions are accompanied by a small amount of irreversible loss of energy due to side reactions and heat generation. The overall reaction can be expressed as follows:

$$v_A A + v_B B \Leftrightarrow v_C C + v_D D \tag{F(2-1)}$$

The overall reaction is the combination of the reduction and oxidation and can be separated into the reaction on the cathode F(2-2) and the anode F(2-3).

$$v_A A + n\,e^- \Leftrightarrow v_C C \tag{F(2-2)}$$

$$v_B B \Leftrightarrow v_D D + n\,e^- \tag{F(2-3)}$$

For example, looking at the combination of lithium metal and silicon as an electrochemical cell, the reactions taking place are the following, with formula F(2-4) as the overall reaction and F(2-5) and F(2-6) as the oxidation and reduction:

$$\mathrm{x\,Li + Si \Leftrightarrow Li_xSi} \tag{F(2-4)}$$

$$\mathrm{x\,Li \Leftrightarrow x\,Li^+ + x\,e^-} \tag{F(2-5)}$$

$$\mathrm{Si + x\,Li^+ + x\,e^- \Leftrightarrow Li_xSi} \tag{F(2-6)}$$

Regarding the cathode materials used for current and future application, Lithium iron phosphate ($LiFePO_4$ or LFP) is a highly promising candidate from the olivine-type family, due to low

costs, non-toxic materials, safety and offers a specific capacity of 170 mAh g^{-1}. During the lithiation and delithiation, the LFP cathode undergoes a single phase transition from $LiFePO_4$ to $FePO_4$:

$$x\,Li + Li_{(1-x)}FePO_4 \Leftrightarrow LiFePO_4 \quad \text{F(2-7)}$$

$$x\,Li \Leftrightarrow x\,Li^+ + x\,e^- \quad \text{F(2-8)}$$

$$Li_{(1-x)}FePO_4 + x\,Li^+ + x\,e^- \Leftrightarrow LiFePO_4 \quad \text{F(2-9)}$$

Side reactions play a major role in the aging of the battery cells, since they consume lithium and increase the resistance of the cell [22]. Two main products of the side reactions are LiF, LiOH, Li_xPF_z, $Li_xPO_yF_z$ and Li_2CO_3. There are several reaction mechanisms proposed in the literature for the production of these species. The most important are the decomposition of the lithium salt in the electrolyte F(2-10) and the decomposition of the electrolyte with the generation of gas F(2-11). These reactions are only an example for the decomposition of the electrolyte and the salt, there are several reactions happening simultaneously. In total, the side reactions are irreversible and the consumed products are lost for further electrochemical and chemical reactions. Nevertheless, in the first cycles, the reaction products can redissolve into the electrolyte, but this is limited to the beginning of the cycle life of the cell [23,24].

$$LiPF_6 \Rightarrow LiF + PF_5 \quad \text{F(2-10)}$$

$$(CH_2O)_2CO + 2\,e^- + 2\,Li^+ \Rightarrow Li_2CO_3 + C_2H_4(g) \quad \text{F(2-11)}$$

2.5 Degradation Mechanisms in Li-ion Batteries – Current State of Research

Since the commercial introduction of the Li-ion battery by Sony in 1991 there has been extensive study on the degradation of Li-ion batteries and the list of degradation mechanisms is up to now extremely comprehensive. However, the introduction and combination of new analysis methods and instruments provides further insights into the material and internal processes. Therefore, even after almost 30 years of commercialization, new insights on the degradation mechanism are still discovered.

The degradation mechanisms in Li-ions batteries can be divided into five groups, i) the morphology of the electrodes, ii) the electrolyte, iii) the separator, iv) the surface layers at the

interface between electrodes and electrolyte and v) the current collectors. Each group shows different mechanisms influencing the degradation. However, the main consequences of the degradation are the increase of impedance and the decrease in capacity.

2.5.1 Electrode Morphology

Electrolyte co-intercalation

The changes of the morphology are not only limited to the electrode surface, as well the bulk material exhibits morphological changes leading to the degradation of the battery. Nevertheless, the electrode-electrolyte interface is an important element for a stable operation of the battery. In the electrolyte, a solvation shell, due to the opposite charges of the Li-ions and electrolyte species, surrounds the Li-ions. During intercalation of the ions into the host, the solvation shell can intercalate as well into the host material leading to expansion of the host layer and finally resulting in the exfoliation of active material [22,25,26].

Generation of cracks

Linked to the co-intercalation of the electrolyte is the generation of cracks, which can be induced by co-intercalation, repeatedly volume changes during cycling, degradation of binder material and mechanical instability of the electrodes. These cracks can induce contact loss of the active material to the electrode or electrical conductive network, which leads to loss of active material and decrease the electrical conductivity of the electrode and therefore increase the impedance of the battery [27–30].

Structural changes

The electrode material is highly stressed during the cycling due to chemical and electrochemical influences. The cycling can generate lattice defects in the crystal structure of the active material, due to the oxidation and dissolution of oxygen into the electrolyte. These lattice defects can be filled with Li-ions or transition metal ions, leading to the loss of active material and the polarization of the electrode. Likewise, oxidation of the active material leads to the generation of an isolating oxide layer on the particles, which increases the impedance. A decrease of the electrode porosity increases the impedance further. The porosity is decreasing due to the generation of the solid electrolyte interface on the anode side and the solid permeable interface on the cathode side and clogging of the pores inside the electrode. The decrease of the porosity slows down the ionic diffusion and increases the impedance and polarization of the electrode. The particle size changes during aging, phase transitions and volume changes lead to cracking

of particles (*electrochemical milling*). Following the particle cracking, small particles tend to combine and generate bigger agglomerates, since bigger particles are energetically more stable than smaller ones. This process decreases the active area, generates inhomogeneity in temperature and state of charge inside the electrode, decreases the electric and ionic conductivity and therefore increases the impedance. Another mechanism affecting the structure of the electrode are phase changes due to changes in the chemical composition. Depending on the materials, phase changes can generate volume changes of 200 % and more as it is for the lithiation of silicon. These volume changes affect the mechanical stability and generate cracks in the electrode, as it is mentioned above. In addition, incomplete phase transitions can lead to the trapping of active material. The phase change from $LiFePO_4$ to $FePO_4$ and back is sometimes assumed to proceed by a core-shell mechanism. An incomplete phase transition traps lithium inside the core with $FePO_4$ surrounding it. Therefore, the trapping of lithium decreases the capacity due to the loss of active material. [22,29–39].

Dendrites

Dendrites are needle like structures consisting, in case of the battery, of lithium. The growth of dendrites is caused by different mechanisms such as i) a steep ionic concentration gradient in the electrolyte leading to the polarization at the electrode-electrolyte interface, ii) a non-uniform SEI layer generating current density variations and iii) differences in the diffusion speed and electric field due to rough surfaces [40]. Dendrites can grow through the separator and create a shortcut, which leads to the failure of the cell or even to a thermal run-away. In case the dendrite does not grow through the separator but breaks off, the active material is lost into the electrolyte, which leads to a capacity decrease [22,25,34,41–48].

2.5.2 Electrolyte

The decomposition of the electrolyte is affecting the impedance of the battery cell. It decomposes due to instability at certain potentials and due to the presence of dissolved transition metal ions. Some of the reaction products of the electrolyte decomposition are gaseous and can therefore generate pressure inside the cell and lead to delamination of carbon layers at the anode. Other decomposition reactions consume the electrolyte solvent and salt additive leading to an increase in the electrolyte impedance [22,23,25,42,47,49,50].

2.5.3 Separator

The main task of the separator is to isolate the cathode and anode electrically and, at the same time, act as a permeable layer for the Li-ions to travel back and forth between the electrodes. However, the porosity of the separator can decrease during cycling due to pore clogging with electrolyte components, oxidation of the separator material and deformation of the separator pore network due to external (e.g. external loading of the cell) or internal (e.g. SEI growth, gas generation or volume expansion of the electrode) compression. The mechanical stability of the separator is affected by the electrolyte, leading to swelling and softening of the separator. All of these effects increases the battery impedance and lower the permeability for ions [22,32,51–54].

2.5.4 Surface Layers on the Electrodes

Anode surface layer

The surface layer on the anode side is the *solid electrolyte interface* (SEI) and consists of decomposition products due to reduction of the electrolyte. The first decomposition products are considered to be organic species. At lower potentials, these organic species are partially transformed to inorganic precipitants. The SEI is mainly generated during the first few cycles and ideally stays stable during the further aging. However, partial damages of the SEI can induce further growth of the layer, which is accompanied by further decomposition of the electrolyte and consumption of electrolyte salt, and lithium, which leads to a decrease of the capacity and an increase of the impedance, due to the reduced ionic conductivity of the electrolyte. Some side reactions are accompanied by the generation of gaseous reaction products, these products induce cracks in the SEI and generate new SEI growth. In addition, the gas increases the pressure inside the cell, which can lead to leakages [22,25,29,32,47,55,56].

Cathode surface layer

Similar to the anode, the cathode surface forms a surface layer with decomposition products due to oxidation of the electrolyte as well. Edström et al. proposed the name *solid permeable interface* (SPI) for the cathode surface layer. Contrary to the SEI, the SPI does not cover the entire cathode surface and grows over the entire lifetime of the electrode. The layer consists of organic and inorganic decomposition products. The inorganic species show a dependency on the electrode material, while the formed organic species are generally the same. The surface layer reduces the electronic conductivity, hinders ionic diffusion and therefore increases the impedance of the electrode. In case the conductivity is not only reduced, but the particle is entirely isolated, the capacity decreases, due to the loss of active material [25,29,32,36,41,57–59].

Lithium plating

The deposition of a lithium metal layer on the surface of the anode emerges mainly at low temperatures during the charging process. Due to the reduced diffusion at low temperatures, the Li-ion intercalation is hindered. This leads to the accumulation of Li-ions at the surface and finally to the deposition. High charging rates and high potentials are amplifying the effect. Electrode misbalancing can influence the probability of lithium plating. In case the anode capacity is too small, Li-ion intercalation is blocked at a certain point and the remaining Li-ions are depositing on the anode surface. The process is partly reversible and lithium is stripped off the anode surface during discharge. However, some of the lithium is lost, which leads to the reduction in capacity. The deposited lithium is reacting with the electrolyte forming a SEI layer, which reduces the ionic conductivity of the electrolyte and increases the impedance, due to the additional surface layer. Additionally, the metallic surface layer reduces the electrode porosity and therefore reduces the active material surface, which increases the current density on the remaining material surface and amplifies the lithium plating. In addition, active material can get isolated, which reduces the capacity [22,32,60].

2.5.5 Current Collector

The current collector serves as an electrically conductive substrate for the electrode material. Since it is also in contact with the electrolyte, side reactions can lead to the corrosion of the current collector surface. Corrosion increases the impedance of the cell, since the contact resistance between electrode material and current collector increases. Moreover, the increase of the contact resistance increases the ohmic overpotentials. Additionally, corrosion leads to inhomogeneous current distributions in the electrode, which facilitates lithium plating. Severe current collector corrosion leads to the contact loss between collector and active material and therefore to a decrease of the capacity [22,31,48,61].

2.5.6 Degradation Mechanism Summary

The degradation mechanisms can be put into two groups, in the first group are mechanisms leading to a capacity decrease and in the second group are mechanisms leading to an increase of the overall cell impedance.

Capacity decrease:

- Co-intercalation of electrolyte with resulting delamination of electrode material

- Agglomeration of particles
- Dissolution of active material into the electrolyte with resulting deposition on the anode surface
- Generation of dendrites on the anode surface
- Incomplete phase transitions with isolated active material
- Consumption of active material, due to surface layer build-up on the electrodes
- Electrically isolation of active material

Impedance increase:

- Decrease of the electrode and separator porosity
- Decomposition of the electrolyte
- Build-up of additional surface layers on the electrodes (SEI, SPI, Li plating)
- Corrosion of the current collectors
- Decrease of electrical conductive electrode network
- Increase of diffusion length inside particles due to agglomeration

3 Measurement and Analysis Methods

This chapter describes the methods and analysis tools used for examine battery electrode degradation. Part of this work has already been published in the same or similar form in [62,63].

3.1 Atomic Force Microscopy

Atomic force microscopy (AFM) is one technique out of the group of scanning probe microscopy (SPM). It is based on the general principle of scanning tunnelling microscopy (STM), which uses a similar set-up. STM was primary introduced by Binning and Rohrer in 1979 [64]. The STM technique uses a sharp, needle-like tip, which is scanned in close contact over the surface of the sample. The lift height of the tip over the sample surface is controlled by the tunnelling current measured between the tip and the sample. Since the feedback loop of the microscope is depending on the tunnelling current, utilization of STM is limited to conductive materials in vacuum.

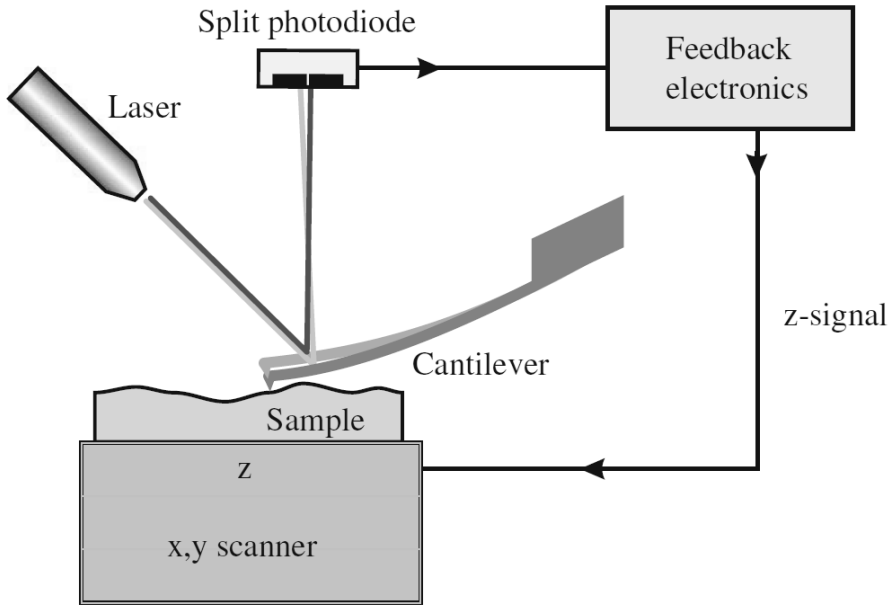

Figure 3-1: Principle set-up of an AFM [65]

AFM, developed by Binning and his co-workers [66], is an advanced SPM technique, which uses a cantilever with a tip at the end to track the sample surface. The tip can be constantly in contact with the surface (contact mode) with a constant deflection of the cantilever as set-point, oscillate over the sample and touch the surface frequently (intermittent mode) or lifted over the sample surface and oscillating with no contact at all (non-contact mode). To track the bending of the AFM tip due to the interaction with the surface, a laser is focused on the end of the cantilever

and reflected onto a photodiode with four quadrant. Figure 3-1 illustrates the principle set-up of an AFM. Due to the intensity differences on the photodiode quadrant, the vertical and lateral displacement is tracked. The signal of the photodiode is fed to the feedback loop of the control system and used to adjust the actual set-point to the desired value. AFM analysis provides high-resolution images comparable to Transmission Electron Microscopy (TEM) down to the visualization of atoms [65]. At the same time, more advanced AFM modes deliver not only the surface topography, but also material properties like elasticity, stiffness, work function and conductivity. In addition, the measurement environment is not limited to vacuum, as it is for TEM analysis, but can be in ambient air or in liquids.

There are different ways to extract material properties from AFM measurements. Either by force-distance curves or by analysing the change in amplitude and frequency shifts in the oscillation of the AFM tip [65,67–69]. For the measurements presented here, force-distance curves are used to extract the material properties. An example of a force-distance curve is shown in Figure 3-2. The black solid line represents the approach of the tip towards the sample surface. With decreasing distance between the tip and the surface, a negative force due to attracting forces between the tip and the surface emerges. At a certain distance between the tip and the surface a snap-in of the tip towards the surface occurs, now the tip is in contact with the sample surface. With the further movement of the piezo towards the sample surface, the repulsion force increases, the cantilever of the AFM tip starts bending and a deformation occurs. Ideally, the deformation is reversible and limited to the sample surface. Worst case, the deformation is irreversible and only limited to the tip, which leads to degradation and destruction of the tip. Which of these two cases occurs is depending on the surface stiffness, spring constant of the tip, surface roughness, applied force and tip material.

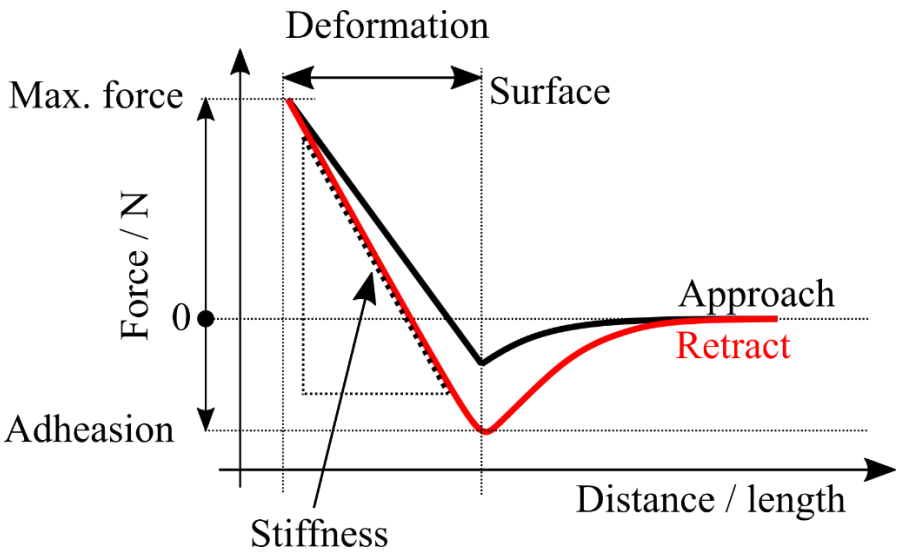

Figure 3-2: Example of a force-distance curve

Figure 3-3 gives an example for some material properties extracted from force-distance curves. The sample is a silicon composite anode fabricated at the German Aerospace Centre in Stuttgart. The marked areas are examples for differences in the material properties. Figure 3-3b) is the adhesion and c) is the DMT (Derjaguin, Muller and Toporov) Modulus, which represents the stiffness of the material, without any clear visible difference in the topography in a).

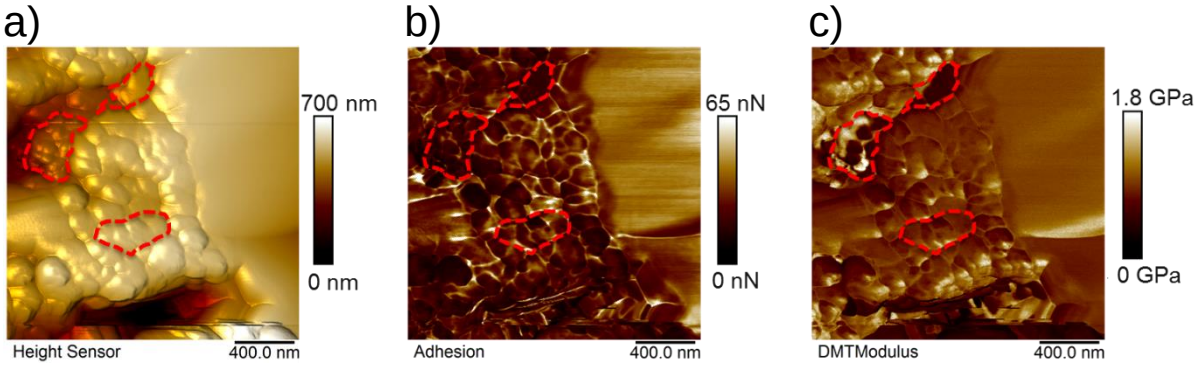

Figure 3-3: Example of an AFM measurement showing a) the topography, b) the adhesion and c) the DMT Modulus. The marked areas are examples for different behaviours of the material properties.

The AFM tips are generally made from silicon or doped silicon and fabricated by an anisotropic wet etching technique using for example potassium hydroxide (KOH). In several etching and coating steps, the shape of the AFM tip is etched out of bulk material. Afterwards, surface coatings are added to increase the laser beam reflection on the top side or to add an electric conductive or magnetic layer on the tip side of the AFM cantilever [65]. Figure 3-4 shows some examples of AFM tips, a) shows the tip with part of the cantilever and b) is a zoom onto the very end of another AFM tip, which has a tip radius of about 25 nm.

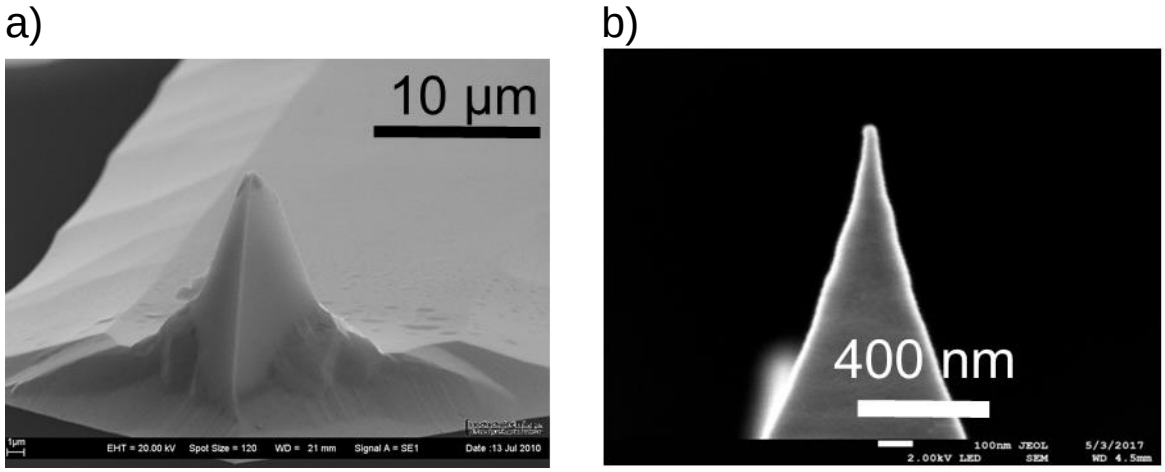

Figure 3-4: a) SEM image of an AFM tip, b) zoom onto the tip

The AFM measurements presented were performed using a Bruker Icon installed inside a MBraun Glovebox.

For the AFM analysis, various signals are presented, (i) the height image, which represents the sample topography, (ii) the Peak Force Error, which is the feedback signal for the set-point control and serves as a representation of the sample surface, without the influence of height differences, (iii) the adhesion, which is the force needed to detach the AFM probe from the sample surface and (iv) the Peak Current, which is the measured electrical current during the time of the highest force and (v) the DMT-modulus, which represents the stiffness of the sample. For the conductivity measurements, a bias voltage of usually 3.0 V was applied between tip and sample. Commercially available AFM tips from NT-MDT (Etalon HA_FM/W2C+, 75 kHz, 3.5 N/m) with an electrical conductive W_2C coating or Bruker (SCM-PIT, 75 kHz, 3.0 N/m) with an electrical conductive Pt-Ir coating are used. Analysis of AFM measurements was conducted using NanoScope Analysis 1.9 software.

3.2 Scanning Electron Microscopy and Energy Dispersive X-ray Spectroscopy

In scanning electron microscopy (SEM) a focused electron beam is scanned over the sample surface. Different detectors detect the electrons scattered from the sample surface and the intensity of the scattered electrons is transformed into a grey scale image. The primary electrons (PE) are emitted either by thermionic emission or by field electron emission. In thermionic

emission, a filament cathode, usually tungsten, is heated up, which leads to the emission of electrons. In field electron emission, a high negative potential is applied to an electron emitter, creating high extraction fields of more than 10^9 V m^{-1}, which finally leads to the emission of primary electrons. The emitted primary electrons are focused by magnetic lenses and used to scan the focused electron beam over specific locations on the sample surface. The sample chamber is operated under vacuum during the measurements to minimize the contamination on the primary electron source and to reduce attenuation of the energy of the primary electrons by interactions with particles in the sample chamber.

The primary electrons are generating various signals after striking the sample surface (see Figure 3-5a), such as secondary and backscatter electrons, X-ray photons, visible light photons and Auger electrons. For imaging of the sample surface the secondary and backscatter electrons are used. Secondary electrons (SE) are generated by collision of the primary electrons with valence band electrons of the sample, which are afterwards emitted from the sample. Back-scattered electrons (BSE) are primary electrons, which propagate through the sample by recurring collisions and are emitted again from the sample. For the evaluation of elements in the sample, the X-ray photons are used. This technique is called energy dispersive X-ray spectroscopy (EDX), the signal generation is shown in Figure 3-5b) [70]. The electrons in the core shells are ionized by the incident PE beam, leaving behind a hole, which is filled by another electron from an outer shell. The drop of electrons from the outer shell leads to the emission of a characteristic X-ray fluorescence line. In the case shown in Figure 3-5b), the 1s electron is ionized and leaves behind a hole, which is filled by a 2s electron from the outer shell. The drop from the 2s shell to the 1s shell leads to the emission of a Kα X-ray with a specific energy, which is characteristic for each individual element. Depending on the shell level, from which the hole-filling electron is originating either Kα or Kβ (drop from M or L to K shell) or Lα or Lβ (drop from M to L shell) X-rays are emitted.

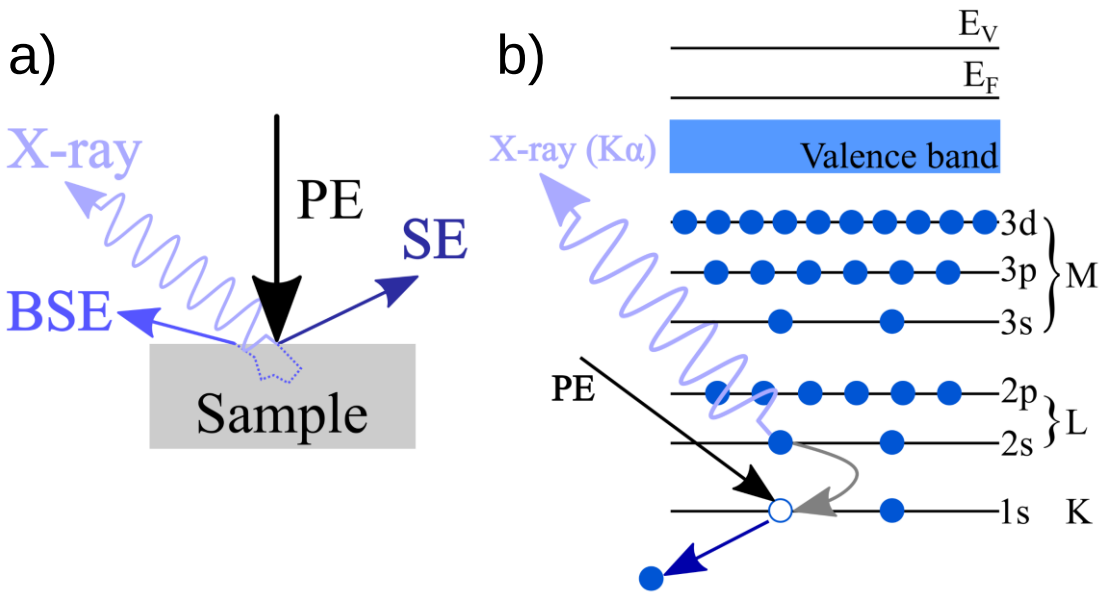

Figure 3-5: a) generation of SE, BSE and X-ray by the focused PE electron beam from the sample surface and b) signal generation for the detection of the element specific X-ray for EDX analysis

The SEM and EDX measurements were performed using a Jeol JSM-7200F equipped with a Bruker Quantax EDX system. Cross-section cuts were conducted using an unfocused Ar ion beam (Jeol IB-19520 CCP, 6kV for 4h) equipped with a sample transfer chamber, to avoid any contact with the ambient air during the preparation process [71].

3.3 X-ray Photoelectron Spectroscopy

X-ray photoelectron spectroscopy (XPS) is used to analyse the chemical composition and chemical bonding of surface layers with a thickness of up to 10 nm. Except for helium and hydrogen, all other elements can be observed.

The X-ray photon irradiation on the sample surface with the energy $h\nu$ leads to the photoemission of core level electrons with a specific kinetic energy, if the excitation energy is sufficient for the electron to leave the sample. The binding energy is then afterwards calculated by the known X-ray photon energy, the measured kinetic energy of the emitted electron and the work function of the spectrometer. Each element has a characteristic binding energy and shifts in the binding energy provide information about the binding state.

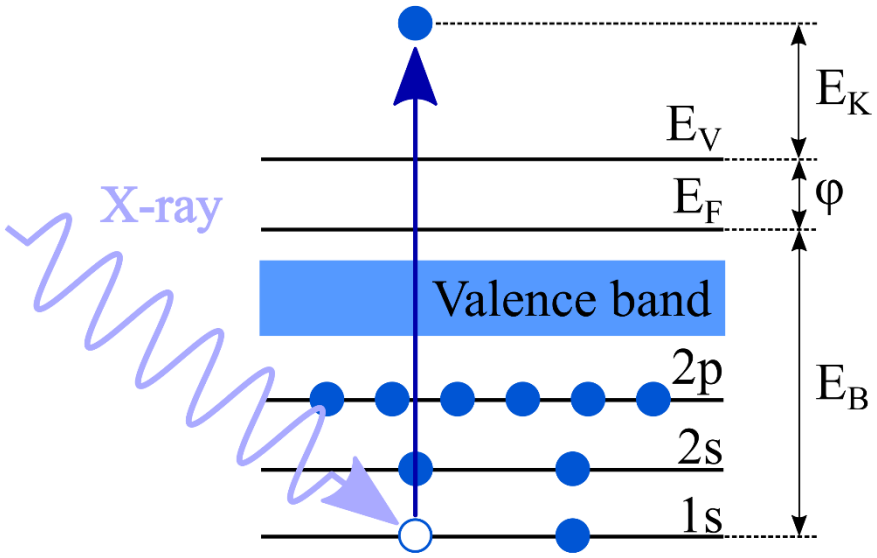

Figure 3-6: Illustration of the emission of an electron from the 2p level by X-rad photo irradiation. 1s, 2s and 2p are representing core levels, E_V the vacuum level, E_F the Fermi level, E_K the kinetic energy, φ the work function of the sample and E_B the binding energy.

In Figure 3-6, the illustration of the emission of an electron from the core level by the X-ray photon irradiation is displayed. In case the excitation energy $h\nu$ from the X-ray photon exceeds the binding energy E_B and the work function of the sample φ, the electron is ejected from the sample.

The results of the XPS analysis presented here was conducted using an Al Kα source with an energy of 1486.6 eV and a hemispherical analyser (Thermo Scientific ESCALAB 250) at a base pressure of $2x10^{-10}$ mbar. Spectra were energy calibrated with reference to the $Ag3d_{3/2}$ signal of a clean etched silver surface. Spectra are displayed normalised, and numerical peak signal fitting was carried out using Voigt peak shapes using OriginLab software. Depth profiling was carried out by Ar^+ ion bombardment at argon pressure of ~$2.5x10^{-8}$ mbar and with an average sample current of 2.0 µA.

3.4 Electrochemical Impedance Spectroscopy

Electrochemical impedance spectroscopy (EIS) is a powerful tool for the investigation of electrochemical reactions and transport processes inside a system. In combination with the fitting of electric circuits to the resulting spectra, physical parameters like resistances and capacitances can be extracted. The basic concept is the measurement of a resulting electrical response of a system, due to the application of a voltage or current signal. The response has the same frequency as the applied signal, but is usually shifted in the phase. The theoretical

treatment of the system is done in the frequency domain, since the solutions in time domain contain differential equation. Thus, the impedance can be written as:

$$Z(i,\omega) = \frac{F\{V(t)\}}{F\{I(t)\}} \tag{3.1}$$

Here, $F\{\}$ represents the Fourier transformation of the voltage and current signal and $Z(i,\omega)$ the impedance in imaginary and frequency space. The impedance is the sum of the real (3.3) and imaginary part (3.4), which are depending on the phase angle θ.

$$Z(i,\omega) = Z' + i\,Z'' \tag{3.2}$$

$$\mathrm{Re}(Z) = Z'(i,\omega) = |Z|\,\cos\theta \tag{3.3}$$

$$\mathrm{Im}(Z) = Z''(i,\omega) = |Z|\,\sin\theta \tag{3.4}$$

Even though electrochemical cells are non-linear systems, small excitations can result in a linear response of the system. The linear response is needed to validate the use of Ohm's law in equation (3.1), for non-linear responses, the theoretical treatment gets more complicated and the given equations do not hold anymore. For potentiostatic EIS, small excitations are voltage amplitudes below the thermal voltage $V_T = RT/F$ which is about 25 mV at room temperature, in the literature the voltage amplitude is normally in the range of about 5 – 10 mV.

The disadvantage of EIS is the sensitivity of the results to external interferences, system stability and internal noise. Therefore, it is necessary to use a faradaic cage if possible, to minimize the contact resistances at connections and the inductive influence of cables and to shield the electrochemical cell from interferences coming from the counter and working electrodes. Additionally, the system needs to be at equilibrium and it needs to be assured, that the response is solely due to the applied excitation [15,72].

3.5 Incremental Capacity and Differential Voltage Analysis

Incremental capacity analysis (ICA) and its counterpart differential voltage analysis (DVA) are non-destructive techniques to investigate phase changes and intercalation of ions during electrochemical processes [73,74]. It was first applied by Balewski and Brenet in 1967 for half cells [75]. Thompson used a similar technique to analyse the ordering of lithium ions in TiS_2 crystal layers [76], Dahn determined the staging steps of lithium ions in graphite [77] and several groups are using it to reveal the degradation mechanisms in Li-ion batteries [35,48,73,78–84]. It is used to monitor the ageing of the cell and can serve as a tool to estimate the state of health (SOH) of the cell [85–90]. We are using ICA and DVA for the evaluation of the degradation mechanisms, since these techniques are complementary to each other and can be used as a

verification of observed degradation mechanisms. However, certain degradation mechanisms such as the change of cell impedance is only observed in the ICA curves, while loss of lithium inventory and loss of active material are more clearly observed in the DVA curves. Therefore, both methods are employed for the evaluation of the degradation mechanisms.

Peaks in the ICA curves represent staging or intercalation of ions during one phase equilibrium. In DVA curves, the peaks represent the phase transitions [48,73,82,91]. Even though the system should be at or near equilibrium for the calculation of the ICA and DVA, the analysis delivers reasonable results at C-rates around 1C. Weng et al. show that a C/2 rate for the charge and discharge process can be used for the identification of the peaks in ICA curves [89] and Dubarry et al. use C/5 and C/2 rates to determine the ICA. In their investigation it is observed, that some ICA peaks have a rate dependency and that in general lower C-rates show more distinguishable peaks [83]. Li et al. compare C/25 with 1C discharging current. The main peaks are visible in both discharging rates, but with C/25, additional, less pronounced peaks are observable [86]. The presented ICA and DVA results are derived from C/2 measurements, knowing that the system is not at equilibrium. However, all expected peaks are observed with sufficient intensity (five peaks for the ICA and four peaks for the DVA) for the peak tracking over ageing.

The ICA is defined as the derivative of charge or discharge capacity Q with respect to the voltage V and is written as *dQ/dV*. For the numerical calculation of the ICA the derivative *dQ/dV* is approximated by $\Delta Q/\Delta V$ where the step size Δ is chosen to minimize the noise without losing any significance of the ICA peaks. The DVA is defined as the derivative of the voltage V in respect to the capacity Q and is written as *dV/dQ*. As for the ICA, the derivative is approximated with $\Delta V/\Delta Q$. Afterwards, smoothing of the resulting curves is done with different techniques. Division by zero can occur in the ICA (due to flat voltage profiles during phase transitions, dV can be equal to zero), but this does not hinder the analysis of the ICA data [73]. Noise reduction in the ICA and DVA curves is done using standard techniques such as moving mean average [86,92], Gaussian filter [86], support vector regression [88,90] and centre least square method [90]. We used the moving mean average filter to reduce noise in the data with a moving window of 50 data points for ICA and DVA arrays with a length of about 6400 data points. Application of the moving mean filter did not have any significant influence on peak intensity and location. The charge and discharge processes were recorded with the battery cycler (CTS-XL, BaSyTec GmbH) and analysed in Matlab® (Release 2018).

An example for the resulting ICA and DVA curves and the corresponding features of the discharge potential profile is presented in Figure 3-7. It shows a potential profile of a discharge process of a fresh, commercial LFP cell (Figure 3-7a) and the resulting ICA (Figure 3-7b) and DVA (Figure 3-7c) curves. The visualization shows the transformation of potential plateaus into peaks for the ICA and valleys of the DVA. The transitions from one potential plateau to the next are transformed into peaks in the DVA and valleys in the ICA [93].

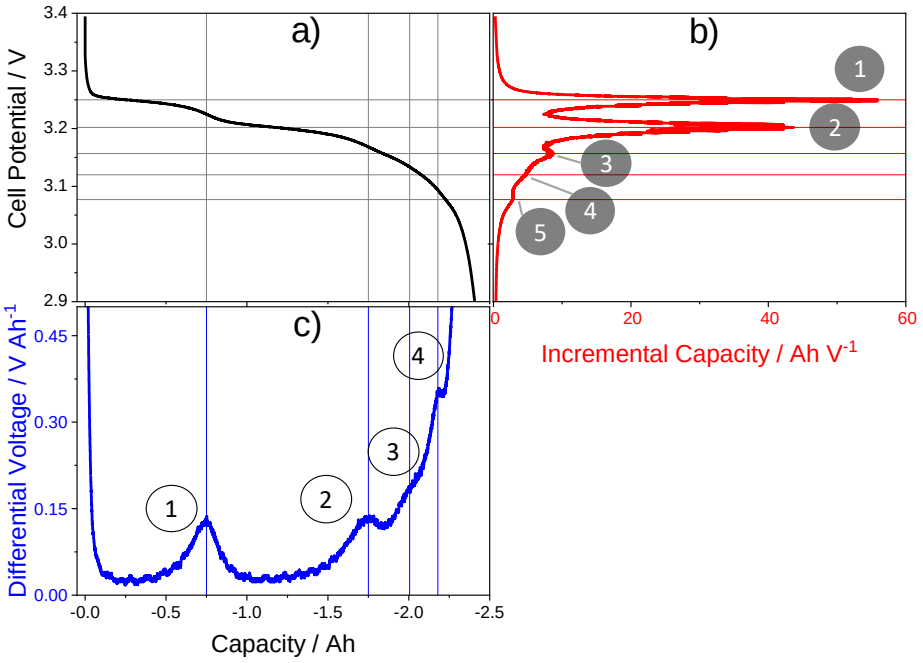

Figure 3-7: Discharge profile of a fresh LFP cell in a) and the resulting ICA (b) and DVA (c) curves [93]

3.6 Pseudo-OCV and non-equilibrium OCV tracking

The OCV was evaluated using C/2 charging and discharging curves to calculate the pseudo-OCV curve with $E_{OCV} = {}^{1}/_{2}\,(E_C + E_D)$. Additionally, a here so-called non-equilibrium OCV (nonequi-OCV) for the EOC and EOD was recorded using the cell resting voltage after charging or discharging with 1C to the cut-off voltage and with only five minutes of resting time. The evolution of the OCV shows, that the system does not reach electrochemical equilibrium after five minutes, hence the denotation non-equilibrium OCV.

4 Focus on Electrochemical Strain Microscopy Technique

4.1 Principle of Electrochemical Strain Microscopy (ESM) and the Tailored ESM Technique

The principle set-up and underlying signal formation principle are presented in Figure 4-1.

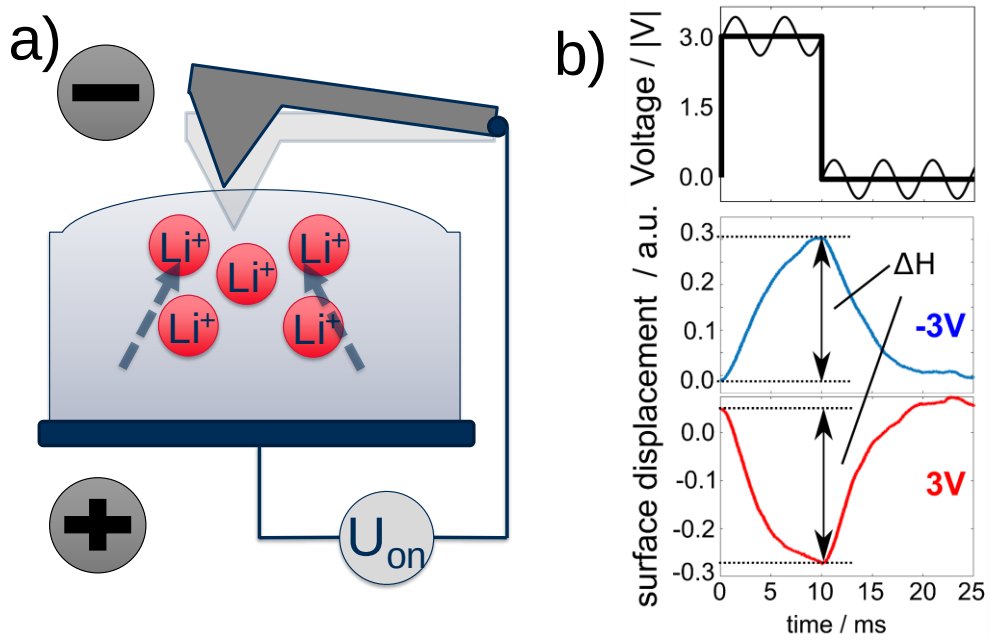

Figure 4-1: Basic signal formation principle (a) and application of the voltage step with resulting surface displacements, called ESM signal (b).

The tailored time domain ESM (t-ESM) technique uses a different approach compared to the originally published technique by Balke et al. [94] and was proposed as time domain measurements performed by Jesse et al. [95]. In the original technique of Balke et al., an ac-voltage is applied between the tip and the sample, which is assumed to induce an oscillation of the ions in the solid sample. The oscillation of the ions induces an oscillating volume change and is transferred to the sample surface. Its movement is measured as deflection of the AFM tip. In the time domain measurement, a dc-voltage of several milliseconds is applied to the tip to induce a concentration change, which is tracked using the surface displacement amplitude at the ac-voltage frequency. To increase the sensitivity of the measurement, the signal can be amplified using the contact resonance frequency of the AFM tip with the sample-tip contact resonance frequency as the driving frequency of the applied ac-voltage. Since the contact resonance frequency is linked to the material properties and topography, it changes during the

surface scan and needs to be tracked using a phase looked loop (PLL) [21,96,97], dual resonance frequency tracking (DRFT or DART) [98,99], or band excitation (BE) [100–102]. Hence, errors in the tracking of the resonance frequency may lead to artefacts in the data. Using just a single frequency out of the contact resonance range leads to a lower amplification, but has the advantage that it is insensitive to material properties and topography crosstalk.

In a first approach, the relationship between the change in ionic concentration and the surface strain $\varepsilon_{i,j}$ is given by Hooke's law in equation (4.1) [20,103–106].

$$\varepsilon_{i,j} = \beta_{i,j}\, \delta c_{i,j}^{Li} + \frac{1+\nu}{E}\, \sigma_{i,j} \tag{4.1}$$

The first term on the right-hand side $\beta_{i,j}\, \delta c_{i,j}^{Li}$ represents the chemical contribution to the strain, while the second term on the right-hand side $\frac{1+\nu}{E}\, \sigma_{i,j}$ represents the contribution of internal stress. In this case, $\beta_{i,j}$ is the Vegard expansion tensor, $\delta c_{i,j}^{Li}$ is the change in Li-ion concentration, ν is the Poisson's ratio, E is the modulus of elasticity and $\sigma_{i,j}$ are the stress components. Other contributions to the surface strain are discussed in section 4.2, but are assumed to play a minor role and are neglected. Following the implications of equation (4.1) with the assumption that the chemical component is the only relevant contribution to the surface strain, it can be concluded that the change in Li-ion concentration $\delta c_{i,j}^{Li}$ is proportional to the resulting surface strain $\varepsilon_{i,j}$. Morozovska et al. presented a general solution for the surface displacement $u_{i,j}$ based on the strain from equation (4.1) [107]. Their solution demonstrates that the surface displacement $u_{i,j}$ is proportional to the concentration change of the ionic species and dependent on the Vegard expansion tensor, which is expressed in equation (4.2) [21].

$$u_{i,j} \propto \beta_{i,j}\, \delta c_{i,j}^{Li} \tag{4.2}$$

Therefore, the resulting surface displacement amplitude is proportional to the change in Li-ion concentration $\delta c_{i,j}^{Li}$, which is linked to the mobility of the ions in the material beneath the tip [101,108,109]. The change in surface displacement amplitude is therefore correlated to the change in ionic concentration, and in addition the transient behavior to the diffusion of the ions.

The measurement is divided in two time periods. In the first period the electric field is the driving force for the ionic movement, while at the same time, the concentration gradient is directed in the opposite direction of the electric field hindering the migration (migration/ diffusion). This yields an effective migration/ diffusion coefficient D1. In the second period, the driving force is the concentration gradient, which is induced by the increased/decreased

local ion concentration built up by the migration in the first range and leads to a diffusion coefficient D2, which is solely caused by the concentration gradient.

$$c(x,t) = A_0 \exp(\frac{-x^2}{4Dt}) \quad (4.3)$$

$$c^*(x,t) = a \exp(-b\,t) + c \quad (4.4)$$

Local diffusion coefficients were extracted by fitting the data points retrieved from the expansion/retraction curves. The analytical solution for the diffusion calculated thereby is given in equation (4.3) with the diffusion coefficient D and a pre-exponential component $A_{0.}$ Jesse et al., Luchkin et al. and Guo et al. proposed an exponential behavior as it is seen in equation (4.3) [95,108,110–112]. The characteristic time constant with $b = {}^{1}/_{\tau_{x,y}}$ was retrieved using equation (4.4), the diffusion coefficient was calculated using $D_{x,y} = \frac{l^2}{\tau_{x,y}}$. The characteristic length l is the tip radius.

Depending on the polarization, the local ionic concentration beneath the tip increases or decreases, accompanied by a surface expansion or contraction and is recorded by the vertical deflection of the tip. During the applied voltage pulse, migration and diffusion take place in opposite directions; after the applied voltage pulse relaxations takes place due to pure diffusion. With this set-up, the change of local ionic concentration and the dynamic movement of ions are mapped simultaneously. The dependence on time of the characteristic time constants for every image point delivers local information on the diffusion and migration of the ions in the material [62].

4.1.1 Measurement Set-Up

The experimental set-up used is shown in Figure Figure 4-1a. A Bruker Icon system installed inside a glovebox, equipped with PeakForce Mode and a Zurich Instruments (HF2LI) lock-in is used. As AFM probes either Bruker SCM-PIT with a spring constant of 2.8 N/m, Pt/Ir coating and a resonance frequency of approximately 75 kHz or probes from NT-MDT with 3.5 N/m, W_2C coating and a resonance frequency of approximately 77 kHz were used. Voltage pulse generation and data recording was performed with a LabVIEW (V. 2016) routine on an additional computer. The voltage pulses were applied directly to the AFM tip using a modified PFM module with an amplitude of 3 V for the dc-voltage pulses and 2 V for the superimposed ac-excitation at 25 kHz or 40 kHz. The dc-voltage induces the change in the ionic concentration, which is tracked using the amplitude of the oscillating surface at the ac-voltage frequency and

further referred to as “surface displacement” with arbitrary units. The photodiode signals of the AFM were extracted using a Bruker break-out box (SAM V) and recorded with a National Instruments PCI card (NI 6111). The surface displacement signal is the real, in-phase signal amplitude (X) of the lock-in from the vertical deflection photo diode AFM signal. Morozovska et al. show, that the real part of the surface displacement is mainly determining the absolute signal, especially at lower frequencies for concentration driven processes, which corresponds to the dc-voltage off period of our measurement [107,113]. The proposed theory of Morozovska et al. is in agreement with our observation, namely the X signal showing nearly the same signal intensity compared to the amplitude R (Figure 4-2).

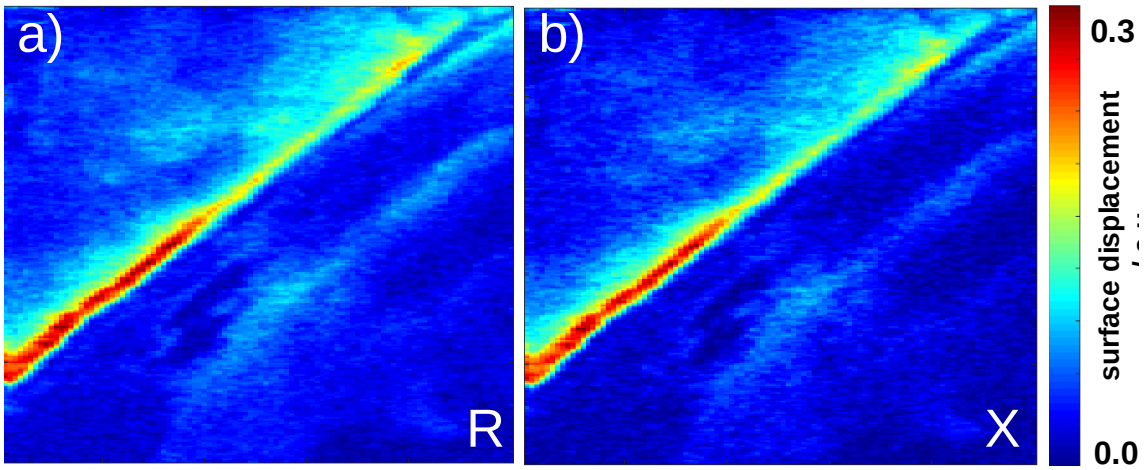

Figure 4-2: Amplitude R signal in a) and in-phase signal X in b) showing the same signal intensity [62]

The AFM measurements provide the two standard signals, the topography of the sample and the deflection error, which is the feedback signal of the control unit. The measurements are performed in contact mode with an additional interleave scan line. In the first scan line, the topography and deflection error are recorded as trace and retrace scans. This is the standard contact mode. In the second scan line, the tip scans the same location again. The voltage pulses are applied to the tip with a positive polarity during trace, and negative polarity during retrace. The standard scanning mode is not influenced by the applied potentials at the tip. The data analysis of the recorded AFM mappings was performed for every data point separately using MATLAB (Release 2018a) [62].

Tip calibration was performed by the thermal tune of the AFM with the adaption of the deflection sensitivity. The measurements have a pixel density of 256 x 100 measurement points,

which means that the pixels have a rectangular shape in the direction of the scan direction (left to right) and are not squares [63].

4.1.2 Measurement of Dynamic Behavior

An example of the recorded signal at one data point is given in Figure 4-1b) for a measurement on Si/C electrodes. The surface displacement (ESM signal amplitude, which is extracted from the vertical photo diode signal as the response of the ac-voltage) is drawn against the time. The middle part gives the surface displacement during the negative applied voltage step, the lower part the surface displacement due to a positive applied voltage step. The surface displacement is indicated as ΔH, which is the signal amplitude difference from the beginning of the voltage pulse to the end of the voltage pulse. If not otherwise stated a voltage step of ±3 V was applied for 10 ms, and recorded for further 15 ms to include the relaxation process. During the negative polarization of the tip, Li-ions are accumulating in the material and move towards the tip. In case of the positive polarization of the AFM tip, Li-ions are migrating in the opposite direction, away from the AFM tip. Using this set-up, differences in the response of ion movement due to the polarity at the AFM tip are recorded at the same location.

4.2 Vegard and Non-Vegard Contributions to the ESM Signal

Different effects are possible to influence the surface expansion of the sample surface. The main effects are discussed here. The surface displacement due to Vegard's law is assumed by some authors to be the main effect, causing the surface displacement in the ESM experiments [103,107,114]. Other groups are proposing different effects as the origin of the ESM signal. Amanieu et al. consider a Lorenz-like electric force to induce the ionic vibration in the lattice [21], while Lushta et al. [115] and Schön et al. [109] are assuming electrostatic forces to play a major role in the generation of the ESM signal [62].

4.2.1 Vegard's Law

Vegard reported in his work from 1921 changes he observed in the X-ray diffraction spectra of mixed crystals with different ionic salts and concentrations in the crystal [116,117]. Vegard showed, that at constant temperature, a linear relationship exists between the concentration of the ionic salt and the lattice constants. He proposed an "Additivitätsgesetz" which is now known as Vegard's law, it is given in (4.5). Here a_m is the lattice constant of the mixed crystal, a_A and

a_B the lattice constants of the pure elements and p the molar fraction in percent of the element a_B in the mixture.

$$a_m = \frac{p - 100}{100}\, a_A + \frac{p}{100}\, a_B \tag{4.5}$$

The idea behind this expression is the assumption, that the combined crystal cell is a simple combination of the atomic sizes of the individual, isolated elements [118]. The results using Vegard's law are often not precisely correct and deviations are observed. Therefore, it is an approximation for first analysis, but not an exact calculation [119–121].

Denton and Ashcroft identified the atomic size as one major impact on the crystal structure of the mixed crystal, but they point out, that other effects like relative volume per valence electron, Brillouin-zone effects and electrochemical differences of the elements, do have an influence on the lattice [117].

The contribution of the Vegard's law on the strain ε_V^A is dependent on the concentration change of the involved ionic species δc_A and the Vegard strain tensor $\beta_{i,j}^A$, given by:

$$\varepsilon_V^A = \beta_{i,j}^A\, \delta c_A \tag{4.6}$$

For simplification, the Vegard strain tensor is assumed to be isotropic and contains only entries on the main diagonal, so that $\beta_{i,j}^A = \beta_{11}^A = \beta_{22}^A = \beta_{33}^A = \beta^A$ [103].

Morozovska et al. derived approximations for the surface displacement during $u_V^A(t < t_0)$ and after the voltage pulse $u_V^A(t > t_0)$ for the assumption of an ionic flux driven process [107].

$$u_V^A(t < t_0) \approx -(1 + \nu) \cdot \left(\frac{4\, \beta^A\, V_0}{\sqrt{\pi}}\right) \cdot \sqrt{Dt} \tag{4.7}$$

$$u_V^A(t > t_0) \approx -(1 + \nu) \cdot \left(\frac{4\, \beta^A R_0^2 t_0}{6\, \sqrt{\pi D}\, t^{3/2}}\right) \tag{4.8}$$

Here, t_0 and V_0 are the duration and amplitude of the voltage pulse, R_0 is the AFM tip radius and D is the diffusion coefficient.

4.2.2 Piezoelectricity, Flexoelectricity and Electrostriction

The piezoelectric effect can occur either as the direct or as the inverse piezoelectric effect. In the direct piezoelectric effect, an applied force working on the crystal lattice displaces the equilibrium arrangement of the atoms. In equilibrium, the net charge is zero, since the opposite charges cancel out. In case of a deformation due to an applied force, the centres of the positive and negative charge do not align anymore, which induces a polarization of the crystal. For the inverse piezoelectric effect, an electric field induces a change of the polarization out of the equilibrium position, which induces stress and leads to a deformation.

Piezoelectricity is only found in crystals, which show a non-centrosymmetric crystal lattice. If the change in temperature of the materials leads to a change of the polarization due to volume change, the material is additionally pyroelectric. If the polarisation of the crystal can be switched by an electric field, the material is ferroelectric [118].

Flexoelectricity is similar to piezoelectricity, a deformation induces polarization and vice versa. The crucial difference is the strain distribution. For the piezoelectric effect, polarization is coupled to a homogeneous strain, whereby for the flexoelectric effect, polarization is coupled to a strain gradient. In contrary to the piezoelectric effect, which is only observed in non-centrosymmetric crystals, flexoelectricity can appear in all material structures [122]. Especially for electric fields generated by AFM tips, flexoelectricity should be considered in the analysis of the results of ESM measurements, since the generated strains due to ionic redistribution are likely not homogeneously distributed in the material. Ma calculated the stress due to flexoelectricity, induced by an AFM tip in a ferroelectric perovskite, in the order of several GPa with only 1 V applied to the tip [123]. Flexoelectricity is more likely influencing the ESM measurements compared to piezoelectricity when assuming the stress in the material due to the difference in ionic concentration, which is indeed not homogeneous. In addition, for polycrystalline materials, piezoelectricity should play a minor role, since the net polarization change is zero due to the polycrystalline arrangement of the dipoles [118].

The strain due to piezoelectricity and flexoelectricity is given by:

$$\varepsilon_{P,Z}^{A} = g_{lij}^{*} P_l + \Omega_{ijkl} \frac{\partial P_l}{\partial x_k} \tag{4.9}$$

With g_{lij}^{*} as the converse piezoelectric tensor, Ω_{ijkl} the flexoelectric strain tensor, P_l the polarization and x_k as the coordinate [123].

Electrostriction is the generation of mechanical strain based on the electrical polarization. The electromechanical strain ε_E^A based on electrostriction can be simplified for materials with a centre of symmetry and by neglecting higher order polarization as:

$$\varepsilon_E^A = Q_{ijmn} P_m P_n \tag{4.10}$$

In equation (4.10), Q_{ijmn} represents the electrostriction tensor coefficient for symmetric materials (all odd locations of the tensor are zero) and P_m and P_n the polarization in the respective direction [124].

Piezoelectricity, flexoelectricity and electrostriction are assumed not to be the primary mechanism for the signal generation for the ESM measurements presented here, due to measurements on fresh silicon, Si/C anode, carbon, HOPG and polyether ether keton (PEEK), which did not show a signal generation dependency on the applied voltage profile.

Nevertheless, since ions are influencing these effects, especially electrostriction, it is difficult to rule them out completely in the lithiated samples. However, Kalinin and Morozovska are reporting their influence to be at least one order of magnitude smaller, compared to the Vegard expansion [103].

4.2.3 Electron-Phonon Coupling

In electron-phonon coupling, stress and strains in materials can lead to conduction band edge shifts and redistribution of the concentration of electrons in the conduction and holes in the valence band. As for the piezoelectric effect, the converse effect exists, in which strain and stress in materials is induced by band edge shift and concentration redistribution. The strain due to electron-phonon coupling can be expressed as:

$$\varepsilon_{ij}(r) = s_{ijkl}\sigma_{kl}(r) - \Xi^{C}_{kl}[n_C(r) - n_{C0}] - \Xi^{V}_{kl}[p(r) - p_0] \qquad (4.11)$$

With Ξ^{C}_{kl} and Ξ^{V}_{kl} as the deformation potential tensors of electrons in the conductive and holes in the valence band, $n_C(r)$ and $p(r)$ the density of electrons and holes in the conductive and valence band during the presence of strains, n_{C0} and p_0 the density of electrons and holes during equilibrium and s_{ijkl} as the tensor of elastic compliances [125].

The electron-hole and electron-phonon coupling are expected to be at least one order of magnitude smaller compared to Vegard expansion [103,125–127].

4.2.4 Electrostatic Influence

The electrostatic influence on the ESM signal is generated by two different mechanisms. The first mechanism contributes to the ESM signal by the electrostatic force generated by the polarized AFM tip and acting on the tip and the cantilever and therefore influencing the bending of the cantilever [128–131]. This influence is not related to the movement or presence of ions and can therefore generate wrong interpretation of the underlying ESM signal. The second mechanism, which is contributing to the ESM signal and based on the presence of charges in the material, is the force acting on the cantilever due to the attractive or repulsive force generated by the polarized AFM tip and charges trapped inside the material [132]. However, a highly polarized AFM tip can inject charges into the material surface. Afterwards, the injected charges influence the electrostatic force between the AFM tip and the charges, which have been already present before [128,131,133,134]. However, charge injection from the AFM tip is unlikely, since only small voltage amplitudes are used, but cannot be ruled out completely. Trapped charges and charge injection would have occurred at the fresh samples during the control

experiments, which were not observed. The influence of surface and space charges can be evaluated using the Maxwell-Wagner relaxation time. Using typical values for the dielectric permittivity of LFP (between 5 and 12 [135]) and the electrical conductivity of around 10^{-6} S/m [136], the relaxation time ($\tau = \frac{\varepsilon\varepsilon_0}{4\pi\sigma}$, with $\varepsilon_0 = 8.85 \cdot 10^{-12}$ As $V^{-1}m^{-1}$ leading to roughly 10^{-6} s and lower) is several orders of magnitude smaller than the measured signal relaxation time (around 10^{-3} – 10^{-1} s). For silicon, the dielectric permittivity of silicon is around 12 and the electrical conductivity around $1.5 \cdot 10^{-3}$ S/m, using these values leads to the relaxation time of roughly 10^{-8} s, which is several orders of magnitude smaller than the measured signal relaxation time (around 10^{-3} – 10^{-1} s) and values found in the literature for the relaxation time [95,110].

4.2.5 Lorentz-like Force

Some authors assume an electronic Lorentz-like force acting on the ions in the sample as the primary source of the ESM signal. The Lorentz force acts on charges within a magnetic or electric field. In case of the electric field, the force acts on moving and resting charges likewise. These authors assume that the ions do not hop from lattice site to another lattice site, which would lead to the Vegard expansion, but vibrate on the lattice site, due to the alternating electric field [21,109,115].

$$F_{AC} = \int_V z_{Li} c_{Li}(t) F E dV \tag{4.12}$$

In equation (4.12), z_{Li} represents the number of charges per Li-ions, $c_{Li}(t)$ the concentration of Li-ions in the volume varying with time, F the Faraday constant, E the electrical potential due to the varying AC voltage and V the volume, which is affected by the concentration change. The Lorenz-like force is assumed to be proportional to the measured signal intensity $S_{Li}(t)$ and $c_{Li}(t)$.

4.2.6 Temperature Influence

The ESM measurements are usually performed with the sample in mechanical, electrical, chemical and thermal equilibrium conditions. However, the application of electric potentials between the AFM tip and the sample surface can generate heat due to energy dissipation, since the tip-sample junction acts as a resistor. The dissipated energy Q, as well called Joule heating, is given in the simplest form:

$$Q = \frac{\Delta\phi}{R_{t-s}^2} \tag{4.13}$$

With $\Delta\phi$ as the electrical potential difference between the tip and the sample and R_{t-s}^2 as the contact resistance between tip and sample surface [137,138]. With the energy Q given and limiting the energy dissipation to the change of the temperature of the sample surface ΔT_s and a small, cubic volume element of the sample surface under the tip V_s, the change in temperature is given by:

$$\Delta T_s = \frac{Q}{V_s\, \rho_s\, c_p} \tag{4.14}$$

With ρ_s as the density of volume element of the sample surface, which is influenced by the heating, and c_p as the heat capacity of the sample surface at constant pressure [118]. The change in temperature follows a strain ε_T^A or deformation u_T^A of the sample surface:

$$\varepsilon_T^A = \alpha_S\, \Delta T_s \tag{4.15}$$

$$u_T^A = \int_{l_0}^{l^V} \alpha_S\, \Delta T_s \tag{4.16}$$

Here, α_S is the thermal expansion coefficient of the sample surface and $l_0^{V_s}$ is the vertical length of the volume element [139,140]. Assuming a contact resistance of 100 MOhm between a conductive tip and the sample , a potential difference of 10 V, a volume of $1 \cdot 10^{-21}$ m^3 of the sample to be influence by the heating, the density of silicon with 2320 kg m^{-3}, a specific heat capacity of silicon with 703 J kg^{-1} K^{-1} and a thermal expansion coefficient of silicon with $2.6 \cdot 10^{-6}$ K^{-1}, the thermal deformation is in the range of about 100 fm [141–143]. Using the density of LFP with 3600 kg m^{-3}, a specific heat capacity of LFP of roughly 800 J kg^{-1} K^{-1} [144] and a thermal expansion coefficient of LFP with $5.3 \cdot 10^{-5}$ K^{-1} [145], the thermal deformation is in the range of about 10 fm and therefore at least two orders of magnitude smaller than the measured signal intensity.

Comparing thermal deformation with ionic deformation, the ionic contribution is in the range from 5-100 pm, depending on the material [95,98,99,110]. Hence, in this case, the contribution of the thermal deformation can be neglected. In addition, assuming the dissipated energy is only converted into heating of the sample is surely not entirely correct, but valid for a preliminary calculation. The tip environment is heated up as well as the sample, this decreases the thermal deformation of the sample under more realistic conditions. However, the thermal deformation is highly dependent on the contact resistance and the heated volume. The combination of a better electric connection between the tip and the sample can decrease the contact resistance, while a material with a low thermal conductivity can decrease the heated volume. Therefore, the thermal deformation can increase by at least one order of magnitude and can influence the

measurement. Here we assumed for simplification, that all the dissipation energy is transferred into the sample. The surrounding media as well as the tip will absorb some of the dissipated energy, which will decrease the temperature change of the sample and the volume expansion [62].

4.2.7 Electrochemical Reactions Influencing the Detected Signal

Electrochemical surface reactions can occur if the electrical potential of the AFM tip is high enough for the reaction to overcome the activation energy barrier. Regarding battery electrodes, surface reactions can occur with remains of electrolyte or by extraction of species out of the material. If the applied potential is high enough, extraction of ions from the sample surface is possible. This leads to the irreversible formation of surface features. Arruda et al. studied the growth of surface particles on a lithium ion conducting glass-ceramic (LICGC) depending on the applied potential and the counter electrode [146,147]. They demonstrate the growth of large particles on the surface with more than 100 nm in height with the application of around -4 V at the tip. The particles consist of lithium and their growth rate depends on the availability of lithium in the sample. The influence by the generation of surface features can easily be evaluated by rescanning the measured area after the application of voltage pulses. Interestingly, Lu et al. reported a dependency of the ESM signal of NiO on the surrounding gas and moisture level. The measurements, which were conducted in an argon atmosphere with the absence of any moisture, did not show any ESM signal. However, the same measurements conducted with moisture free synthetic air and at ambient air exhibited a clear ESM signal and the bias induced growth of surface particles.

Another possible reaction influencing the detected signal are processes taking place at the AFM tip itself. Most AFM tips consist of a doped silicon base, which is coated with a metallic material. For conductive tips, Pt is often used, which shows only low wear resistance during scanning, especially during contact mode AFM. Therefore, in the presence of an electrolyte, such as water, and an electrical field, the exposed silicon base can react with the ions in the sample. This changes the tip geometry and leads to an expansion due to the reaction itself. An example for electrochemical reactions at the tip itself is given in Figure 4-3. In Figure 4-3a) and b) the tip shows a characteristic shape of lithiated silicon, as it was observed for silicon pillars [148]. In comparison to the lithiated silicon tip, Figure 3-4b) shows a fresh AFM tip with the typical conical shape. The influence of a contaminated tip on the measured signal is more difficult to determine. However, image artefacts and a decrease of the resolution can give some information about the tip condition.

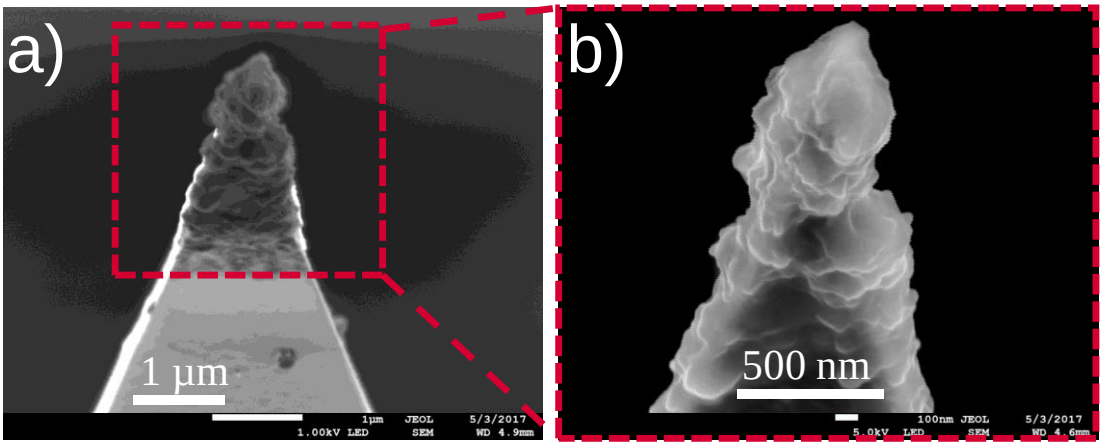

Figure 4-3: AFM tip with silicon base lithiated due to damaged Pt coating. a) shows the lithiated silicon tip, b) is a higher magnification of a)

5 Visualizing the Ionic Mobility in Laboratory Silicon Composite Anodes

This section is taken and adapted from [62].

5.1 Electrochemical Cycling of Cross-Section Holder and Swagelok Cell

The lithiation of the silicon particles is assumed to follow a core-shell process (Figure 5-1e) comparable to the one described by Obrovac and Krause [149] due to the low current density and polarization losses in the cross-section holder. During the lithiation, a two-phase structure consisting of an amorphous, lithiated, silicon surface phase and a crystalline, non-lithiated, silicon phase in the core of the grain is generated. This explains the overall low capacity of the electrode, since only the outer surface of the silicon grains is available for the electrochemical reaction. In the subsequent cycles, the amorphous shell is cycled, which can be seen in the shift of the voltage curve characteristics during the 2nd and 3rd cycle and a crystalline core persists. The slope is indicative of a solid solution behavior as is expected for the lithiation of amorphous Si. Considering the thickness of the amorphous, lithiated phase is unknown, it is difficult to determine the exact Li_xSi_y phase composition. However, generation of the amorphous phase is evident due to the appearance of the voltage plateau during first lithiation and the shifted voltage profile during the second lithiation (Figure 5-1b and Figure 5-1d). The horizontal gap between the first and second lithiation (Figure 5-1a and Figure 5-1c) is the irreversible capacity loss, which is characteristic for silicon anodes. The characteristic shift of the voltage profile from the first to second cycle, the long voltage plateau during the first lithiation and the capacity loss from the first to the following lithiations are observed in both measurement set-ups, showing the comparable electrochemical behavior of the electrode in the cross-section holder. The unstable voltage profile is attributed to the open cell design of the cross-section holder.

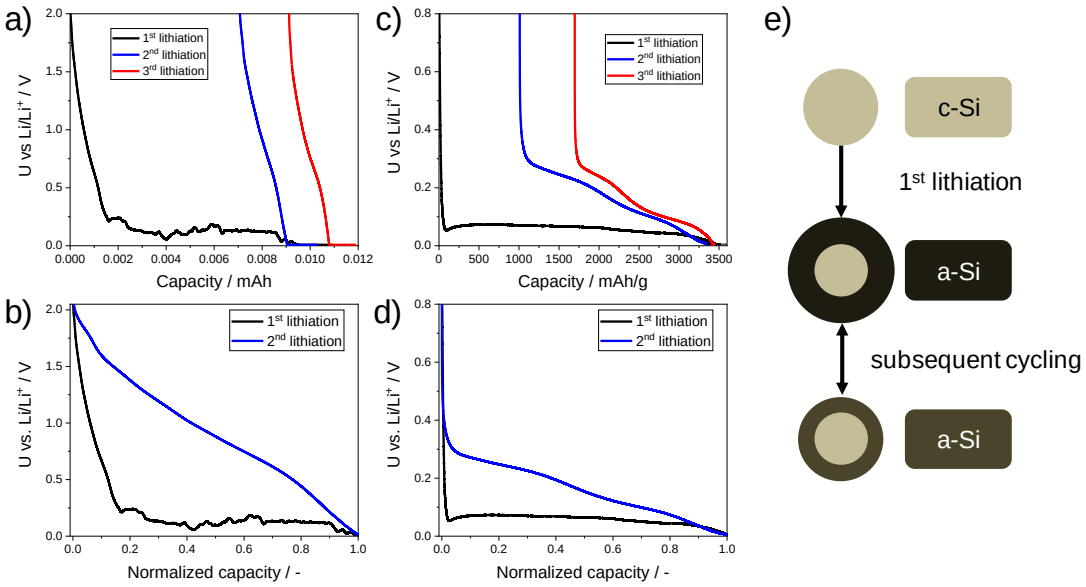

Figure 5-1: Cycling behavior and comparison of cross-section holder in a) and b) and Swagelok cell in c) and d) and lithiation process in e)

5.2 t-ESM Measurements on a Silicon Wafer, Non-Lithiated Si/C Anode, Lithiated Carbon Black and on HOPG

An intrinsic silicon wafer was examined to measure the surface change of non-lithiated crystalline silicon and an non-lithiated Si/C anode. Measurements at different positions are given in Figure 5-2a for the non-lithiated silicon wafer and in Figure 5-2b for the non-lithiated Si/C anode. The curves in Figure 5-2a show neither a trend following the applied voltage pulse nor a relaxation following the voltage pulse but only noise. The measurements of the non-lithiated Si/C anode show only noise in the surface displacement signal (image d in Figure 5-2b). Similar results were obtained with polyether ether ketone (PEEK), an industrial high-duty polymer without any mobile ions such as the silicon wafer (results not shown here). During the recorded time interval, no expansion/contraction of the surface caused by the piezoelectric or flexoelectric effect was observed for piezoelectric materials such as Si that may influence the ESM measurements. Their magnitude was either too small to be detected or induced volume changes had already relaxed.

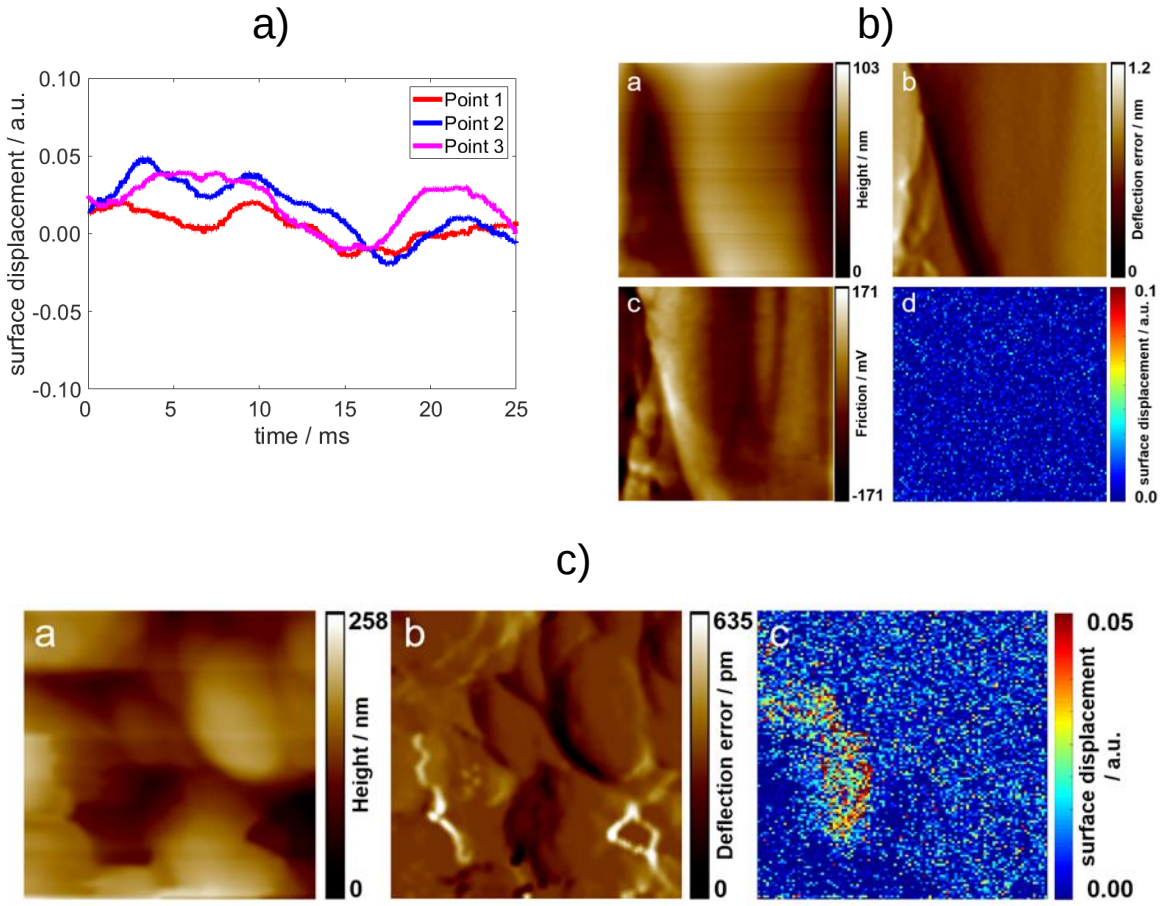

Figure 5-2: In Figure 5-2a measurement curves of an intrinsic, non-lithiated silicon wafer surface with an applied voltage pulse of -3 V for 10 ms. In Figure 5-2b fresh, non-lithiated Si/C anode measured with -3V dc-voltage amplitude, a) topography, b) deflection error, c) friction and d) surface displacement. In Figure 5-2c lithiated carbon black shows a small signal intensity. Image size 300 nm. -3 V dc-voltage, 2 V ac-voltage amplitude with 25 kHz.

HOPG and carbon black was examined to study the influence of the conductivity-enhancing additive. The results of carbon black are similar to the results from HOPG and are given in Figure 5-2c. Lithiated carbon black (CB) with CMC (90:10, CB:CMC) was measured. The sample was difficult to measure using AFM, due to the poor coating stability. It was cycled once vs. lithium metal from 1.5 to 0.01 V in 1 M LiPF6 in EC:DMC at 5 µA cm-2, washed with DMC and dried at room temperature under vacuum at 0.1 bar. It was then measured in lithiated state. However, it was possible to conduct some measurements which show only a small signal intensity at some specific locations, similar to HOPG, but no signal at most of the measured area. An example is given in Figure 5-2b. However, the signal intensity is close to the noise level and therefore it is difficult to evaluate the contribution. Nevertheless, for areas with a high

signal intensity on the lithiated Si/C electrode, the lithiated silicon is the main influence of the signal.

Figure 5-3 shows the deflection error signal caused by the Li-ion concentration change during a negative voltage pulse of -3 V at the tip (Figure 5-3a), the resulting Li-ion concentration change (Figure 5-3b), and the local height change with time at different sample positions (Figure 5-3c). Areas with a higher surface expansion in Figure 5-3b partly correspond to specific surface features visible in Figure 5-3a, but occurred also at areas of flat HOPG layers (top of the image). Comparing the results from HOPG in Figure 5-3c and the Si wafer in Figure 5-2, the surface displacement of HOPG shows an influence of the applied voltage pulse and a subsequent relaxation. As expected from HOPG, the surface displacement due to the change of Li-ion concentration is small (expected volume expansion due to lithiation of around 10 % [150,151]) and the curves exhibit a small signal to noise ratio. Measurements on other locations of the HOPG sample gave similar results as on the non-lithiated Si wafer with no measureable surface displacement. Comparing these results with Figure 5-2 it can be concluded that for Si/C anodes, the lithiation of silicon is the main mechanism leading to the surface displacement. A contribution of the volume change of carbon black to a displacement to the overall signal is one order of magnitude smaller (0.06 a.u. for HOPG and 0.3 a.u. for the Si/C anode) and can be neglected. Furthermore, the carbon black layer thickness is much smaller than the HOPG sample, which further decreases the Li-ion storage capacity and is limiting the possible concentration change in the carbon black layer.

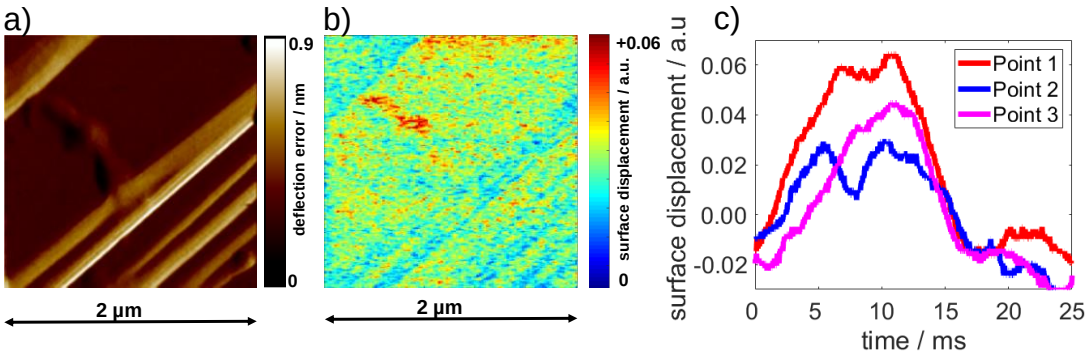

Figure 5-3: HOPG surface in lithiated state, a) deflection error, b) mapping of surface displacement due to the negative tip polarization, and c) volume change with time at different sample positions. Voltage pulse of -3 V for 10 ms.

The results of the control experiments show, that only lithiated samples show a surface displacement signal. Nevertheless, the signal intensities of HOPG and carbon black are much

smaller compared to the lithiated Si/C electrode, which leads us to conclude, that the main mechanism generating the signal is the ionic concentration change in the silicon.

5.3 Analysis of Li-ion Mobility in Silicon Composite Electrode Material

Silicon composite anodes are a promising candidate as a next generation anode material but exhibit so far only low cycling stability due to their large volume expansion of up to 300 % in fully lithiated state [152,153]. Figure 5-4 shows an example of the t-ESM measurement of the cross-section of an aged Si/C anode. For the grain structure after the cycling we assume a lithiated, amorphous silicon shell with a non-lithiated, crystalline silicon core. Cycling data and a comparison of the electrochemical behavior of the cross-section holder with the cycling in a Swagelok cell are provided in Figure 5-1. In Figure 5-4a, the deflection error mapping is shown. Figure 5-4b and Figure 5-4c give the change in ionic concentration due to the applied positive and negative potential of ±3 V at the AFM tip. The surface contracted during the positive applied potential (Figure 5-4b), and expanded during the negative applied potential (Figure 5-4c). Since the height changes in Figure 5-4b and Figure 5-4c show similar areas corresponding to large changes in ionic concentration, one can rule out significant topographic and tip-related contributions to the height change that may be caused by a variation in the tip-sample contact area to the measurement signal. Furthermore, artefacts due to the scan direction, i.e. by a different tip orientation and different tip-sample contact can be ruled out since the trace (Figure 5-4b) and retrace (Figure 5-4c) mappings are similar [65].

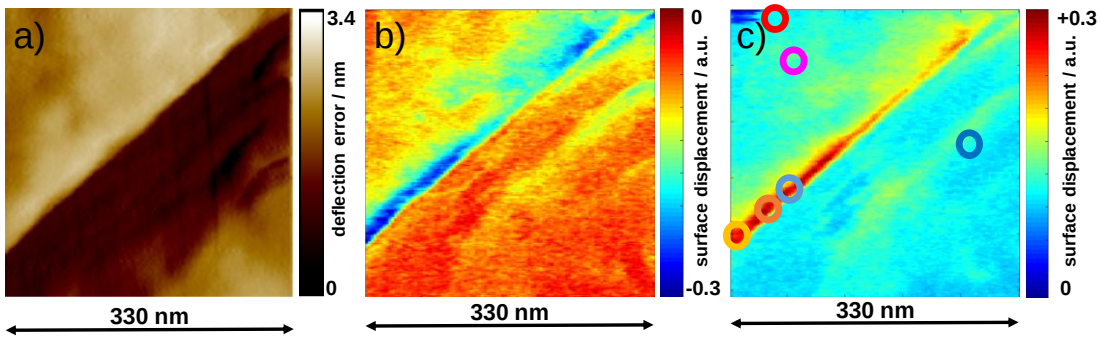

Figure 5-4: Aged silicon composite anode, a) deflection error mapping, b) surface displacement, trace with +3 V at the tip, and c) surface displacement, retrace with -3 V at the tip.

The step, which runs diagonally across the image, is clearly visible in all three images. For Figure 5-4b and Figure 5-4c, the step exhibits a higher change in ionic concentration compared to the grain centers, which is in agreement with results from other groups and due to the

dependency of fast diffusion paths on the crystal orientation [20,94,100,101]. In Figure 5-5a and Figure 5-5b, surface displacements over time at different sample positions marked in Figure 5-4c are plotted with the colors corresponding to the line colors in Figure 5-5. The curves in Figure 5-5a represent measurement points at the step, while Figure 5-5b shows measurement points inside the grains.

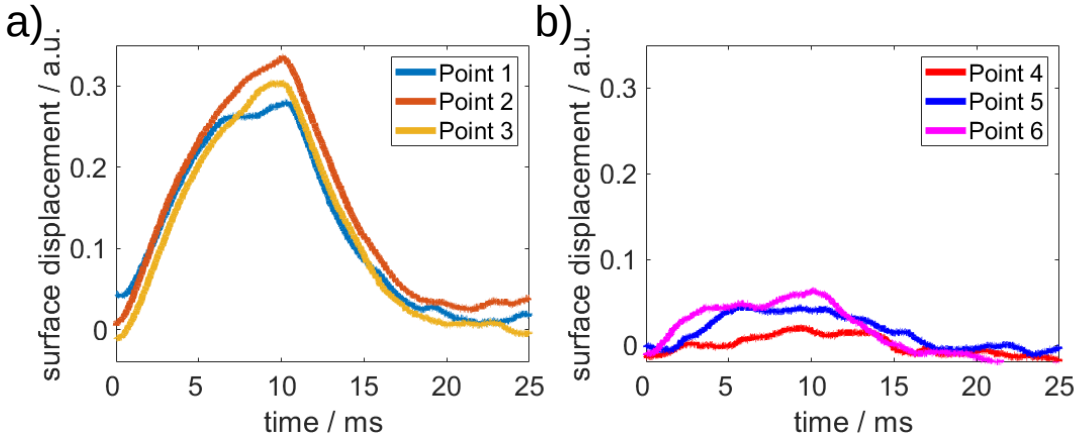

Figure 5-5: Extracted expansion curves at data acquisition points out of Figure 5-4c (line colors are matching to the colors of the circles in Figure 5-4c), a) data points with a high surface displacement at the step, and b) with lower or no surface displacement moving away from the step. The dc-voltage of -3 V was applied for 10 ms.

The higher signal intensity at the step can be explained by a higher mobility of ions compared to the grain interior. Assuming a homogeneous Li-ion concentration across the grain and the step, a higher ionic mobility, due to a different crystal orientation at the step, will lead to a more pronounced surface displacement due to the faster change in concentration. This assumption is valid for the case that the maximum ion concentration was not reached by the applied voltage pulse. The interdependency of the ionic mobility and the crystal orientation is reported for layered $LiCoO_2$, V_2O_5, microcrystalline silicon and single crystal silicon [101,112,148,154–156].

In addition to the ionic mobility, saturation of Li-ion concentration can limit the surface displacement. Hence, the dependency of the surface displacement on the applied dc-voltage amplitude was studied. The same area was scanned with different dc-voltage pulse amplitudes. The resulting surface displacement maps are shown in Figure 5-6a. The magnitude of surface displacement at three spots was extracted and plotted over the corresponding dc-voltage, shown in Figure 5-6b. The dots were averaged over three adjacent data pixel and the error bars give

the standard deviation. The overall surface displacement of all data points in the image is plotted as a histogram in Figure 5-6c.

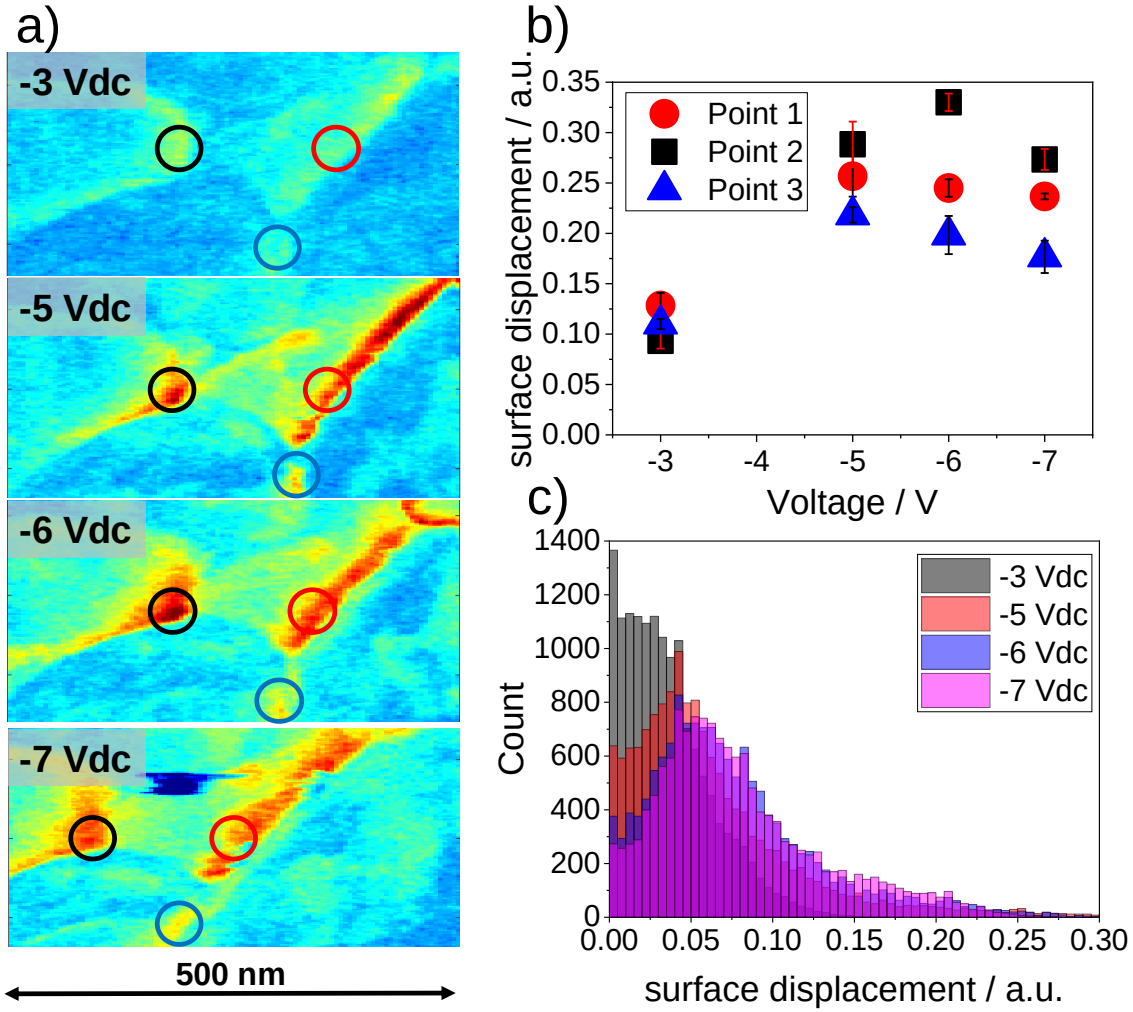

Figure 5-6: Resulting surface displacement for different applied voltages, a) mappings of surface expansion, b) surface expansion at data points marked in (a), and c) histogram of surface displacements of all measured image points. Point 1 is marked in red, point 2 is marked in black and point 3 is marked in blue.

For all three positions, the displacement is the same for -3 V pulse amplitude, a significant height increase occurred for all positions upon a voltage step from -3 to -5 V. At point 1, a saturation of the height change is achieved with -5 V; a further increase of the voltage does not increase the surface displacement any more. At point 2, the surface displacement increased linearly up to -6 V and slightly drops for a higher applied voltage. At point 3 an increase from -3 to -5 V and a further decrease for higher voltages is visible. The histograms of all surface displacement values of the different dc-voltage pulse amplitudes (Figure 5-6c) indicate that the distribution broadens, leading to an increase of the overall amount of higher surface

displacement counts with increasing dc-voltage amplitude, while the peak height of the distribution decreased and shifts towards higher values for the surface displacement. The resulting measured surface displacements reflects a steady-state between an increase of ion concentration generated by the electric field and an increasing velocity of back-diffusion due to the higher concentration gradient. These two opposite effects result in a net surface displacement, which depends on the relative contribution of each effect. The steady rise of the net peak height of the surface displacement in Figure 5-6b indicates the increase of migration over the increase of back diffusion. At the same time, the levelling or decrease of net peak height (point 1 and 3) of the surface displacement with higher voltage at the same positions in Figure 5-6b must be caused by higher back-diffusion compared to migration. The shift of the peak position of point 2 to higher voltages indicates a higher ion saturation at this position before back-diffusion starts to predominate. The migration process cannot maintain the ionic flow towards the surface and back-diffusion starts to dominate. Another possible explanation for the decrease of the surface displacement with increasing voltage amplitude could be irreversible concentration or structural changes inside the probed volume. There are no visible surface changes after the measurements, therefore no surface reactions occurred, which could influence the kinetic properties. However, changes inside the material cannot be ruled out. Yang et al. reported a similar behavior for LiCO2 with decreasing ESM signal over several measurements of the same location. They assume irreversible concentration changes inside the material and decreased activity of Li-ions [157].

Nevertheless, for the measurements shown in Figure 5-4, which are performed with a dc-voltage of -3 V, the results from Figure 5-6 validate that a saturation concentration in the material was not reached. Therefore, the different surface displacements are a result of a difference in ionic mobility and not limited by the ion concentration.

5.4 Calculation of Local Diffusion Coefficients for a Silicon Composite Electrode

As described above, the dynamic response of the surface displacement delivers information on the dynamics of the ionic movement inside the material. Diffusion and migration/diffusion coefficients are extracted by fitting an exponential curve to the data points for each of the two time periods.

Data fitting was limited to data points with at least 15% surface displacement of the maximum value. This threshold reduced the amount of diffusion coefficients extracted out of the measured data, but ensured the validity of the fitting process. Some examples for the fitting results are given in Figure 5-7.

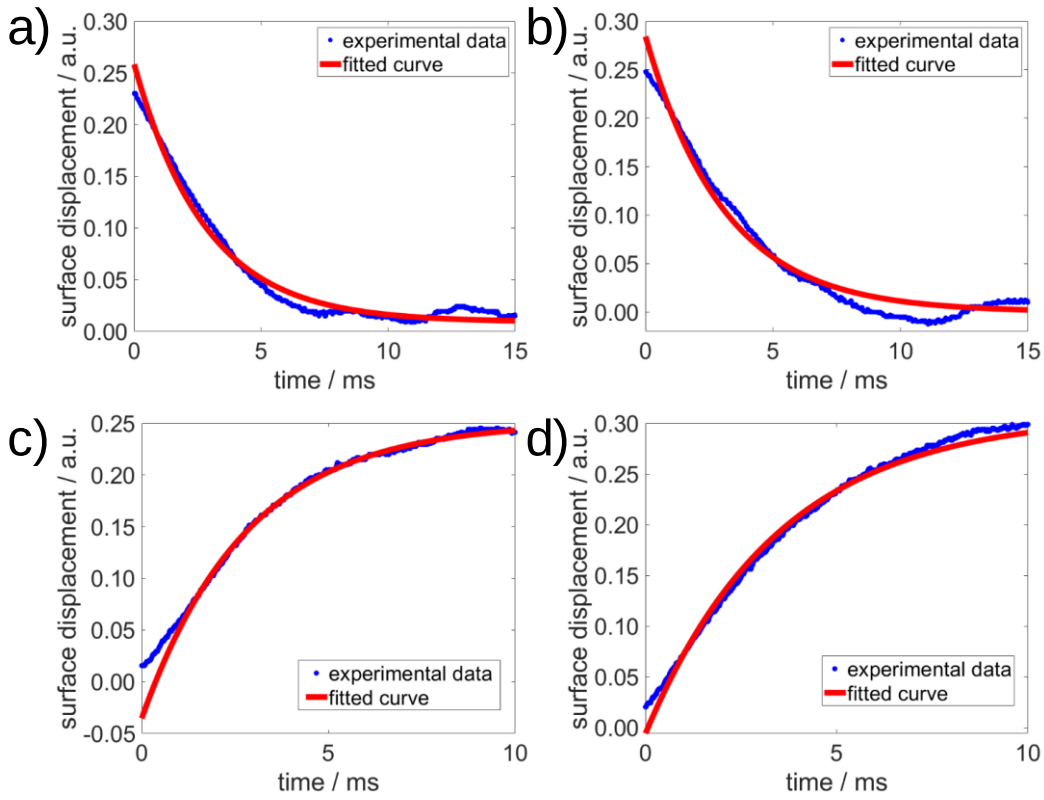

Figure 5-7: Examples of the exponential fit with a) and b) for the diffusion and c) and d) for the migration process.

Figure 5-8 presents a mapping of the resulting diffusion coefficients. Figure 5-8a gives the diffusion coefficients D2 calculated from the data points after the applied voltage pulse and solely governed by the concentration gradient. The mapping of the effective migration coefficient D1 that is reduced by back diffusion is shown in Figure 5-8c. Both coefficients are in the range of around 10^{-14} to 10^{-12} m^2 s^{-1}, which is within the range, but at the lower bound of diffusion coefficients reported for silicon in the literature and close to theoretical values given by Johari et al. [95,158–162]. The differences of the diffusion coefficient compared to literature values can be explained by the dependence of the diffusion coefficient on the used diffusion length, which is assumed to be the tip radius due to the penetration of the electric field inside

the material [94,95,163]. A short discussion about the discrepancies of the experimentally determined diffusion coefficients for silicon was done by Ozanam and Russo [154].

The distribution of the diffusion coefficients shows higher coefficients around $1 \cdot 10^{-12}$ m^2 s^{-1} at the step and at some positions away from the step. Moving away from the step, the coefficients decrease towards approximately $6 \cdot 10^{-13}$ m^2 s^{-1} and slightly increase again, visible in the top left of Figure 5-8a. Part of the step from the marked red square is shown in the zoom of Figure 5-8b and exhibits a thickness of approximately 12 nm. The white marked area in Figure 5-8a shows a second step of approximately 35 nm, which exhibits similar diffusion coefficients as the step in Figure 5-8b. The higher diffusivity at the step points towards a preferential material structure for the diffusion of ions, which is presumably more amorphous, since amorphous silicon is expected to have a higher diffusivity compared to crystalline silicon [160,164].

In contrast, ESM time spectroscopy results of Guo et al. on $LiCoO_2$, and Jesse et al. on amorphous silicon report lower diffusion coefficient of the grain boundaries compared to the grains itself [95,110]. The different results might be explained by the significant difference in material structure with different properties of the grain boundaries, which leads to differences in Li-ion concentration and mobility.

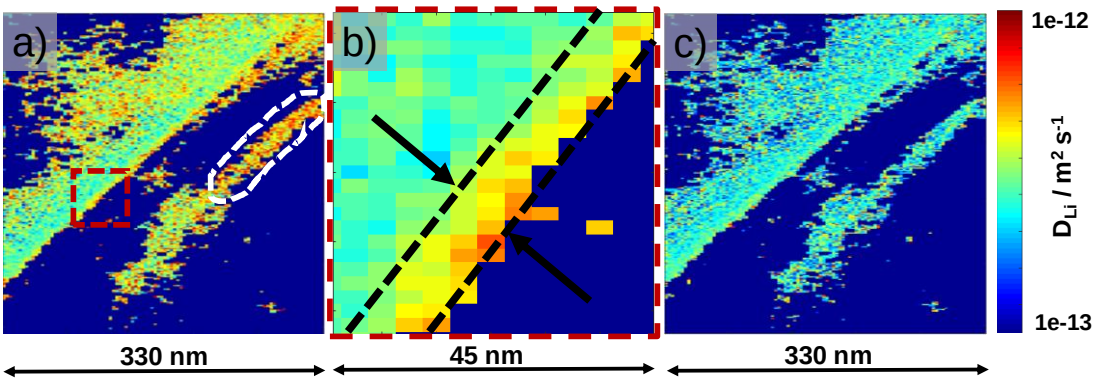

Figure 5-8: Mappings of calculated coefficients D1 and D2 at same location as in Figure 4, a) diffusion coefficient (D2) due to concentration gradient after voltage pulse of -3 V, b) zoom into marked area of step in a), and c) effective migration/diffusion coefficient (D1) due to the electric field during voltage pulse and simultaneous back diffusion.

A comparison of the diffusion coefficients during the voltage pulse in Figure 5-8c (D1) and after the voltage pulse (D2) in Figure 5-8a exhibits lower effective diffusion coefficients for the migration/diffusion process D1 compared to the concentration gradient-driven diffusion leading to D2. The histogram in Figure 5-9 visualizes the histograms for D1 and D2 regarding all image

points above the threshold. The peak for the migration driven process reaches the maximum counts near $2 \cdot 10^{-13}$ m^2 s^{-1}, while the concentration gradient driven process has a larger maximum near $4 \cdot 10^{-13}$ m^2 s^{-1}. This difference is expected because for the migration driven process a steady-state of migration and oppositely directed back-diffusion arises. The built-up concentration gradient due to the electric field hinders the further movement of the ions, therefore decreases the diffusion coefficient during the migration-driven process and leads to smaller coefficients D1 compared to D2. These results indicate that the solid-state migration of ions has a similar velocity range as the solid-state diffusion if the electric field is strong enough.

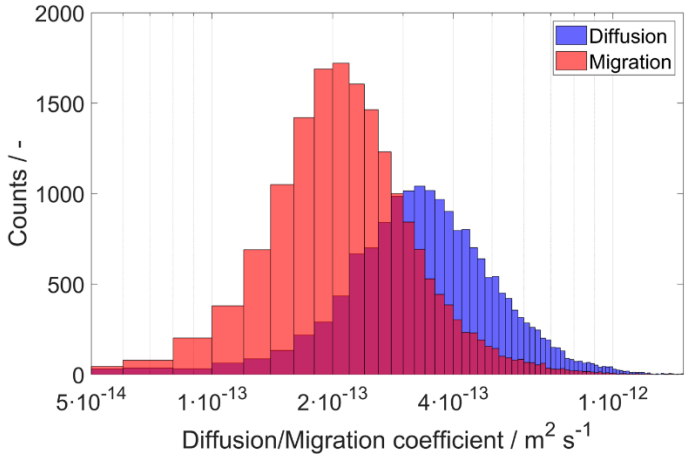

Figure 5-9: Distribution of diffusion coefficients of all image points above the threshold for D1 (red) and D2 (blue).

5.5 Conclusions for the Visualization of the Ionic Mobility in Silicon Composite Anodes

The chapter 5 presents a tailored ESM technique to visualize the ionic concentration change in the sample volume under the AFM tip and recorded the dynamics of ionic diffusion. For silicon composite anodes, the signal emerged from the Li-ion concentration change in the silicon particles; further contributions such as piezoelectricity or flexoelectricity had no significant influence. The results indicated a higher ionic mobility at the step, probably due to a different material structure. Analysis of the dc-voltage amplitude dependence showed a saturation of the surface displacement at high dc-voltages due to concentration limitations inside the material or irreversible concentration change in the probed volume. Using the measurement curves, diffusion coefficients were calculated and the resulting values are consistent with literature values. The benefit of the technique is the ability to generate mappings of local diffusion

coefficients on the nanometer scale. The results present strong variations of the diffusion coefficient within one grain.

6 Analysis of Aging Mechanisms of Commercial $LiFePO_4$ Cathodes using t-ESM

6.1 Cycling of Commercial Cells and Sample Preparation

The cells are commercial 26650 LiFePO4 cells from A123 Systems LLC with a nominal capacity of 2.5 Ah and a voltage window from 2.0 to 3.6 V. A group of cells was cycled at +55°C using a part from the worldwide harmonized light vehicles test procedure (WLTP) driving profile and one cell out of it was used for further analysis in comparison with a fresh cathode. After the cell reached a total discharge capacity of 2000 Ah it had a remaining discharge capacity at 1C of 2.156 Ah, which represents a capacity loss of 17% with respect to its original value. The cells were disassembled inside a glovebox under Argon (MBraun, O2 and H2O < 2 ppm) and washed with dimethylcarbonate (DMC, Sigma Aldrich). Cross-section cuts were obtained with an unfocused argon beam cross-section polisher (Jeol, 19520-CCP). Transfer of samples was done inside a transfer vessel to avoid any contact with air.

Full cell and three-electrode test cell measurements are conducted using a battery cycler (CTS-XL, BaSyTec GmbH) with a two-electrode and three-electrode configuration. Three-electrode test cell measurements are conducted using electrodes with 18 mm in diameter, which are punched out of the fresh and aged electrode foils from the commercial cells., A PP/PE membrane (FS-5P, EL-CELL GmbH) was used as separator. For the three-electrode tests, the electrolyte was 1 Mol $LiPF_6$ in EC/DMC (1:1 vol%, Sigma Aldrich). The three-electrode tests were conducted using a commercial test cell (PAT-Core, EL-CELL GmbH) with a lithium metal ring as reference electrode. One side of the electrode material was removed from the current collector using N-Methyl-2-pyrrolidone (NMP, Sigma Aldrich). The three-electrode test cells were assembled using a fresh or aged cathode in combination with a fresh anode from the uncycled full cell to avoid any ageing influence from the anode side. EIS measurements are conducted using a Princeton Applied Research Versastat 450 potentiostat with an AC amplitude of 10 mV in the frequency range from 500 kHz to 0.5 mHz at OCV. EIS data is analyzed using the impedance.py python package [165]. The voltage over discharge capacity plot of the commercial full cells are shown in Figure 6-1.

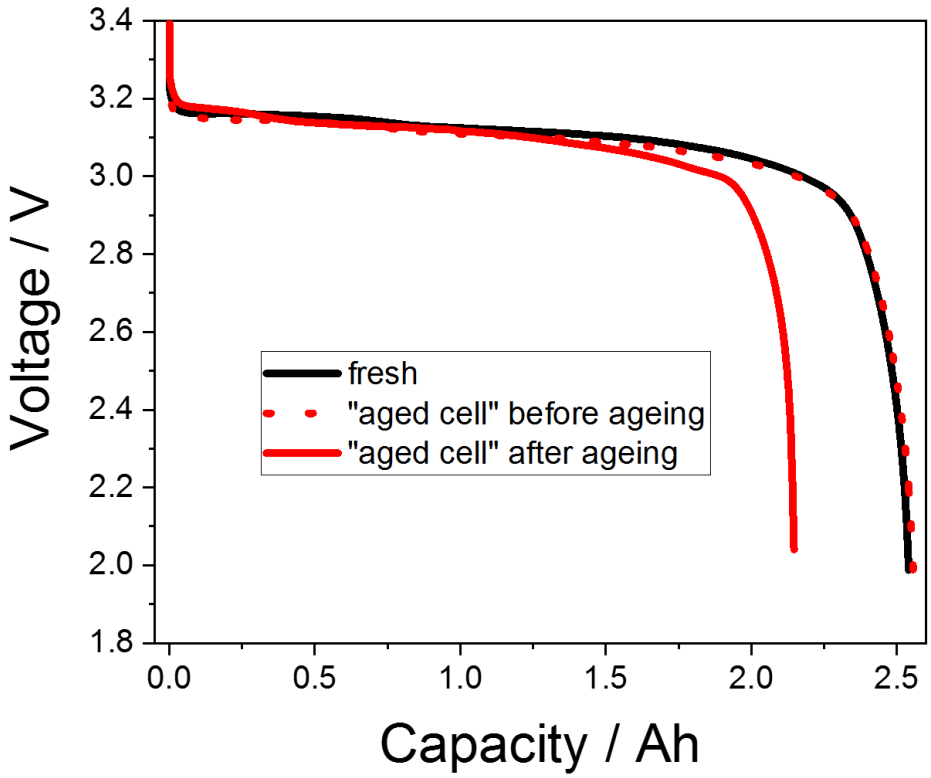

Figure 6-1: Voltage over capacity of the fresh and aged full cell

It displays the capacity loss of the aged full cell after cycling. Due to the anode contribution to the capacity loss in the commercial full cell setup, the cathode was additionally analysed separately. The cathode ageing is observed in the Nyquist plot in Figure 6-2 from the fresh and aged cathode vs lithium metal reference electrode in a three-electrode test cell. Following the approach proposed in the literature, the first semi-circle at high frequencies is assigned to the cathode and the second semi-circle at mid frequencies to the lithium anode [166,167]. The aged sample exhibits a bigger first semi-circle due to ageing and the second semi-circle stays nearly constant, since the lithium reference anode is not affected by the cycling. In Figure 6-3, the fresh and aged cathode are cycled in a three-electrode setup combined with a fresh anode for both cathodes. Looking at the first charging step, the aged cathode exhibits a smaller charge capacity compared to the fresh cathode. This indicates a smaller amount of lithium stored or available for the electrochemical process or a reduced amount of electrochemically active cathode material. The capacity loss from first charge to first discharge is attributed to surface layer generation (anode: solid electrolyte interface, SEI; cathode: solid permeable interface, SPI) on both electrodes, since they were rinsed before the full-cell assembly. After the first

cycle, the capacity stays constant (not shown here). The discharging capacity is higher for the fresh cathode compared to the aged.

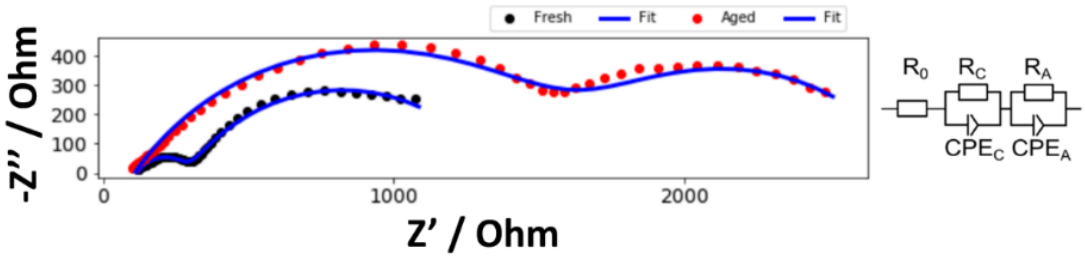

Figure 6-2: Nyquist plot of the fresh (black) and aged (red) cathode vs. a lithium reference ring electrode in discharged state

$R_{C,\ fresh} = 172\ \Omega$ $R_{A,\ fresh} = 1060\ \Omega$

$R_{C,\ aged} = 1140\ \Omega$ $R_{A,\ aged} = 1530\ \Omega$

Figure 6-3 displays the first charge and discharge step from the three-electrode test cells with a fresh and aged cathode, both with a fresh anode. The voltage curve represents the potential between cathode and anode. We used 0.185 mA as charge and discharge current, since that represents roughly C/20, and therefore provide the maximum of the accessible capacity. The cell was first charged up to 3.6 V with a constant voltage step until the current dropped below 0.120 mA and afterwards discharged to 2.0 V.

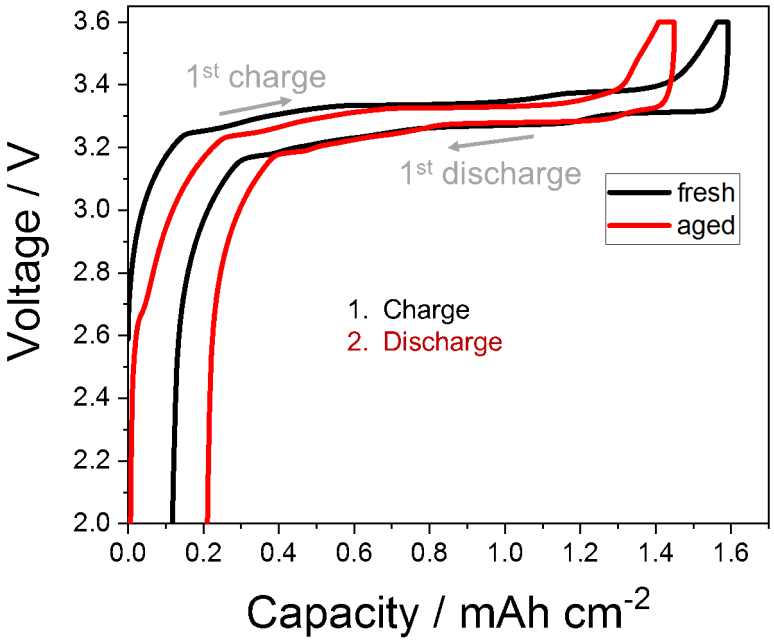

Figure 6-3: Full-cell test of the fresh and aged cathode combined with a fresh anode

For the cyclic voltammetry (CV) presented in Figure 6-4, the three-electrode setup with a fresh or aged cathode in combination with a fresh anode and a lithium metal reference ring was used. The scan rate was set to 1 mV s^{-1} in the range from 2.0 V to 3.6 V regarding the potential between cathode and anode.

The area under the CV peaks or the available capacity during the anodic scan for the fresh cathode – fresh anode combination is 4.6 mAh and for the aged cathode – fresh anode combination only 4.0 mAh. The capacity during the cathodic scan for the fresh cathode – fresh anode combination is 4.7 mAh and for the aged cathode – fresh anode combination only 4.0 mAh.

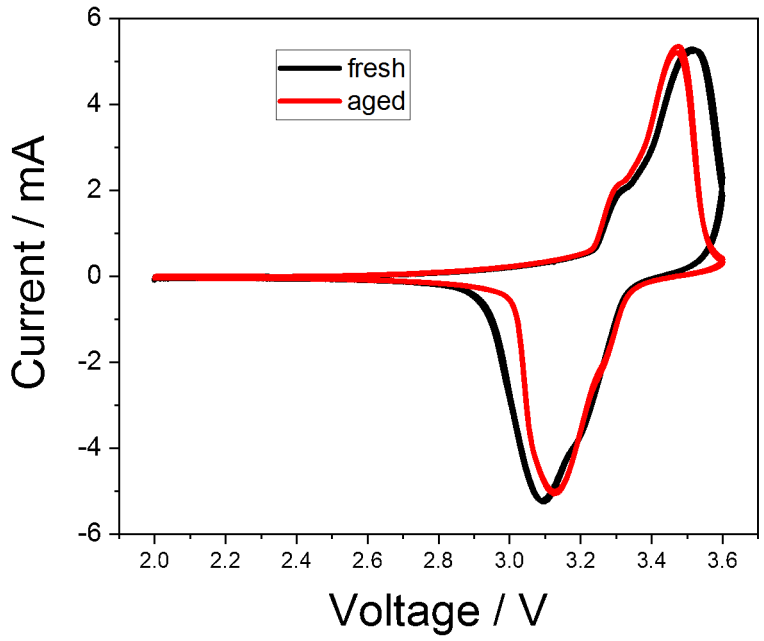

Figure 6-4: CV of the full-cell test setup with the fresh (black) and aged (red) cathode combined with a fresh anode. The potential is measured between cathode and anode.

The ESM analysis was conducted inside of particles of the cross-sections of the fresh and aged cathodes. Two examples of the cross-section structure of the cathodes are given in Figure 6-5.

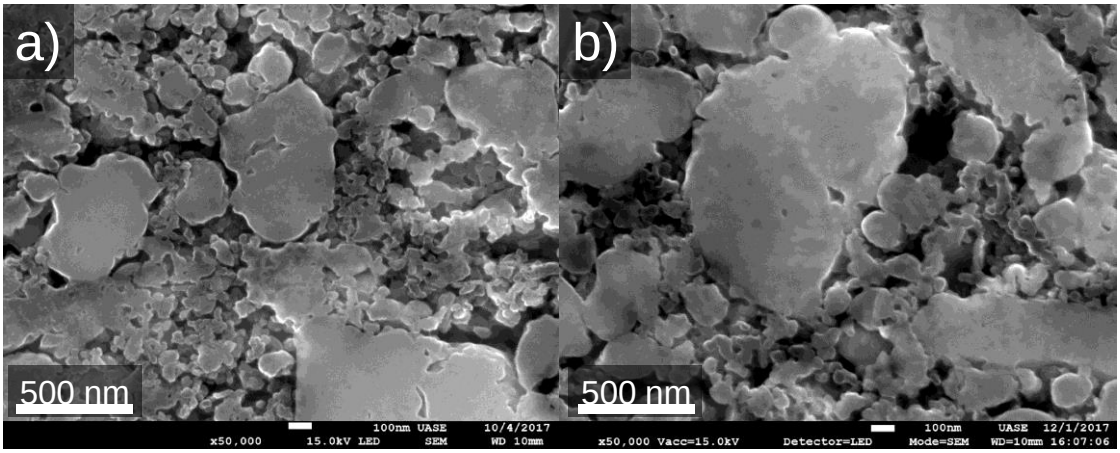

Figure 6-5: SEM cross-section view of the fresh (a) and aged (b) cathode

In Figure 6-5a) the fresh and in b) the aged cathode cross-section is shown. The electrode consists of particles ranging from 50 nm to a few micrometres in diameter. No evident differences can be discerned on this scale when comparing pristine and aged samples.

6.2 Analysis of the ESM Signal of the Fresh Cathode Cross-Section

The ESM measurement in Figure 6-6 displays differences of the ESM signal within one particle. In Figure 6-6a) and b), the topography and the deflection error of the particle and in Figure 6-6c) and d) the ESM signal due to the application of a positive and negative voltage pulse are shown. Figure 6-6e) displays the applied voltage pulse with the dc and ac-voltage part at the top and the resulting ESM signal at the bottom, which is generated due to the increase or decrease of the ionic concentration in the probed volume due to the electric field. During accumulation of Li-ions with the dc-voltage pulse, due to the electric field driven migration, the ESM signal increases. Afterwards, when the dc-voltage is turned off, the ESM signal decreases due to the concentration driven diffusion and the decrease of the ionic concentration in the probed volume. The difference between the signal intensities at the beginning and at the end of the dc-voltage pulse is extracted (indicated by the arrow in the bottom part) and represents one pixel in the 2D presentation of the ESM data.

The ESM signal which we observe on carbon coated LFP is not only limited to structural boundaries within one single grain, which are known to exhibit a high mobility for ions due to structural disordering, high concentration of defects and lower energy barrier [112,168,169]. We also observe a homogeneous high signal on planar locations inside the particle. The variation of the

ESM signal inside the particle is most likely caused by the anisotropic ionic mobility of the olivine structure of $LiFePO_4$. The olivine structure exhibits preferential lithium ion transport along the [010] channel of the lattice [135,170], which therefore influences the ESM signal intensity, since the preferential lithium ion transport direction induces a high concentration change during the dc-voltage pulse, while for ionic blocking directions, no concentration change is achieved and therefore no change in the ESM signal is produced. The olivine crystal structure on the planar locations is not the only influence on the ionic mobility, but it is an additional factor next to the structural disordering, high concentration of defects and lower energy barrier and more important on planar locations than on structural boundaries.

We can exclude any significant influences due to changes of the tip-sample contact or edge artefacts in the ESM signal, since trace and retrace, or positive and negative dc-voltage pulse respectively, show similar signals for the sample locations. If tip-sample artefacts and increase of the tip-sample contact area would influence the signal generation, the collected signals from trace and retrace would show locations with different response for trace and retrace and a direction dependence for the tip movement. In Figure 6-6f), the ESM signal from Figure 6-6d) is overlaid on the topography from Figure 6-6a). It indicates, that the signal is not influenced by the topography of the sample, since the flat locations in the top and bottom of the image show a distinct ESM signal. Additionally, due to the slow scan speed of 0.2 Hz, we assume a stable tip-sample contact during the measurement. Considering the measurements are conducted on cross-sections of particles, we neglect the carbon coating or binder material to influence the results. The ESM signals show some precise and fine structures and clear separations within the particles. Assuming a rather large probed volume of the cubic tip radius (R_{tip} around 30 nm) or even larger, the ESM signal would exhibit rather diffuse signal allocation. Therefore, it is more reasonable to assume a limited probed volume close to the surface of the tip-sample junction of only a few nanometres in depth.

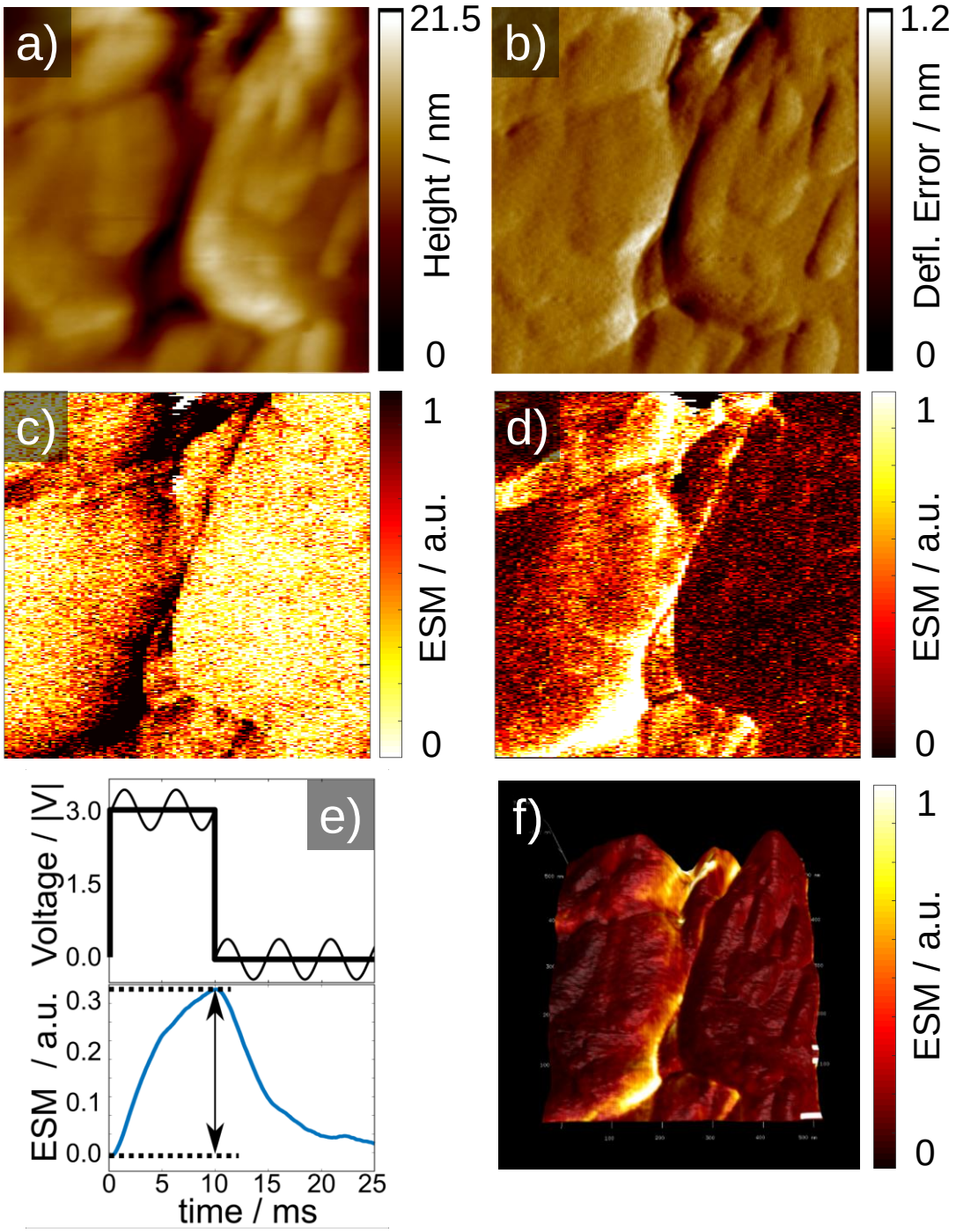

Figure 6-6: Topography (a), deflection error (b) and ESM amplitude due to the positive and negative voltage pulse (c and d) at the fresh cathode. In e), an example of the measured ESM signal with the applied voltage pulse are shown. In f) is the result from d) overlaid on the topography in a). Scan size is 1x1 µm²

6.3 Dependency of the ESM Signal Intensity During Stepwise Increasing DC-Voltage Amplitude in Fresh and Aged Cathodes

To analyse the dependency of the ESM signal on the applied dc-voltage amplitude, the same location was measured repeatedly with a stepwise increased dc-voltage amplitude after each measurement. The results for the different dc-voltage amplitudes are displayed in Figure 6-7 with a) |2|V, b) |3|V, c) |5|V, d) |6|V and |7|V dc-voltage amplitude in e). The middle row shows the ESM signal due to the positive and the bottom row due to the negative voltage pulse.

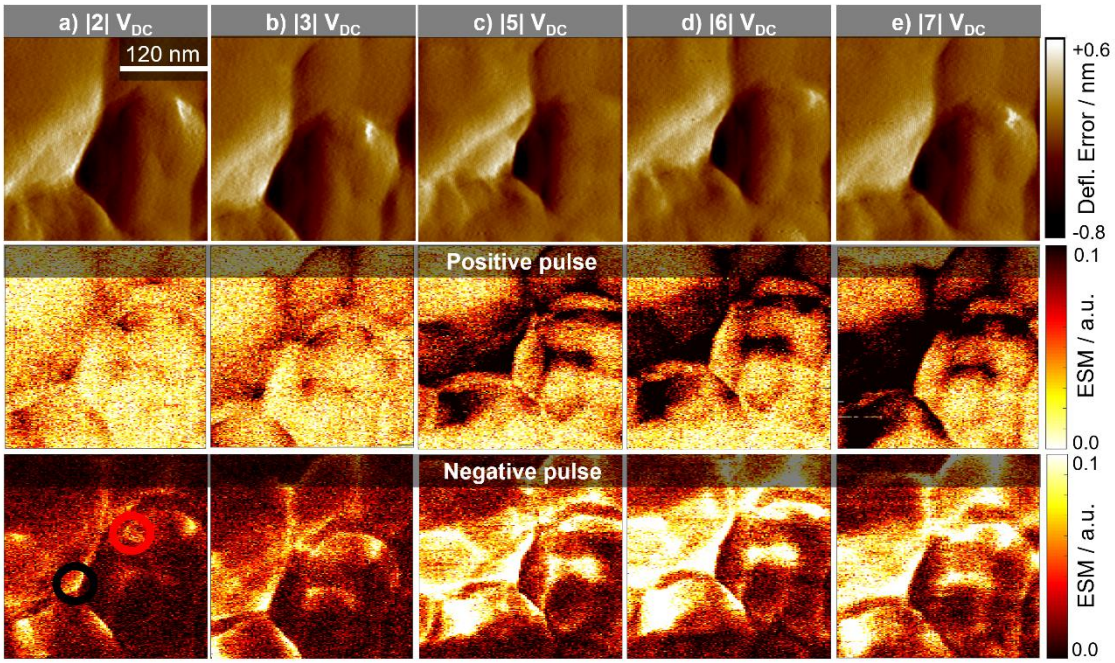

Figure 6-7: Comparison of different dc-voltage amplitudes at the same location of a fresh cathode. The top row shows the deflection error, the middle row the ESM signal during positive and the bottom row during negative dc-voltage pulse. In a) with |2|V, b) with |3|V, c) with |5|V, d) with |6|V and e) with |7|V. Scan size is 0.33x0.33 µm².

With increasing dc-voltage amplitude, the overall active area of the sample increases, as can be seen by the increasing fraction of the sample showing a distinct ESM signal. At lower dc-voltage amplitudes (|2|V and |3|V), there are mainly structural boundaries visible in the ESM signal. At |3|V, areas with roughly 50 nm diameter are visible. Stepping up the dc-voltage amplitude further increases the overall active area. Still, some locations in the sample stay inactive, even at a dc-voltage of |7|V. Contrary to other publications, irreversible changes or the generation of surface features at higher voltage amplitudes (|5|V to |7| V) are not observed [147,157]. This is probably due to the smaller excitation dc-voltage amplitudes, the short excitation time of only 10 ms and the inert gas atmosphere. This prevents the generation of a water droplet

meniscus at the tip-sample junction, which can serve as an electrolyte for electrochemical reactions.

The increase of the ESM signal intensity for the fresh cathode is shown in Figure 6-9a). It exhibits a linear increase of the ESM signal with increasing dc-voltage amplitude, which is in agreement with theoretical work done by Morozovska et al. [107]. Only at location 1, at -7V dc-voltage amplitude, the signal intensity decreases as compared to -5V and -6V. This indicates either an irreversible change in the ionic concentration in the probed volume due to the preceding measurements or a degradation of the material structure due to the applied electric field. Since the ESM signal depends on the change in ionic concentration during the applied dc-voltage pulse, an irreversible accumulation of Li-ions in the probed volume due to the preceding measurements would decrease the feasible change in concentration and therefore could reduce the ESM signal intensity. Similar, structural degradation could influence the ESM signal intensity by the reduction of the ionic conductivity. Yang et al. observed a similar decrease of the ESM signal intensity, after scanning the same location several times, which they attributed to either changing ionic concentration or degradation of the electrochemical activity [157]. The second location shows a linear increase of the ESM signal intensity over the whole range of the applied dc-voltage amplitudes, but with a smaller slope compared to location 1 and ESM signal intensity. The ESM signal, generated with different dc-voltage amplitudes on the aged sample is shown in Figure 6-8 using the same image structure as Figure 6-7. The lower ESM signal intensity increase of the aged cathode compared to the fresh cathode is already observed by comparing Figure 6-7 and Figure 6-8 and evaluated in Figure 6-9b).

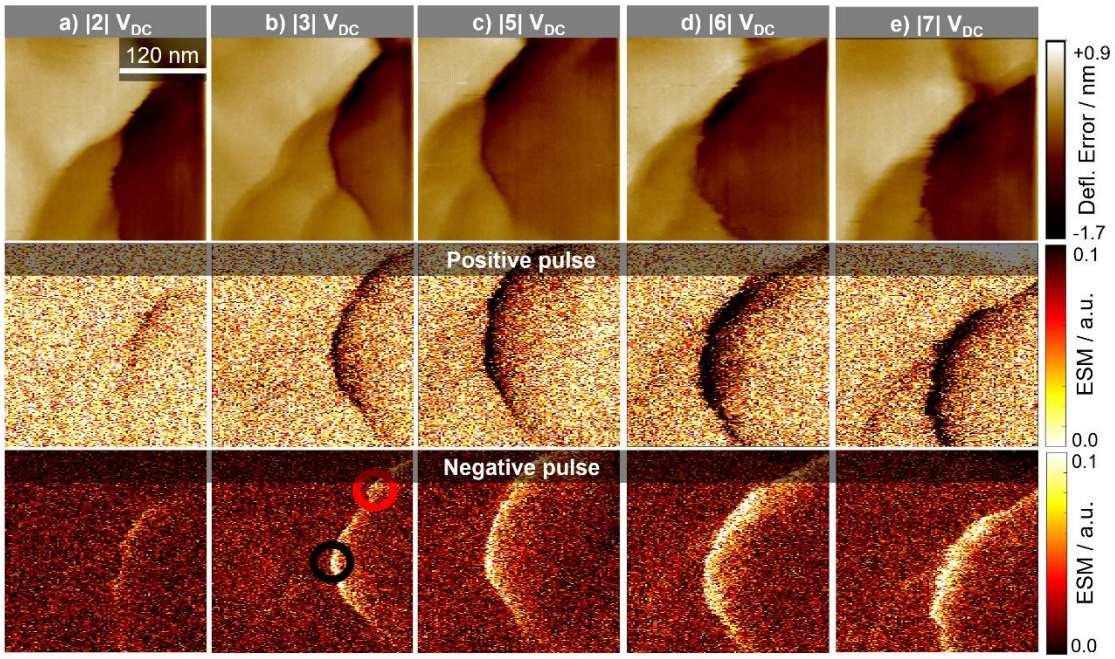

Figure 6-8: Aged cathode, comparison of different dc-voltage amplitudes at the same location. The top row shows the deflection error, the middle row the ESM signal during positive and the bottom row during negative dc-voltage pulse. In a) with |2|V, b) with |3|V, c) with |5|V, d) with |6|V and e) with |7|V. Scan size is 0.33 µm.

The measurements in Figure 6-7 show a clear dependency of the ESM signal intensity on the excitation voltage. The inactive locations - to be precise: the locations, which do not generate any ESM signal in the sample - stay inactive and cannot be activated by an increasing dc-voltage amplitude, at least for the dc-voltages applied here. Structural boundaries in the particle exhibit in general higher ESM signal intensity compared to homogeneous and planar locations, which points towards the importance of nanostructuring of battery materials to increase the boundary density. Moreover, the results from Figure 6-7 indicate, that by using a |3|V dc-voltage amplitude for further measurements, the limiting factor for the resulting ESM signal intensity is not the concentration limit in the probed volume, but the mobility and activity of the Li-ions, which is influenced by structural aspects.

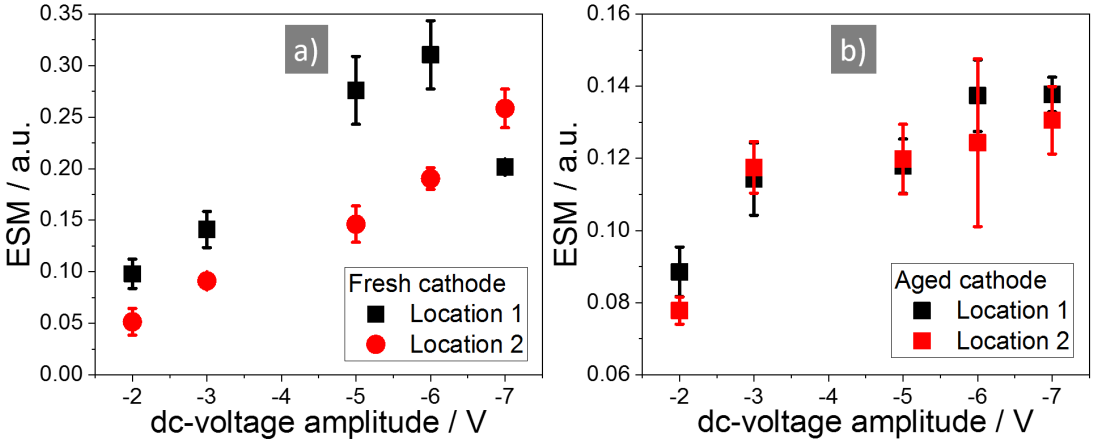

Figure 6-9: Evolution of the ESM signal intensity at the fresh cathode in a) and aged cathode in b) with the stepwise increasing dc-voltage pulse. The locations for the fresh cathode are marked in Figure 6-7a) in the bottom. For the aged cathode see Figure 6-8.

6.4 Comparison of the ESM Signal Intensity at Fresh and Aged Cathodes

Ageing of battery material is a complex process with different mechanisms happening simultaneously and influencing each other. Here we analyse the change of the ESM signal over ageing by comparing the fresh cathode with an aged cathode sample. Figure 6-10 compares the ESM signal of the fresh (a – c) and aged (d – f) sample with the deflection error (a and d), the ESM signal due to the positive (b and e) and negative (c and f) dc-voltage pulse. In the fresh sample, structural boundaries and homogeneous planar locations show a distinct ESM signal. In the aged sample, only structural boundaries possess a distinct ESM signal. Large parts of the measured area are inactive and exhibit nearly no ESM signal at all. Additionally, the ESM signal intensity is smaller compared to the fresh sample, at least for voltages higher than |5| V. The voltages at |2| and |3| V show comparable ESM signal intensities at the analysed locations for the fresh and aged sample. However, as it is shown in Figure 6-11 and the following discussion, the overall ESM signal intensity decreases in the aged compared to the fresh sample already with a voltage amplitude of |3| V. This indicates, that in the aged sample with the same magnitude of the electric field, only a smaller degree of concentration change at fewer locations in the sample is generated. As can be seen in the stepwise increase of the dc-voltage pulse amplitude in Figure 6-8 and Figure 6-9b), especially with higher dc-voltage amplitudes only a smaller increase of the ESM signal intensity compared to the fresh sample can be obtained (see Figure 6-9a). Hence, the slope of the ESM signal upon stepwise increasing voltage amplitude is strongly reduced at the aged compared to the fresh cathode. The stepwise increase of the

ESM signal intensity for the aged sample is nearly the same for both locations, while the slope differs in the two locations from the fresh sample. This could point towards a homogeneous redistribution of the remaining Li-ions within the aged sample and a levelling of the activity over aging. Additionally, the absolute ESM signal intensity is much smaller compared to the fresh cathode.

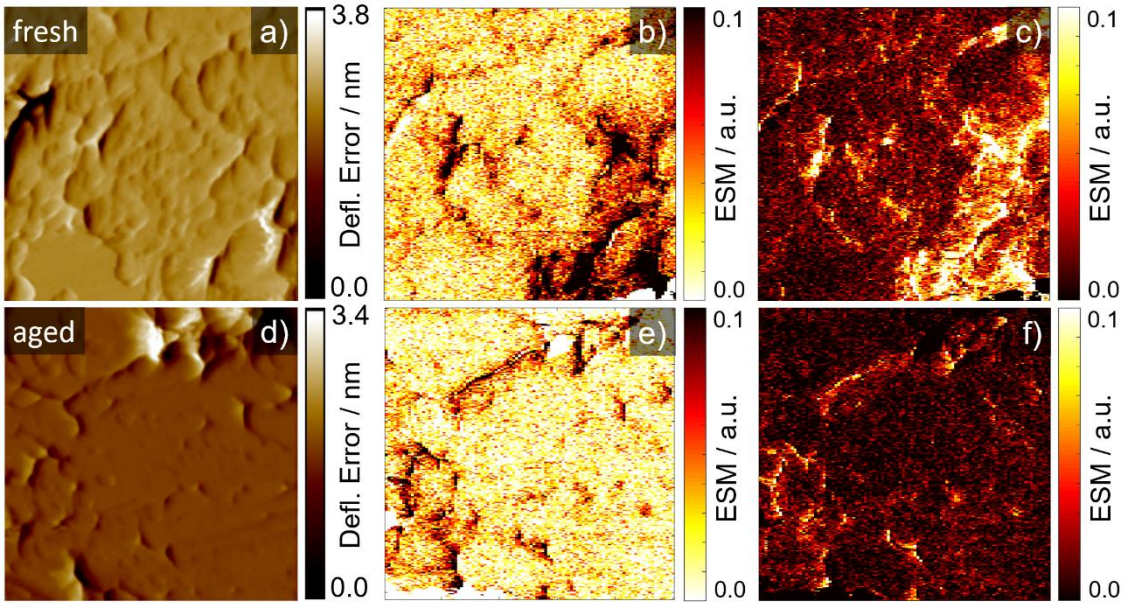

Figure 6-10: ESM measurements of a fresh (top row) and aged cathode (bottom row) cross-section. a) and d) show the deflection error, b) and e) ESM signal during positive and c) and f) during negative voltage pulse. Scan size is 1x1 µm².

The decrease of the ESM signal intensity is more evident in the histograms in Figure 6-11. Figure 6-11a) shows the ESM signal intensity due to the positive and Figure 6-11b) due to the negative dc-voltage pulse. The histograms are a combination of five measurements from different locations in the cathodes, each with a scan size of 1 µm. Both histograms show a decrease of the ESM signal at higher intensity and an increase of the lower ESM signal intensities from the aged cathode in comparison to the fresh sample. We used the two-sample Kolmogorov-Smirnov test (*kstest2* in Matlab R2018) with a significance level of p = 0.05 to evaluate, if the datasets represent different distributions [171]. Indeed, both datasets passed the test, which indicates a different distribution for the fresh and aged dataset and thereby shows a significant change in the ESM signal due to the ageing. To exclude any tip related influence on the ESM signal intensity decrease, the AFM tip, which was used to collect the measurements for the fresh sample, was reused for the aged sample to compare the measurements of the reused tip with the measurements of a fresh AFM tip. The reused tip from the fresh sample showed the

same ESM signal intensities in the aged sample than a fresh AFM tip, which verified the tip-independent ESM signal intensity decrease in the aged sample.

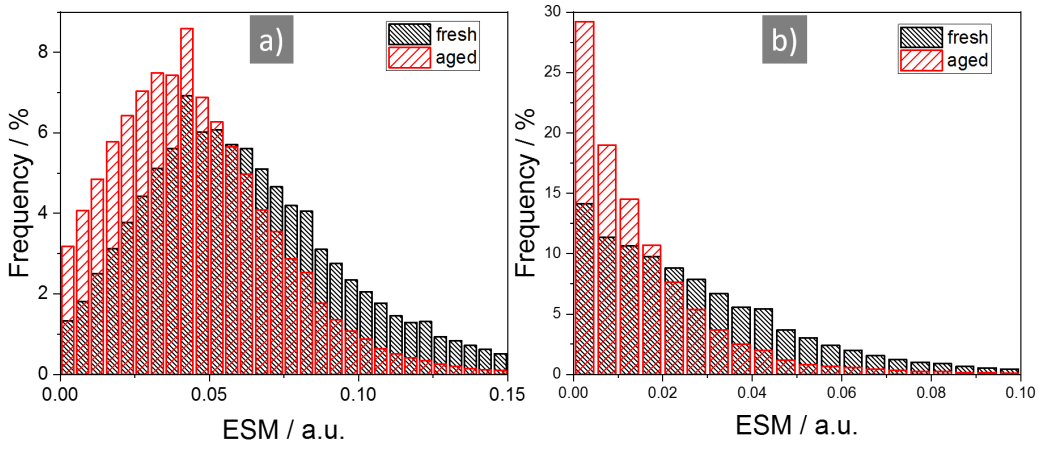

Figure 6-11: Comparison of ESM signal intensity of the fresh and aged cathode, a) shows the ESM signal due to the positive and b) the negative dc-voltage pulse.

Several groups link the ESM signal intensity to the electrochemical activity of Li-ions [95,98,102,110,147,157,172,173], following the approach applied for the analysis of piezoresponse force microscopy (PFM), for which the signal amplitude represents the electromechanical activity [174–176]. Similar to the ESM and PFM signal, digital volume correlation (DVC) in combination with in-situ X-ray tomography microscopy (XTM) was used by Pietsch et al. [177] for graphite and silicon anodes and by Finegan et al. [178] for a $LiMnO_2$ cathode to visualize volume expansion of the electrodes, which was used to link the local volume expansion of the material to its local activity. Following this assumption, a decrease of the overall ESM signal with ageing would imply a decrease of the electrochemical activity of the Li-ions in the cathode material due to ageing. A decrease of the electrochemical activity of the cathode could result in a smaller current peak intensity in a CV experiment, though. Performing CV with the fresh and an aged cathode in combination with a fresh graphite anode as counter electrode for both cathodes under test, showed a minor decline of the resulting current of the aged cathode and a decrease of the capacity during the anodic and cathodic scans (Figure 6-4) , which could indicate a reduction of the active phase. However, since not all particles are participating simultaneously in the lithiation and delithiation process, the current does not represent the actual, local current density at the particles itself, since only a fraction of the active area is involved [179,180]. Deactivation of particles or loss of active material, which is a known degradation mechanism for LiFePO4 cathodes [35,181,182], could be compensated by an increasing local current density at the remaining active particles. Since the CV technique evaluates the entire electrode area, information about

local variations are not obtained. However, the reduction of the current and capacity in the CV could support the assumed decrease of the electrochemical activity, suggested by the reduction of the ESM signal intensity. In former studies of LFP degradation the main effect observed was iron dissolution and Fe^{2+} migration to the anode and redeposition. Fe particles on the anode play a decisive role in accelerated SEI formation [183–185]. Iron dissolution from LFP has been found to increase with water content of the electrolyte and phase impurities in the cathode. The dissolution of iron leads to Fe-deficient inactive phases. The aged cathode showed a higher Fe content on the cathode surface and lower Fe content in the cross-section (Fe mass content fresh: 32.1 ±0.3% and aged: 27.8 ±0.8%), indicating Iron dissolution from the bulk material [71].

Another factor influencing the ESM signal is the structure of the material. Chen et al. observed a dependency of the crystallinity of $LiFePO_4$ on the ESM signal and concluded, that the nanocrystalline sample must exhibit a higher diffusivity than the compared microcrystalline structure [98]. We do not expect a change in the overall structure of the sample and therefore neglect this possibility as an influence. Other possible variations of the ESM signal intensity might result from material stiffness or elasticity, because these material properties are influencing the volume expansion. Harder materials are supposedly showing a smaller surface displacement respectively volume expansion than softer materials. Analysis of the elasticity of the cathode materials was conducted with PeakForce QNM measurements for which the deformation (penetration depth of the tip) of the measurements was evaluated (Figure 6-12). For the fresh and aged sample, a total area of 32 µm² was analysed, using the same settings and the same tip.

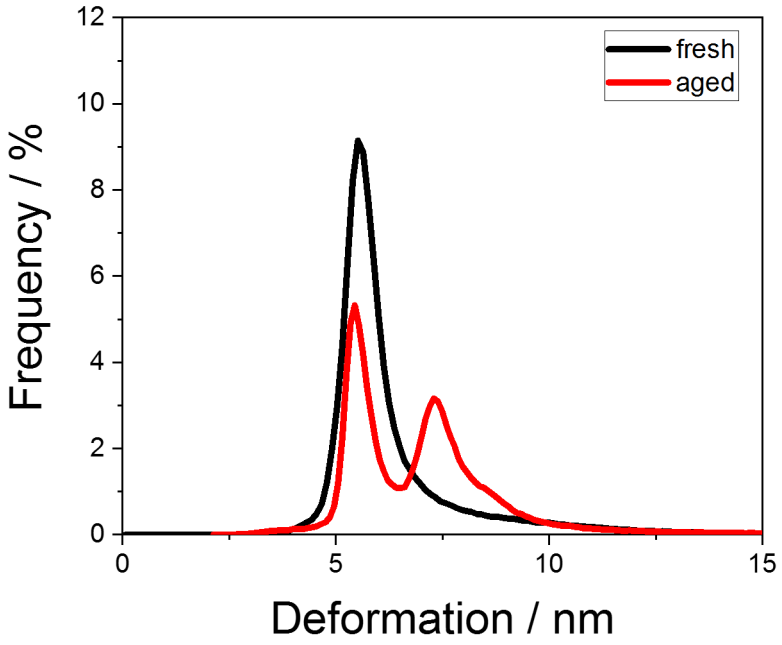

Figure 6-12: Comparison of the deformation distribution of the fresh and aged cathode cross-section

The results are indicating a constant deformation for the fresh sample, while the aged cathode shows some areas with a higher deformation, indicating a softer material. The change of the material property itself would not influence the decline of the ESM signal intensity over ageing, since the softening would promote higher ESM signal intensities. However, if the softer response represents the Fe-deficient inactive phase as a consequence of iron dissolution the lower ESM signal is a direct consequence. It is noted that this is probable, as Fe-dissolution has been reported as the prominent degradation mechanism of LFP [49,57,183].

The dynamics of the relaxation process after the dc-voltage pulse are further analysed in Figure 6-13 and Figure 6-15. Figure 6-13 shows the same sample location as in Figure 6-10 but Figure 6-13b) and e) are now presenting relaxation times after a positive and Figure 6-13c) and f) after the negative dc-voltage pulse.

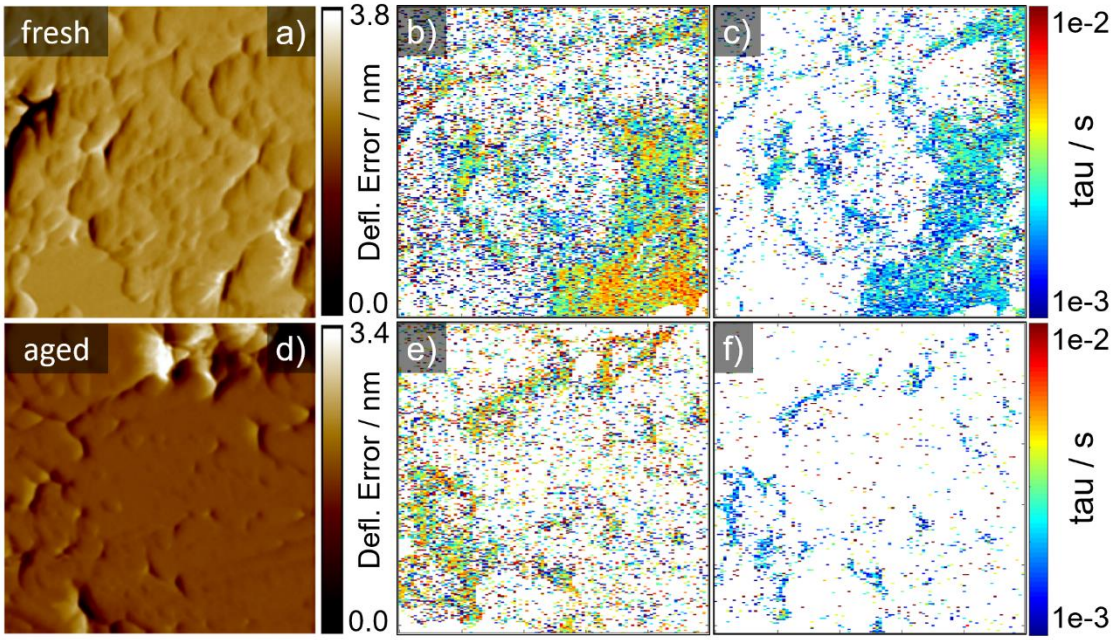

Figure 6-13: Fitted time constants from Figure 6-10 of a fresh (top row) and aged cathode (bottom row) cross-section. a) and d) show the deflection error, b) and e) the time constants during positive and c) and f) during negative voltage pulse. Scan size is 1x1 µm².

We excluded data points below a certain threshold, since a minimal ESM signal intensity is needed to generate a fit. Two examples for the resulting fits are given in Figure 6-14. The overall mean RMSE for all fits is in the order of 0.013.

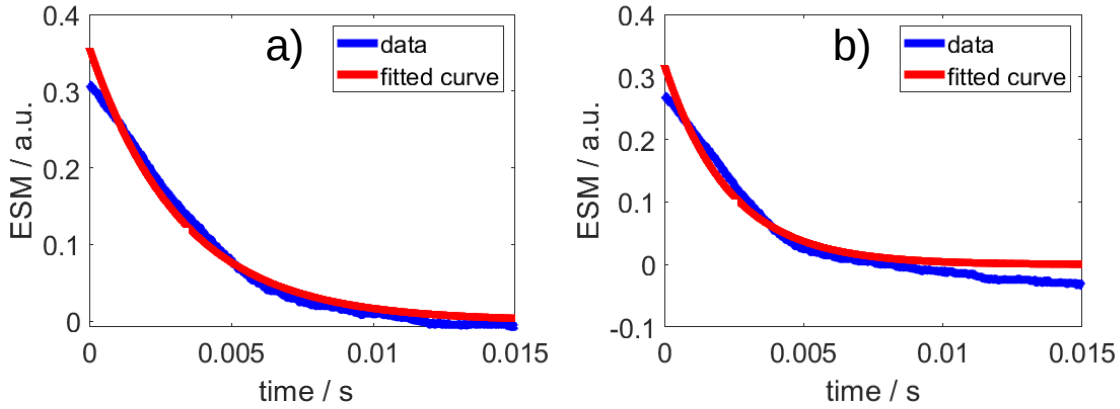

Figure 6-14: Fitting examples for the relaxation ESM signal

The time constants are in the range between 1 and 10 ms, the negative dc-voltage pulse resulting in smaller time constants as compared to the positive pulse. In Figure 6-15 the relative distribution of the time constants of the fresh and the aged cathode are compared, Figure 6-15a) shows the positive and Figure 6-15b) the negative dc-voltage pulse. The histograms result from

a combination of five different measurements at different locations, the same as for the histograms in Figure 6-11. Interestingly, the distributions of the positive and negative dc-voltage pulse differ, the negative dc-voltage pulse showing smaller time constants compared with the positive pulse. This indicates a different behaviour of the diffusivity depending on an accumulation (negative pulse) and a depletion (positive pulse) of the Li-ions. The distributions do not show any significant change from the fresh to the aged cathode, indicating an unaffected diffusivity in the material providing the signal. Using $\tau = {R_V^2}/{(2D)}$ describing the diffusion in a thin film [112] with a time constant τ of 2 ms and a depth of the probed volume R_V of roughly 10 nm leads to diffusion coefficients of about $2.5 \cdot 10^{-14}$ m² s^{-1}. This value is at the higher bound of experimental values given in the literature which range between $1 \cdot 10^{-14}$ to $1 \cdot 10^{-20}$ m² s^{-1} [186–188] and lower bound of theoretically calculated diffusion coefficients. Theoretical work gives values ranging from $1 \cdot 10^{-11}$ to $1 \cdot 10^{-14}$ m^2 s^{-1}, which depends on the direction of the diffusion channels considered [135,170,179,189]. The experimentally generated diffusion coefficients are strongly dependent on the measurement method applied and its analysis (e.g. EIS, PITT, GITT, CV). These techniques assume a simultaneous participation of all LFP particles in the electrodes, when a "domino-cascade" is presumed to more accurately reflect the reaction model [135,179,190]. This faulty assumption affects the diffusion coefficients extracted from experimental data. Additionally, the preparation of the material influences the diffusion coefficient [187,189].

The assumed 10 nm of probed depth are a reasonable assumption considering the sharp boundaries observed in the ESM signals. Smaller values for the probed depth are however possible, which would change the diffusion coefficients by one or two orders of magnitude. Regarding the comparison of fresh and aged diffusion coefficient distributions, the minor differences between the fresh and aged cathodes point towards a stable diffusivity of the cathode material, which is not influenced by any mechanical, electrical or electrochemical degradation. Sun et al. compared the diffusion coefficients of aged and fresh $LiFePO_4$ cathodes from half-cell measurements and found only a minor decrease of the diffusion coefficient due to ageing, which they however correlate to the surface layer build up on the cathodes and not to any degradation of the cathode material itself [181]. Regarding the discrepancy from experimentally and theoretically derived diffusion coefficients, Malik et al. [179] pointed out, that the experimentally generated diffusion coefficients with cell level measurements are representing the cathode as a whole system and not the bulk properties of $LiFePO_4$ particles. For cell level measurements, all particles are assumed to lithiate or delithiate simultaneously. However, this assumption does not hold for a multi-particle system like the electrodes consisting from nano-

and microsize particles [179,180]. The assumption leads to an overestimation of the active particle area and therefore to an underestimated diffusion coefficient. The 'domino-cascade' model by Delmas et al. takes into account the coexistence of a lithiated and delithiated phase for $LiFePO_4$ [190]. Additionally, other mechanisms and factors e.g. the generation of surface layers, porosity and tortuosity of electrodes, electrolyte salts and concentration gradients in the electrodes are affecting the ion transport and therefore influence the diffusion coefficients measured on the cell level [191–194]. The formation of an inactive phase by ageing which does not significantly contribute to the ESM signal is consistent with our observation that diffusion coefficients do not change.

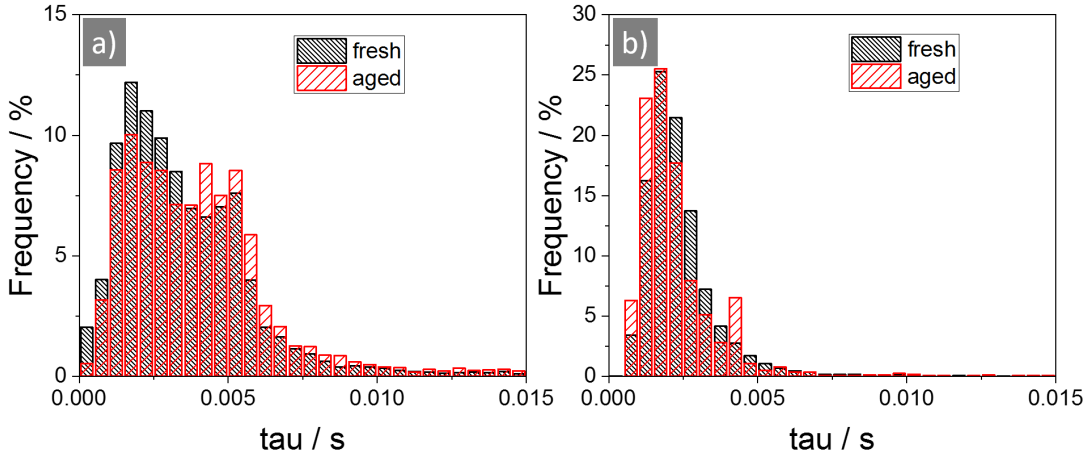

Figure 6-15: Comparison of time constants of the fresh and aged cathode, a) shows the time constants due to the positive and b) the negative dc-voltage pulse.

Combining the results from the reduction of the ESM signal intensity with the unaffected diffusion coefficient over ageing, the reduced lithium concentration in the aged cathode and the results of the CV from the fresh and aged cathode leads us to the conclusion, that the reduction of the ESM signal intensity is representing a decrease of the Li-ion concentration inside the probed volume of the aged cathode compared to the fresh cathode and a formation of an inactive phase. A reduced active Li content in the aged cathode reduces the amount of ions, which can be driven by the electric field, which in turn decreases the ionic concentration change and therefore leads to a decrease of the ESM signal intensity. The reduced activity is the result of deactivation of cathode material, which turned partially electrochemical inactive over ageing. However, since the ionic concentration is as well affecting the activity, it is difficult to clearly state the main source for the reduced ESM signal intensity [195]. If the ESM signal would only

represent the mobility of the Li-ions, the reduction of the ESM signal intensity would be visible in the decrease of the diffusion coefficient, which is not observed.

6.5 Conclusion for the Comparison of the Fresh and Aged Cathode Using a Tailored ESM Technique

The chapter 6 presents a tailored ESM technique, which is used to study the ageing of LFP cathodes. First, a fresh cathode cross-section is analysed. The measurements show a higher ESM signal intensity at structural borders within single grains, but as well active locations at homogenous and planar areas. The activity and the ionic concentration in the material are influencing the ESM signal. Using ESM voltage spectroscopy, a linear increase of the ESM signal is observed for the fresh cathode with no visible side reactions on the cross-section surface. Comparison with the ESM signal at the cross-section of an aged cathode reveals a distinct different behaviour. There is a smaller amount of ESM active area on the cross-section surface and the overall, absolute signal intensity is smaller compared to the fresh cathode. ESM voltage spectroscopy indicates, as it was observed for the fresh cathode, a linear dependency of the ESM signal with the voltage amplitude. However, the slope of the ESM signal is much smaller for the aged cathode, as compared to the fresh one. Fitting the ESM relaxation after the applied voltage pulse provides time constants which represent diffusion coefficients in the range of $2.5 \cdot 10^{-14}$ m^2 s^{-1}. These values are in the range of theoretical and experimental values found in the literature. Combining all the analysis leads to the conclusion, that a reduction in the electrochemical activity and Li content in the cathode is responsible for the reduction of the ESM signal intensity most probably by formation on an inactive phase. Both mechanisms are likewise influencing the remaining cathode capacity, which is reduced due to the ageing.

7 Influence of cycling profile, depth of discharge and temperature on commercial LFP/C cell ageing

7.1 Cell Level Analysis with ICA, DVA and OCV Measurements

The results are based on [93].

7.1.1 Cycling of Cells

Commercially available LiFePO4 cylindrical cells (size 26650, ANR26650M1B) with a specific capacity according to the data sheet of 2.5 Ah (and based on measurements on 100 cells, which results in a mean capacity of 2.584 Ah ± 0.017 Ah) and manufactured by A123 Systems LLC are used for the investigation. SEM analysis shows that the cells consist of double sided coated cathodes and anodes with a thickness of 65 µm and 40 µm, respectively. SEM-EDX analysis of the cathode show the common elements for the LFP cathodes, such as C, Fe, P, O, F and additionally V, which is presumably used as a dopant to enhance electrochemical performance. This detailed composition analysis is provided in the appendix. SEM measurements of the cathodes indicate, that the cathode consists of particles ranging from 50 nm to roughly 1 µm in diameter. The anode consists of graphite flakes of up to 10 µm length. The electrolyte salt used is (as indicated by the safety data sheet) $LiPF_6$ in a carbonate-base electrolyte mixture [196]. We assume the N/P ratio to be in the range of 1.4, as it is found for high power cells [84].

The cells were cycled using part of the “worldwide harmonized light vehicles test procedures” (WLTP), since the degradation of the cells should reflect the automotive ageing and the degradation mechanism due to automotive usage. The WLTP was recorded using a Smart fortwo. The last part of the WLTP was selected for the ageing (called “extra high”), since it shows the highest current loads in the test procedure (called “AP1”). To generate an accelerated ageing procedure, a version with the doubled current load, called here “extra high 2”, was used as a second load profile (called “AP2”). Simultaneously, different depths of discharge (DOD) and different temperatures were selected for the ageing. The matrix of the test plan is summarised in Table 1. The ageing process was conducted as follows: the cells were cycled with the determined WLTP test cycle (AP1 or AP2), until the DOD (50% equivalent to 1.25 Ah, 70% equivalent to 1.75 Ah or 100% equivalent to 2.5 Ah) regarding the discharge capacity during one cycle was reached (or before, in case the lower cut-off voltage of 2.0 V was reached). Afterwards, the cells were charged using 1C until 100% SOC and the WLTP test cycle restarted. After a specified total discharge capacity was passed through the cells over several cycles

(between 200 to 500 Ah), the cells were stored for 1 day at room temperature (25°C, RT) for thermal equilibration. After checking the capacity, OCV and impedance, the cells were brought back to their ageing temperature, and equilibrated for another day. Finally, the ageing process restarted until the next total discharge capacity step was reached.

The cells were cycled with a battery testing potentiostat (Basytec CTS-XL) and stored inside a temperature chamber (Binder MK53). Electrochemical impedance measurements (EIS) were performed using a Princeton Applied Research Versastat 450 after the test routine in potentiostatic mode with 4 mV amplitude at controlled temperature (25°C). Figure 7-1 shows the load profiles which were used for the ageing of the cells and which are extracted from the WLTP driving cycle. Since the battery cycler is limited to a current of maximum 5 A the C-rate is limited to 2 C in the test protocol. A negative C-rate stands for discharging, a positive C-rate for charging. The C-rate is referred to the 2.5 Ah capacity of the cells. For the three-electrode tests, selected cells were transferred into an argon filled glovebox (MBraun, O_2 and H_2O < 1 ppm) and dissembled. Samples of the electrodes were cut out close to the first current collector tap (diameter of 18 mm) and rinsed with dimethyl carbonate (DMC, Sigma Aldrich, Alfa Aesar) to wash off the remaining electrolyte. The electrodes were assembled in three-electrode test cells (EL-CELL GmbH, Germany) with a lithium ring as reference electrode, a FS-5P separator (all from EL-Cell GmbH) and LP30 (Sigma Aldrich). For the three-electrode tests, the aged cathodes were combined with fresh anode samples. This way, the Li content stored in the cathode and the cathode capacity could be evaluated. The three-electrode tests were performed with a current density of 48 µA cm^{-2}, which represents roughly C/20. In the fresh state, the ratio of negative to positive electrode capacity for the three-electrode tests was 1.9.

The evaluation of the ageing process for 55°C and -20°C was conducted using the analysis of one cell aged at 50% DOD and one aged at 100% DOD, both from AP2.

Table 1: test matrix of ageing plan

	at +55°C and -20°C		
AP1	50% DOD	70% DOD	100% DOD
(C_{MEAN} = -0.77)	(100 – 50 % SOC)	(100 – 30% SOC)	(100 – 0% SOC)
AP2	50% DOD	70% DOD	100% DOD
(C_{MEAN} = -1.33)	(100 – 50 % SOC)	(100 – 30% SOC)	(100 – 0% SOC)

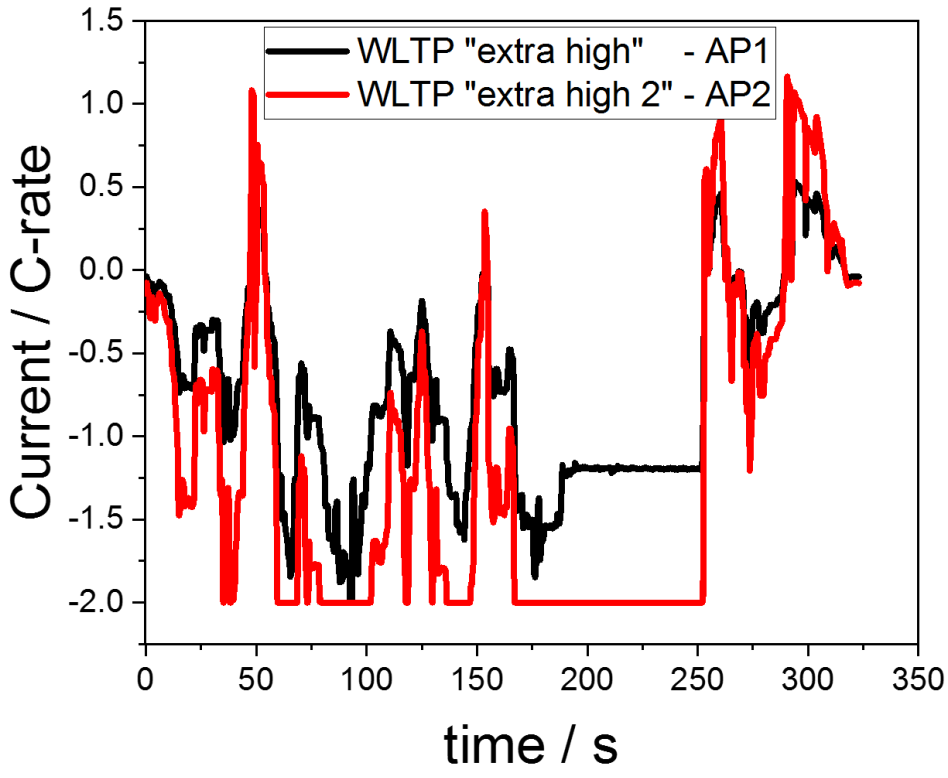

Figure 7-1: Load profiles applied extracted from the WLTP driving cycle

7.1.2 Comparison of C-rates for the Calculation of the ICA and DVA

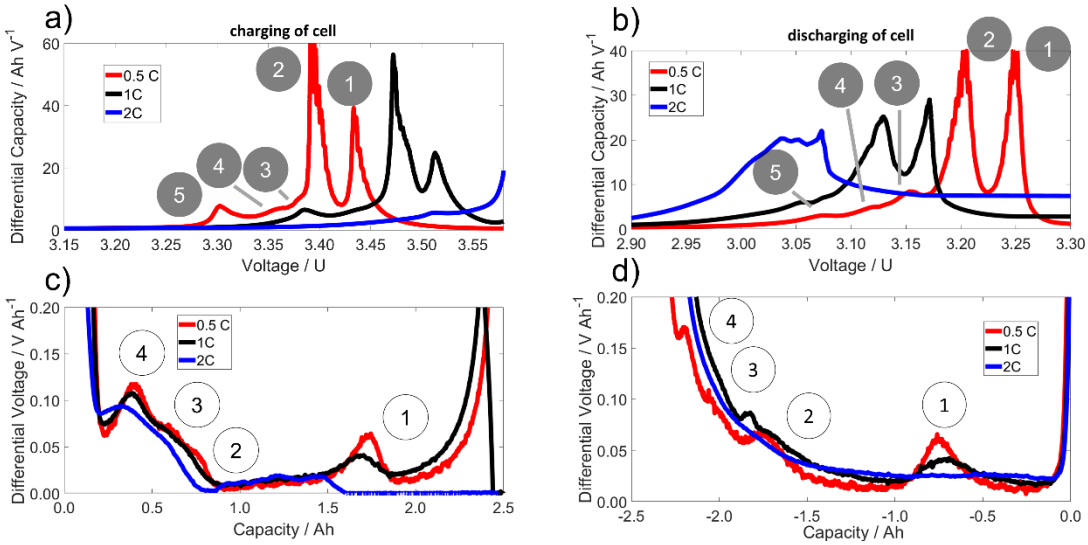

Figure 7-2: Influence of the C-rate on the resulting ICA (a and b) and DVA (c and d) during charging (a and c) and discharging (b and d)

The comparison of a C/2, 1C and 2C charge and discharge process of a cell shows clearly a difference in the resulting amount of peaks, intensity and location (Figure 7-2). Comparing the

0.5C and 2C processes shows a clear difference in peak quantity of the ICA and DVA curves. In addition, a shift of the peaks on the voltage axis for the ICA and on the capacity axis for the DVA is apparent. As expected, the most pronounced peaks appear in the curves using the C/2 charge and discharge current. The charging and discharging ICA with 0.5C show both five peaks and the DVA shows four peaks, which are corresponding to the four different intercalation stages of Li-ions into graphite [91,197]. The results from Figure 7-2 suggest that for a valid ICA and DVA analysis, the C-rate cannot exceed 1C, since several peaks are missing and the peak intensity dramatically reduces for 2C. However, to a certain extent, 1C measurements deliver enough peak intensity to produce distinct peaks in the ICA and DVA curves. For a further increase of the signal to noise ratio and to track the changes over ageing more reliably, the C-rate should be C/2 or lower, though.

7.1.3 Separation of Cathode and Anode Influence on ICA and DVA Peaks

As it is seen in Figure 7-3, the resulting ICA and DVA are calculated from the full cell voltage profile E_{cell}, which is a combination of the cathode and anode voltages. Due to the phase transition from $Li_{xmin}FePO_4$ to $Li_{xmax}FePO_4$, the voltage profile of the $LiFePO_4$ cathode is rather constant over the whole lithiation and delithiation process. This is depicted in Figure 7-3g), which shows the DVA curves for the anode, cathode and full cell using an experimental cell with Li reference electrode. The cathode potential E_C vs. Li/Li^+ is extracted from the three-electrode setup and the anode potential E_A vs. Li/Li^+ is calculated, since $E_{cell} = E_C - E_A$. The separate potentials are plotted in Figure 7-3d), e) and f). The DVA curve of the full cell has the same shape as the anode DVA curve. The cathode DVA curve shows a small peak around 0.4 mAh cm^{-2}. Hence, there is a small contribution of the cathode to the full cell DVA curve, at least in the first peak. The other two noticeable peaks are not affected by the cathode potential. The origin of the contribution from the cathode to the DVA peak is not entirely clear yet. It could indicate the existence of a vanadium doping of the cathode, since V was detected in the cathode. Doping of V is performed to enhance the electrochemical performance of LFP material [198]. The calculated ICA curves of the anode, cathode and the full cell are plotted in Figure 7-3a), b) and c), respectively. The ICA curve of the anode and the full cell exhibit the same shape, but inverted due to the voltage profiles. The drawback of the ICA is the possibility to reach nearly zero in the denominator of the division and therefore causing the ICA to rise steeply, which is visible in Figure 7-3b) for the cathode. If the anode would be the only factor influencing the ICA of the full cell, the ratio of the two main peaks would need to be the same in the anode and

full cell ICA. The ratio of the $^{P_1}/_{P_2}$ with P_1 and P_2 as the peak intensities of ICA peak 1 and 2 (see Figure 7-3b) is ≈ 0.75 for the anode and ≈ 0.85 for the full cell. Hence, the cathode contributes as well to the ICA of the full cell and especially to peak 1, otherwise the ratio of the peaks 1 and 2 would be the same for the full cell and anode.

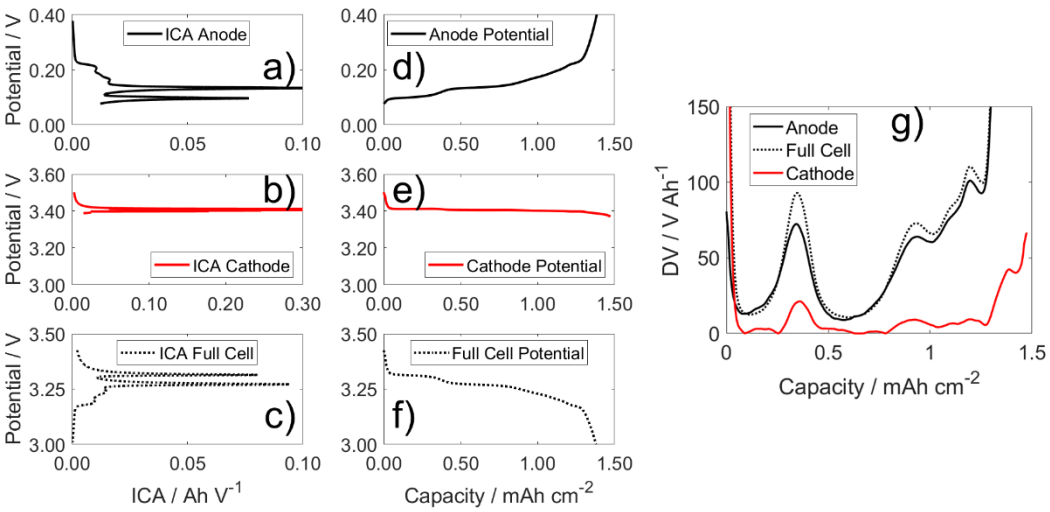

Figure 7-3: Separation of the ICA and DVA peaks from fresh cathode and fresh anode potentials. In the left column the ICA of the fresh anode in a), the aged cathode in b) and the three-electrode full cell in c), the middle column shows the potentials of the fresh anode in d), the aged cathode in e) and the three-electrode full cell in f) and finally the DVA separation in g).

By using the half-cell ICA of the anode, the anode potential profile, the full cell ICA and the allocated staging process in the anode potential (see Figure 7-4), we can assign the ICA peak 1 to stage 1, peak 2 to stage 2, peak 3 to stage 3, peak 4 to stage 1d+4 and peak 5 to stage 1d of the anode. As is already explained by the ratios of ICA peak 1 and 2, the cathode likewise influences these peaks, but the anode potential profile is the main factor of origin.

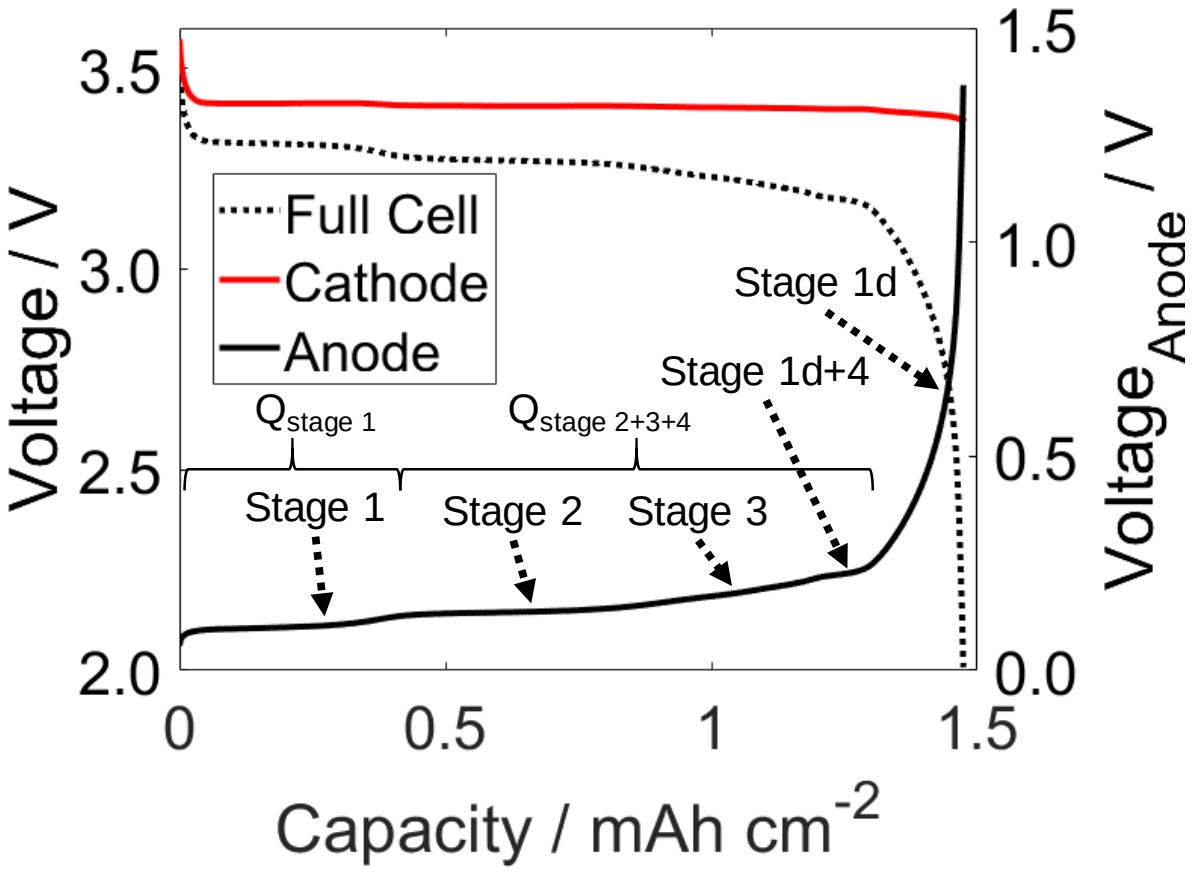

Figure 7-4: Cathode and anode potential of LFP – graphite full cell with the indication for the different staging processes and capacities of the stages.

7.1.4 Ageing at 55°C

7.1.4.1 Influence of the cycling profile on the capacity fading and IC and DV parameters

The cycling profiles in this paper differ by the applied current load and the DOD. Starting with the comparison of the influence of the profiles on the ageing at the same temperature, Figure 7-5a and b show the capacity degradation of the cells aged at 55°C with the different loads applied and grouped in the three different DODs (50%, 70% and 100%). Each point represents two or three cells with an error bar representing the standard deviation. The results in Figure 7-5 indicate a homogeneous ageing of the cells, since the results within the groups itself are differing only by a few mAh as indicated by the error bars. After the initial capacity drop after 300 Ah total discharge capacity, the cells follow a linear trend of the capacity decay. Spingler et al. did not observe any capacity drop for LFP cells from A123, therefore we assume the initial capacity drop to be finished early on in the ageing process [199].

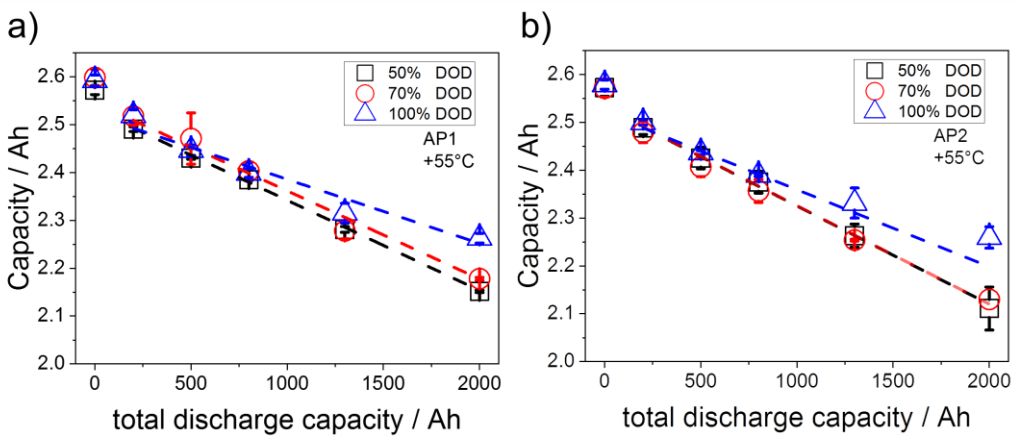

Figure 7-5: Degradation of cell capacity depending on ageing profile, AP1 in a) and AP2 in b), at different ageing steps. The linear fit excludes the initial capacity.

As can be seen, the DOD influences the capacity fading during the ageing process. Cycling at 50% DOD leads to the highest capacity loss, followed by 70% DOD cycling, which shows nearly the same capacity fading compared to 50% DOD cycling and 100% DOD cycling with the markedly lowest capacity fading at EOL. Higher current loads increase the capacity fading of the cells, visible when comparing the cells cycled with loading profile AP1 in Figure 7-5a with AP2 (Figure 7-5b). However, the ageing profiles with 100% DOD show a rather similar trend of the capacity degradation and the higher current load does not lead to a significantly higher capacity loss over ageing. Until roughly 800 Ah total discharge capacity, the cell capacity loss is the same for all ageing profiles, after this ageing step, the difference in cell capacity loss starts to deviate. The capacity loss of the 100% DOD AP2 decreases with further ageing (visible in the deviation towards higher cell capacities of the characterisation points at 1300 Ah and 2000 Ah from the linear fit), while for 50% and 70% DOD it stays constant throughout the cycle life until the end of ageing is reached.

Figure 7-6a and b shows the IC analysis of the cell at charging and discharging, and Figure 7-6c and d the DV analysis. The IC reveals five peaks labelled 1 to 5 and the DV in total four peaks labelled 1 to 4. During the ageing process, only peak 1 and 5 are showing any changes in the IC (Figure 7-6b). In the DV, peak intensities and positions are only changing during the discharging process, namely peak 1 and 5 (Figure 7-6c and d). The peak intensity of IC peak 1 decreases during ageing and the peak intensity of peak 5 increases, but only during the discharging process. The position of the IC peaks shift slightly on the voltage axes during charging towards smaller and during discharging towards higher voltages. In the DV of the charging process, the peaks do not change noticeably, the peak positions and intensities stay

constant throughout the ageing. Only the steep increase after the first peak moves towards smaller capacities, which is indicating the cell capacity loss. During the discharging, the peaks are shifted and change their intensities. The intensity of peak 1 increases slightly, while the peak 5 decreases regarding the absolute value during ageing. Looking at the relative change of the intensity of peak 4 though, the vertical distance from peak top to the valley on its left hand side (parameter ΔMinMax) increases during ageing for the cell aged at 50% DOD, AP2 (Figure A4a). For the cell aged with 100% DOD, AP2, the parameter stays constant after 500 Ah (Figure A4b). Similar to the charging DV, the steep increase after DV peak 4 shifts towards smaller capacities in the discharge DV, which indicates the end of the discharging process. The shift is especially pronounced for the first discharge DV peak 1, which represents the extractable capacity during stage 1 of the anode ($Q_{stage\ 1}$). The reduction of the extractable capacity during the stage 1 is shown in Figure 7-7e, which shows, that the capacity of $Q_{stage\ 1}$ decreases by roughly 75%. The distance between discharge DV peak 1 and 4, which represents the extractable capacity $Q_{stage\ 2+3+4}$ during stage 2, 3 and 1d+4, stays rather constant throughout the ageing and even increases slightly at the EOL (see Figure 7-7e) [81,91,200]. Contrary to the cell aged at 50% DOD, AP2, the cell aged with 100% DOD, AP2 shows a smaller decrease of $Q_{stage\ 1}$ of only about 40%, but a loss of $Q_{stage\ 2+3+4}$ of about 7% (see Figure 7-7f). Similar observations were found by Li et al. with cells cycled at 60°C showing a higher loss of $Q_{stage\ 2+3+4}$ at 100% DOD compared to 30% DOD (100% - 70% SOC) [201].

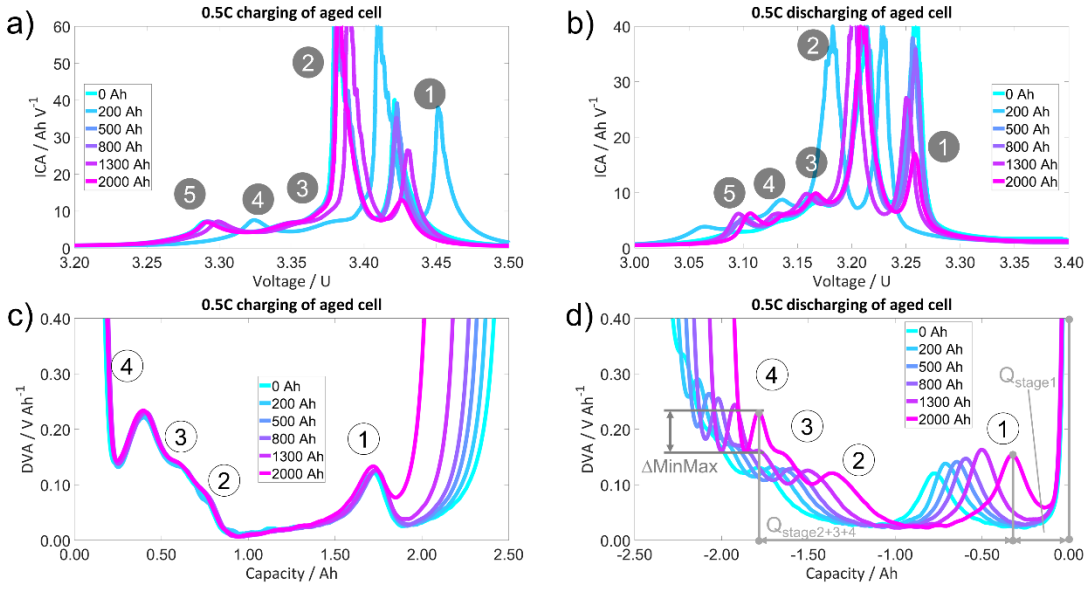

Figure 7-6: ICA (a and b) and DVA (c and d) analysis of a commercial LFP cell, cycled at 55°C with 50% DOD and AP2 at different ageing steps. Charging in a) and c) and discharging in b) and d).

Peak tracking analysis was conducted, to follow the changes of peaks in the IC and DV curves. The peak tracking reveals that several peaks change their intensity over the ageing and the changes are depending on the ageing process applied. Figure 7-7 displays the changes over ageing of the discharge peak 1 of the IC of different cells. Figure 7-7a compares the peak intensities of peak 1 of the discharge IC of cells with 50% DOD and different ageing profiles. The higher current load of AP2 does not lead to a higher peak intensity decrease, when compared to the AP1. The cells retain a capacity of 2.154 Ah (50% DOD, AP1) and 2.156 Ah (50% DOD, AP2). In Figure 7-7b the decrease of the peak intensity of IC peak 1 of cells from AP2 with the different DODs are compared. Similar to the different trends of the remaining capacity over ageing, the peak intensities exhibit a different slope. 50% and 70% DOD follow the same trend with a similar slope, while for 100% DOD the decrease of the peak intensity flattens after 800 Ah and shows a smaller slope compared to the beginning of the ageing. Peak 1 of the charging IC decreases in intensity similar to the discharging IC and reaches a smaller absolute value at the EOL. Contrary to IC discharge peak 1, the intensity of peak 5 increases over ageing, see Figure A2a, which compares the cells from AP2 with the different DODs. Contrary to the discharging, the peak intensity of peak 5 in the charging IC is constant throughout the complete ageing process. The DV discharge peak 1 shows a similar behaviour than the IC peak 5 during discharge. The increase of the peak intensity of DV discharge peak 1 is plotted in Figure 7-7c, comparing the cells of AP2 and the different DODs. The increase of the peak intensity and the overall trend are the same for all cells in the AP2 group.

The decreasing capacity follows the same trend as the changes in the peak intensity of the IC discharge peak 1. Both follow a linear decrease over ageing as it is shown in Figure 7-7d (for better visualisation, only one ageing profile is plotted, for additional profiles see Figure A7 and later on Figure 7-16). The same is visible when comparing the changes in peak intensity of the discharge peak 1 in the IC within the same ageing profile group. The changes in the peak intensities in Figure 7-7b follow the same trend as the capacity fading observed in Figure 7-5b (plotted in one figure in Figure A7a).

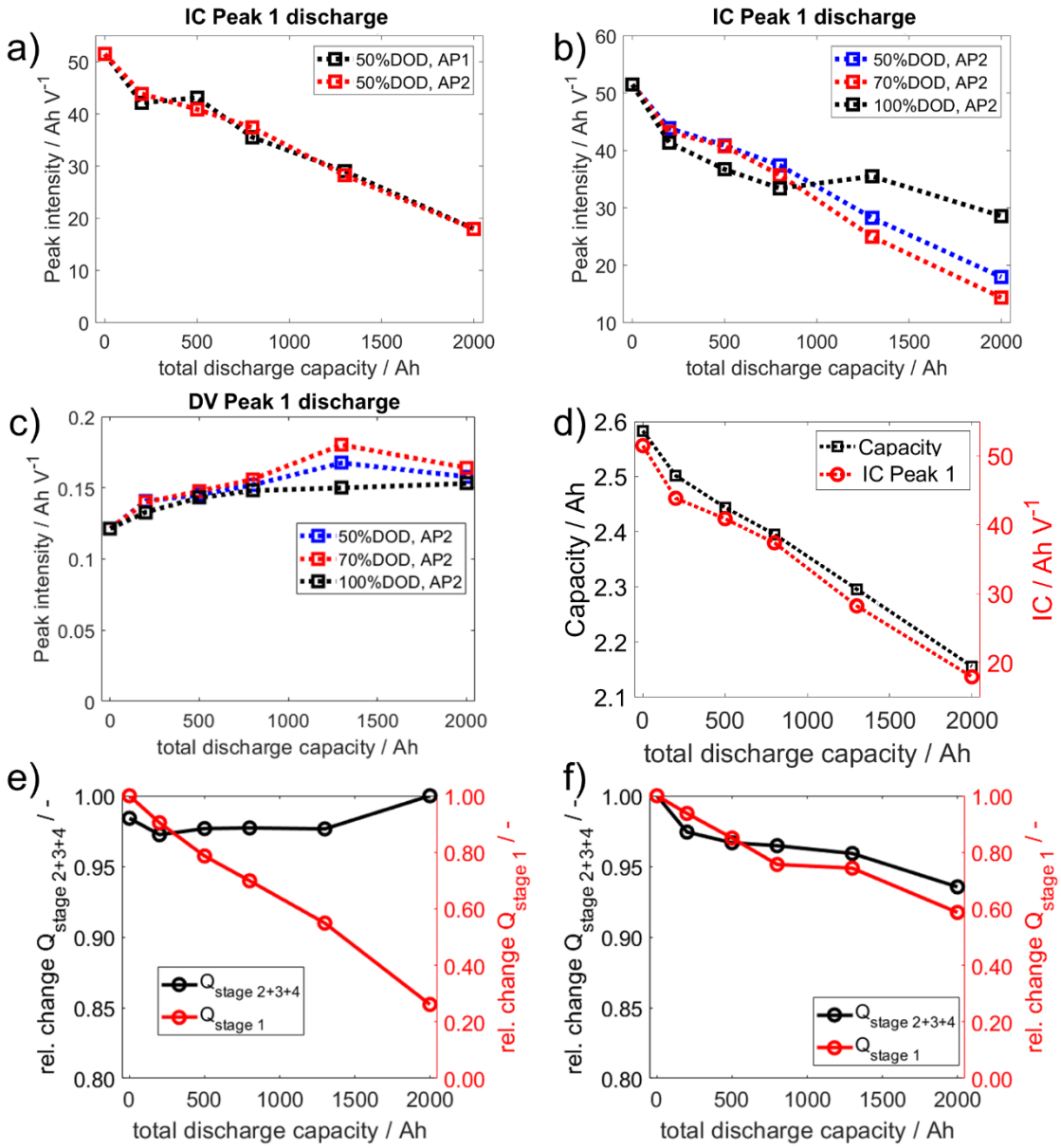

Figure 7-7: Changes at 55°C in the IC peak 1 during discharge of a) cells aged at 50% DOD with AP1 and AP2, b) all at AP2 with 50%, 70% and 100% DOD, c) comparing the change of the DV peak 1 intensity over ageing of the three groups, the correlation of the IC peak 1 intensity with the capacity fading in d) , relative change of the extracted capacity during stage 1 and the combination of stage 2, 3 and 4 for 50% DOD, AP2 in e) and 100% DOD, AP2 in f); both at 55°C aging

Half-cell measurements of the aged cathode (50% DOD with AP2) in combination with a fresh anode show a reduced discharge capacity of the three-electrode cell of 1.2 mAh cm^{-2} compared to the fresh cathode in Figure 7-3f with 1.5 mAh cm^{-2}. Additionally, the cell showed an initial charge capacity of 1.4 mAh cm^{-2}, compared to the fresh cathode with 1.6 mAh cm^{-2}, which shows that the aged cathode contained roughly 14% less cycable lithium. The half-cell

measurements were used, to generate IC and DV for full cell, cathode and anode. Figure 7-8 shows the separate IC and DV curves for the electrodes and the full cell setup. In the DV curves, the anode DV alone represents the full cell DV curve and the influence of the cathode on the first DV peak is completely vanished. In the IC curve analysis, the first IC peak of the full cell disappeared entirely, even more severe than for the commercial cell. The anode IC represents the shape of the full cell and still shows a noticeable peak at the first IC peak.

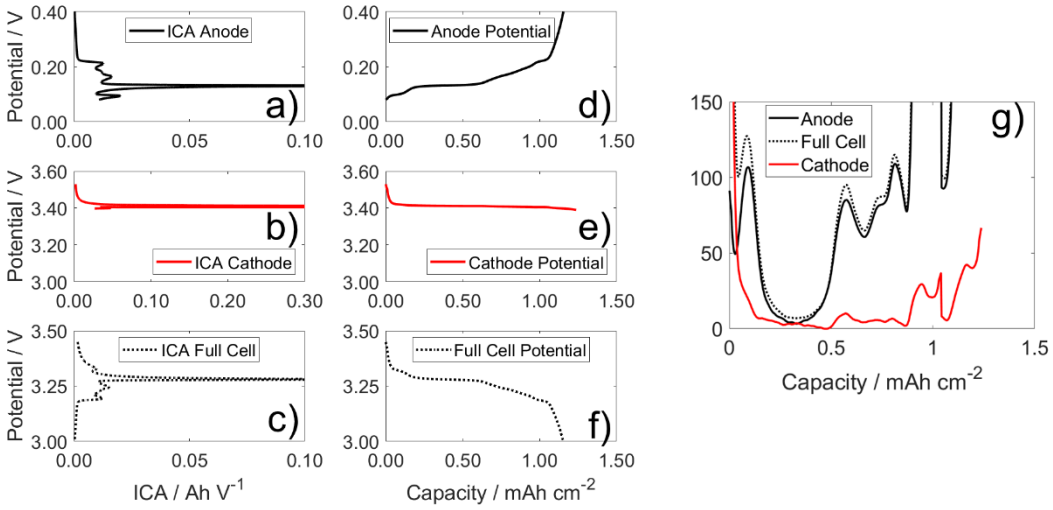

Figure 7-8: Separation of the IC and DV peaks from aged cathode (55°C, AP2, 50% DOD) and fresh anode potentials. In the left column the IC of the fresh anode in a), the aged cathode in b) and the three-electrode full cell in c), the middle column shows the potentials of the fresh anode in d), the aged cathode in e) and the three-electrode full cell in f) and finally the DV separation in g).

7.1.4.2 Changes in the OCV curves due to ageing at 55°C

The evolution of the OCV of a single cell aged at 50% DOD with AP2 is plotted in Figure 7-9a. The OCV curve shifts slightly towards lower voltages in most SOC areas with ageing. At 70% to 90% the decrease is more pronounced compared to the rest of the SOC range. The decrease of the OCV curve and the loss of the OCV step around 70% SOC was already observed in the literature for LFP [197,202,203]. Figure 7-9b displays the OCV evolution of a cell aged at 100% DOD and AP2. The OCV curve still contains the step around 80% SOC, which results in a nearly unchanged IC peak intensity of peak 1 (see Figure A1). The OCV at 100% SOC increased more distinct for the 100% DOD cell than for the 50% DOD with AP2 cell (Figure 7-9c). The OCV at 0% SOC decreases for both cells over ageing and is more pronounced for the 50% DOD ageing. The increase of the OCV at EOC for $LiFePO_4$ cells was

likewise observed by Safari and Delacourt, however, to a rather negligible extent [91]. The different behaviour of the OCV due to the ageing is shown in Figure 7-9d. The OCV of six cells, from each ageing group one, is plotted at the EOL. Both cells, which are aged at 100% DOD, exhibit the highest OCV value at 100% SOC in their group and still contain the step at around 80% SOC, which is not observed anymore in the other cells (see Figure 7-9a and b).

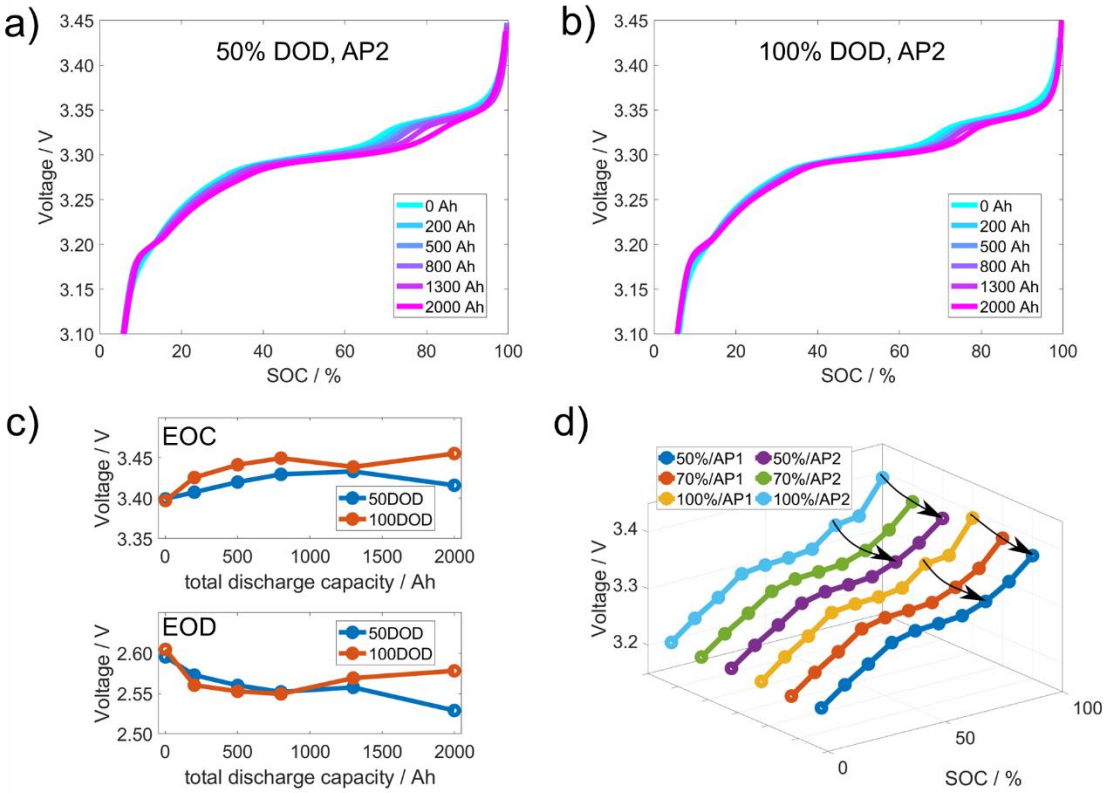

Figure 7-9: Evolution of the OCV of single cells, 50%DOD, AP2 in a) and 100%DOD, AP2 in b), the OCV at EOC and EOD in c) and in d) the OCV curves of cells from each group aged at 55°C at EOL. The arrows indicate most distinct changes of the OCV curve over ageing.

7.1.5 Ageing at -20°C

7.1.5.1 Influence of the cycling profile on the capacity fading and IC and DV parameters

For both groups, AP1 (Figure 7-10a) and AP2 (Figure 7-10b), the 50% DOD cells exhibit the highest loss in capacity, similar to the 55°C ageing. The cells aged at -20°C show an overall smaller capacity loss compared to 55°C and the cells aged with 100% DOD with AP1 show the lowest capacity loss of merely 6%. The cells aged with AP2 show a strong capacity decrease after the first characterisation, followed by a smaller, linear capacity decline

afterwards. At AP1, the groups are well separated. The cells aged with AP1 show a smaller, initial capacity drop and a linear capacity decay after the first characterisation. For the cells aged at 100% DOD with AP2, the constant linear capacity decay starts only with the third characterisation at 600 Ah.

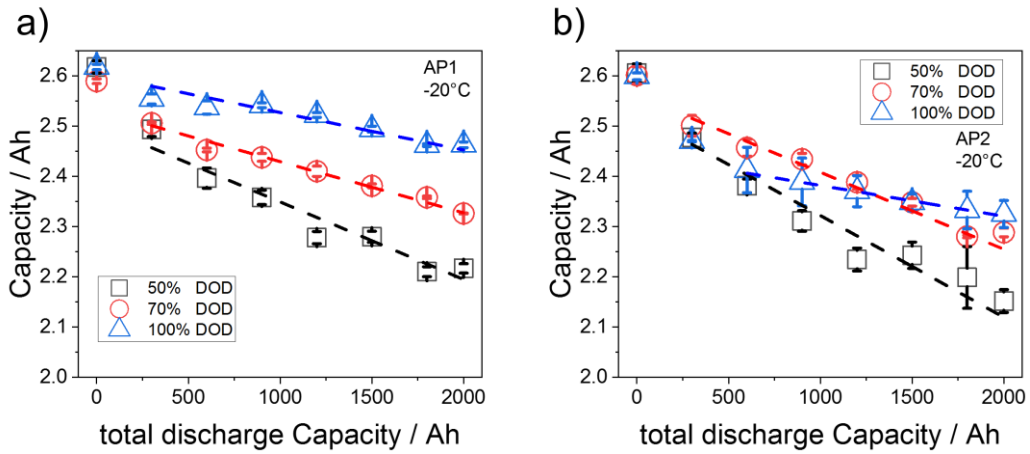

Figure 7-10: Degradation of cell capacity depending on ageing profile, AP1 in a) and AP2 in b), at different ageing steps, aged at -20°C. The linear fit excludes the initial capacity, for the 100% DOD with AP2, the initial value and the value at 300 Ah are excluded.

The IC and DV of a cell aged at 50% DOD with AP2 is shown in Figure 7-11. The IC exhibits the same features as for the 55°C cycled cell (see Figure 7-6). The IC (Figure 7-11a and b) peak 1 declines over ageing for charging and discharging. This is plotted in Figure 7-12a, which compares the change for the cell with 50% DOD with AP1 and AP2. Both cells exhibit a comparable decay of the peak intensity, with the cell aged with AP2 showing a more pronounced decrease of the peak intensity, which is reflected by the lower remaining capacity at EOL with 2.134 Ah compared to 2.225 Ah for the cell of AP1. The comparison of the capacity decay and the decline of the peak intensity is summarised in the plot in Figure 7-12 and Figure A7b. The trends exhibit a higher variance compared to the ageing at 55°C, for whom the trends of the capacity and peak intensity coincide well. The fact, that the 100% DOD ageing at AP2 exhibits a higher capacity decay compared to the 70% DOD ageing is reflected in the decline of the peak intensity of IC peak 1 (Figure 7-12b). Similar to the cells aged at 55°C, peak 5 in the discharge IC emerges at the beginning of the ageing. The trend of peak 5 is plotted in Figure A6a, comparing the different DOD groups of ageing profile AP2. For 50% and 70% DOD, the peak intensity of peak 5 increases constantly over ageing, whereas for 100% DOD, the peak intensity increases up to 600 Ah and declines afterwards until EOL is reached. The other peaks in the IC curves do not show a noticeable change in peak intensity. The peaks shift towards

lower voltages for the charging and higher voltages of the discharge IC plot, as it is already seen for the cell aged at 55°C (Figure 7-6). The DV peaks at -20°C exhibit a shift towards smaller capacities during the charging process, the peaks during the discharging process shift in a similar manner compared to the 55°C ageing. However, the DV peak 1 during discharging exhibits a decreasing peak intensity (Figure 7-12c) and increasing peak width (Figure A6b) during ageing and disappears completely at 1500 Ah discharge capacity.

The DV peak 1 disappears around 1500 Ah completely. Meanwhile, beginning at 900 Ah, the evolution of peak 0 starts. It is likewise observable in the IC charge and discharge curves, where it is indicated as peak 0 and was already observed before by others [204,205]. For the charging IC, the peak 0 is merely observable as a bump. In the discharging IC it is however clearly visible as a distinct peak. Peak 0 appears around 3.57 V and 3.37 V during charge and discharge, respectively. This new feature is only observed at cells cycled with 50% DOD and appears in AP1 and AP2 (not shown here).

Analogue to the ageing at 55°C and the features in the DV curves, the decrease of the capacity can be separated into the loss of the first stage of the anode ($Q_{stage\ 1}$) and the second, third and fourth stage ($Q_{stage\ 2+3+4}$). Similar to the ageing at 55°C of 50% DOD with AP2, the capacity of $Q_{stage\ 1}$ decreases linear over ageing, but exhibits a higher slope of the capacity decay for $Q_{stage\ 1}$ (see Figure 7-12e). After 1200 Ah total discharge capacity, $Q_{stage\ 1}$ can no longer be evaluated, since the DV peak 1 disappeared. However, up to 1200 Ah, $Q_{stage\ 1}$ decreases in capacity by 60%. The capacity of $Q_{stage\ 2+3+4}$ stays constant throughout the ageing, as long as it can be evaluated, since it depends on the DV peak 1. Comparing the ageing of the cell aged at 50% DOD, AP2 with the cell aged with 100% DOD, AP2 (Figure A3 and Figure 7-12f), a capacity decay of $Q_{stage\ 1}$ in a comparable extend and linear slope is observed. The capacity of $Q_{stage\ 2+3+4}$ increases over ageing by roughly 10%, showing that to some extend the capacity loss of $Q_{stage\ 1}$ can be extenuated. The parameter ΔMinMax (Figure A4c and d) increases for the cells aged at -20°C, but stays constant after 600 Ah and 300 Ah total discharge capacity for the 50% and 100% DOD cell, respectively.

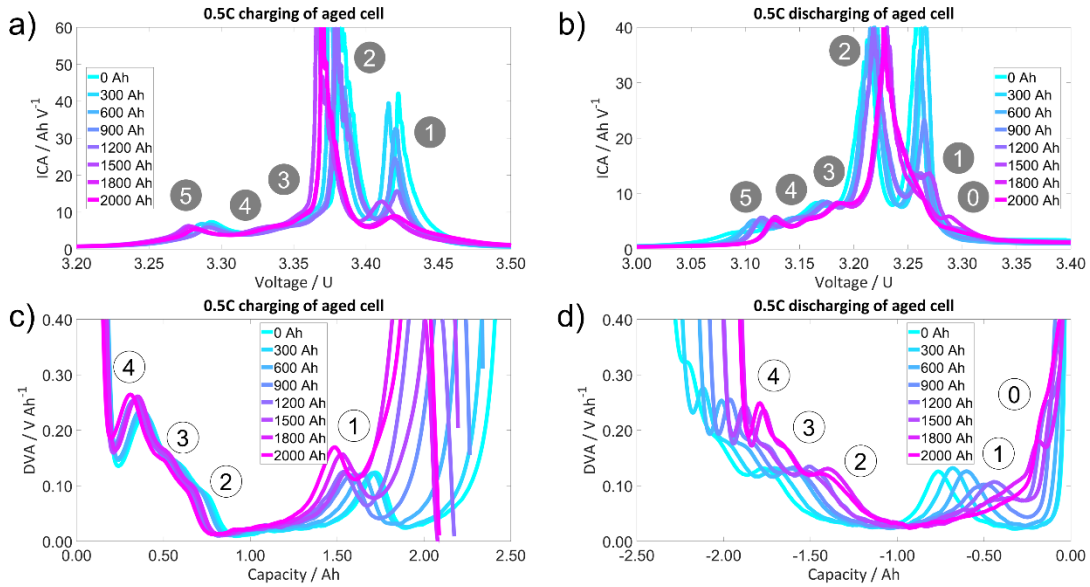

Figure 7-11: ICA (a and b) and DVA (c and d) analysis of a commercial LFP cell, cycled at -20°C with 50% DOD and AP2 at different ageing steps. Charging in a) and c) and discharging in b) and d).

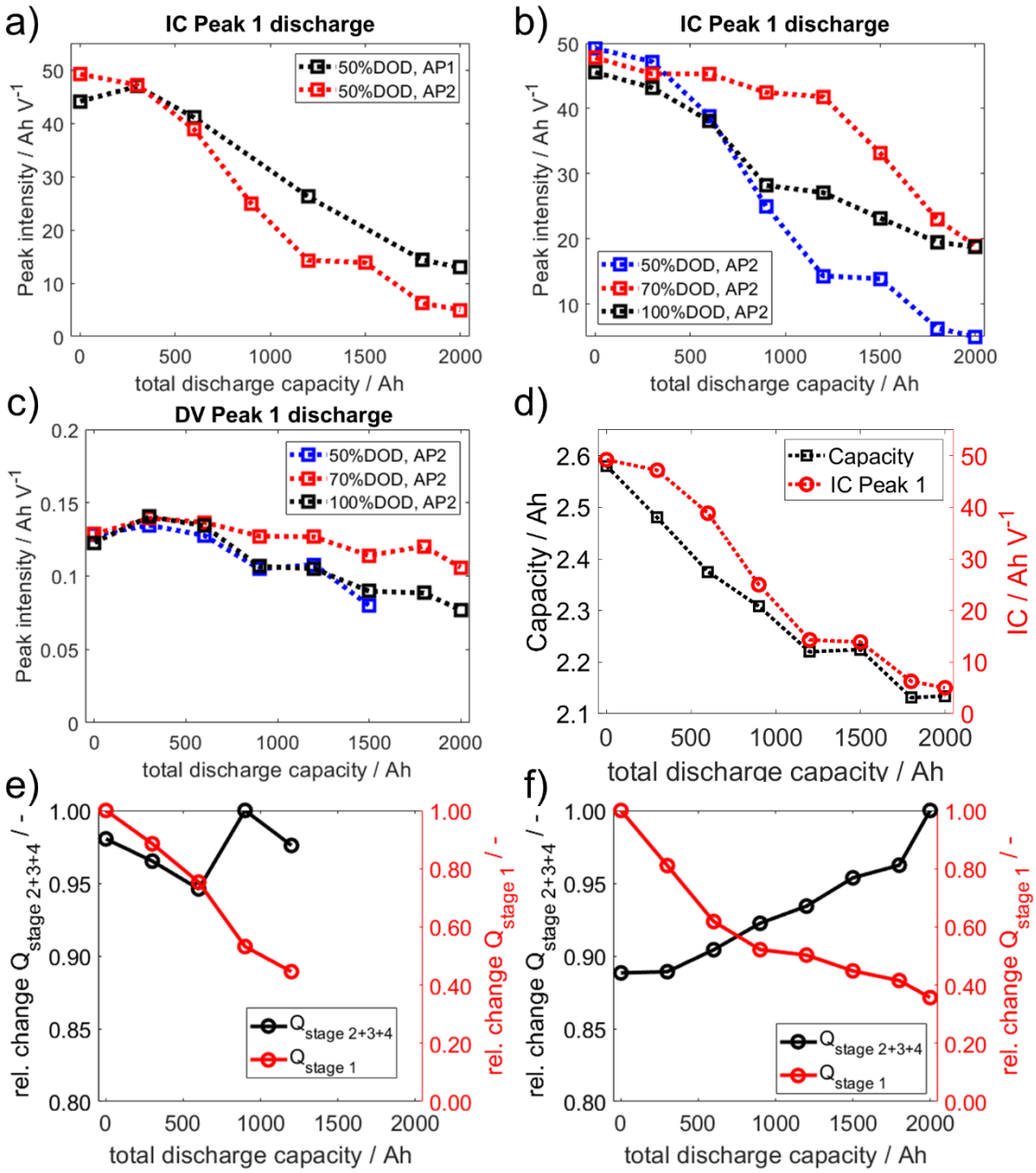

Figure 7-12: Changes at -20°C in the IC peak 1 during discharge of a) cells aged at 50% DOD with AP1 and AP2, b) all at AP2 with 50%, 70% and 100% DOD, c) comparing the change of the DV peak 1 intensity over ageing of the three groups, the correlation of the IC peak 1 intensity with the capacity fading in d), relative change of the extracted capacity during stage 1 and the combination of stage 2, 3 and 4 for 50% DOD, AP2 in e) and 100% DOD, AP2 in f); both at 55°C aging.

As for the ageing at 55°C, a three-electrode setup was used to separate the electrode potentials from the full cell voltage to generate the separate IC and DV curves. The half-cell potentials vs. Li/Li^+ for the aged cathode, fresh anode and three-electrode full cell are shown in

Figure 7-13d, e and f, respectively. The resulting IC curves are shown in Figure 7-13a, b and c for the fresh anode, aged cathode and full cell. Similar to the three-electrode setup for the cathode aged at 55°C, the IC curves from the three-electrode setup match the aged, commercial full cell ICA. Comparing the three-electrode setup ICA curves using the at -20°C aged cathode (Figure 7-13) to the three-electrode setup IC curves using a fresh cathode (Figure 7-3) the decline of the IC peak 1 peak intensity is observed. The DV curve of the full cell is likewise mainly shaped by the DV of the fresh anode. However, compared to the 55°C cell, the cathode still influences the DV peak 1, which is well pronounced in the full cell DV.

Approximately 1.5 mAh cm^{-2} could be extracted during the initial charge of the three-electrode setup, which is roughly 6% less compared to the fresh cathode with 1.6 mAh cm^{-2}. The discharge capacity was approximately 6% smaller with 1.4 mAh cm^{-2} for the aged cathode compared to 1.5 mAh cm^{-2} for the fresh.

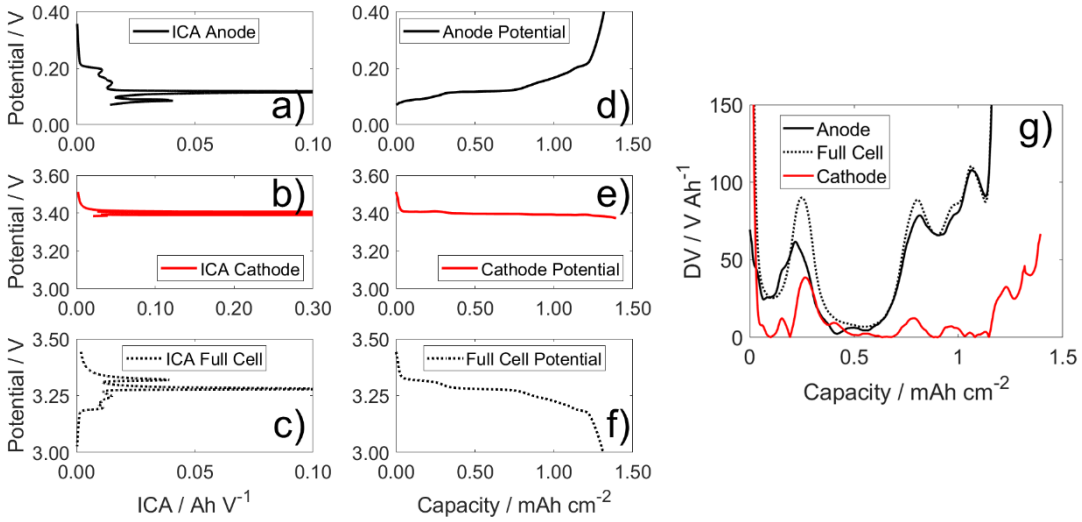

Figure 7-13: Separation of the IC and DV peaks from aged cathode (-20°C, AP2, 50% DOD) and fresh anode potentials. In the left column the IC of the fresh anode in a), the aged cathode in b) and the three-electrode full cell in c), the middle column shows the potentials of the fresh anode in d), the aged cathode in e) and the three-electrode full cell in f) and finally the DV separation in g).

7.1.5.2 Changes in the OCV curves due to ageing at -20°C

Figure 7-14a and b present the evolution of the OCV voltage over ageing of the cell aged with 50% DOD with AP2 and 100% DOD with AP2, respectively. As already observed in the DV curves, the voltage plateau around 3.33 V shifts to higher SOC values and decreases in length. The appearance of the voltage plateau around 10% SOC is similar to the cells aged at 55°C. The cell aged with 100% DOD shows a less pronounced reduction of the voltage

plateau around 3.33 V, but similar evolution of the plateau around 10% SOC. The cells aged at -20°C exhibit a distinct shift of the voltage profile between 100% and 90% SOC, which is more pronounced for the cell aged at 50% DOD compared to the 100% DOD cell. The newly generated peak due to plating and stripping of lithium on the anode surface in the IC and DV curve for the 50% DOD cell is observable as a bump in the voltage profile around 95 % SOC (marked with the black ellipse). As expected from the IC and DV curves for the 100% DOD cell, this feature is not observable in the OCV plot for this cell. Figure 7-14c shows the OCV at EOC and EOD for the cells aged with 50% DOD and 100% DOD and AP2. As already observed for the cells aged at 55°C, the OCV at EOC increases and decreases at EOD over ageing. The increase of the OCV at EOC is smaller and the decrease of the OCV is higher at EOD compared to the cells aged at 55°C. The changes are more pronounced for the cell aged with 50% DOD. Contrary to the cells aged at 55°C, the cells with 50% DOD show the highest OCV at 100% SOC and the cells aged at 100% DOD the lowest OCV value at the EOL (see Figure 7-14d).

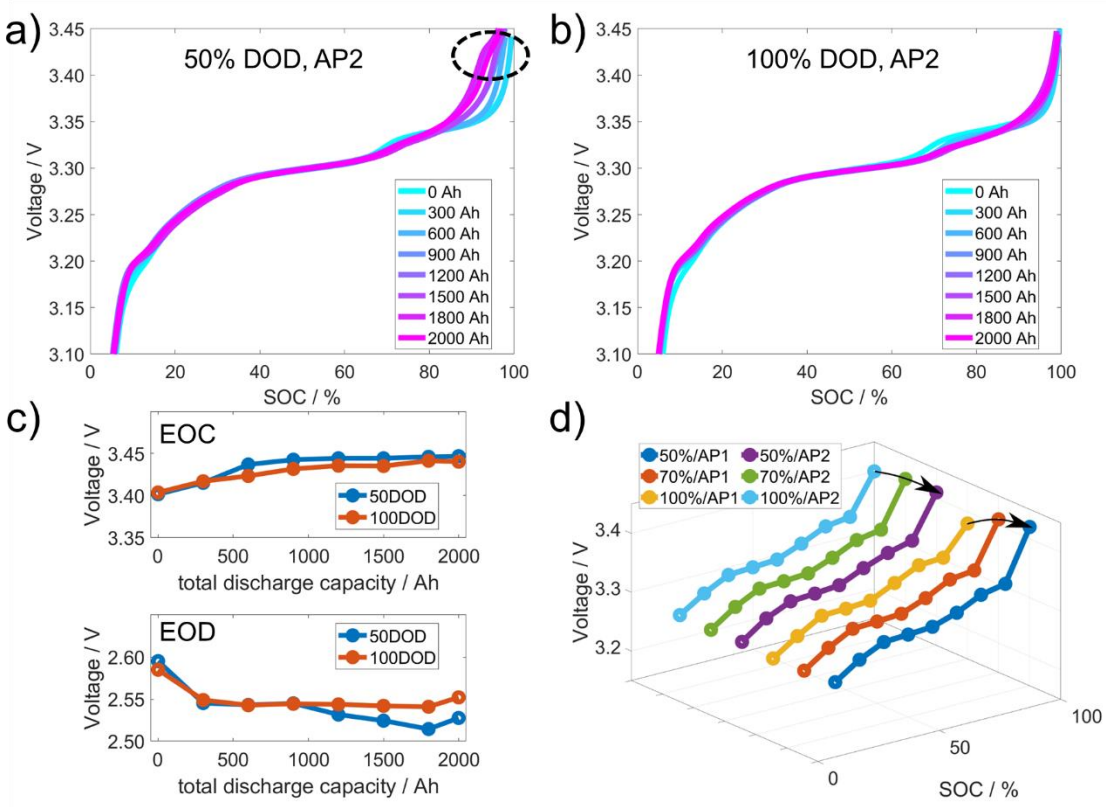

Figure 7-14: Evolution of the OCV of single cells, 50%DOD, AP2 in a) and 100%DOD, AP2 in b), the OCV at EOC and EOD in c) and in d) the OCV curves of cells from each group aged at -20°C at EOL. The circle in a) indicates the influence of Li plating and stripping.

7.1.5.3 Variation of the first IC peak intensity of the cells aged at 55°C and -20°C

As already shown in Figure 7-7e, Figure 7-12e and Figure A7, the first IC peak intensity follows the same trend as the cell capacity over ageing. Therefore, the peak intensity can be used in our case as an evaluation of the SOH and for the ageing parameters used here as a basic cell capacity prediction tool. Figure 7-15a and b display the first IC peak intensity, plotted over the cell capacity for charge and discharge. The trend of the peak intensities was fitted using a linear function. For the vanishing point of the IC peak 1, charge and discharge show for 55°C and -20°C a variance of 1% to 3%, respectively. Once the first IC peak vanishes, using the linear prediction for 55°C and -20°C, the cell exhibits a remaining cell capacity of 1.90 Ah (± 0.010 Ah) and 1.89 Ah (± 0.025 Ah), respectively. Figure 7-15c and d displays the evolution of the first IC peak intensity of the cells aged at 55°C and -20°C (50% DOD with AP2), but now plotted over the total discharge capacity. The decline of the peak intensity was likewise fitted with a linear function to predict the total discharge capacity, for which the first IC peak vanishes. The charge and discharge fitting show variations of 5% and 7% for the ageing at 55°C and -20°C, respectively. For the cell aged at 55°C, the vanishing point is predicted for 3181 Ah (± 74 Ah) and for -20°C for 2715 Ah (± 95 Ah) total discharge capacity. Using Figure 7-15c and d, the predicted cell capacity for the vanishing point of the first IC peak can be extracted. Therefore, assuming a further linear cell capacity decline, the cell aged at 50% DOD with AP2 at 55°C would reach a remaining cell capacity of approximately 1.90 Ah after a total discharge capacity of 3181 Ah. For the cell aged at -20°C, the remaining cell capacity of roughly 1.90 Ah would be reached after already 2715 Ah.

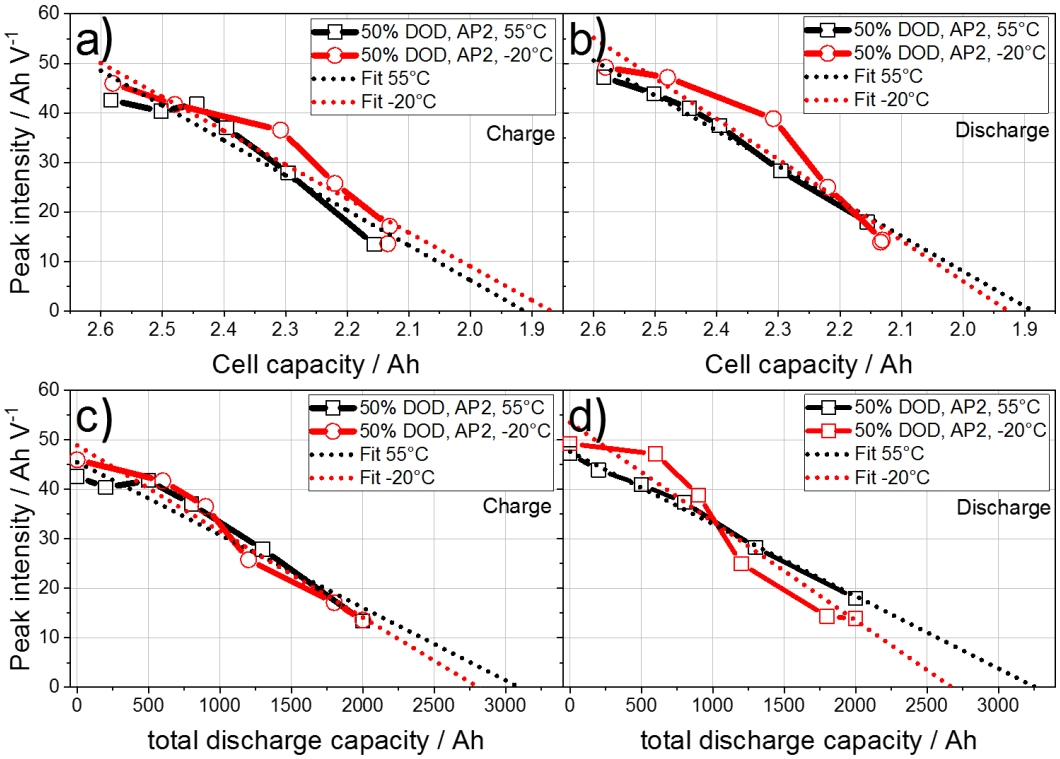

Figure 7-15: Measured and linear prediction of cell capacity for 55°C and -20°C using the first IC peak intensity. The charge peak intensity over cell capacity in a), the discharge peak intensity over cell capacity in b), the charge peak intensity over total discharge capacity in c) and the discharge peak intensity over total discharge capacity in d).

An evaluation of the first IC discharge peaks for each cell group at each temperature is presented in Figure 7-16. In Figure 7-16a and b, the intensity of the first IC peak is plotted as a function of the cell capacity for all cells aged at 55°C and -20°C are. The plots of all cells from one temperature follow the behaviour of the single cell analysis from Figure 7-15 The cells at 55°C all follow a linear trend and only small overall deviations (± 3.4 Ah V^{-1}) regarding the peak intensity slope are observed. The predicted cell capacity, as concluded from the disappearance of the first IC peak averaged over all cells cycled at 55°C agrees well with the single cell prediction, estimated cell capacity is around 1.9 Ah. For the cells aged at -20°C, a more scattered distribution with higher deviations (± 6.5 Ah V^{-1}) from the linear trend is observed. Due to the higher scattering of the IC peak intensities, the prediction using all cells at -20°C differs from the single cell prediction. Considering all cells at -20°C, the cell capacity for the vanishing point of the first IC peak is estimated to be around 2.04 Ah, while for the single cell it is around 1.89 Ah. In Figure 7-16c, the linear trends for the ageing at 55°C and -20°C are compared. The -20°C ageing exhibits a higher slope and uncertainty compared to the

ageing at 55°C. For Figure 7-16d, the data from the ageing at 55°C and -20°C was combined and fitted linearly. It exhibits, due to the higher scattering of the cells aged at -20°C, a higher, but still acceptable deviation of ± 4.5 Ah V^{-1}.

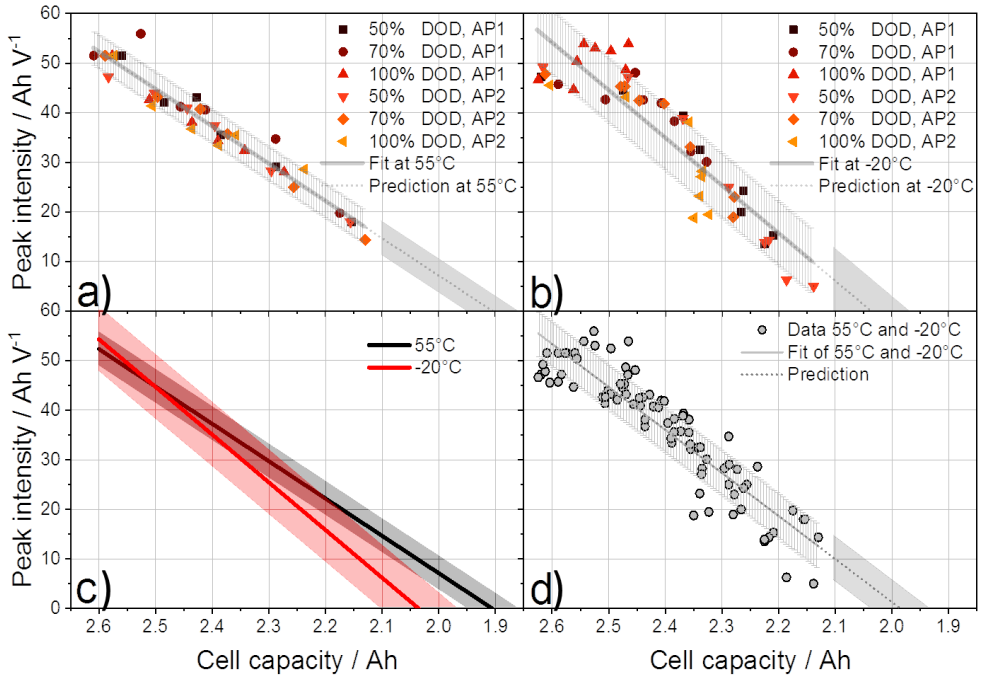

Figure 7-16: Measured and linear prediction of cell capacity for all cells aged at 55°C and -20°C using the first IC peak intensity. In a) peak intensity over cell capacity for all cells aged at 55°C and in b) for -20°C. c) compares the linear fits of 55°C and -20°C and d) shows the linear fit with prediction when using all data at 55°C and -20°C combined.

7.1.6 Discussion of the results

7.1.6.1 Capacity decay for the cells aged at 55°C and -20°C

Interestingly, smaller DOD and cycling at higher SOC leads to an increase of the capacity loss, which was already observed by other groups for $LiFePO_4$ cells [200,201,206]. Cycling at higher SOC (>50% SOC) was therefore more detrimental than cycling over the whole SOC range (100 – 0% SOC), this is valid for both ageing temperatures. The separation of the different ageing groups is more clearly observed at -20°C, while the ageing at 55°C shows a comparable capacity decay for 50% and 70% DOD. The deviation from the linear capacity decay for the cells aged at 100% DOD with AP1 and AP2 at 55°C and 100% DOD with AP2 at -20°C could be an indication for the passive electrode effect resulting by the utilisation of former unutilized Li inventory stored in the anode overhang [207,208]. This effect is more pronounced if the SOC

variation within the anode is high, which is the case for the cells aged with 100% DOD. The SOC variations leads to lateral Li flow within the anode. The former unutilized Li migrates laterally from the anode overhang into the active part of the anode and participates afterwards in the following cycling, reducing the loss of lithium inventory and limiting the capacity decay. The 50% and 70% DOD cycling leads to only smaller SOC variations within the anode and therefore to a minor passive electrode effect, which does not counteract the loss of lithium inventory. Lewerenz et al. observed as well the fact that smaller DODs exhibit higher capacity loss compared to higher DOD ageing profiles [200]. They used 10%, 50% and 100% DOD and observed a quicker capacity loss with 10% DOD compared to 100% DOD with 1C cycling rate. They cycled between 45 and 55% SOC with 1C, in our experiments, cycling was performed between 50 and 100% SOC with a dynamic current profile. Therefore, the 50% DOD cell capacity loss should have different underlying ageing mechanisms. Nevertheless, 50% DOD cycling leads to a higher cell capacity loss compared to the 100% DOD cycling.

7.1.6.2 Variations of the OCV for the cells aged at 55°C

Changes in the OCV are influenced by the Li stoichiometry in the electrodes, the available amount of active material and its particle size distribution. Variations of these factors are induced by LLI, LAM, premature under charge or under discharge and structural degradation. Kinetic effects are negligible due to close-to or at equilibrium conditions [82,209–211]. The evolution of the voltage step around 10% SOC explains the appearance of the IC peak 5 and its slow increase over ageing during discharge (see Figure 7-7d). Further, the increasing voltage slope and shortening of the voltage plateau of the OCV around 80% SOC is the source of the decreasing first IC peak, which is observed in Figure 7-6a and b and plotted in Figure 7-7a and b. The pseudo-OCV evolves for the ageing at 50% DOD and 100% DOD with AP2 very similar, up to 1300 Ah total discharge capacity. Afterwards, the 50% DOD with AP2 cell deviates from the 100% DOD cell and the length of the first voltage plateau decreases quickly.

An increase of the OCV at 100% SOC can emerge due to a loss of cycable lithium (LLI) and active material at the cathode (LAM_{PE}). Following the analysis of Birkl et al. [210], the LLI and LAM_{PE} leads during charging to an increasing amount of lithium, which is extracted from the remaining cathode active material. The decreasing amount of Li stoichiometry in $Li_{xmin}FePO_4$ at EOC increases the cathode potential compared to the fresh state and as well the full cell potential.

Likewise, LAM_{PE} and LAM_{NE} explain the decrease of the OCV at EOD. Since the remaining cathode active materials needs to accept more lithium compared to the fresh state, it

reaches a lower cathode potential compared to the fresh state. Inversely, the remaining anode material needs to donate more lithium compared to BOL, which reduces the Li stoichiometry and translates into a higher anode potential and lower OCV [210]. Additionally, Safari and Delacourt argue the LLI leads to the decrease the OCV at EOD. The decrease of the amount of lithium in the cathode during discharge leaves the anode with lower stoichiometric values compared to BOL and therefore a higher anode potential, which translates into a lower full cell potential [91]. Regarding the decrease of the cathode capacity, attributed partially to LAM_{PE}, and the observed LLI due to reduction of $Q_{stage\ 1}$ and half-cell measurements, both mechanisms are presumably responsible for the reduction of the OCV at EOD.

7.1.6.3 Half-cell measurements of cathodes from cells aged at 55°C

The reduced discharge capacity of the aged cathode points towards loss of active material at the positive electrode (LAM_{PE}), since only a smaller fraction of the cathode can accept the remaining lithium and is therefore lithiated faster. The reduced charge capacity of the half-cell indicates LLI. Assuming the contribution of the cathode to the first DV peak of the full cell at beginning of life (BOL) is indeed based on the presence of V-doping in the cathode, the disappearance indicates the loss of doped V, presumably through dissolution. Post-mortem EDX analysis indicates a reduction of the V content in the cathode cross section and the appearance of V on the anode surface after ageing [71]. The first IC peak is suppressed in the full cell IC, since the stored Li inventory in the aged cathode is lower compared to the BOL and the loss of active cathode material due to ageing (LAM_{PE}). The observed IC curve of the three-electrode setup matches the IC curves from the aged commercial full cells. Therefore, the half-cell measurements point towards LLI and LAM_{PE} as degradation mechanisms for the aged full cell.

7.1.6.4 Analysis of the IC and DV peaks for the cells aged at 55°C

The overall trend and shape of the IC and DV curves are the same for all cells aged at 55°C. They differentiate only in the changes of the peak intensities during ageing and the shift of the peaks on the capacity and voltage axes respectively. The shift of the ICA peaks at 200 Ah stands out from the other characterisation steps and is not seen in a resistance increase of R_{total} or R_1 in the EIS measurements (Figure 7-17 and Figure A8). We assume the shift to be induced by changes in the contact resistance, likely due to corrosion of the battery contacts, which was removed in subsequent tests due to repetitive insertion of the cell into the cell holder.

The cycling at 100% DOD shows a decrease of the distance between the discharge DV peak 1 and 4, which is indicating a loss of active anode material LAM_{NE} (see Figure 7-7f). The higher decrease of the associated LAM_{NE} at 100% DOD is in agreement with analysis done by Lewerenz et al. [200]. They ascribe the LAM_{NE} to the volume expansion of the anode during cycling. Additionally, the authors performed the 50% DOD cycling between 25% and 75% SOC and found no significant LAM_{NE} (decreasing distance between the DVA peaks). They cycled the anode in a stoichiometric region with smaller volume expansion compared to the regions below y=0.2 and above y=0.6 for Li_yC_6 [10] and concluded, that the cycling in the region with smaller volume expansion leads to smaller LAM_{NE}. Since our 50% DOD cycling was conducted between 100% and 50% SOC, there is likewise a rather high volume expansion expected for the anode, but no LAM_{NE} (change of $Q_{stage\ 2+3+4}$, see Figure 7-7e) is observed, at least until the EOL specified here. The overall cell capacity loss is the sum of the change in length of each staging process. Regarding the cell aged at 50% DOD with AP2, the capacity of $Q_{stage\ 1}$ decreased over ageing by roughly 0.44 Ah, while the capacity of $Q_{stage\ 2+3+4}$ increased by 0.02 Ah. Summing the two changes leads to the total capacity loss of 0.42 Ah for the cell.

Contrary to Lewerenz et al., the difference in the discharge DV peak 4 and the valley on the left side (regarding the discharge process) of the peak increases with ageing (parameter ΔMinMax, see Figure A3a and b and Figure A4). The authors linked the decreasing distance between the peak and the valley to an increase in the inhomogeneity of the lithium distribution in the anode, which is generated by a diffuse overlap of the stage 4 and 3 of the lithium intercalation into the anode. Since the distance between the peak and the valley is increasing for the cells in Figure 7-6d and Figure A1d, it indicates an increasing homogeneous lithium distribution within the anode, likely due to the LLI. The increase of the distance between peak and valley is more pronounced for the 50% DOD with AP2 than for the 100% DOD with AP2 cell, which can be explained by the higher degree of LLI for the 50% DOD with AP2 compared to the 100% DOD with AP2 cell (see Figure A4a and b) and LAM_{NE} for the cell aged at 100% DOD. The increasing homogeneity of the lithium distribution is likewise observed in the reduced peak width of the discharge DV peak 1 in Figure A2b. The reduced peak width indicates a sharper separation in the voltage plateaus from the transition from stage 1 to stage 2 of the anode. The increasing distance between the discharge DV peak 4 and the valley on its left side is linked to the increasing peak intensity of the discharge IC peak 5 over ageing. Over ageing, the plateau of stage 4 and 3 becomes more pronounced (visible as well in the OCV curve in Figure 7-9a) due to an increase in the lithium homogeneity (due to LLI), which

translates in an increasing peak intensity of the discharge IC peak 5. The peak intensity of the discharge IC peak 5 is not correlating with the capacity loss of the cells.

LLI results, according to Dubarry et al. [81], in a shift of the discharge IC peak 5 towards higher voltages and a decrease of the peak intensity of peak 1 and 2. Additionally, the LAM_{PE} in lithiated state results in a decrease of the IC peak 1, while the other peaks stay constant in peak intensity and location. Therefore, for the 50% DOD with AP2 cell, the main reason for the capacity fading is LLI until roughly 500 Ah total discharge capacity. Afterwards, the IC peak 5 reached a constant height and location on the voltage axes. The decrease of the peak intensity of IC peak 1 is additionally induced by LAM_{PE} afterwards. According to the analysis done by Dubarry et al. [81], active material loss is solely attributed to the cathode, since a LAM_{NE} leads to a decline of all IC peak intensities, which is not observed and in agreement with the DV interpretation of constant distance between the DV peak 1 and 4. The reduced charge and discharge capacity of the cathode during the three-electrode setup test indicates LLI and LAM_{PE}. LLI explain the increase of the OCV at EOC and LAM_{NE} and LLI the decrease of the OCV at EOD.

The different evolution of the capacity fading for cells aged at 50% DOD and 100% DOD with AP2 after 1300 Ah total discharge capacity is observed in the reducing decline of Q_{stage1} after 1300 Ah total discharge capacity for the cell aged at 100% DOD with AP2, while $Q_{stage\ 1}$ decreases linearly until EOL for the cell aged with 50% DOD with AP2.

The solid electrolyte interface (SEI) formation at the anode is enabled at high SOCs due to the low potential and the high degree of lithiation in the anode, which leads to a thick and stable surface layer. High temperatures on the other hand destabilize the outer part of the SEI and generates a porous surface layer [212]. Therefore, cycling at high SOC and elevated temperatures leads to a continuous generation of an unstable and porous outer SEI, accompanied by constant trapping of Li ions. However, the inner part of SEI seems to protect the anode against exfoliation for the cell aged at 50% DOD, since no LAM_{NE} is observed. Additionally, post-mortem analysis of the anodes showed higher degree of fluorine and phosphorous on the 50% DOD compared to the 100% DOD anode, which can be explained by a thicker inner SEI [71]. The above interpretation is similar to the proposed degradation model by Li et al. [201], however, our results show LAM_{NE} for the 100% DOD cell, but not for the 50% DOD cell. This indicates that the recurrent cycling at 100% DOD and elevated temperatures destabilized the outer and inner SEI in a higher extend than the 50% DOD cycling at high SOC and therefore does not protect the anode against exfoliation and electrical disconnection of anode particles due to crack formation. Additionally, Fe-dissolution, which is a well-known

degradation mechanism for all transition metal electrodes, destabilizes the SEI and promotes SEI growth (Fe was found on aged anode surfaces at 55°C [71]). During the 50% cycling, the electrodes remain for a longer time in the highest (cathode) and lowest (anode) electrode potential windows, the oxidation and reduction of the electrolyte is more severe at the cathode and anode compared to the 100% DOD cycling. EIS measurements confirm the increase of the SEI related resistance R_1 over ageing. For the cell aged with 50% DOD, R_1 increases by 26% and only by 12% for the 100% DOD cycled cell (see Figure A7). Similar results regarding the capacity fading depending on the SOC cycling range are presented by Li et al.. They show a higher decrease of the first staging plateau for 100 – 70% SOC cycling compared to 100 – 0% SOC [201]. Therefore, a higher LLI is found for the cycling at 50% DOD compared to the 100% DOD due to the higher consumption of Li. The LLI leads to a higher degree of Li homogeneity in the anode, which is reflected by the sharpening of the first DV peak, an increase of the IC peak 5 intensity and an increase of ΔMinMax. Contrary to our observation, Lewerenz et al. observed mainly a constant or decrease of ΔMinMax [200]. They attributed a decrease to the generation of a covering layer, which leads to the deactivation of active material. The LAM_{PE} is attributed to Fe dissolution and generation of an inactive phase in the cathode. Post-mortem analysis showed an electrically isolating surface layer on the cathodes, which could isolate cathode material from electrochemical reactions and lead to additional LAM_{PE}. The appearance of Fe on the anode surface confirms the Fe dissolution from the cathode. LAM_{PE} is additionally confirmed by half-cell measurements for the cell aged with 50% DOD, which shows a decrease of the Li inventory compared to a fresh cathode and a lower discharge capacity. IC and DV analysis reveals a higher amount of LLI and LAM_{PE} for the cell aged at 50% DOD, compared to the 100% DOD. However, the cell aged with 100% DOD exhibits LAM_{NE}, which is not observed for the 50% DOD cell. Moreover, electrochemical inactive material can trap lithium, which is afterwards isolated for further cycling. The active material can be deactivated by electrical contact loss, structural changes and electrochemical fatigue. The reduction of electrochemical activity of cathode material due to cycling was shown for LFP cathodes [63].

In addition to the peak intensity, the width of the peaks delivers additional information about the different voltage plateaus and phase transitions. A decrease in the peak width indicates for the IC a flattening of the voltage plateau, while for the DV it indicates a decrease of the length (regarding time or capacity) of the voltage transition during the phase transformation. Figure A2b presents the changes in width of the peak 1 of the IC and DV during discharging. Both peaks exhibit a decrease in the peak width with ageing. Since the area under the IC peak presents the capacity, which can be extracted during the voltage range, a decrease in peak

intensity and width results in a decrease of the extractable capacity of the voltage range around 3.25 V (full cell voltage). Combining the results from Figure 7-7 leads to the conclusion, that the capacity loss is mainly a result of the reduced intercalation process during the first voltage plateau during discharge. Following the analysis proposed by Dubarry et al. [81] and Lewerenz et al. [200], the combination of the reduced peak intensity of IC peak 1 during discharge, while the other peaks in the IC do not change their shape and position, the reduced peak width of IC peak 1 and the shift of the DV discharge peak 1 to lower capacities indicates a loss of lithium inventory (LLI). Since the LLI is reduced, the remaining lithium can be distributed more evenly in the electrode material, which explains the reduced width of the DV peak 1.

The peak intensity of the ICA peak 1 is for the here observed ageing an indication for the cell capacity loss. This observation is likely based on the fact, that the tested cells are mainly affected by LLI and LAM_{PE}, while LAM_{NE} is not observed. LLI and LAM_{PE} are both leading to a decrease of the reduction of the first IC peak intensity. Additionally, LAM_{PE} is observed in the half-cell measurements, as shown in Figure 7-8. The contribution of LAM_{NE} to the capacity decay would likely distort the straightforward relation between the IC peak 1 intensity and the capacity fading [213]. The same trend is observed in the shift of the DV discharge peak 1 on the capacity axes to lower absolute capacities during ageing (see Figure 7-6d), which is evaluated as parameter $Q_{stage\ 1}$. The origin for the decrease of the IC peak intensity and the shift of the DV peak 1 is the increase in the voltage slope during discharge from the voltage plateau at around 3.25 V of the full cell and a decrease of the extractable capacity of the potential plateau.

7.1.6.5 Variations of the OCV for the cells aged at -20°C

The increase of the OCV and OCV in Figure 7-14c and d at EOC results from the LLI, due to the lower stoichiometric lithium amount in the cathode $Li_{xmin}FePO_4$ compared to BOL, which increases the cathode potential. For the cells aged at -20°C, the OCV is assumed to be solely affected by LLI, since LAM_{NE} is not observed. At EOD, the LLI leads to a lower stoichiometric lithium amount in the anode, which translates into a higher anode potential and therefore a lower full cell potential, visible in the decreasing OCV [91,210]. The further decrease of the OCV at EOD of the 50% DOD with AP2 cell at 1200 Ah could be explained by an increasing amount of the lithium plating. The irreversibly plated lithium does not intercalate into the anode, more lithium is immobilized which decreases the lithium inventory even further, leading to an additional lowering of the Li stoichiometry in the anode and therefore higher anode potential.

The shift of the OCV between 80% and 100% SOC is an indication for the lithium plating [214,215]. The OCV curves show, that Li plating starts after around 600 Ah total discharge

capacity for the 50% DOD with AP2 cell and increases until it reaches its maximum at 1800 Ah total discharge capacity. Afterwards, it decreases slightly. This is additionally visible in Figure A5, comparing the 0.5C charge and discharge during characterisation. According to the OCV curve, the maximum of the Li plating process at constant current was reached at 1800 Ah and the OCV curve shifts back towards lower voltages at the EOL. The cell aged at 100% DOD with AP2 shows only a minor shift in this SOC range. The increase of the OCV at EOD at 2000 Ah of the 50% DOD with AP2 cell can be explained by the release of some plated lithium, which intercalates into the anode and leads to a lower Li stoichiometry compared to 1800 Ah. The lower Li stoichiometry leads to a lower anode potential and therefore a higher OCV. The release of plated Li is additionally observed in the cell capacity, which increases slightly from 1800 Ah (cell capacity: 2.131 Ah) to 2000 Ah (cell capacity: 2.134 Ah) total discharge capacity. Next to reversible Li plating, the anode overhang can explain the increase of the capacity over ageing, since Li, which was stored as electrochemically inactive Li-ions in the anode overhang, migrates laterally towards the centre of the anode and balances the LLI.

7.1.6.6 Half-cell measurements of cathodes from cells aged at -20°C

The ageing at -20°C had only a smaller influence on the amount of Li stored in the cathode and the active material of the cathode. The initial charging and discharging process showed roughly 6 % lower capacity compared to the fresh cathode, indicating lower cathode degradation compared to ageing at 55°C. Assuming the cathode DV peak indicates V-doping, the existence points towards a less affected V dissolution in the cathode over ageing compared to the ageing at 55°C. Post-mortem analysis reveals a smaller reduction and increase of the V content in the cathode and anode, respectively, compared to 55°C ageing. Considering, the three-electrode cell setup contains a fresh anode, it is expected, that the full cell DV shows the same features at the BOL. Nevertheless, the cathode still exhibits a distinct peak at the DV peak 1, indicating an unchanged cathode behaviour in the three-electrode cell setup.

7.1.6.7 Analysis of the IC and DV peaks for the cells aged at -20°C

The overall trend and shape of the IC and DV are again the same for all cells aged at -20°C, as it is observed for 55°C ageing. The appearance of a new peak in the IC curve in Figure 7-11 is associated with the appearance of a new redox reaction, similar to the appearance of a new peak during cyclic voltammetry [82,216]. Post-mortem analysis of the anode revealed lithium plating on anodes cycled with 50% DOD and 100% DOD [71]. Petzl and Danzer used DV curves of $LiFePO_4$ cells to analyse lithium plating and showed, that the generation of the additional

voltage plateau at this potential and under these conditions is due to the stripping (regarding the discharge) of plated lithium from the anode surface [205]. The generation of lithium plating influences the charging and discharging IC and DV curves and is observed in the generation of peak 0. This is interesting, since plating is generally assumed to occur during the constant voltage phase of the charging process, which is not included in the IC and DV analysis [205]. The stripping of plated lithium leads to the generation of a noticeable voltage plateau, which is converted into a peak of the discharge IC and the transition from the lithium stripping to the stage 1 voltage plateau of the anode, is transformed into a peak of the discharge DV curve. Figure A5 shows the cell voltage during the RT characterisation process for different ageing steps. Beginning with 900 Ah the voltage plateau is observed in the charge and discharge process. For the cell aged at 100% DOD, AP2, these voltage plateaus are not observed, neither in the IC nor in the DV (see Figure A3). It is important to point out again, that the characterisation procedure to check the capacity and generate the data for IC and DV is conducted at 25°C and not at the ageing temperature. The plated lithium therefore forms a stable surface layer and acts afterwards as a catalyst for further, reversible Li plating, even at RT. For the charging IC and DV of the 50% DOD with AP2 cell, the peak 0 is out of the plotted range, but likewise visible.

The plated lithium can react on the anode surface with electrolyte and increases the irreversible Li consumption [217]. Petzl and Danzer show, that at high SOCs, the plated Li is mainly irreversibly deposited on the anode surfaces [205]. Therefore, the higher capacity loss of the cell aged at 50% DOD compared to 100% DOD can be explained by a higher amount of irreversible Li plating. The increasing Li inhomogeneity (based on increasing width and decreasing intensity of DV peak 1 and decreasing peak intensity of IC peak 5) can be attributed to the inhomogeneous Li plating in the anode surfaces. The parameters ΔMinMax and IC peak 5 intensity, which are increasing for all cells, independent from the ageing parameter indicate an increase in the Li homogeneity, which at first seems to contradict the other parameters pointing towards an increasing Li inhomogeneity. However, the homogenisation of the Li distribution derived by the parameters ΔMinMax and IC peak 5 intensity is limited to the transition from stage 1d+4 to stage 3. The LLI might facilitate the homogenisation, which could explain the increase of these two parameters over ageing. Further, the potential difference between these two phases is higher, compared to the other phases observed in the DV and IC curves. The potential difference supports the lateral flow of Li ions and drives the homogenisation [182]. Since ΔMinMax stays constant after 600 Ah total discharge capacity for the cell aged with 50% DOD and 300 Ah total discharge capacity for the cell aged with 100%

DOD total discharge capacity, the increase of the Li homogeneity occurs only at the beginning of ageing.

The width of the IC peak 1 follows the same trend than the intensity and declines over ageing (Figure A7b), which indicates a decrease of the extractable capacity from the first voltage plateau, analogous to the ageing at 55°C. The LLI is visible in the reduced peak intensity and width of IC peak 1, the shift of IC peak 5 towards higher voltages and the decrease of $Q_{stage\ 1}$. The cell aged at 50% DOD with AP2 at -20°C exhibits a shift of the discharge IC peak 5 up till 1200 Ah total discharge capacity. Afterwards, until the EOL at 2000 Ah, it remains stable on the voltage axes and in intensity. According to the interpretation of Dubarry et al. [81], LLI is the main source of the capacity loss until 1200 Ah and only afterwards, LAM_{PE} is mainly responsible for further capacity decline. This is consistent with the evolution of the cell capacity. The LAM_{PE} is found to partly contribute to the capacity fading, since, firstly, the half-cell measurements show a decrease of the discharge capacity of the aged cathode by roughly 6% in comparison to the fresh cathode and secondly, since the in post-mortem analysis observed Li plating can lead to deactivation of cathode material, which is opposite of the plated Li on the anode side [182]. Up to 1200 Ah total discharge capacity, the cell capacity decreases by 14%. From 1200 Ah to 2000 Ah total discharge capacity, the cell capacity decreases by only 3% more, which indicates only a slight degradation of the cathode, as it is observed in the half-cell measurements.

For the cell aged with 100% DOD with AP2, the discharge IC peak 5 reaches its maximum intensity and stable voltage position after 600 Ah. With further ageing, the intensity decreases constantly, while the position stays stable. The decline in intensity should indicate LAM_{NE} or LAM_{PE} [81,218]. However, the DV does not indicate any LAM_{NE} (no decline of $Q_{stage\ 2+3+4}$ observed). If attributed to LAM_{PE}, the question arises, why it is not observed for the cell 50% DOD with AP2 aged at 55°C for which LAM_{PE} is clearly detected. Possibly, the difference arises from the different states of LAM_{PE}, lithiated and delithiated. For the cells aged at 55°C, the LAM_{PE} is in lithiated state, which does not affect the IC peak 5. Contrary, for the 100% DOD with AP2 cell at -20°C, the LAM_{PE} is in delithiated state, which is assumed to lead to a decrease of the IC peak 5 intensity. The shift of IC peak 5 towards higher voltages, the decreasing intensity and width of IC peak 1 and the reduction of $Q_{stage\ 1}$ are indicating LLI. The decrease of $Q_{stage\ 1}$ can be assigned to LLI, which is partially due to the immobilization and trapping of Li ions in the surface layers of the electrodes and at -20°C due to irreversible lithium plating on the anode. Nevertheless, since the shift of IC peak 5 stops at 600 Ah and its intensity declines after, other mechanisms are influencing the cell capacity fading. Since the intensity of

IC peak 5 increases first and $Q_{stage\ 2+3+4}$ does not decrease during ageing, the additional capacity loss is attributed to LAM_{PE}. Post-mortem analysis of the anodes aged at 100% DOD with AP2 revealed intense Li plating [71]. Since the Li plating is not observed in the IC, DV or OCV as it is seen for the cell aged with 50% DOD, the plating process must have occurred during the constant voltage regime and be irreversible, due to the missing stripping peak.

7.1.6.8 Prediction of cell capacity and remaining cycle life using the first IC peak intensity

It should be noted that the observed straight forward relation between the first IC peak and capacity fading will be probably distorted in case of significant occurrence of LAM_{NE}, since other features of the IC and DV are additionally affected by LAM_{NE} and the related capacity fading due to the anode, which is however not considered, when only focusing on the first IC peak. As Dubarry et al. have already shown, the second IC peak starts to decline, once the first IC peak has vanished completely [81]. This is in agreement with the observations presented here, since the second IC peak does not change significantly over ageing. Using the first IC peak for SOH and cell capacity prediction has one major disadvantage. The SOH analysis and cell capacity prediction stops, once the first IC peak vanishes. Nevertheless, the tool can be used until a remaining cell capacity of roughly 75% compared to BOL is reached. The linear fit using all data from 55°C and -20°C indicates, that the cell capacity can be estimated from the first IC peak intensity with a uncertainty of ± 50 mAh until the first IC peak vanishes, which appears around 2.0 Ah cell capacity or roughly 76% of the initial cell capacity. This is an acceptable value for a straightforward analysis.

7.1.7 Concluding ICA, DVA and OCV Analysis for 55°C and -20°C

The observed changes over ageing are summarised in the Table 2 and Table 3 with the underlying origins based on [35,81,91,200,201,218] and observed in our experiments:

Table 2: Summary of the changes in the ICA and DVA curves and the related origins. Black colour indicates the changes related to 55°C and red colour to -20°C ageing.

55°C / -20°C			
	50% DOD	**100% DOD**	**Origin**
ICA peak 1, intensity	Declines until EOT by 65%	Declines until EOT by 46%	LLI and LAM_{PE} in lithiated state.

	Declines until EOT by 84%	Declines until EOT by 59%	Mainly LLI.
ICA peak 1, location	Shifts to higher voltages	Shifts to higher voltages	Increase of resistance, visible in increase of R_1 and R_{total} (EIS, see Figure A8).
	Stays nearly constant	Stays nearly constant	No change in resistance R_{total} stays constant and R_1 decrease (EIS, see Figure A8).
ICA peak 1, width	Declines by 68%	Declines by 38%	Reduction of the grain size at the PE, due to electrochemical milling.
	Declines by 96%	Declines by 69%	
ICA peak 5, intensity	Increases until EOT	Increases until EOT	Increase: improved kinetics and reduction of grain size, increasing Li homogeneity.
	Increase up to 1200 Ah, after constant	Increases up to 600 Ah and decreases after until EOT	Decrease: LAM_{PE} delithiated state and surface layer growth, in our case Li plating, increasing Li inhomogeneity.
ICA peak 5, location	Shifts to higher voltages until EOL	Shifts to higher voltages until EOL	LLI.
	Shifts to higher voltages up to 1200 Ah	Shifts to higher voltages up to 600 Ah	
DVA peak 1, intensity	Increases by 26%	Increases by 26%	Increasing Li homogeneity.
	Decreases by 15% up to 1200 Ah and disappears after	Decreases by 38%	Increasing Li inhomogeneity.
$Q_{stage\ 1}$	Declines by 75%	Declines by 40%	LLI.
	Declines by 60% up to 1200 Ah and disappears after	Declines by 65%	
	Declines by 28%	Declines by 24%	Increasing Li homogeneity.

DVA peak 1, width	Increases by 19% up to 1200 Ah and disappears after	Increases by 10%	Increasing Li inhomogeneity.
$Q_{stage\ 2+3+4}$	Increases of roughly 2%	Declines by roughly 7%	Decline: $LAM_{NE.}$ Increase: increasing Li inhomogeneity.
	Constant until DVA peak 1 vanishes.	Increases of roughly 11%	
ΔMinMax	Increase by 1000% until EOL	Increase by 800%, constant after 500 Ah	Increasing Li homogeneity. A decrease would indicate deactivation of electrode material.
	Increase by 475%, constant after 600 Ah	Increase by 360%, constant after 300 Ah	

Table 3: Summary of the changes in the pseudo-OCV and the related origins. Black colour indicates the changes related to 55°C and red colour to -20°C ageing.

55°C / -20°C			
	50% DOD	**100% DOD**	**Origin**
Pseudo-OCV at EOC	Increase ≈ 2 mV	Increase ≈ 5 mV	LLI, LAM_{NE},
	Increase ≈ 4 mV	Increase ≈ 3 mV	LLI
Pseudo-OCV at EOD	Decrease ≈ 7 mV	Decrease ≈ 2 mV	$LAM_{PE,}$ LLI
	Decrease ≈ 7 mV	Decrease ≈ 5 mV	LLI

7.1.8 Impedance Evolution of full Cells Aged at 55°C and -20°C

Figure 7-17 displays the evolution of the impedance from two full cells, one aged at 55°C (in a) and at -20°C (in b), both using the AP2, 50% DOD profile. The EIS measurements are performed at 100% SOC after a 2 h resting time. The cells show the typical Nyquist plots for LFP cells, consisting of a depressed semi-circle, followed by a diffusion tail [181,219]. The Nyquist plots were shifted, to have the Z' axes crossing with 500 Hz. The cell aged at 55°C (Figure 7-17a) exhibits an increase in the semi-circle diameter over ageing. For the cell aged at -20°C, the diameter of the semi-circle does not change significantly over ageing. For further evaluation

of the EIS measurements, the Nyquist plots were fitted to an equivalent electrical circuit (EEC). Several different EEC models for LFP full cells are used in the literature to fit EIS measurements, ranging from the Randles model using one resistor – capacitor (RC) element in addition with a Warburg element to several RC elements in series and in combination with Warburg elements [220–225]. Since the Nyquist plots contains only one semi-circle with a diffusion tail, we used the Randles model including a Warburg element to fit the spectra (displayed in Figure 7-17e).

The increase of the semi-circle diameter in Figure 7-17a) is observed in the results of the fitting parameters, presented in Figure 7-17d). The parameter R_1 represents the mid-frequency semi-circle and is attributed to the charge-transfer resistance R_{ct} of the electron charge transfer step and the resistance of the surface layers on the electrodes R_{sl} (SEI for the anode and solid permeable interface for the cathode (SPI)). For the cell aged at 55°C, a constant increase until EOL of R_1 of about 35% is observed. The cell aged at -20°C exhibits a decrease of R_1 at EOL compared to BOL of 12% though. However, since the values for R_1 are scattered during the ageing process, it is difficult to make an accurate statement. Changes in the contact resistance due to repeatedly mounting and unmounting of the cells for the EIS measurements are assumed to mainly affect the series resistance R_0 (which is not shown due to the before mentioned problems), but might contribute likewise to the scattering of R_1. Nevertheless, a decreasing trend of R_1 for the cell aged at -20°C is observed. Since R_1 is a combination of R_{sl} and R_{ct}, both effects need to be considered. Post-mortem analysis of the aged cell revealed a large decrease of 40 to 70% of the electrically conductive surface area on the cathode surface for the cells aged at 55°C [71]. Regarding the anode at 55°C, the SEI formed at higher temperatures is assumed to be thicker and less stable compared to room temperature SEI, as shown by Wang et al. [212]. Steinhauer et al. show an increase of the SEI resistance from 45°C to 55°C, which they attribute to thermal side reactions [226]. Post-mortem analysis of the anode surfaces showed an electrical isolating surface covering on all anodes aged at 55°C, even after washing the anode surface [71]. The decrease of the conductive surface area for the cathode and the generation of the thick, covering SEI leads to an increase of R_{sl}. The charge transfer resistance R_{ct} is dependent on the SOC of the cell and has its minimum at 100% SOC [227]. Therefore, remaining Li-ions in the cathode after the complete charging process (an indication for LLI and LAM_{PE}) can lead to an increase of R_{ct} in the aged cells. The increase of R_{sl} and R_{ct} leads to the observed increase of R_1.

Regarding the cells aged at -20°C, post-mortem analysis of the cathodes showed only a smaller decrease of the conductive surface area of about 5 to 20%. The post-mortem analysis of the anodes from the cells aged at -20°C exhibited areas with bare, uncovered graphite flakes, which indicates a thinner SEI. Therefore, for the cells aged at -20°C, a smaller increase of R_{sl} is expected. Since the EIS measurements are performed at room temperature, the ageing at -20°C does not seem to have irreversibly influenced the electrode kinetics, which would lead to an increase of R_{ct}. Additionally, a constant value of R_{ct} or a decrease over ageing have been reported in the literature [91,222,223]. Combining the observation for R_{sl} and R_{ct} can explain the observed decrease of R_1 for the cell aged at -20°C. Next to R_1, the total resistance R_{total}, which represents the distance on the Z' axes from the crossing of the Z' axes to the lowest frequency. It includes the semi-circle and the diffusion tail, which is influenced by transport limitations. Additionally, LAM can increase the total impedance of the cells. For the cell aged at 55°C, R_{total} increases until EOL up to 70% with the biggest rise during the last ageing step. The cell aged at -20°C increases by only 5% until EOL (see Figure A8). Until 1300 Ah total discharge capacity, the overall impedance increase of the cell aged at 55°C is mainly based on the increase of R_1. However, during the last ageing step, the strong increase of R_{total} is not based on R_1, since it increases continuously, but on structural degradation of the cathode material, namely LAM_{PE}.

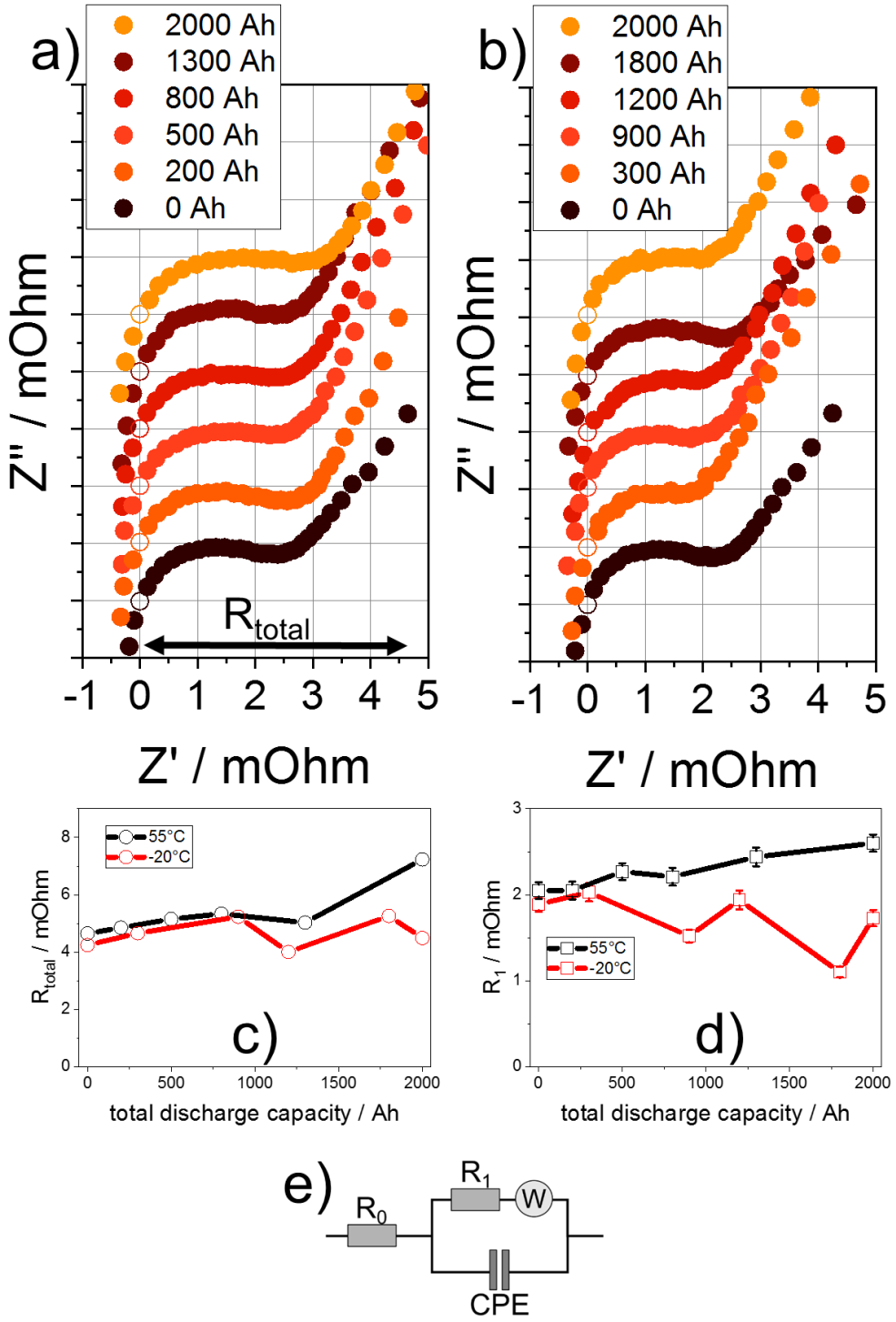

Figure 7-17: Evolution of the Nyquist plot over ageing of the cell aged at 55°C in a) and -20°C in b), both using AP2, 50% DOD. EIS measurements performed at 100% SOC. The evolution of the total resistance R_{total} in c) and resistance R_1 in d) over ageing are presented. Fitting of parameter R_1 was done using the equivalent electrical circuit shown in e).

7.1.9 Summarising the ageing at 55°C and -20°C

The observed features of the IC, DV and OCV analysis with the related degradation mechanisms are summarized in table 2 and 3. Combining the ageing of the cells at 55°C and -20°C and separating the degradation mechanisms as described in the sections before, the degradation can be summarised with the individual influences over the total discharge capacity in Figure 7-18. From the half-cell measurements of the cathode, which was aged at 55°C, we observed a 14% loss of lithium, which could be extracted from the aged $LiFePO_4$ cathode during the first charge compared to a fresh $LiFePO_4$ cathode. Therefore, we conclude that LLI accounts for 14% capacity loss. The remaining 4% capacity loss (since in total 18% capacity loss was observed) for the aged $LiFePO_4$ cathode in the half-cell test is attributed to LAM_{PE}. Hence, at 55°C, LLI is responsible for roughly 80% and LAM_{PE} for roughly 20% of the capacity loss. Since the pseudo-OCV evolution is similar, the ageing process is assumed to be comparable for the 50% DOD and 100% DOD cell aged at 55°C. The cell aged at 100% DOD shows a 7% decrease of $Q_{stage2+3+4}$, which is an indication for LAM_{NE}. Therefore, next to LLI with 80% share on capacity fading, LAM_{NE} and LAM_{PE} are assumed to contributed both with roughly 10%. LAM_{PE} follows the evolution of R_{total}, since the resistance is assumed to be mainly influenced by the loss of active material and only to a smaller extend by loss of lithium inventory. LAM_{NE} is extracted by the capacity loss from $Q_{stage2+3+4}$ over ageing. However, since we assume the LAM_{PE} to occur in lithiated state (otherwise IC peak 3 to 5 would reduce in intensity if it would occur in delithiated state), it contributes likewise to the loss of lithium inventory, which makes it challenging to differentiate precisely between LAM_{PE} in lithiated state and LLI. Since the half-cell measurements indicate a small amount of LAM_{PE} for the cathode aged at -20°C and the shift of the IC peak 5, a small contribution of LAM_{PE} is likewise observed in the cells aged at -20°C. Summing up, LLI is overall the main mechanism responsible for the capacity fading, followed by LAM_{PE} and for the cell aged at 100% DOD with AP2 at 55°C small contribution of LAM_{NE}.

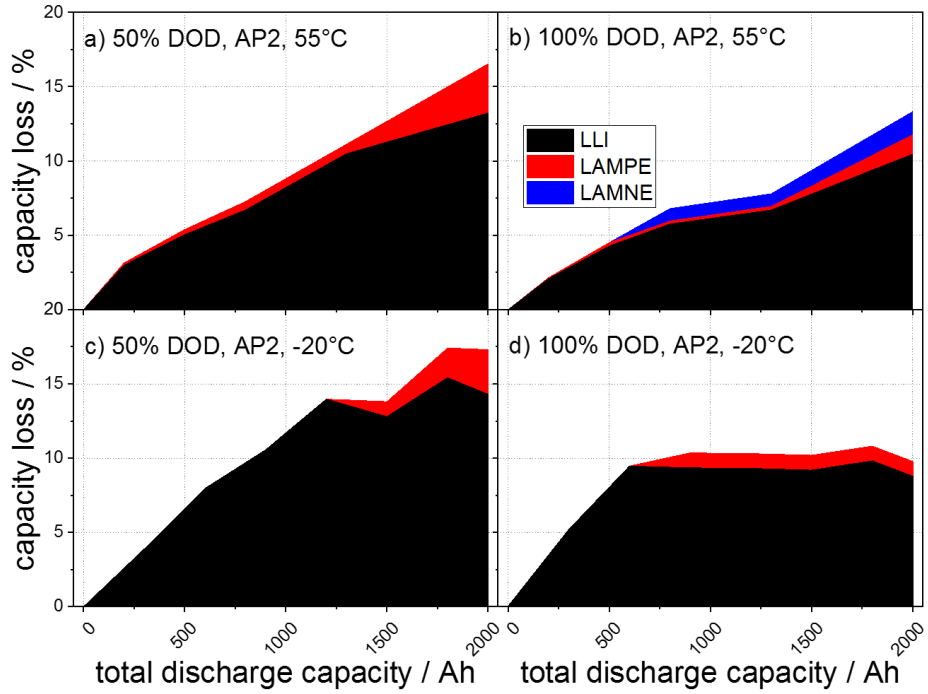

Figure 7-18: Evolution of the degradation mechanisms for the cells aged with AP2 and using 50% DOD at 55°C in a), 100% DOD at 55°C in b), 50% DOD at -20°C in c) and 100% DOD at -20°C in d).

7.1.10 Concluding remarks for the monitored aging of commercial cells at 55°C and -20°C using ICA, DVA and OCV

Cyclic ageing of commercial cells was conducted at 55°C and -20°C within the SOC range from 100 – 50%, 100 – 70% and 100 – 0% and using a dynamic current profile with two different current loads. The first important result is the observation, that cycling at high SOC with a small DOD leads to a higher capacity fading compared to the higher DOD profiles. This fact is independent from the ambient temperature. This can be used to optimise the utilisation window of the cells to limit the capacity fading during cycling. To evaluate the origin of the capacity fading, IC, DV and OCV analysis was conducted during the check up, followed by half-cell tests for selected cathodes.

For the ageing at 55°C, the capacity fading is attributed to LLI (based on IC peak intensity 1 decrease, IC peak 5 location shift, $Q_{stage\ 1}$ decrease, OCV increase at EOC and decrease at EOD) and LAM_{PE} (half-cell measurements, IC peak intensity 1 decrease, OCV increase at EOC and Fe dissolution [71]). The LLI is based on the continuous consumption of Li in the growing SEI.

For the cells aged at -20°C, the main source of capacity fading is found to be LLI. This is based on the decrease of the first IC discharge peak intensity, the shift of the location of the IC discharge peak 5, the decrease of parameter $Q_{stage\ 1}$ and the increase and decrease of the OCV at EOC and EOD, respectively. LAM_{PE} has only a minor influence, since no Fe dissolution is observed and half-cell measurements of the aged cathode showed almost no decrease of the discharge capacity (only 6% loss compared to the fresh cathode). The LLI is mainly based on the occurrence of irreversible Li plating

Accurate and simple evaluation of the remaining capacity of a cell is an important task for different applications and the estimation of the second life capability. The analysis presented here shows that the IC and DV delivers useful and accurate information, which is generated by simple calculations. The IC discharge peak 1 and the location on the capacity axes of the DV discharge peak 1 correlate well with the remaining capacity of the cell, in the case when only negligible amount of LAM_{NE} is observed. Therefore, these parameters are a possible tool for a quick estimation and cycle life prediction, as it was shown for the discharge IC peak 1. Even though more sophisticated models exist, which are based on the first IC peak or additional information for the remaining cell capacity estimation, this approach uses a straight forward analysis and needs only a short time of charging and discharging with an accuracy of roughly ± 50 mAh for the remaining cell capacity.

The samples for the three-electrode setup measurements were all taken from the area of the first current collector tab and from the side of the electrode sheets facing the inside of the cell. As Bach et al. [228] show, the ageing is not uniform throughout the cell itself, due to different bending curvatures, corresponding pressure differences and temperature distributions. Analysing the differences in ageing is however out of the scope of this paper, but offers interesting questions for further investigations.

7.2 Post-Mortem Material Analysis of Aged Commercial LFP Cells

7.2.1 Sample Preparation

After ageing, the cells were discharged to 0% SOC using 1C (regarding nominal capacity), transferred into an argon filled glovebox (MBraun, Germany) and disassembled. Samples were cut out of the electrode sheets from around the first current tab and from the electrode side facing the inside of the cell. Afterwards, the samples were rinsed using dimethyl carbonate (DMC, Sigma Aldrich, Alfa Aesar) and stored inside a glovebox.

7.2.2 Cell Capacity Fading Over Ageing

The capacity fading follows a linear trend from the beginning to the end for the cells aged at 50% DOD. For the cells aged at 100% DOD, the capacity fading starts to level during the ageing. The levelling is more pronounced for the cells aged at -20°C compared to 55°C (Figure 7-19). The cells aged at -20°C using 100% DOD exhibit a noticeable capacity decline at the beginning of the ageing process and only afterwards the levelling of the capacity fading is observed. For both temperatures, the ageing profiles using 50% DOD exhibit a higher capacity fading compared to 100% DOD. At 55°C, the difference between AP1 and AP2 is nearly negligible. At -20°C, the ageing at 50% DOD with AP1 and with AP2 shows likewise nearly the same capacity decline over ageing. Only the cells aged with 100% DOD exhibit a distinct difference in the capacity fading. However, with AP2 and 100% DOD, most of the capacity decline is observed during the first 600 Ah total discharge capacity. Afterwards, the slope of the following capacity decline is practically the same for 100% DOD with AP1 and with AP2. The degradation within one ageing group is homogeneous, as can be observed by the small error bars in the capacity. Therefore, we used one or two cells from each group for post-mortem analysis.

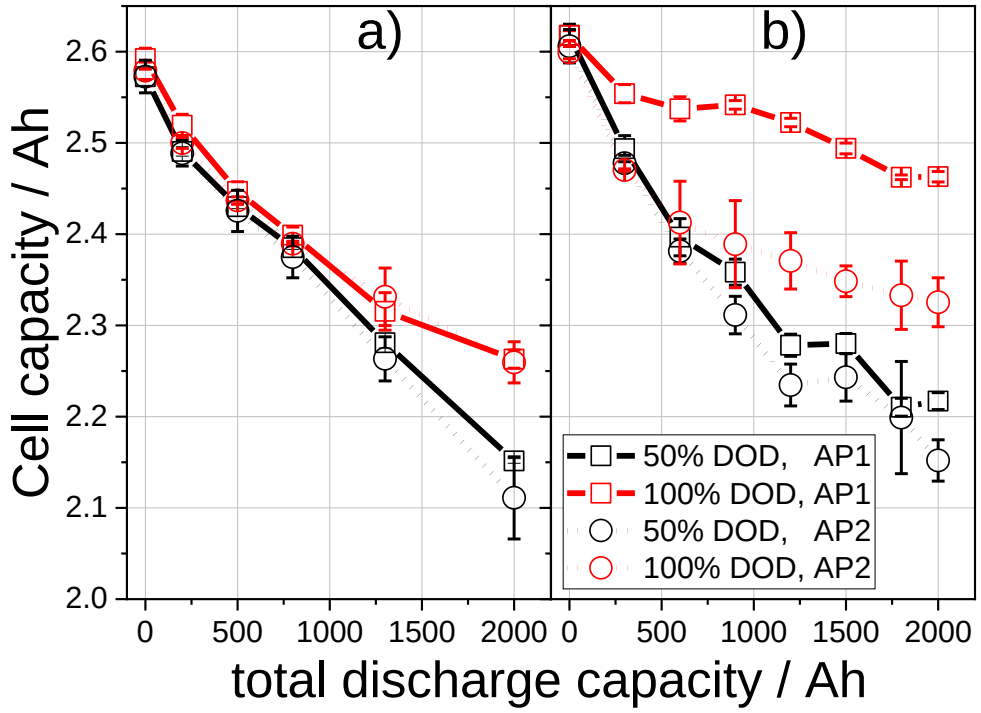

Figure 7-19: Capacity decay of cells aged at 55°C (a) and -20°C (b) using AP1 and AP2 and 50% and 100% DOD [93]

7.2.3 Structure and Morphology of Anode Surfaces

The anode surfaces clearly exhibit some changes compared to the fresh anode surface, but show a similar morphology for the same temperature. The anodes of cells aged with AP1 are not shown here, but they show similar results compared to the AP2 anode surfaces. The anode surfaces of a fresh anode at the beginning of life (BOL) show graphite flakes with nearly no coverage (Figure 7-20a) and illustration in b). The edges of the graphite flakes are clearly visible. It has to be noted, that the anode surfaces underwent washing with DMC. Therefore, any surface layer is removed that is not stable. The anode surfaces of the cells aged at 55°C are entirely covered with a surface layer (Figure 7-20c), d) and illustration in e). As mentioned earlier, one major mechanism contributing to the capacity decline is the loss of lithium inventory (LLI). This is based on the continuous consumption of Li in the surface layer. High temperatures lead to the formation of a less stable, thicker and more porous SEI, which continuously dissolves and reforms [212,229,230]. Therefore, the cycling at 55°C consumes Li in the surface layer generation. The generated surface layer which is observed in the SEM images is stable enough to remain on the anode surface at the end of life (EOL), even after washing with DMC. A noticeable difference in surface morphology between the 50% DOD and 100% DOD cycling in Figure 7-20c) and Figure 7-20d) is not observed. Ageing at -20°C did not generate a

dense surface layer, as it is observed for the anodes aged at 55°C. The covering of the graphite flakes shows similar features as for the fresh anode (Figure 7-20f). However, similar structures and precipitation on the anode surfaces aged at -20°C, similar to the anodes aged at 55°C, indicate electrolyte deposition on the anode surface, but in a smaller extend (see Figure 7-20g), illustration h) and Figure A9d) and e) in the appendix. For SEM images with lower magnification see Figure A9 in the appendix. Additionally, small crystal-like structures of up to 500 nm developed, which could indicate LiF, since LiF crystals have been observed before on aged anodes [231,232]. The crystals are found in both samples cycled at -20°C, but not on the anode aged at 55°C.

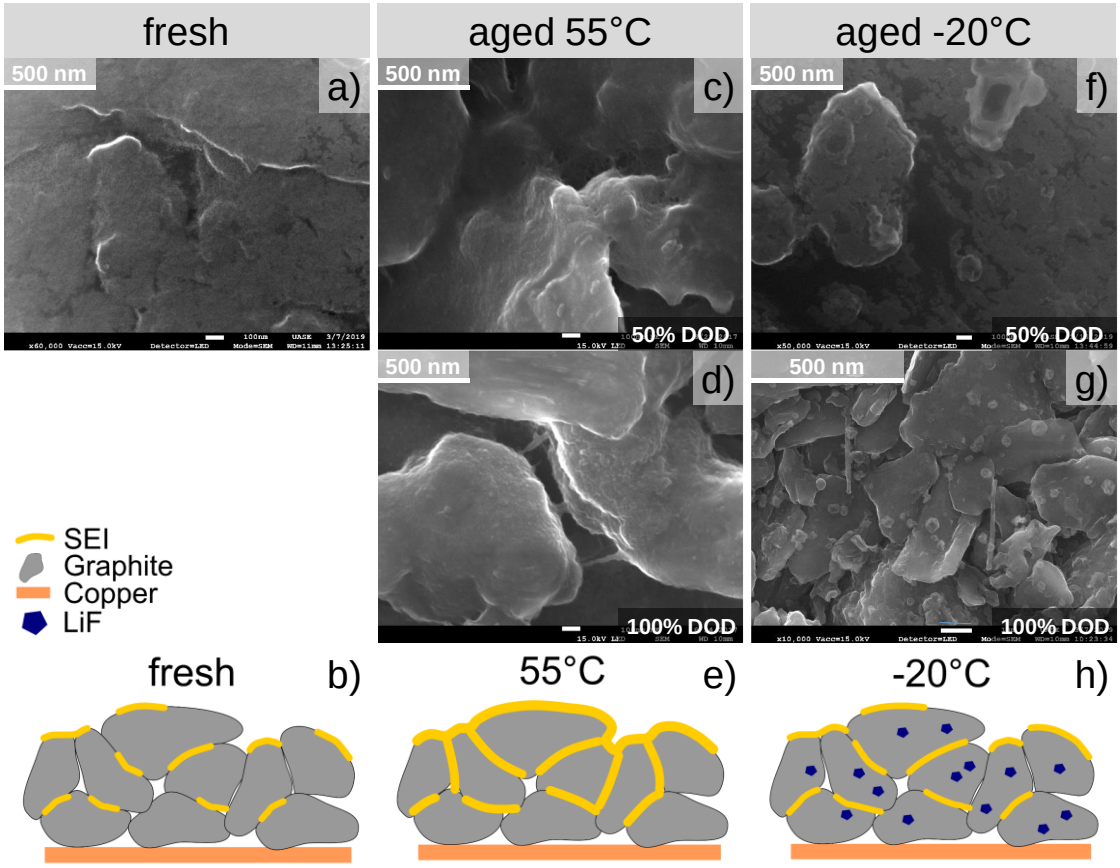

Figure 7-20: SEM images of anode surfaces from different ageing profiles with the corresponding illustrations. Fresh (a), aged 50% DOD with AP2 (c), aged 100% DOD with AP2 at 55°C (d) and 50% DOD with AP2 (f) and 100% DOD with AP2 (g) at -20°C. Illustration for the fresh anode in (b), anodes surfaces aged at 55°C in (e) and -20°C in (h). The images show a magnification of 5.000 and 60.000 for the inset (inset (e) only 10.000). The fresh and at -20°C aged anodes shows sharp edges, while the anodes aged at 55°C exhibit a smooth surface coverage

Next to the SEI layer on the anodes, the anodes aged at -20°C exhibited Li plating. The formation of plated Li is independent from the cycling profile, since it is found on anodes aged with 50% DOD with AP1 and 100% DOD with AP2 (Figure 7-21). Li plating contributes to LLI, if Li is irreversibly plated. Moreover, the irreversibly plated Li can deactivate anode and cathode material, since covered surfaces on the anode and opposite to that on the cathode are no longer electrochemically active. Since the cells are disassembled in discharged state, the plated Li was not stripped off the anode surface during the discharge process. Therefore, the observed Li plating is irreversible and contributes to the capacity fading of the cells aged at -20°C. The plated Li formed large connected islands with a net-like structure on the top.

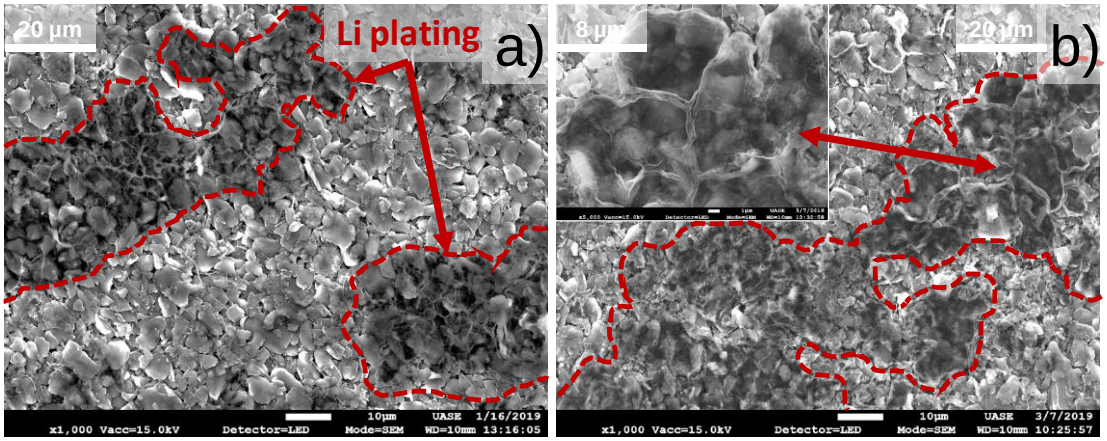

Figure 7-21: SEM images of anode surfaces showing Li plating, aged at -20°C using 50% DOD, with AP1 (a) and 100% DOD, with AP2 (b)

The anode surfaces were additionally examined using AFM. In Figure 7-22, the height and the Peak Force Error (PFE) images of the anode surfaces are displayed. The fresh anode shows the typical large graphite flakes, which exhibit a flat surface (Figure 7-22a) and b). This is easily observed in the inset of the PFE image, which displays a zoom into the PFE image with an image size of 5.1 µm side length. During conductivity measurements, the fresh anode showed electrically conductive areas, which was not observed for any other sample (not shown here). Therefore, the flat surface of the graphite flakes and the measurable electrical conductivity indicate a very thin or not existing SEI on the fresh anode after washing. Moreover, this indicates, that the first characterisation cycles and formation did not generate a stable and thick SEI yet. The anode surface from the cell aged at 55°C exhibits - as already seen in the SEM images in Figure 7-20b) - a covering layer on the graphite flakes (Figure 7-22c) and d). Especially in the PFE, the morphological changes of the graphite flakes are clearly visible (see inset of PFE). The surface roughness increased due to ageing by 5%, probably due to the

formation of the rough SEI structure on top of the smooth graphite flakes. Therefore, washing of the anode surface did not remove all of the SEI, a considerable amount remained on the anode surface. This suggests a more stable and thicker SEI layer, compared to the BOL. The AFM images of the other anodes aged at 55°C are shown in Figure A10 in the appendix. The anodes exhibit a surface coverage on all of the graphite flakes similar to Figure 7-22c) and Figure 7-22d. The anode surface of the cell aged using 50% DOD with AP2 at -20°C exhibits an increase in surface roughness by 3%, which is mainly due to the precipitation of the crystal-like structures with roughly 200 – 600 nm diameter on the anode surfaces. The graphite flakes likewise exhibit an increase of the surface roughness, due to the remaining, partially covering layer. However, the surface layer does not cover all graphite flakes entirely, since some smooth and flat locations on the graphite flakes are still observed (marked by blue ellipses). The anode surface of the cell aged at 100% DOD with AP2 at -20°C contains as already observed in the SEM images in Figure 7-21 an island-like covering layer, which is attributed to the Li plating (marked by red arrows). Conductivity measurements using the AFM reveal no measurable current, which indicates electrically isolated Li plating (not shown here). The roughness increase by 6% is due to the crystal-like features, a layer on the graphite flakes and the plated Li. The AFM images of the other anodes aged at -20°C are shown in Figure A11 in the appendix. The measurements indicate a surface layer covering parts of the graphite flakes, while some flakes exhibit a flat and smooth surface with a distinct change in adhesion, which indicates the bare graphite flakes. Therefore, the cycling at -20°C leads to a less pronounced surface coverage of the graphite flakes, compared to ageing at 55°C. Several studies show a temperature dependent SEI growth and thickness over ageing, with higher temperatures leading to thick and homogeneous and lower temperatures to thin and non-uniform SEI layers [217,230,233–235]. These observations confirm that temperature is a significant driving force for the reaction rate leading to the formation of the SEI layer. This relation explains the observed overall surface coverage of the graphite flakes for the anodes aged at 55°C (Figure 7-22c), d) and Figure A10 in the appendix) and the only partial coverage of graphite flakes for the anodes aged at -20°C (Figure 7-22e), f), g), h) and Figure A11 in the appendix).

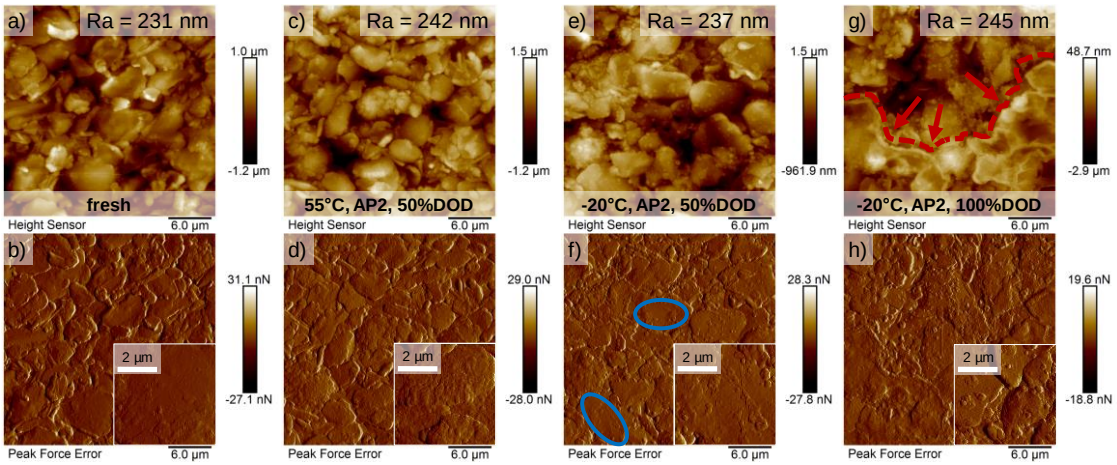

Figure 7-22: AFM images showing height (top row) and Peak Force Error (bottom) of the fresh (a,b), aged at 55°C using AP2, 50% DOD (c,d), aged at -20°C using AP2, 50% DOD (e,f) and -20°C using AP2, 100% DOD (g,h). The blue ellipses are indicating flat surfaces on graphite flakes and the red arrows and the dashed line indicate Li plating

7.2.4 Chemical Compositions of Anode Close-to-Surface Material and Surface Layers

The chemical composition of the anode surfaces was analysed using EDX and XPS. We used an acceleration voltage of 15 kV for the EDX measurements to be able to detect the Fe Kα line. As the information depth with this method is 1-3 µm, in comparison to only a few nm in XPS. EDX results represent close-to-surface material composition, and XPS results represent the topmost surface layers. The anode surfaces contained, in addition to C, mainly O, F, P, Fe and V. The precipitation of phosphorus and oxygen is based on the reduction of electrolyte and of electrolyte salt ($LiPF_6$) on the anode surface, since the anode potential is lower than the chemical stability window of these components. The mass content of P increases due to cycling by the factor of 2 – 4. Within one ageing profile (AP1 or AP2), the anode surface cycled at 50% DOD exhibits a higher P content compared to the 100% DOD cycling at the same ageing profile (see Figure 7-23). This is explained by the well-known observation that cycling at higher SOC leads to more pronounced SEI generation compared to lower SOC cycling [24,232,236]. The cycling at 50% DOD leads to a longer duration at high SOC ranges (compared to 100% DOD) of the cells with more electrolyte and salt decomposition. Furthermore, an important difference between the 50% DOD cycling and the 100% DOD cycling is the number of charge-discharge cycles. One cycle for the 50% DOD cells represents 1.25 Ah $cycle^{-1}$, leading to roughly 1600 cycles until EOL, while for the 100% DOD cells (2.5 Ah $cycle^{-1}$) only about 800 cycles are performed until EOL is reached. The higher amount of potential cycles for the 50% DOD cycling leads to a thicker SEI, which consumed more Li during the ageing. The anodes aged at

-20°C exhibit likewise an increase of P and O on the surfaces in a similar extent, even though a less pronounced SEI is observed in the SEM and AFM images. This is due to the plated Li, which reacts with the electrolyte to form decomposition products on the anodes aged at -20°C, even when the surface of the graphite flakes is not covered entirely, as it is the case for the graphite flakes aged at 55°C.

Similar trends for the oxygen content as already found for phosphorus are observed on the anodes aged at 55°C. The mass of oxygen increased due to ageing by a factor of 4 – 6. The underlying origin is the same as for phosphorus. However, at -20°C, the anode surfaces show a different behaviour. The cells aged at 100% DOD show a higher oxygen content compared to the cells aged with 50% DOD. This observation could be based on the existence of plated Li, which reacts with oxygen from the electrolyte or during the transfer of the sample from the glovebox into the SEM observation chamber. Petzl and Danzer [205] assume that the Li plated at lower SOC (100% DOD cycling) is thicker and more stable compared to high SOC plating (50% DOD cycling).

The observed Fe dissolution exhibits the assumed temperature dependency. The anode surfaces aged at 55°C show clearly the presence of Fe, while the anodes aged at -20°C do not show any significant amount. The Fe dissolution does not show any clear dependency on the DOD. This clearly shows that high temperatures promote the Fe dissolution, while it is suppressed at low temperatures. Lastly, vanadium is observed on the anode surfaces. Due to the low electronic and ionic conductivity of LFP, it is doped with multivalent cations (like V^{3+}) to improve the conductivity [237]. All transition metals commonly used in Li-ion batteries are dissolved from the cathode into the electrolyte upon ageing [238,239]. As will be shown later, the mass content of V decreased in the cathodes after ageing, indicating dissolution of V from the cathode and precipitation on the anode surface. The V content is generally higher at the anodes cycled at 55°C. A notable exception is the anode aged at 100% DOD with AP2 at -20°C, which showed a distinct higher amount as compared to the other cells. The origin of this observation is not entirely clear yet, but might indicate inhomogeneous deposition of V. The transition metals V and Fe act as catalysts at the anode surface for the formation and subsequent growth of the SEI [183,240]. The deposition of transition metals is in addition hindering the Li intercalation into the graphite anode by clogging anode pores [182,240,241]. The increase of the surface layer related resistance was analyzed using EIS in [242]. It was observed, that the cells aged at 55°C exhibit a surface layer related increase of resistance between 12

and 27%. The formation of surface layers consumes Li, which is afterwards lost for subsequent cycling, and deactivates anode material by blocking the intercalation and de-intercalation process.

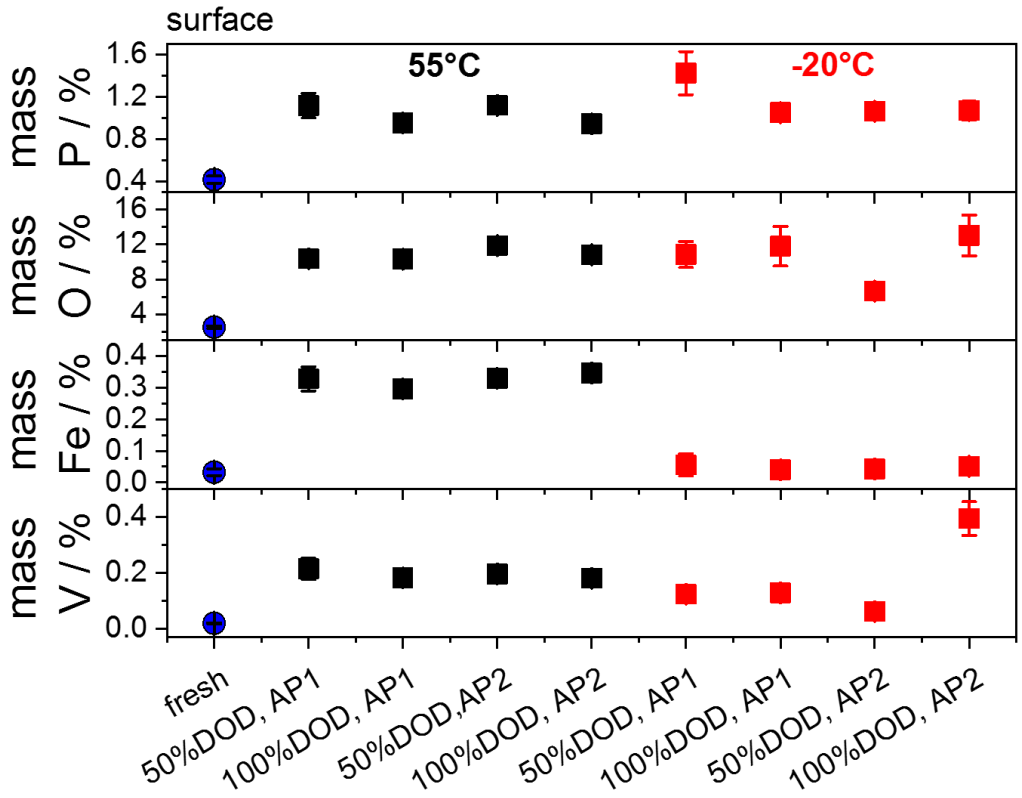

Figure 7-23: EDX analysis of anode surfaces regarding the P, O, Fe, O and V mass content

Figure 7-24 shows the XPS spectra of anodes aged at -20°C (1st and 2nd row each) and 55°C (3rd and 4th row each) using 50% DOD with AP1 (2nd and 4th row) and AP2 (1st and 3rd row) in comparison to the fresh anode (5th row). The bulk spectra refer to the surface laid open after ion etching for a total time of 2660 s, while the surface spectra were recorded before. In the C1s surface spectra, the fresh anode shows four peaks around 284, 287, 288 and 292 eV. The peak around 284 eV is assigned to C-C and C-H species. After ageing at 55°C, the peak is no longer observed, while at -20°C these species are still found. The vanishing of the peak around 284 eV for the anodes aged at 55°C indicates a thick and homogeneous surface layer covering the entire anode surface. Since the peak is still observed in the anodes aged at -20°C, the surface layer is only partially covering the anode, as it was already observed in the AFM measurements (Figure 7-22). The peaks at 287 eV and 288 eV are assigned to C-O and C=O bonds, respectively. The peak at 292 eV is assigned to decomposition products of the carbonate-based electrolyte.

Interestingly, the carbonate-based peak is not observed in the aged samples, neither in the surface layer nor in the bulk. After ion etching for 2660 s, the bulk material of all anodes exhibits only the two peaks of the C-C / C-H and the C-O species. Two peaks around 685 eV and 689 eV dominate the F1s surface spectra. They are attributed to $Li_xPO_yF_z$ and Li_xPF_z, respectively, which are decomposition products of $LiPF_6$. However, PVDF (polyvinylidene difluoride) as an assumed binder material in the electrodes can influence the peak around 689 eV, due to the C-F bond. $Li_xPO_yF_z$ is additionally observed in the P2p surface spectra of all anodes at 136 eV. The anode aged at -20°C with AP1 exhibits a higher relative intensity for the Li_xPF_z peak in the F1s spectrum compared to the other anodes. The P2p surface spectra points likewise to a higher Li_xPF_z concentration on the anodes aged at -20°C compared to 55°C, since the peaks around 138 eV (assigned to Li_xPF_z) are only observed in the low temperature ageing. An additional peak appears around 685 eV for the anodes aged at -20°C in the F1s bulk spectra, which is assigned to LiF. The attribution of LiF crystals to the observed features in the AFM images for the anodes aged at -20°C is therefore verified by the presence of this peak (only detected for the anodes aged at -20°C). For the fresh anode and the anodes aged at 55°C, the O1s surface spectra contains two peaks at 535 eV and 533.5 eV that are assigned to C-O species and $Li_xPO_yF_z$, respectively. The anodes aged at -20°C exhibit an additional peak around 530.5 eV. This peak is attributed to LiOH or Li_2O species [243,244]. The bulk material of the fresh anode generates no significant O1s peak anymore. Contrary, the aged anodes still contain the peaks, which are found on the surface, which indicates a thicker and more stable SEI layer for all aged anodes as compared to the fresh state. In the P2p bulk spectra, the $Li_xPO_yF_z$ peaks of the anodes aged at 55°C are shifted towards lower binding energies, compared to the -20°C data, therefore indicating lower oxidation states. The relative peak intensity of the anode aged at -20°C, 50% DOD with AP2 is very low and non-existing for the fresh anode, which is in agreement with the aforementioned vanishing of the $Li_xPO_yF_z$ peak in the O1s spectra around 533.5 eV. The P2p bulk spectra of the anodes aged at 55°C exhibit an additional peak at around 130.5 eV. P atoms coordinated to a Fe atom are assumed to generate this additional peak at lower binding energies. Since Fe dissolution is not observed for the anodes aged at -20°C, such a peak is not expected and neither observed for these anodes. $Li_xPO_yF_z$ and Li_xPF_z are mainly dominating the L1s spectra at 57 eV. The cells aged at -20°C exhibit additionally a peak around 56 eV, indicating LiF and a small peak around 54 eV, which is assigned to plated Li species which was already observed in SEM and AFM images. The surface and bulk Li1s spectra show similar results.

The elements in the SEI layer are essentially similar for the anodes aged at 55°C and -20°C. However, some deviations are observed: i) only for the anodes aged at -20°C, LiF is observed, ii) additional species such as LiOH or Li_2O (indicating Li plating) are only observed in the anodes aged at -20°C, iii) on the anodes aged at -20°C, a higher amount of Li_xPF_z is present compared to the anodes aged at 55°C, iv) the anodes aged at -20°C show lithium species, as already observed in the SEM and AFM images, and v) for the anodes aged at 55°C, due to Fe dissolution, which is already observed in the EDX analysis, an additional peak due to P atoms coordinated to Fe atoms, is observed.

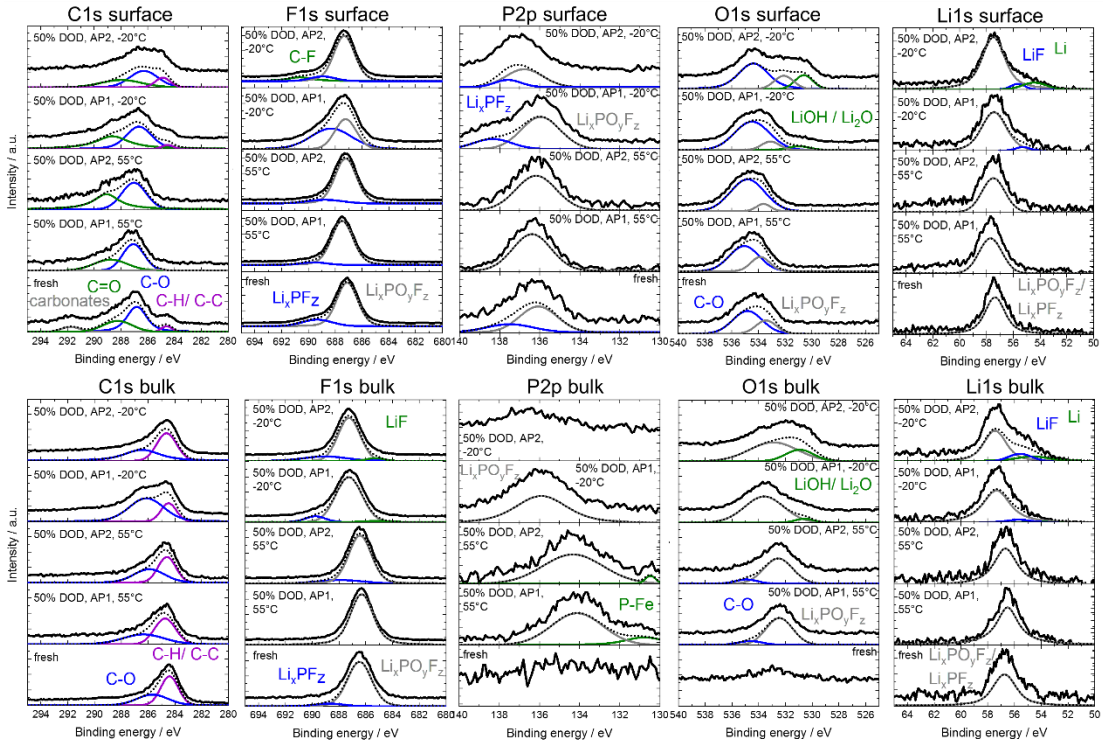

Figure 7-24: XPS spectra of the anode surfaces showing the C1s, F1s, P2p, O1s, and Li1s spectra at the surface (top) and after sputtering for 2660 s (indicated as bulk, bottom set of spectra). The 1st row shows the anode from a cell aged at -20°C, 50% DOD with AP2; the 2nd row -20°C, 50% DOD with AP1; 3rd row 55°C, 50% DOD with AP1; 4th row 55°C, 50% DOD with AP2 and 5th row in fresh state

7.2.5 Structure and Morphology of Cathode Surfaces

The fresh cathode surface is highly conductive (about 80% of the measured surface area is conductive) and consists of small particles of roughly 50 – 200 nm in diameter (Figure 7-25a) and b). After the ageing at 55°C, the cathode surfaces are covered by electrically non-conductive agglomerates having a diameter of roughly 0.5 to 1 µm. The surface coverage is consistently higher for the 100% DOD profile aged with AP1 or AP2 (Figure 7-25e), f) and i),

j) compared to the 50% DOD profile (Figure 7-25c), d) and g), h). The agglomerates consist of smaller particles of roughly 15 – 100 nm in diameter, which show a lower adhesion compared to the agglomerate-free cathode surface (see Figure A12 in the appendix for higher magnification). The adhesion is governed by electrostatic interactions between tip and surface and remaining electrolyte material. Influences of a water meniscus on the adhesion play an important role but can be excluded here, due to the dry argon atmosphere. Using a positive bias voltage, the particles showing a low adhesion are expected to be $LiFePO_4$ particles, while the high adhesion is assigned to binder and electrolyte material due to presence of charges and a higher mechanical pull-off force of the tip from the surface, induced by remaining electrolyte. The appearance of negative adhesion is based on the existence of negatively charged LFP particles $[Li_{(1-x)}FePO4]^{x-}$, due to the loss of lithium inventory over cycling, while applying a positive bias voltage. The loss of lithium inventory is next to the loss of active material the main influence for the capacity decay over aging (see [93] for more information on the degradation of the cells). The nanometer particles forming the agglomerates must be covered with a thicker, isolating surface layer or exhibit a degradation of the conductive carbon coating. Otherwise, the agglomerates would still exhibit a measurable current through the conductive nanometer particle network. Zhu et al. previously observed the appearance of large surface agglomerates for cycled $LiMnO_2$ cathodes [245]. In their study, the agglomerates are assumed to be generated by fragmentation of particles due to cyclic induced stress by continuous lithiation and delithiation and consecutive agglomeration of nanometer particles, which is in agreement with the observed composition of the agglomerates here. Therefore, the continuous lithiation and delithiation leads to cracking and fragmentation of large LFP particles and subsequent agglomeration generates the micrometre size agglomerates. The observed lack of conductivity on these agglomerates indicates disconnection to the electrode electrical network and therefore also a loss of active material due to the generation of an electrochemical inactive phase.

Since the agglomerates are electrically insulating, the quantity of agglomerates controls the overall surface conductivity. The conductivity decreased by 40% to 70% compared to the fresh cathode, see Figure 7-27a) top. Apart from the agglomerates, the surface conductivity is influenced by i) the isolating surface layer, ii) degradation of carbon coating and iii) the contact loss of the particle to the conductive electrode network. The roughness of the cathode surface, which is not covered by the agglomerates, decreased compared to the fresh cathode surface by roughly 25% to 50%, see Figure 7-27a) bottom. Since we exclude the large agglomerates for the surface roughness analysis, the presence of the agglomerates does not affect the resulting

roughness measurements. Most other surface roughness studies on cathodes ($LiCoO_2$, $LiMnO_2$ and $LiFePO_4$) report an increase of the surface roughness over ageing, which is due to the generation of smaller particles due to fragmentation [37,245,246]. The decrease of the agglomerate-free surface roughness is based on the remaining surface layer, which was not removed during the sample preparation process, see Figure 7-27b) for an illustration. Since the samples are measured ex-situ, the sample preparation process influences the surface roughness of the samples. For example Wu et al. used an extensive procedure with acetone and ethanol to wash the cathode surfaces several times, which presumably removed all remaining electrolyte and measured an increase of the surface roughness after ageing [246]. Contrary, we employed a more delicate procedure with DMC in a single process to wash off electrolyte and no further surface treatment for the analysis.

Nevertheless, Kostecki et al. [247] and Demirocak and Bushan [248] observed likewise a decrease in surface roughness after cyclic and calendric ageing of $LiN_{0.8}Co_{0.2}O_2$ and $LiFePO_4$ cathodes, respectively. While Demirocak and Bushan did not elaborate further on this observation, Kostecki et al. attribute this to the formation of a deposit which is not enhanced by electrochemical cycling [247]. The formation of an electrolyte layer on the cathode surface reduces the surface roughness of the analysed aged cathodes. We assume the deposit to exhibit only a thin layer thickness, since the AFM measurements still show a measurable current in these areas. The observed decrease of surface conductivity, which is observed by the reduced magnitude of the measured current in the aged cathode surfaces, is therefore attributed to the degradation of carbon coating on the particle and loss of electrical contact to the electrode conductivity network. The surface layer does not seem to electrically isolate the cathode surface, since the agglomerate-free cathode surfaces still exhibit a measurable current (see also Figure A12 in the appendix for a higher magnification of the agglomerate-free cathode surface). The degradation of the carbon coating and loss of electrical contact leads to a higher electrode resistance, which is observed in the lower absolute current in the peak current measurements (ranging from 0.70 to 3.12 nA for the aged cathodes) compared to the fresh cathode (4.93 nA).

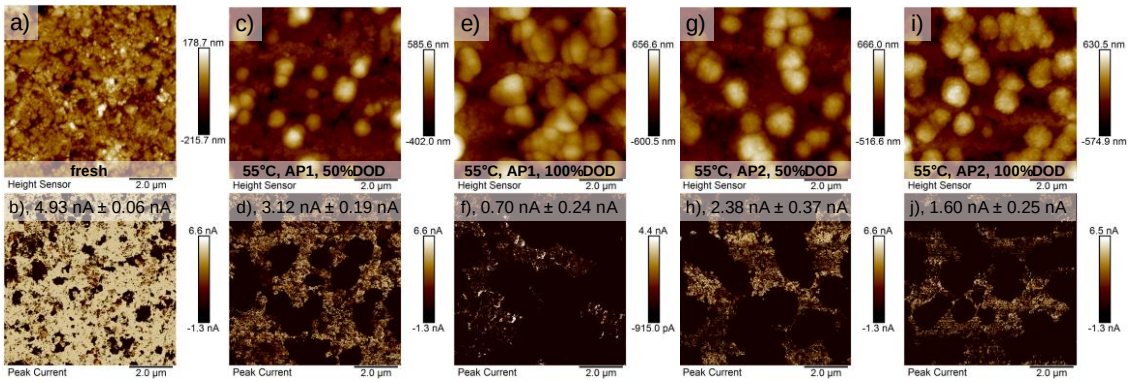

Figure 7-25: AFM surface images of fresh cathodes (a, b) and cathodes aged at 55°C using 50% DOD with AP1 (c, d), 100% DOD with AP1 (e, f), 50% DOD with AP2 (g, h) and 100% DOD with AP2 (i, j). Top row shows the cathode surface topography and the bottom row the (peak) current. In the top of the current images, the average current magnitude of the agglomerate-free surface is given

Contrary to the cathodes aged at 55°C, the cathode surfaces aged at -20°C and prepared using the same procedure for the sample analysis, exhibit nearly no change in surface morphology and structure (Figure 7-26). The surface morphology consists of small particles and exhibits a decrease of the conductive area of only 5 – 20%, see Figure 7-27 top, and the surface roughness increased by 5 – 22% compared to the fresh cathode (Figure 7-27 bottom). The overall magnitude of the measurable current reduced in a lower extend for the cathodes aged at -20°C (ranging from 2.25 to 3.97 nA) compared to the cathodes aged at 55°C. The modest reduction of the conductive area in AFM images is attributed to loss of electrical contact of particles to the electrode conductivity network. Carbon coating degradation does not influence the surface conductivity, but leads to a reduction in the absolute values of the current magnitude due to resistance increase of the electrode. The increase of the surface roughness is attributed to an inhomogeneous surface layer, which does not cover the cathode surface completely, and cracking and fragmentation of LFP particles. This is based on the assumption that thicker, homogeneous and complete surface layers are generating a smooth and flat surface layer, while the bare cathode and a cathode with only small and limited coverage exhibits a rough surface, due to the structure of the uncovered LFP particles. The assumption is summarized in the illustration in Figure 7-27b). The thin surface layer has presumably a negligible influence on the overall surface conductivity.

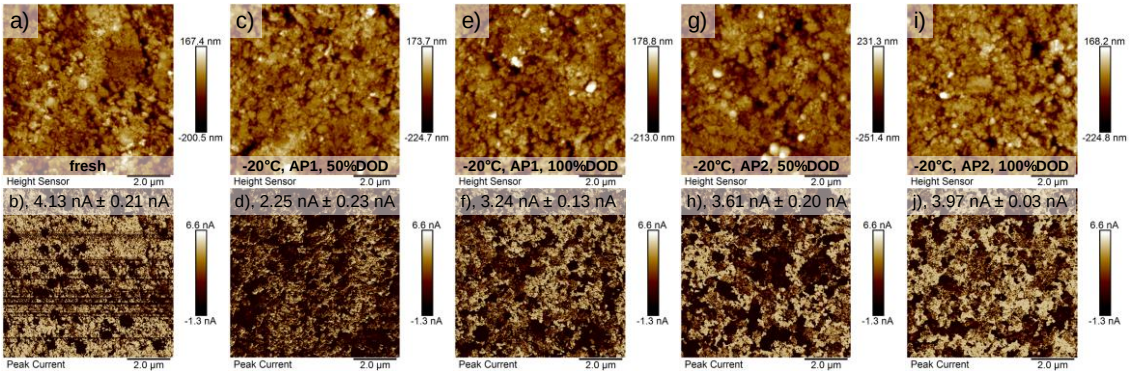

Figure 7-26: AFM surface images of fresh cathodes (a, b) and cathodes aged at -20°C using 50% DOD with AP1 (c, d), 100% DOD with AP1 (e, f), 50% DOD with AP2 (g, h) and 100% DOD with AP2 (i, j). Top row shows the cathode surface topography and the bottom row the (peak) current. In the top of the current images, the average current magnitude of the agglomerate-free surface is given

The surface conductivity of the cathodes aged at 55°C decreased intensely compared to the fresh cathode surface and the cathodes aged at -20°C. However, the cathodes with the highest decrease of surface conductivity (100% DOD with AP1 and AP2) show a decrease of capacity at the EOL of 12% and 13%, while the other cells aged at 50% DOD with AP1 and AP2 show a capacity decrease of 16% and 17%, respectively, but a higher share of conductive area after ageing. A similar trend is observed for the cathodes aged at -20°C, which show an almost constant surface conductivity within the group after ageing, but differ in the remaining cell capacity (Figure 7-19). Therefore, the decrease of the cathode surface conductivity does not seem to have a direct impact on the remaining cell capacity. This observation is plotted in Figure A13, which displays the independency of the remaining cell capacity on the surface conductive area. Next to the cell capacity, the power capabilities, which would be influenced by a resistance increase of the cells, is not affected by the observed reduction of surface conductivity. This observation was reported before by the authors in Figure S11 [242], which depicts the evolution of the internal cell resistance of the electrodes (called R_{total}). For the cells aged at -20°C and the cell aged at 55°C with 100% DOD using AP2, the resistance stays nearly constant throughout the ageing. For the cell aged at 55°C with 50% DOD using AP2 the resistance increases by 70%, however, the cathode exhibits a higher share of surface conductive area compared to the cell aged at 55°C with 100% DOD using AP2. Therefore, especially the power capabilities of the cell aged at 55°C with 100% DOD using AP2 should show any influence by the reduced share of the surface conductive area, which is, however, not observed. Changes in the power characteristics would be influenced by modifications in the cell

resistance, which are, however, only observed for the cell aged at 55°C using 50% DOD, but these are based on different degradation mechanisms (Fe-dissolution, damages to the internal, electrically conductive electrode network and deactivation of before electrochemically active material) and not based on the surface conductivity of the cathodes.

The decrease of surface roughness indicates coverage of particles on the cathode surface, which reduces the overall roughness for the cathodes aged at 55°C. Ageing with 100% DOD leads to a more homogeneous coverage layer, since the surface roughness is smaller compared to the 50% DOD cycling profiles. The roughness follows the same trend as the surface conductivity, with 100% DOD exhibiting a higher decrease of the surface roughness compared to the 50% DOD counterpart. The cathodes aged at -20°C exhibit an unchanged or a slightly increased surface roughness, which shows, that cycling at -20°C generates only very limited coverage of particles upon ageing. The increase of surface roughness is due to the cracking and fragmentation of LFP particles, which are subsequently not entirely covered by a surface layer.

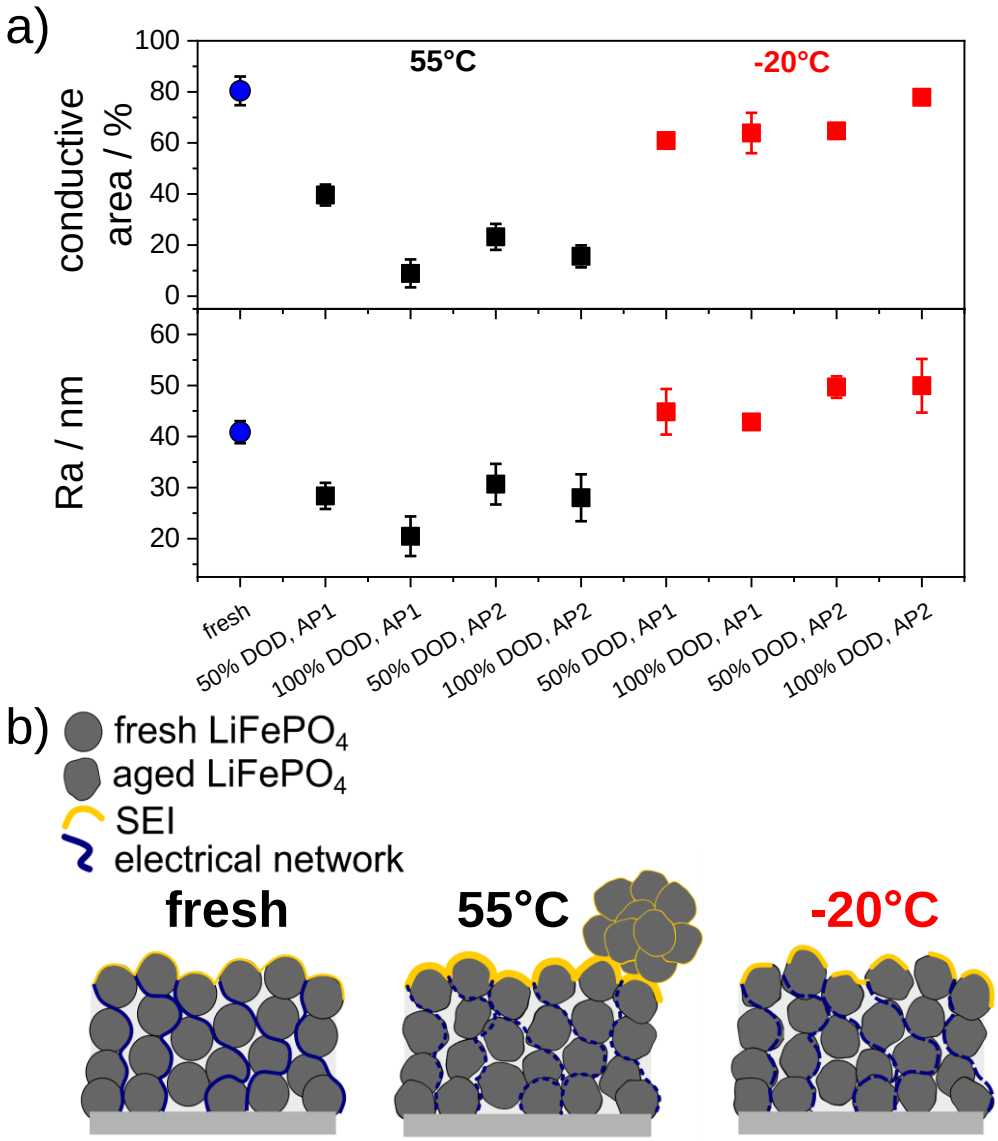

Figure 7-27: Analysis of AFM surface measurements of cathodes aged at 55°C and − 20°C showing in a) the conductive area in the top and the surface roughness in the bottom row and in b) the illustration of the surface layer and electrical network degradation of the fresh cathode and the cathodes aged at 55°C and -20°C

Table 4: Peak assignment (in eV) for the observed species on the anode surface

	P2p	**F1s**	**O1s**	**Li1s**	**C1s**
C-O			535		287
C-C/ C-H					284
C=O					288
Carbonates					292
C-F		691			
Li_xPF_z	138	689		57	
$Li_xPO_yF_z$	136	687	533	57	
LiF		685		56	
P-Fe	131				
LiOH / Li_2O			531		287
Li				54	

7.2.6 Chemical Compositions of Cathode Close-to-Surface Material and Surface Layers

The chemical composition of the cathode surface was analysed using EDX and XPS. The EDX analysis reveals an increase of the mass of P and Fe (Figure 7-28). This is valid for nearly all cathode surfaces, except the cathode aged at -20°C using 100% DOD with AP2, which shows only negligible variations compared to the fresh cathode. Regarding the cells aged at 55°C, the absolute change compared to the fresh cathode surface was continuously higher for the cathode aged at AP1 than for the AP2 ageing.

The Fe content on the cathode surfaces increases for all analysed cathodes. This would be assumed for cathodes aged at elevated temperatures, due to Fe dissolution from the bulk. The appearance of a higher Fe content on the surface of cathodes aged at -20°C, for which no Fe deposition at the anode surfaces is observed, is unexpected. Additionally, the Fe content of the cathode cross-section stays constant or increases slightly (see Figure 7-30). The cathodes aged at 55°C exhibit an increase of the Fe content on the cathode surface and a decrease of the Fe content in the cross-section, which would be expected for the dissolution of Fe from the bulk into the electrolyte. This observation of the Fe content increase on the cathode surface and cross-section for the cathodes aged at -20°C points towards an inhomogeneous Fe redistribution inside the cathode due to ageing, since Fe dissolution towards and deposition on the anode is not observed. Phosphorus follows the same mechanism as observed for Fe, without the

dissolution into the electrolyte, since the P increase on the anode surface is attributed to electrolyte salt decomposition and SEI growth. On the cathode surfaces, a higher P content after ageing is observed, while for the cross-section it decreased. This observation points towards a redistribution of P inside the cathode material, as it is assumed for Fe.

The XPS spectra of the cathode surfaces show species similar to the anode surfaces. The C-C and C-H (284 eV) peaks are well observable in all samples and their intensities on the bulk surface increase only slightly after ion etching (Figure 7-29). A similar observation is found in the O1s spectra for the PO_4^{3-} peak at 531 eV, which is well observable. The pronounced C-C / C-H and PO_4^{3-} peaks indicate only partial coverage of the cathode surface as already observed in the AFM measurements (Figure 7-25 and Figure 7-26). The peak at 688 eV, attributed to $Li_xPO_yF_z$, dominates most of the F1s surface and bulk spectra. Only the cathode surface aged at 55°C, 50% DOD with AP1 exhibits an additional and more pronounced peak at 690 eV, originating from Li_xPF_z species. The other cathode surface aged at 55°C, 50% DOD with AP2 exhibits only a weak signal at 690 eV, similar to the fresh cathode. The cathodes aged at -20°C do not show any observable peak at this binding energy. After ion etching, the intensity of the Li_xPF_z peak increases for the cathodes aged at 55°C. The -20°C cathodes exhibit an additional peak at lower binding energies, which is attributed to LiF (685 eV). The PO_4^{3-} peak at 133 eV dominates the P2p spectra for all cathode surfaces. On the fresh cathode, peaks indicating Li_xPF_z and $Li_xPO_yF_z$ are observed at 137 eV and 136 eV, respectively. The cathodes aged at 55°C contain next to the PO_4^{3-} peak only traces of Li_xPF_z, while the cathodes aged at -20°C exhibit only traces of $Li_xPO_yF_z$. The F1s and P2p spectra indicate that the ageing at 55°C leads to more pronounced precipitation of Li_xPF_z over ageing compared to the ageing at -20°C. Li_xPF_z is formed by decomposition of $LiPF_6$ in the electrolyte [249–251] following reaction (1) and (2). $Li_xPO_yF_z$ is formed due to traces of water in the electrolyte and by reaction with the highly reactive PF_5 through reaction (3) and (4). LiF is not observed on the cathode surfaces aged at 55°C, even though it is a product of the reactions (1), (2) and (4) and often found in $LiPF_6$ based electrolytes [41,249,252]. High temperature cycling might promote LiF dissolution into the electrolyte, which could explain the missing LiF peaks for the cathodes aged at 55°C[244,245].

$$LiPF_6 \rightarrow LiF + PF_5 \quad (1)$$

$$2xLi^+ + 2xe^- + PF_5 \rightarrow Li_xPF_{5-x} + (2-x)\,LiF \quad (2)$$

$$PF_5 + H_2O \rightarrow 2\,HF + PF_3O \quad (3)$$

$$2xLi^+ + 2xe^- + PF_3O \rightarrow Li_xPF_{3-x}O + xLiF \quad (4)$$

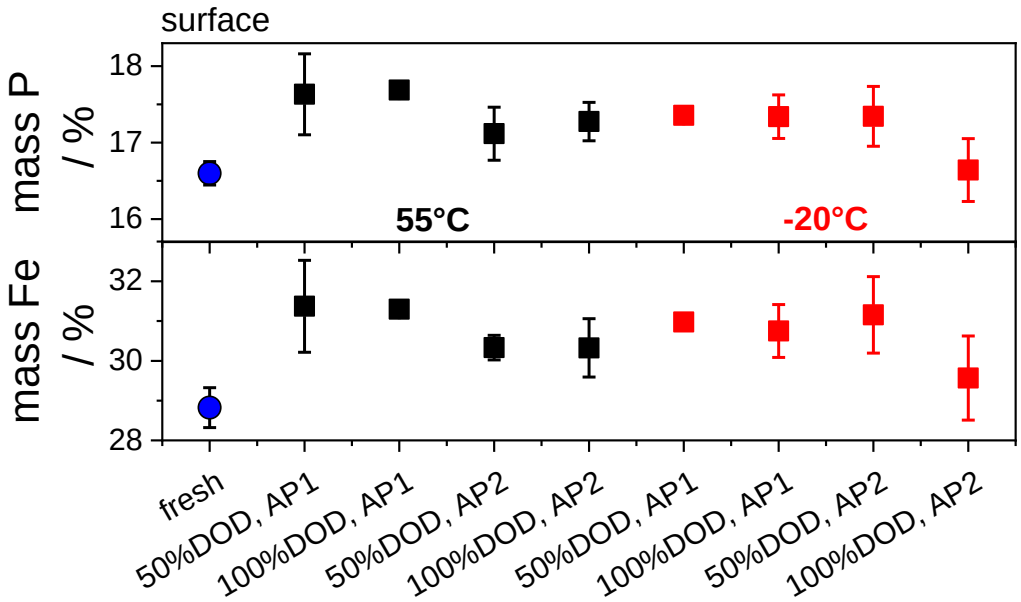

Figure 7-28: EDX analysis of cathode surfaces regarding the P and Fe norm. mass content

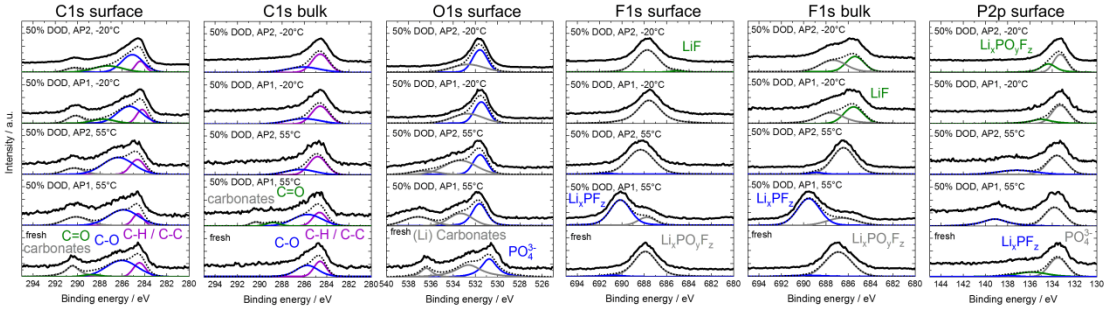

Figure 7-29: XPS spectra of the cathode surfaces showing the C1s, F1s, O1s and P2p spectra at the surface and after sputtering for 2660 s (indicated as bulk). The 1st row shows the anode from a cell aged at -20°C, 50% DOD with AP2; the 2nd row -20°C, 50% DOD with AP1; 3rd row 55°C, 50% DOD with AP1; 4th row 55°C, 50% DOD with AP2 and 5th row in fresh state

Table 5: Peak assignment (in eV) for the observed species on the cathode surface

	P2p	**F1s**	**O1s**	**C1s**
C-C/ C-H				284
C-O				287
C=O				288
Carbonates				290.5
Li_xPF_z	137	690		
$Li_xPO_yF_z$	136	688	533	
LiF		685		
PO_4^{3-}	133		531	

7.2.7 Chemical Compositions of Cathode Bulk Material

Next to the cathode surface, the cross-section of cathodes was investigated using EDX measurements, to analyse the changes due to cycling in the bulk material. For the cathodes aged at 55°C, P and Fe show a similar trend, with a decrease of the P and Fe content for the 50% DOD cycling and a constant or only slight decrease for the cathodes aged with 100% DOD. The decrease of the Fe content in the bulk material is in agreement with the already observed Fe dissolution from the cathode and migration to and deposition on the anode surface (see Figure 7-23). The decrease of the P content in the cathode bulk and the increase of the P content on the cathode surface indicate an accumulation of $FePO_4$ active material in the surface of the electrode and depletion in the bulk of the cathode due to cycling. This effect is more pronounced for the cathodes aged at 50% DOD. This effect might be linked to the overall completed ageing cycles of the cathode. As explained earlier, the 50% DOD cells completed roughly twice as many charge and discharge cycles compared to the 100% DOD cells. The higher amount of cycles leads to an inhomogeneous distribution and accumulation of active material near the surface in the cathode. The increase of the vanadium content on the anode surface is accompanied by the decrease in the cathode bulk. The decrease does not exhibit any distinct dependency on the ageing profile. Transition metal dissolution is therefore not only limited to Fe, but also affects V, a doping agent. The appearance of V dissolution into the electrolyte was already observed by Hovington et al. for $Li_{1.2}V_3O_8$ cathodes [253]. For the cathodes aged at -20°C, no distinct trend for the elemental changes was detected. A decrease in the mass of P is observed for the cathodes aged with AP1, whereas it stays constant or increases slightly for the cathodes aged with AP2. Since the capacity fading is quite different for the cells aged with 50% DOD

and 100% DOD with AP1, but similar changes over ageing are observed in the elemental analysis of the cross-section, we expect the observation in Figure 7-30 to indicate heterogeneous active material distribution within the electrode for the cathodes aged at -20°C. If loss of active material would be responsible for the observed changes in the elemental analysis, the capacity decay over ageing would be comparable, which is however not the case for the 50% and 100% DOD cells aged with AP1. An increasing inhomogeneity for the distribution of lithium was already observed on cell level for the cells aged at -20°C [93]. The reduction of the V content is in agreement with the observed increase on the anode surface. Interestingly, it is detected in a smaller extent for -20 °C compared to the cathodes aged at 55°C. Fe dissolution is not observed. Reduction of V as a doping agent can lead to electrical and ionic resistance increase in the cathode and therefore contribute to an increase of the impedance and decrease of power capabilities over ageing.

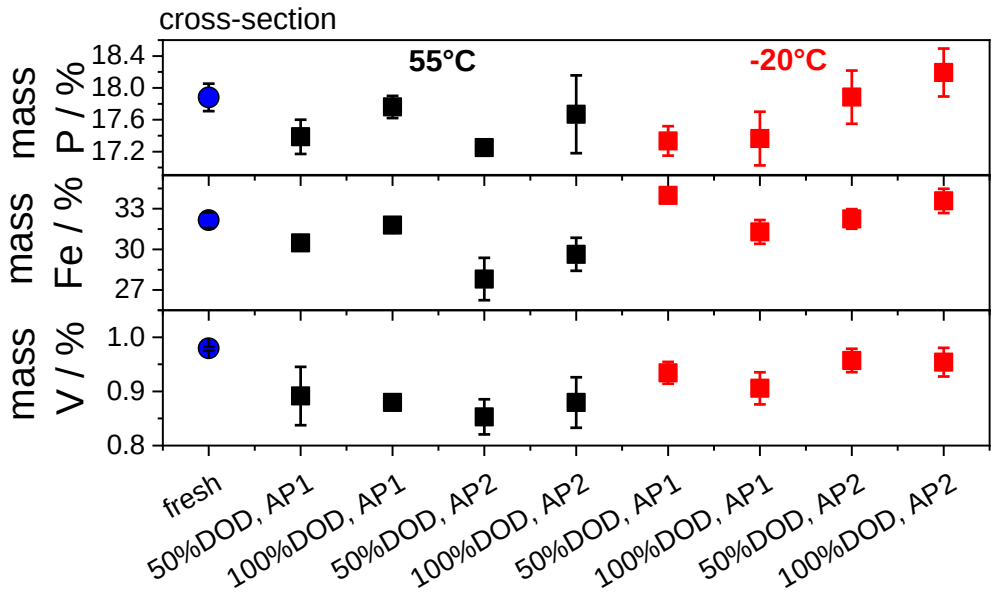

Figure 7-30: EDX analysis of cathode cross-section bulk material regarding the P, Fe and V norm. mass content

7.2.8 Conclusion for the Post-Mortem Analysis of Commercial LFP Cells

Post-mortem analyses of cathodes and anodes of commercial LFP cells aged at 55°C and -20°C and cycled with different dynamic load profiles are presented. The current intensity (difference

from AP1 to AP2) has a smaller influence on the capacity fading than the DOD (see Figure 7-19).

The anode surfaces aged at 55°C show a dense surface layer on the graphite flakes and only to a small extent an electrolyte decomposition layer on the anodes aged at -20°C. The anodes aged at -20°C, however, reveal intense Li plating and the appearance of crystal-like features, which are presumably LiF crystals. LiF, LiOH and Li_2O species are observed in the XPS spectra in the anodes aged at -20°C, but not at the anodes aged at 55°C. Fe resulting from dissolution is well observed on the anodes aged at 55°C, while low temperature cycling completely represses Fe from dissolution. Nevertheless, V is observed on all anode surfaces, independent from temperature, which is similar to the decrease of the V content observed for the cathode bulk. The 50% DOD profile shows consistently higher mass contents of P, O and V and Fe (with only one exception at AP2 for Fe) compared to the 100% DOD counterpart for the ageing at 55°C on the anode, which indicates higher electrolyte decomposition rates due to cycling at higher SOC ranges. Ageing at -20°C does not show any clear pattern, neither in the aged cathode, nor in the aged anode.

The cathodes aged at 55°C exhibit micrometre size and electrically isolating agglomerates consisting of $LiFePO_4$ particles. Particle cracking, fragmentation and subsequent agglomeration of the nanometer particles generate the agglomerates. The agglomerates are electrochemically inactive and responsible for loss of active material, next to the observed Fe dissolution from the cathode into the electrolyte. The remaining cathode surface, which is not covered by the agglomerates, shows an overall lower conductivity compared to the fresh cathode, indicating an additional degradation of the carbon coating on the particles and connection from the particles to the overall electrode electrical network. The surfaces of the cathodes aged at -20°C do not show any surface covering and show no significant change in overall surface conductivity. XPS analysis reveals higher amount of traces of Li_xPF_z at the cathodes surfaces aged at 55°C, while higher amount of traces of $Li_xPO_yF_z$ are observed at the cathodes aged at -20°C. LiF is only observed at the cathodes aged at -20°C. The EDX analysis of cathode surfaces show an increase of the mass content of P and Fe on the surface with a decrease of Fe in the bulk for the cathodes aged at 55°C. The 50% DOD profiles show a higher amount of Fe decrease in the cathode bulk, which points towards a higher Fe dissolution rate at high SOC cycling. The bulk of the cathodes reveal a cycling temperature independent decrease of the mass content of V, which is presumably a doping agent to increase the electrochemical performance.

The main factors leading to the capacity decay are loss of lithium inventory and loss of active material (see as well [93]). Loss of lithium inventory is for the cells aged at 55°C based on the formation of a surface layer on the anode side. For the cells aged at -20°C, Li plating is likely the main source of loss of lithium inventory, since the formation of a surface layer is observed in a smaller extend. The cathode aged at 55°C exhibits formation of surface agglomerates consisting of active material and Fe dissolution from the cathode and deposition on the anode surface. A similar effect is not observed for the cathodes aged at -20°C. Therefore, the ageing at 55°C is the sum of the anode (loss of lithium inventory) and cathode (loss of active material) contribution, while for the ageing at -20°C, the anode (loss of lithium inventory) is the main factor influencing the capacity decay.

The key insights of the presented results are summarised as following: firstly, we show that next to the temperature, the depth of discharge is another factor influencing the Fe dissolution. Secondly, the formation of LiF crystals with roughly 500 nm in diameter are observed, but only for the cells aged at 55°C. Thirdly, structural analyses of the cathode surface show that the surface conductivity is drastically decreased for the cathodes aged at 55°C by the evolution of micrometer sized, electrically isolated $LiFePO_4$ agglomerates. However, the reduction of the surface conductivity does not correlate with the capacity fading, indicating only a minor influence of electrode surface conductivity on the overall capacity fading process. Fourthly, next to the dissolution of iron, vanadium dissolution from the cathode and deposition on the anode is observed, indicating instable doping of $LiFePO_4$ material. Fifthly, the electrolyte deposition species on the cathodes exhibit a higher amount of oxygenated species for the ageing at -20°C compared to 55°C, indicating different decomposition paths. Additionally, the results confirm, that cycling at lower DOD is more detrimental than cycling using the full capacity range [200,201]. The manuscript is linked to another publication [93] on the tracking of cell ageing using cell level analysis techniques. The results are supposed to assist in the correct choice of operation conditions for these highly used commercial cells and cell chemistry and to present the degradation mechanisms related to the ageing.These observations reveal that cycling at elevated temperatures and higher SOC levels have a more detrimental effect on the electrode materials. Cycling at -20°C had only little detrimental effects on the cathodes and for the anodes it resulted mainly in the occurrence of Li plating. The reduction of the surface conductivity does not have any correlation with the remaining capacity, therefore, its influence on cell ageing is assumed negligible.

8 Summary

The combination of material analysis and system level analysis using the voltage and current response of the battery cell is a powerful tool for the evaluation of battery degradation mechanisms. Several different cell level analysis methods were combined with a variety of post-mortem material analysis techniques.

Scanning probe microscopy is a powerful tool for the evaluation of materials. Especially AFM and the here presented t-ESM technique generate further insights into material degradation of battery materials. The technique can be used to visualize and evaluate the ionic mobility of different materials, in this case cross-section cuts of silicon composite anodes and $LiFePO_4$ cathodes. For the silicon composite anodes analysed in chapter 5, the t-ESM measurements indicate material structure dependent ionic mobility. The signal dependency on the dc-voltage amplitude showed a saturation of the ESM signal at high dc-voltage amplitudes. The ESM signal saturation is likely caused by either concentration limitations inside the probed material or irreversible concentration changes in the material directly beneath the AFM tip. The dynamic behaviour of the ESM signal during and after the dc-voltage pulse can be used to analyse the migration and diffusion of Li-ions. The diffusion coefficients, which were fitted to the dynamic ESM signal after the dc-voltage pulse, are distributed around $4 \cdot 10^{-13}$ m^2 s^{-1}, which is consistent with literature values. The technique offers the potential, to visualize and map local diffusion coefficients and time constants on the nano-scale.

Regarding the ageing of $LiFePO_4$ cathodes in chapter 6, the t-ESM measurements show that the activity and ionic concentration are influencing the overall ESM signal. The fresh cathode exhibits a linear increase of the ESM signal intensity with stepwise increase of the dc-voltage amplitude, while the aged cathode exhibits a significantly smaller slope and absolute ESM signal intensity. The electrochemical active area, which is the area of the cathode cross-section, which exhibits a measureable ESM signal, reduced for the aged cathode in comparison to the fresh cathode cross-section. The ESM signal is an indication for the electrochemical activity of Li-ions in materials. Therefore, the reduced overall area with a measureable ESM signal of the cathode cross-sections represents the reduced electrochemical activity and loss of lithium inventory of the aged cathode. The dynamic behaviour of the ESM signal is used to calculate diffusion coefficients on the nano-scale. The diffusion coefficients are in the range of $2.5 \cdot 10^{-14}$ m^2 s^{-1}, which is consistent with theoretical and experimental values found in the literature.

The ageing of commercial battery cells was monitored and evaluated in chapter 7 with different system level techniques, such as ICA, DVA and OCV and post-mortem analysis methods such as AFM, XPS and EDX. Using these techniques, it was possible to separate the degradation mechanisms of commercial battery cells. It was found, that cycling at higher SOC ranges is more detrimental compared to cycling over the entire SOC range. This statement is true for ageing at 55°C and -20°C. The capacity loss of the cells aged at 55°C was mainly due to LLI and LAM_{PE}. The continuous consumption of Li in the surface layer on the anode is mainly responsible for the LLI. The LAM_{PE} is based on the generation of electrochemically inactive phases and the dissolution of Fe from the cathode. For the cells aged at -20°C, the observed Li plating is the main source of the capacity fading. The presented straightforward capacity estimation and prediction tool can be used to quickly test the remaining capacity and lifetime of the battery cell.

The post-mortem analysis show, that the depth of discharge is another factor next to temperature which influences the Fe dissolution from the cathode. LiF crystals are observed on the anode surfaces, however, only on the anodes aged at 55°C. The surface conductivity of cathodes was analysed and it was observed, that the surface conductivity decreases drastically for the cathodes aged at 55°C by the evolution of micrometer sized agglomerates, which, however, does not correlate with the capacity fading. Next to Fe dissolution from the cathode, vanadium dissolution was observed, which indicates an instable doping of the LFP material. The electrolyte decomposition products are similar on the electrodes aged at 55°C and -20°C, but a higher amount of oxygenated species was found at the cathodes aged at -20°C.

The results confirm that LLI, LAM_{PE} and Fe dissolution are the main factors for the degradation of LFP cells. However, new insights are presented, among others the reduction of the electrochemical activity and generation of inactive phases by t-ESM measurements, the depth of discharge dependency of Fe dissolution and the observation of vanadium dissolution from LFP cathodes. A straight-forward tool for the evaluation of the remaining capacity and lifetime is presented and the results assist in the proper choice of the cycling range of commercial LFP cells.

9 Outlook

The ESM technique is a powerful tool for the analysis of degradation mechanisms of Li-ion battery materials. Side reactions and other effects and mechanisms can influence the signal generation, which makes it difficult to analyse and prone to artefacts. So far, the measurements are performed post-mortem and only reflect a static state of the battery material. Even more information could be extracted with a technique, which could analyse the degradation mechanism during operation, so in-operando, of the battery. However, due to side reactions with liquid electrolytes and other electrical influences during the measurements, in-operando ESM measurements are so far not feasible, but offer potential for further improvements.

The ICA and DVA analysis is a straightforward technique to amplify changes of the voltage response of the battery to the current load and link features to degradation mechanisms. However, since several degradation mechanisms are occurring simultaneously and affect each other, the direct extraction of degradation mechanisms solely by ICA and DVA is until now challenging. Especially the degradation mechanisms of the cathode and anode are difficult to separate. Therefore, the insertion of a reference electrode into a commercial LFP cell with subsequent ageing could deliver useful information in the separation of the degradation mechanisms, which are observed with ICA and DVA. Nevertheless, combining ICA and DVA with for example modelling of battery cells using equivalent circuit models (ECM), as it is already done by Dubarry et al. [254], offers the possibility to efficiently estimate the SOH of battery cells.

10 References

(1) Liu, C.; Neale, Z. G.; Cao, G. Understanding Electrochemical Potentials of Cathode Materials in Rechargeable Batteries. *Mater. Today* **2016**, *19* (2), 109–123.

(2) *Handbook of Batteries*, 3rd ed.; Linden, D., Reddy, T. B., Eds.; McGraw-Hill handbooks; McGraw-Hill: New York, 2002.

(3) Tarascon, J.-M.; Armand, M. Issues and Challenges Facing Rechargeable Lithium Batteries. *Nature* **2001**, *414*, 359.

(4) Goriparti, S.; Miele, E.; De Angelis, F.; Di Fabrizio, E.; Proietti Zaccaria, R.; Capiglia, C. Review on Recent Progress of Nanostructured Anode Materials for Li-Ion Batteries. *J. Power Sources* **2014**, *257*, 421–443. https://doi.org/10.1016/j.jpowsour.2013.11.103.

(5) Padhi, A. _ K.; Nanjundaswamy, K. S.; Goodenough, J. B. D. Phospho-Olivines as Positive-Electrode Materials for Rechargeable Lithium Batteries. *J. Electrochem. Soc.* **1997**, *144* (4), 1188–1194.

(6) Knauth, P. Inorganic Solid Li Ion Conductors: An Overview. *Solid State Ion.* **2009**, *180* (14–16), 911–916. https://doi.org/10.1016/j.ssi.2009.03.022.

(7) Goodenough, J. B.; Singh, P. Review—Solid Electrolytes in Rechargeable Electrochemical Cells. *J. Electrochem. Soc.* **2015**, *162* (14), A2387–A2392.

(8) Li, J.; Ma, C.; Chi, M.; Liang, C.; Dudney, N. J. Solid Electrolyte: The Key for High-Voltage Lithium Batteries. *Adv. Energy Mater.* **2015**, *5* (4), 1401408. https://doi.org/10.1002/aenm.201401408.

(9) Thackeray, M. An Unexpected Conductor. *Nat. Mater.* **2002**, *1* (2), 81–82. https://doi.org/10.1038/nmat736.

(10) Hahn, M.; Buqa, H.; Ruch, P. W.; Goers, D.; Spahr, M. E.; Ufheil, J.; Novák, P.; Kötz, R. A Dilatometric Study of Lithium Intercalation into Powder-Type Graphite Electrodes. *Electrochem. Solid-State Lett.* **2008**, *11* (9), A151–A154. https://doi.org/10.1149/1.2940573.

(11) Sethuraman, V. A.; Hardwick, L. J.; Srinivasan, V.; Kostecki, R. Surface Structural Disordering in Graphite upon Lithium Intercalation/Deintercalation. *J. Power Sources* **2010**, *195* (11), 3655–3660. https://doi.org/10.1016/j.jpowsour.2009.12.034.

(12) Atkins, P. W.; De Paula, J. *Atkins' Physical Chemistry*; W.H. Freeman: New York, 2006.

(13) Goodenough, J. B.; Park, K.-S. The Li-Ion Rechargeable Battery: A Perspective. *J. Am. Chem. Soc.* **2013**, *135* (4), 1167–1176. https://doi.org/10.1021/ja3091438.

(14) Yuan, L.-X.; Wang, Z.-H.; Zhang, W.-X.; Hu, X.-L.; Chen, J.-T.; Huang, Y.-H.; Goodenough, J. B. Development and Challenges of $LiFePO_4$ Cathode Material for Lithium-Ion Batteries. *Energy Env. Sci* **2011**, *4* (2), 269–284. https://doi.org/10.1039/C0EE00029A.

(15) Bard, A. J.; Faulkner, L. R. *Electrochemical Methods: Fundamentals and Applications*, 2nd ed.; Wiley: New York, 2001.

(16) Zhang, X.; Shyy, W.; Marie Sastry, A. Numerical Simulation of Intercalation-Induced Stress in Li-Ion Battery Electrode Particles. *J. Electrochem. Soc.* **2007**, *154* (10), A910. https://doi.org/10.1149/1.2759840.

(17) Wang, W. L.; Lee, S.; Chen, J. R. Effect of Chemical Stress on Diffusion in a Hollow Cylinder. *J. Appl. Phys.* **2002**, *91* (12), 9584. https://doi.org/10.1063/1.1477624.

(18) Latz, A.; Zausch, J. Thermodynamic Consistent Transport Theory of Li-Ion Batteries. *J. Power Sources* **2011**, *196* (6), 3296–3302. https://doi.org/10.1016/j.jpowsour.2010.11.088.

(19) García, R. E.; Chiang, Y.-M.; Craig Carter, W.; Limthongkul, P.; Bishop, C. M. Microstructural Modeling and Design of Rechargeable Lithium-Ion Batteries. *J. Electrochem. Soc.* **2005**, *152* (1), A255. https://doi.org/10.1149/1.1836132.

(20) Chung, D.-W.; Balke, N.; Kalinin, S. V.; García, R. E. Virtual Electrochemical Strain Microscopy of Polycrystalline LiCoO2 Films. *J. Electrochem. Soc.* **2011**, *158* (10), A1083–A1089.

(21) Amanieu, H.-Y.; Thai, H. N. M.; Luchkin, S. Yu.; Rosato, D.; Lupascu, D. C.; Keip, M.-A.; Schröder, J.; Kholkin, A. L. Electrochemical Strain Microscopy Time Spectroscopy: Model and Experiment on LiMn2O4. *J. Appl. Phys.* **2015**, *118* (5), 055101. https://doi.org/10.1063/1.4927747.

(22) Vetter, J.; Novák, P.; Wagner, M. R.; Veit, C.; Möller, K.-C.; Besenhard, J. O.; Winter, M.; Wohlfahrt-Mehrens, M.; Vogler, C.; Hammouche, A. Ageing Mechanisms in Lithium-Ion Batteries. *J. Power Sources* **2005**, *147* (1–2), 269–281. https://doi.org/10.1016/j.jpowsour.2005.01.006.

(23) Xu, K. Nonaqueous Liquid Electrolytes for Lithium-Based Rechargeable Batteries. *ChemInform* **2004**, *35* (50). https://doi.org/10.1002/chin.200450271.

(24) Leroy, S.; Blanchard, F.; Dedryvère, R.; Martinez, H.; Carré, B.; Lemordant, D.; Gonbeau, D. Surface Film Formation on a Graphite Electrode in Li-Ion Batteries: AFM and XPS Study. *Surf. Interface Anal.* **2005**, *37* (10), 773–781. https://doi.org/10.1002/sia.2072.

(25) Barré, A.; Deguilhem, B.; Grolleau, S.; Gérard, M.; Suard, F.; Riu, D. A Review on Lithium-Ion Battery Ageing Mechanisms and Estimations for Automotive Applications. *J. Power Sources* **2013**, *241*, 680–689. https://doi.org/10.1016/j.jpowsour.2013.05.040.

(26) Aurbach, D.; Koltypin, M.; Teller, H. In Situ AFM Imaging of Surface Phenomena on Composite Graphite Electrodes during Lithium Insertion. *Langmuir* **2002**, *18* (23), 9000–9009. https://doi.org/10.1021/la020306e.

(27) Channagiri, S. A.; Nagpure, S. C.; Babu, S. S.; Noble, G. J.; Hart, R. T. Porosity and Phase Fraction Evolution with Aging in Lithium Iron Phosphate Battery Cathodes. *J. Power Sources* **2013**, *243*, 750–757. https://doi.org/10.1016/j.jpowsour.2013.06.023.

(28) Ramdon, S.; Bhushan, B.; Nagpure, S. C. In Situ Electrochemical Studies of Lithium-Ion Battery Cathodes Using Atomic Force Microscopy. *J. Power Sources* **2014**, *249*, 373–384. https://doi.org/10.1016/j.jpowsour.2013.10.099.

(29) Abraham, D. P.; Knuth, J. L.; Dees, D. W.; Bloom, I.; Christophersen, J. P. Performance Degradation of High-Power Lithium-Ion Cells—Electrochemistry of Harvested Electrodes. *J. Power Sources* **2007**, *170* (2), 465–475. https://doi.org/10.1016/j.jpowsour.2007.03.071.

(30) Schuster, S. F.; Bach, T.; Fleder, E.; Müller, J.; Brand, M.; Sextl, G.; Jossen, A. Nonlinear Aging Characteristics of Lithium-Ion Cells under Different Operational Conditions. *J. Energy Storage* **2015**, *1*, 44–53. https://doi.org/10.1016/j.est.2015.05.003.

(31) Illig, J.; Schmidt, J. P.; Weiss, M.; Weber, A.; Ivers-Tiffée, E. Understanding the Impedance Spectrum of 18650 LiFePO4-Cells. *J. Power Sources* **2013**, *239*, 670–679. https://doi.org/10.1016/j.jpowsour.2012.12.020.

(32) Broussely, M.; Biensan, Ph.; Bonhomme, F.; Blanchard, Ph.; Herreyre, S.; Nechev, K.; Staniewicz, R. J. Main Aging Mechanisms in Li Ion Batteries. *J. Power Sources* **2005**, *146* (1–2), 90–96. https://doi.org/10.1016/j.jpowsour.2005.03.172.

(33) Ratke, L.; Voorhees, P. W. *Growth and Coarsening: Ostwald Ripening in Material Processing*; 2002; Vol. Springer.

(34) Cai, L.; An, K.; Feng, Z.; Liang, C.; Harris, S. J. In-Situ Observation of Inhomogeneous Degradation in Large Format Li-Ion Cells by Neutron Diffraction. *J. Power Sources* **2013**, *236*, 163–168. https://doi.org/10.1016/j.jpowsour.2013.02.066.

(35) Dubarry, M.; Liaw, B. Y.; Chen, M.-S.; Chyan, S.-S.; Han, K.-C.; Sie, W.-T.; Wu, S.-H. Identifying Battery Aging Mechanisms in Large Format Li Ion Cells. *J. Power Sources* **2011**, *196* (7), 3420–3425. https://doi.org/10.1016/j.jpowsour.2010.07.029.

(36) Shim, J.; Striebel, K. A. Characterization of High-Power Lithium-Ion Cells during Constant Current Cycling. *J. Power Sources* **2003**, *122* (2), 188–194. https://doi.org/10.1016/S0378-7753(03)00351-3.

(37) Ramdon, S.; Bhushan, B. High Resolution Morphology and Electrical Characterization of Aged Li-Ion Battery Cathode. *J. Colloid Interface Sci.* **2012**, *380* (1), 187–191. https://doi.org/10.1016/j.jcis.2012.05.026.

(38) Nagpure, S. C.; Babu, S. S.; Bhushan, B.; Kumar, A.; Mishra, R.; Windl, W.; Kovarik, L.; Mills, M. Local Electronic Structure of LiFePO4 Nanoparticles in Aged Li-Ion Batteries. *Acta Mater.* **2011**, *59* (18), 6917–6926. https://doi.org/10.1016/j.actamat.2011.07.043.

(39) Maher, K.; Yazami, R. A Study of Lithium Ion Batteries Cycle Aging by Thermodynamics Techniques. *J. Power Sources* **2014**, *247*, 527–533. https://doi.org/10.1016/j.jpowsour.2013.08.053.

(40) Steiger, J. Mechanisms of Dendrite Growth in Lithium Metal Batteries, Karlsruhe, Karlsruher Institut für Technologie (KIT), Diss., 2015, 2015.

(41) Edström, K.; Gustafsson, T.; Thomas, J. O. The Cathode–Electrolyte Interface in the Li-Ion Battery. *Electrochimica Acta* **2004**, *50* (2–3), 397–403. https://doi.org/10.1016/j.electacta.2004.03.049.

(42) Aurbach, D.; Markovsky, B.; Levi, M. D.; Levi, E.; Schechter, A.; Moshkovich, M.; Cohen, Y. New Insights into the Interactions between Electrode Materials and Electrolyte Solutions for Advanced Nonaqueous Batteries. *J. Power Sources* **1999**, *81*, 95–111.

(43) Bullard, J. Structural Evolution of the MoO3(010) Surface during Lithium Intercalation. *Solid State Ion.* **2003**, *160* (3–4), 335–349. https://doi.org/10.1016/S0167-2738(03)00189-9.

(44) Clémençon, A.; Appapillai, A. T.; Kumar, S.; Shao-Horn, Y. Atomic Force Microscopy Studies of Surface and Dimensional Changes in LixCoO2 Crystals during Lithium De-Intercalation. *Electrochimica Acta* **2007**, *52* (13), 4572–4580. https://doi.org/10.1016/j.electacta.2006.12.076.

(45) Kubiak, P.; Wolfahrt-Mehrens, M.; Edström, K.; Morcrette, M. Review on Ageing Mechanisms of Different Li-Ion Batteries for Automotive Applications. 2011.

(46) Kim, J.-H.; Pieczonka, N. P. W.; Li, Z.; Wu, Y.; Harris, S.; Powell, B. R. Understanding the Capacity Fading Mechanism in LiNi0.5Mn1.5O4/Graphite Li-Ion Batteries. *Electrochimica Acta* **2013**, *90*, 556–562. https://doi.org/10.1016/j.electacta.2012.12.069.

(47) Zhang, Y.; Wang, C.-Y.; Tang, X. Cycling Degradation of an Automotive LiFePO4 Lithium-Ion Battery. *J. Power Sources* **2011**, *196* (3), 1513–1520. https://doi.org/10.1016/j.jpowsour.2010.08.070.

(48) Han, X.; Ouyang, M.; Lu, L.; Li, J.; Zheng, Y.; Li, Z. A Comparative Study of Commercial Lithium Ion Battery Cycle Life in Electrical Vehicle: Aging Mechanism Identification. *J. Power Sources* **2014**, *251*, 38–54. https://doi.org/10.1016/j.jpowsour.2013.11.029.

(49) Koltypin, M.; Cohen, Y. S.; Markovsky, B.; Cohen, Y.; Aurbach, D. The Study of Lithium Insertion–Deinsertion Processes into Composite Graphite Electrodes by in Situ

Atomic Force Microscopy (AFM). *Electrochem. Commun.* **2002**, *4* (1), 17–23. https://doi.org/10.1016/S1388-2481(01)00264-8.

(50) Aurbach, D. A Short Review of Failure Mechanisms of Lithium Metal and Lithiated Graphite Anodes in Liquid Electrolyte Solutions. *Solid State Ion.* **2002**, *148* (3–4), 405–416. https://doi.org/10.1016/S0167-2738(02)00080-2.

(51) Herb, F. Alterungsmechanismen in Lithium-Ionen-Batterien Und PEM-Brennstoffzellen Und Deren Einfluss Auf Die Eigenschaften von Daraus Bestehenden Hybrid-Systemen, Universität Ulm, 2010.

(52) Peabody, C.; Arnold, C. B. The Role of Mechanically Induced Separator Creep in Lithium-Ion Battery Capacity Fade. *J. Power Sources* **2011**, *196* (19), 8147–8153. https://doi.org/10.1016/j.jpowsour.2011.05.023.

(53) Cannarella, J.; Arnold, C. B. Ion Transport Restriction in Mechanically Strained Separator Membranes. *J. Power Sources* **2013**, *226*, 149–155. https://doi.org/10.1016/j.jpowsour.2012.10.093.

(54) Gor, G. Y.; Cannarella, J.; Leng, C. Z.; Vishnyakov, A.; Arnold, C. B. Swelling and Softening of Lithium-Ion Battery Separators in Electrolyte Solvents. *J. Power Sources* **2015**, *294*, 167–172. https://doi.org/10.1016/j.jpowsour.2015.06.028.

(55) Steinhauer, M.; Stich, M.; Kurniawan, M.; Seidlhofer, B.-K.; Trapp, M.; Bund, A.; Wagner, N.; Friedrich, K. A. In Situ Studies of Solid Electrolyte Interphase (SEI) Formation on Crystalline Carbon Surfaces by Neutron Reflectometry and Atomic Force Microscopy. *ACS Appl. Mater. Interfaces* **2017**, *9* (41), 35794–35801. https://doi.org/10.1021/acsami.7b09181.

(56) Käbitz, S.; Gerschler, J. B.; Ecker, M.; Yurdagel, Y.; Emmermacher, B.; André, D.; Mitsch, T.; Sauer, D. U. Cycle and Calendar Life Study of a Graphite|LiNi1/3Mn1/3Co1/3O2 Li-Ion High Energy System. Part A: Full Cell Characterization. *J. Power Sources* **2013**, *239*, 572–583. https://doi.org/10.1016/j.jpowsour.2013.03.045.

(57) Koltypin, M.; Aurbach, D.; Nazar, L.; Ellis, B. More on the Performance of LiFePO4 Electrodes—The Effect of Synthesis Route, Solution Composition, Aging, and Temperature. *J. Power Sources* **2007**, *174* (2), 1241–1250. https://doi.org/10.1016/j.jpowsour.2007.06.045.

(58) Abraham, D. P.; Liu, J.; Chen, C. H.; Hyung, Y. E.; Stoll, M.; Elsen, N.; MacLaren, S.; Twesten, R.; Haasch, R.; Sammann, E.; Petrov, I.; Amine, K.; Henriksen, G. Diagnosis of Power Fade Mechanisms in High-Power Lithium-Ion Cells. *J. Power Sources* **2003**, *119–121*, 511–516. https://doi.org/10.1016/S0378-7753(03)00275-1.

(59) Shim, J. Electrochemical Analysis for Cycle Performance and Capacity Fading of a Lithium-Ion Battery Cycled at Elevated Temperature. *J. Power Sources* **2002**, *112* (1), 222–230. https://doi.org/10.1016/S0378-7753(02)00363-4.

(60) Petzl, M. Zerstörungsfreie Charakterisierung von Lithium-Plating in Lithium-Ionen-Batterien. Dissertation, Universität Ulm, Ulm, 2015.

(61) Hausbrand, R.; Cherkashinin, G.; Ehrenberg, H.; Gröting, M.; Albe, K.; Hess, C.; Jaegermann, W. Fundamental Degradation Mechanisms of Layered Oxide Li-Ion Battery Cathode Materials: Methodology, Insights and Novel Approaches. *Mater. Sci. Eng. B* **2015**, *192*, 3–25. https://doi.org/10.1016/j.mseb.2014.11.014.

(62) Simolka, M.; Heim, C.; Friedrich, K. A.; Hiesgen, R. Visualization of Local Ionic Concentration and Diffusion Constants Using a Tailored Electrochemical Strain Microscopy Method. *J. Electrochem. Soc.* **2019**, *166* (3), A5496–A5502. https://doi.org/10.1149/2.0711903jes.

(63) Simolka, M.; Kaess, H.; Friedrich, K. A. Comparison of Fresh and Aged Lithium Iron Phosphate Cathodes Using a Tailored Electrochemical Strain Microscopy Technique. *Beilstein J. Nanotechnol.* **2020**, *11*, 583–596. https://doi.org/10.3762/bjnano.11.46.

(64) Rohrer, H.; Binnig, G. Scanning Tunneling Microscopy. **1983**. https://doi.org/10.5169/seals-115309.
(65) Voigtländer, B. *Scanning Probe Microscopy*; Springer Berlin Heidelberg: New York, NY, 2015.
(66) Binnig, G.; Quate, C. F.; Gerber, C. Atomic Force Microscope. *Phys. Rev. Lett. 56* (9), 5.
(67) Pittenger, B.; Erina, N.; Su, C. Application Note #128 Quantitative Mechanical Property Mapping at the Nanoscale with PeakForce QNM.
(68) Asylum Research. Contact Resonance Viscoelastic Mapping Mode. 4.
(69) Asylum Research. AM-FM Viscoelastic Mapping Mode. 4.
(70) *Principles and Practice of Variable Pressure/Environmental Scanning Electron Microscopy (VP-ESEM)*, 1st ed.; John Wiley & Sons, Ltd, 2008. https://doi.org/10.1002/9780470758731.
(71) Simolka, M.; Heger, J.-F.; Kaess, H.; Friedrich, K. A. Influence of Cycling Profile, Depth of Discharge and Temperature on Commercial LFP/C Cell Aging – Post-Mortem Material Analysis of Structure, Morphology and Chemical Composition. *J. Appl. Electrochem.* **under review**.
(72) *Impedance Spectroscopy: Theory, Experiment, and Applications*, 2nd ed.; Barsoukov, E., Macdonald, J. R., Eds.; Wiley-Interscience: Hoboken, N.J, 2005.
(73) Bloom, I.; Jansen, A. N.; Abraham, D. P.; Knuth, J.; Jones, S. A.; Battaglia, V. S.; Henriksen, G. L. Differential Voltage Analyses of High-Power, Lithium-Ion Cells. *J. Power Sources* **2005**, *139* (1–2), 295–303. https://doi.org/10.1016/j.jpowsour.2004.07.021.
(74) Tillement, O.; Quarton, M. Theoretical Study of Ordering Effects During Electrochemical Insertion. *J. Electrochem. Soc.* **1993**, *140* (7), 1870–1876. https://doi.org/10.1149/1.2220731.
(75) Balewski, L.; Brenet, J. P. A New Method for the Study of the Electrochemical Reactivity of Manganese Dioxide. *Electrochem Technol* **1967**, *5*, 527–531.
(76) Thompson, A. H. Electrochemical Potential Spectroscopy: A New Electrochemical Measurement. *J. Electrochem. Soc.* **1979**, *126* (4), 608–616.
(77) Dahn, J. R. Phase Diagram of LiC6. *Phys Rev B* **1991**, *44* (17), 9170–9177. https://doi.org/10.1103/PhysRevB.44.9170.
(78) Bloom, I.; Jones, S. A.; Polzin, E. G.; Battaglia, V. S.; Henriksen, G. L.; Motloch, C. G.; Wright, R. B.; Jungst, R. G.; Case, H. L.; Doughty, D. H. Mechanisms of Impedance Rise in High-Power, Lithium-Ion Cells. *J. Power Sources* **2002**, *111* (1), 152–159.
(79) Bloom, I.; Cole, B. W.; Sohn, J. J.; Jones, S. A.; Polzin, E. G.; Battaglia, V. S.; Henriksen, G. L.; Motloch, C.; Richardson, R.; Unkelhaeuser, T.; others. An Accelerated Calendar and Cycle Life Study of Li-Ion Cells. *J. Power Sources* **2001**, *101* (2), 238–247.
(80) Bloom, I.; Walker, L. K.; Basco, J. K.; Abraham, D. P.; Christophersen, J. P.; Ho, C. D. Differential Voltage Analyses of High-Power Lithium-Ion Cells. 4. Cells Containing NMC. *J. Power Sources* **2010**, *195* (3), 877–882. https://doi.org/10.1016/j.jpowsour.2009.08.019.
(81) Dubarry, M.; Truchot, C.; Liaw, B. Y. Synthesize Battery Degradation Modes via a Diagnostic and Prognostic Model. *J. Power Sources* **2012**, *219*, 204–216. https://doi.org/10.1016/j.jpowsour.2012.07.016.
(82) Dubarry, M.; Svoboda, V.; Hwu, R.; Yann Liaw, B. Incremental Capacity Analysis and Close-to-Equilibrium OCV Measurements to Quantify Capacity Fade in Commercial Rechargeable Lithium Batteries. *Electrochem. Solid-State Lett.* **2006**, *9* (10), A454. https://doi.org/10.1149/1.2221767.

(83) Dubarry, M.; Liaw, B. Y. Identify Capacity Fading Mechanism in a Commercial LiFePO4 Cell. *J. Power Sources* **2009**, *194* (1), 541–549. https://doi.org/10.1016/j.jpowsour.2009.05.036.

(84) Dubarry, M.; Truchot, C.; Liaw, B. Y. Cell Degradation in Commercial LiFePO4 Cells with High-Power and High-Energy Designs. *J. Power Sources* **2014**, *258*, 408–419. https://doi.org/10.1016/j.jpowsour.2014.02.052.

(85) Jiang, Y.; Jiang, J.; Zhang, C.; Zhang, W.; Gao, Y.; Guo, Q. Recognition of Battery Aging Variations for LiFePO 4 Batteries in 2nd Use Applications Combining Incremental Capacity Analysis and Statistical Approaches. *J. Power Sources* **2017**, *360*, 180–188. https://doi.org/10.1016/j.jpowsour.2017.06.007.

(86) Li, Y.; Abdel-Monem, M.; Gopalakrishnan, R.; Berecibar, M.; Nanini-Maury, E.; Omar, N.; van den Bossche, P.; Van Mierlo, J. A Quick On-Line State of Health Estimation Method for Li-Ion Battery with Incremental Capacity Curves Processed by Gaussian Filter. *J. Power Sources* **2018**, *373*, 40–53. https://doi.org/10.1016/j.jpowsour.2017.10.092.

(87) Weng, C.; Sun, J.; Peng, H. An Open-Circuit-Voltage Model of Lithium-Ion Batteries for Effective Incremental Capacity Analysis. In *ASME 2013 Dynamic Systems and Control Conference*; American Society of Mechanical Engineers, 2013; p V001T05A002-V001T05A002.

(88) Weng, C.; Feng, X.; Sun, J.; Peng, H. State-of-Health Monitoring of Lithium-Ion Battery Modules and Packs via Incremental Capacity Peak Tracking. *Appl. Energy* **2016**, *180*, 360–368. https://doi.org/10.1016/j.apenergy.2016.07.126.

(89) Wang, L.; Pan, C.; Liu, L.; Cheng, Y.; Zhao, X. On-Board State of Health Estimation of LiFePO4 Battery Pack through Differential Voltage Analysis. *Appl. Energy* **2016**, *168*, 465–472. https://doi.org/10.1016/j.apenergy.2016.01.125.

(90) Weng, C.; Cui, Y.; Sun, J.; Peng, H. On-Board State of Health Monitoring of Lithium-Ion Batteries Using Incremental Capacity Analysis with Support Vector Regression. *J. Power Sources* **2013**, *235*, 36–44. https://doi.org/10.1016/j.jpowsour.2013.02.012.

(91) Safari, M.; Delacourt, C. Aging of a Commercial Graphite/LiFePO4 Cell. *J. Electrochem. Soc.* **2011**, *158* (10), A1123. https://doi.org/10.1149/1.3614529.

(92) Pastor-Fernández, C.; Uddin, K.; Chouchelamane, G. H.; Widanage, W. D.; Marco, J. A Comparison between Electrochemical Impedance Spectroscopy and Incremental Capacity-Differential Voltage as Li-Ion Diagnostic Techniques to Identify and Quantify the Effects of Degradation Modes within Battery Management Systems. *J. Power Sources* **2017**, *360*, 301–318. https://doi.org/10.1016/j.jpowsour.2017.03.042.

(93) Simolka, M.; Heger, J.-F.; Traub, N.; Kaess, H.; Friedrich, K. A. Influence of Cycling Profile, Depth of Discharge and Temperature on Commercial LFP/C Cell Ageing – Cell Level Analysis with ICA, DVA and OCV Measurements. *J. Electrochem. Soc.* **in revision**.

(94) Balke, N.; Jesse, S.; Morozovska, A. N.; Eliseev, E.; Chung, D. W.; Kim, Y.; Adamczyk, L.; García, R. E.; Dudney, N.; Kalinin, S. V. Nanoscale Mapping of Ion Diffusion in a Lithium-Ion Battery Cathode. *Nat. Nanotechnol.* **2010**, *5* (10), 749–754. https://doi.org/10.1038/nnano.2010.174.

(95) Jesse, S.; Balke, N.; Eliseev, E.; Tselev, A.; Dudney, N. J.; Morozovska, A. N.; Kalinin, S. V. Direct Mapping of Ionic Transport in a Si Anode on the Nanoscale: Time Domain Electrochemical Strain Spectroscopy Study. *ACS Nano* **2011**, *5* (12), 9682–9695. https://doi.org/10.1021/nn203141g.

(96) Chen, Q. N.; Adler, S. B.; Li, J. Imaging Space Charge Regions in Sm-Doped Ceria Using Electrochemical Strain Microscopy. *Appl. Phys. Lett.* **2014**, *105* (20), 201602. https://doi.org/10.1063/1.4901102.

(97) Chen, Q. N.; Ou, Y.; Ma, F.; Li, J. Mechanisms of Electromechanical Coupling in Strain Based Scanning Probe Microscopy. *Appl. Phys. Lett.* **2014**, *104* (24), 242907. https://doi.org/10.1063/1.4884422.

(98) Nataly Chen, Q.; Liu, Y.; Liu, Y.; Xie, S.; Cao, G.; Li, J. Delineating Local Electromigration for Nanoscale Probing of Lithium Ion Intercalation and Extraction by Electrochemical Strain Microscopy. *Appl. Phys. Lett.* **2012**, *101* (6), 063901. https://doi.org/10.1063/1.4742933.

(99) Li, J.; Li, J.-F.; Yu, Q.; Chen, Q. N.; Xie, S. Strain-Based Scanning Probe Microscopies for Functional Materials, Biological Structures, and Electrochemical Systems. *J. Materiomics* **2015**, *1* (1), 3–21. https://doi.org/10.1016/j.jmat.2015.03.001.

(100) Balke, N.; Eliseev, E. A.; Jesse, S.; Kalnaus, S.; Daniel, C.; Dudney, N. J.; Morozovska, A. N.; Kalinin, S. V. Three-Dimensional Vector Electrochemical Strain Microscopy. *J. Appl. Phys.* **2012**, *112* (5), 052020. https://doi.org/10.1063/1.4746085.

(101) Balke, N.; Kalnaus, S.; Dudney, N. J.; Daniel, C.; Jesse, S.; Kalinin, S. V. Local Detection of Activation Energy for Ionic Transport in Lithium Cobalt Oxide. *Nano Lett.* **2012**, *12* (7), 3399–3403. https://doi.org/10.1021/nl300219g.

(102) Jesse, S.; Kumar, A.; Arruda, T. M.; Kim, Y.; Kalinin, S. V.; Ciucci, F. Electrochemical Strain Microscopy: Probing Ionic and Electrochemical Phenomena in Solids at the Nanometer Level. *MRS Bull.* **2012**, *37* (07), 651–658. https://doi.org/10.1557/mrs.2012.144.

(103) Kalinin, S. V.; Morozovska, A. N. Electrochemical Strain Microscopy of Local Electrochemical Processes in Solids: Mechanism of Imaging and Spectroscopy in the Diffusion Limit. *J. Electroceramics* **2014**, *32* (1), 51–59. https://doi.org/10.1007/s10832-013-9819-7.

(104) Tselev, A.; Morozovska, A. N.; Udod, A.; Eliseev, E. A.; Kalinin, S. V. Self-Consistent Modeling of Electrochemical Strain Microscopy of Solid Electrolytes. *Nanotechnology* **2014**, *25* (44), 445701. https://doi.org/10.1088/0957-4484/25/44/445701.

(105) Zhang, X.; Sastry, A. M.; Shyy, W. Intercalation-Induced Stress and Heat Generation within Single Lithium-Ion Battery Cathode Particles. *J. Electrochem. Soc.* **2008**, *155* (7), A542. https://doi.org/10.1149/1.2926617.

(106) Dal, H.; Miehe, C. Computational Electro-Chemo-Mechanics of Lithium-Ion Battery Electrodes at Finite Strains. *Comput. Mech.* **2015**, *55* (2), 303–325. https://doi.org/10.1007/s00466-014-1102-5.

(107) Morozovska, A. N.; Eliseev, E. A.; Balke, N.; Kalinin, S. V. Local Probing of Ionic Diffusion by Electrochemical Strain Microscopy: Spatial Resolution and Signal Formation Mechanisms. *J. Appl. Phys.* **2010**, *108* (5), 053712. https://doi.org/10.1063/1.3460637.

(108) Luchkin, S. Yu.; Romanyuk, K.; Ivanov, M.; Kholkin, A. L. Li Transport in Fresh and Aged LiMn2O4 Cathodes via Electrochemical Strain Microscopy. *J. Appl. Phys.* **2015**, *118* (7), 072016. https://doi.org/10.1063/1.4927816.

(109) Schön, N.; Gunduz, D. C.; Yu, S.; Tempel, H.; Schierholz, R.; Hausen, F. Correlative Electrochemical Strain and Scanning Electron Microscopy for Local Characterization of the Solid State Electrolyte $Li_{1.3}Al_{0.3}Ti_{1.7}(PO_4)_3$. *Beilstein J. Nanotechnol.* **2018**, *9*, 1564–1572. https://doi.org/10.3762/bjnano.9.148.

(110) Guo, S.; Jesse, S.; Kalnaus, S.; Balke, N.; Daniel, C.; Kalinin, S. V. Direct Mapping of Ion Diffusion Times on LiCoO2 Surfaces with Nanometer Resolution. *J. Electrochem. Soc.* **2011**, *158* (8), A982–A990.

(111) *Computational Materials Engineering: An Introduction to Microstructure Evolution*; Janssens, K. G. F., Ed.; ScienceDirect; Academic Press: Amsterdam ; Heidelberg [u.a.], 2007.

(112) Shewmon, P. G. *Diffusion in Solids*, 2.ed.; Minerals, Metals & Materials Society: Warrendale, Pa, 1989.
(113) Morozovska, A. N.; Eliseev, E. A.; Kalinin, S. V. Electromechanical Probing of Ionic Currents in Energy Storage Materials. *Appl. Phys. Lett.* **2010**, *96* (22), 222906. https://doi.org/10.1063/1.3446838.
(114) Morozovska, A. N.; Eliseev, E. A.; Kalinin, S. V. Electrochemical Strain Microscopy with Blocking Electrodes: The Role of Electromigration and Diffusion. *J. Appl. Phys.* **2012**, *111* (1), 014114. https://doi.org/10.1063/1.3675508.
(115) Lushta, V.; Bradler, S.; Roling, B.; Schirmeisen, A. Correlation between Drive Amplitude and Resonance Frequency in Electrochemical Strain Microscopy: Influence of Electrostatic Forces. *J. Appl. Phys.* **2017**, *121* (22), 224302. https://doi.org/10.1063/1.4984831.
(116) Vegard, L. Die Konstitution Der Mischkristalle Und Die Raumfüllung Der Atome. *Z. Für Phys. Hadrons Nucl.* **1921**, *5* (1), 17–26.
(117) Denton, A. R.; Ashcroft, N. W. Vegard's Law. *Phys. Rev. A* **1991**, *43* (6), 3161.
(118) Tilley, R. J. D. *Understanding Solids: The Science of Materials*; John Wiley & Sons, Ltd, 2004.
(119) Kuo, Y.-K.; Liou, B.-T.; Yen, S.-H.; Chu, H.-Y. Vegard's Law Deviation in Lattice Constant and Band Gap Bowing Parameter of Zincblende InxGa1−xN. *Opt. Commun.* **2004**, *237* (4–6), 363–369. https://doi.org/10.1016/j.optcom.2004.04.012.
(120) Zhang, L.; Li, S. Empirical Atom Model of Vegard's Law. *Phys. B Condens. Matter* **2014**, *434*, 38–43. https://doi.org/10.1016/j.physb.2013.10.066.
(121) Zhou, D.; Usher, B. F. Deviation of the AlGaAs Lattice Constant from Vegard's Law. *J. Phys. Appl. Phys.* **2001**, *34* (10), 1461–1465. https://doi.org/10.1088/0022-3727/34/10/304.
(122) Zubko, P.; Catalan, G.; Tagantsev, A. K. Flexoelectric Effect in Solids. *Annu. Rev. Mater. Res.* **2013**, *43* (1), 387–421. https://doi.org/10.1146/annurev-matsci-071312-121634.
(123) Ma, W. A Study of Flexoelectric Coupling Associated Internal Electric Field and Stress in Thin Film Ferroelectrics. *Phys. Status Solidi B* **2008**, *245* (4), 761–768. https://doi.org/10.1002/pssb.200743514.
(124) Sundar, V.; Newnham, R. E. Electrostriction and Polarization. *Ferroelectrics* **1992**, *135* (1), 431–446. https://doi.org/10.1080/00150199208230043.
(125) Morozovska, A. N.; Eliseev, E. A.; Tagantsev, A. K.; Bravina, S. L.; Chen, L.-Q.; Kalinin, S. V. Thermodynamics of Electromechanically Coupled Mixed Ionic-Electronic Conductors: Deformation Potential, Vegard Strains, and Flexoelectric Effect. *Phys. Rev. B* **2011**, *83* (19). https://doi.org/10.1103/PhysRevB.83.195313.
(126) Kleinman, L. Deformation Potentials in Silicon. I. Uniaxial Strain. *Phys. Rev.* **1962**, *128* (6), 2614–2621. https://doi.org/10.1103/PhysRev.128.2614.
(127) Fischetti, M. V.; Laux, S. E. Band Structure, Deformation Potentials, and Carrier Mobility in Strained Si, Ge, and SiGe Alloys. *J. Appl. Phys.* **1996**, *80* (4), 2234–2252. https://doi.org/10.1063/1.363052.
(128) Balke, N.; Maksymovych, P.; Jesse, S.; Herklotz, A.; Tselev, A.; Eom, C.-B.; Kravchenko, I. I.; Yu, P.; Kalinin, S. V. Differentiating Ferroelectric and Nonferroelectric Electromechanical Effects with Scanning Probe Microscopy. *ACS Nano* **2015**, *9* (6), 6484–6492. https://doi.org/10.1021/acsnano.5b02227.
(129) Colchero, J.; Gil, A.; Baró, A. M. Resolution Enhancement and Improved Data Interpretation in Electrostatic Force Microscopy. *Phys. Rev. B* **2001**, *64* (24). https://doi.org/10.1103/PhysRevB.64.245403.

(130) Gruverman, A.; Kholkin, A. Nanoscale Ferroelectrics: Processing, Characterization and Future Trends. *Rep. Prog. Phys.* **2006**, *69* (8), 2443–2474. https://doi.org/10.1088/0034-4885/69/8/R04.
(131) Balke, N.; Maksymovych, P.; Jesse, S.; Kravchenko, I. I.; Li, Q.; Kalinin, S. V. Exploring Local Electrostatic Effects with Scanning Probe Microscopy: Implications for Piezoresponse Force Microscopy and Triboelectricity. *ACS Nano* **2014**, *8* (10), 10229–10236. https://doi.org/10.1021/nn505176a.
(132) Nakamura, M.; Yamada, H. 6 Electrostatic Force Microscopy. 9.
(133) Eliseev, E. A.; Morozovska, A. N.; Ievlev, A. V.; Balke, N.; Maksymovych, P.; Tselev, A.; Kalinin, S. V. Electrostrictive and Electrostatic Responses in Contact Mode Voltage Modulated Scanning Probe Microscopies. *Appl. Phys. Lett.* **2014**, *104* (23), 232901. https://doi.org/10.1063/1.4882861.
(134) Balke, N.; Jesse, S.; Yu, P.; Ben Carmichael; Kalinin, S. V.; Tselev, A. Quantification of Surface Displacements and Electromechanical Phenomena via Dynamic Atomic Force Microscopy. *Nanotechnology* **2016**, *27* (42), 425707. https://doi.org/10.1088/0957-4484/27/42/425707.
(135) Islam, M. S.; Driscoll, D. J.; Fisher, C. A. J.; Slater, P. R. Atomic-Scale Investigation of Defects, Dopants, and Lithium Transport in the LiFePO $_4$ Olivine-Type Battery Material. *Chem. Mater.* **2005**, *17* (20), 5085–5092. https://doi.org/10.1021/cm050999v.
(136) Johnson, I. D.; Lübke, M.; Wu, O. Y.; Makwana, N. M.; Smales, G. J.; Islam, H. U.; Dedigama, R. Y.; Gruar, R. I.; Tighe, C. J.; Scanlon, D. O.; Corà, F.; Brett, D. J. L.; Shearing, P. R.; Darr, J. A. Pilot-Scale Continuous Synthesis of a Vanadium-Doped LiFePO4/C Nanocomposite High-Rate Cathodes for Lithium-Ion Batteries. *J. Power Sources* **2016**, *302*, 410–418. https://doi.org/10.1016/j.jpowsour.2015.10.068.
(137) Ansari, M. Z.; Cho, C. An Analytical Model of Joule Heating in Piezoresistive Microcantilevers. *Sensors* **2010**, *10* (11), 9668–9686. https://doi.org/10.3390/s101109668.
(138) Cole, K. D.; Çetin, B. Modeling of Joule Heating and Convective Cooling in a Thick-Walled Micro-Tube. *Int. J. Therm. Sci.* **2017**, *119*, 24–36. https://doi.org/10.1016/j.ijthermalsci.2017.05.010.
(139) Landau, L. D.; Lifshitz, E. M. Theory of Elasticity. **1970**, 177.
(140) Czichos, H.; Skrotzki, B.; Simon, F.-G. *Das Ingenieurwissen: Werkstoffe*; Springer Berlin Heidelberg: Berlin, Heidelberg, 2014. https://doi.org/10.1007/978-3-642-41126-7.
(141) Tsukruk, V. V.; Singamaneni, S. *Scanning Probe Microscopy of Soft Matter: Fundamentals and Practices*; Wiley, 2012.
(142) Chowdhury, F. K.; Pourzand, H.; Tabib-Azar, M. Ni, Cr, Ti, Cu AND Al OVER REPEATED HOT-CONTACT SWITCHING. 4.
(143) De Wolf, P.; Snauwaert, J.; Clarysse, T.; Vandervorst, W.; Hellemans, L. Characterization of a Point-contact on Silicon Using Force Microscopy-supported Resistance Measurements. *Appl. Phys. Lett.* **1995**, *66* (12), 1530–1532. https://doi.org/10.1063/1.113636.
(144) Nanda, J.; Martha, S. K.; Porter, W. D.; Wang, H.; Dudney, N. J.; Radin, M. D.; Siegel, D. J. Thermophysical Properties of LiFePO4 Cathodes with Carbonized Pitch Coatings and Organic Binders: Experiments and First-Principles Modeling. *J. Power Sources* **2014**, *251*, 8–13. https://doi.org/10.1016/j.jpowsour.2013.11.022.
(145) *Ceramic Materials for Energy Applications*; Katoh, Y., Fox, K. M., Lin, H.-T., Belharouak, I., Eds.; John Wiley & Sons, Ltd, 2011.
(146) Arruda, T. M.; Kumar, A.; Kalinin, S. V.; Jesse, S. Mapping Irreversible Electrochemical Processes on the Nanoscale: Ionic Phenomena in Li Ion Conductive

Glass Ceramics. *Nano Lett.* **2011**, *11* (10), 4161–4167. https://doi.org/10.1021/nl202039v.

(147) Arruda, T. M.; Kumar, A.; Jesse, S.; Veith, G. M.; Tselev, A.; Baddorf, A. P.; Balke, N.; Kalinin, S. V. Toward Quantitative Electrochemical Measurements on the Nanoscale by Scanning Probe Microscopy: Environmental and Current Spreading Effects. *ACS Nano* **2013**, *7* (9), 8175–8182. https://doi.org/10.1021/nn4034772.

(148) Lee, S. W.; McDowell, M. T.; Choi, J. W.; Cui, Y. Anomalous Shape Changes of Silicon Nanopillars by Electrochemical Lithiation. *Nano Lett.* **2011**, *11* (7), 3034–3039. https://doi.org/10.1021/nl201787r.

(149) Obrovac, M. N.; Krause, L. J. Reversible Cycling of Crystalline Silicon Powder. *J. Electrochem. Soc.* **2007**, *154* (2), A103. https://doi.org/10.1149/1.2402112.

(150) Nitta, N.; Wu, F.; Lee, J. T.; Yushin, G. Li-Ion Battery Materials: Present and Future. *Mater. Today* **2015**, *18* (5), 252–264.

(151) Qi, Y.; Harris, S. J. In Situ Observation of Strains during Lithiation of a Graphite Electrode. *J. Electrochem. Soc.* **2010**, *157* (6), A741–A747. https://doi.org/10.1149/1.3377130.

(152) Boukamp, B. A.; Lesh, G. C.; Huggins, R. A. All-Solid Lithium Electrodes with Mixed-Conductor Matrix. *J. Electrochem. Soc.* **1981**, *128* (4), 725–729. https://doi.org/10.1149/1.2127495.

(153) Baggetto, L.; Niessen, R. A. H.; Roozeboom, F.; Notten, P. H. L. High Energy Density All-Solid-State Batteries: A Challenging Concept Towards 3D Integration. *Adv. Funct. Mater.* **2008**, *18* (7), 1057–1066. https://doi.org/10.1002/adfm.200701245.

(154) Ozanam, F.; Rosso, M. Silicon as Anode Material for Li-Ion Batteries. *Mater. Sci. Eng. B* **2016**, *213*, 2–11. https://doi.org/10.1016/j.mseb.2016.04.016.

(155) Pharr, M.; Zhao, K.; Wang, X.; Suo, Z.; Vlassak, J. J. Kinetics of Initial Lithiation of Crystalline Silicon Electrodes of Lithium-Ion Batteries. *Nano Lett.* **2012**, *12* (9), 5039–5047. https://doi.org/10.1021/nl302841y.

(156) Garcia, M. E.; Garofalini, S. H. Molecular Dynamics Simulation of the Effect of Crystal Orientation on Lithium-Ion Diffusion at the V 2 O 5 / Li2SiO3 Interface. *J. Electrochem. Soc.* **1999**, *146* (3), 840–849. https://doi.org/10.1149/1.1391690.

(157) Yang, S.; Yan, B.; Li, T.; Zhu, J.; Lu, L.; Zeng, K. In Situ Studies of Lithium-Ion Diffusion in a Lithium-Rich Thin Film Cathode by Scanning Probe Microscopy Techniques. *Phys Chem Chem Phys* **2015**, *17* (34), 22235–22242. https://doi.org/10.1039/C5CP01999K.

(158) Balke, N.; Jesse, S.; Kim, Y.; Adamczyk, L.; Tselev, A.; Ivanov, I. N.; Dudney, N. J.; Kalinin, S. V. Real Space Mapping of Li-Ion Transport in Amorphous Si Anodes with Nanometer Resolution. *Nano Lett.* **2010**, *10* (9), 3420–3425. https://doi.org/10.1021/nl101439x.

(159) Wang, M.; Xiao, X.; Huang, X. Study of Lithium Diffusivity in Amorphous Silicon via Finite Element Analysis. *J. Power Sources* **2016**, *307*, 77–85. https://doi.org/10.1016/j.jpowsour.2015.12.082.

(160) Johari, P.; Qi, Y.; Shenoy, V. B. The Mixing Mechanism during Lithiation of Si Negative Electrode in Li-Ion Batteries: An Ab Initio Molecular Dynamics Study. *Nano Lett.* **2011**, *11* (12), 5494–5500. https://doi.org/10.1021/nl203302d.

(161) Ruffo, R.; Hong, S. S.; Chan, C. K.; Huggins, R. A.; Cui, Y. Impedance Analysis of Silicon Nanowire Lithium Ion Battery Anodes. *J. Phys. Chem. C* **2009**, *113* (26), 11390–11398. https://doi.org/10.1021/jp901594g.

(162) Tritsaris, G. A.; Zhao, K.; Okeke, O. U.; Kaxiras, E. Diffusion of Lithium in Bulk Amorphous Silicon: A Theoretical Study. *J. Phys. Chem. C* **2012**, *116* (42), 22212–22216. https://doi.org/10.1021/jp307221q.

(163) Schirmeisen, A.; Taskiran, A.; Fuchs, H.; Roling, B.; Murugavel, S.; Bracht, H.; Natrup, F. Probing Ion Transport at the Nanoscale: Time-Domain Electrostatic Force Spectroscopy on Glassy Electrolytes. *Appl. Phys. Lett.* **2004**, *85* (11), 2053–2055. https://doi.org/10.1063/1.1790034.

(164) Ding, N.; Xu, J.; Yao, Y. X.; Wegner, G.; Fang, X.; Chen, C. H.; Lieberwirth, I. Determination of the Diffusion Coefficient of Lithium Ions in Nano-Si. *Solid State Ion.* **2009**, *180* (2–3), 222–225. https://doi.org/10.1016/j.ssi.2008.12.015.

(165) *A Python Package for Working with Impedance Data. Contribute to ECSHackWeek/Impedance.Py Development by Creating an Account on GitHub*; ECS Hack Week, 2019.

(166) Wurster, V.; Engel, C.; Graebe, H.; Ferber, T.; Jaegermann, W.; Hausbrand, R. Characterization of the Interfaces in LiFePO4/PEO-LiTFSI Composite Cathodes and to the Adjacent Layers. *J. Electrochem. Soc.* **2019**, *166* (3), A5410–A5420. https://doi.org/10.1149/2.0621903jes.

(167) Schmidt, J. P.; Chrobak, T.; Ender, M.; Illig, J.; Klotz, D.; Ivers-Tiffée, E. Studies on LiFePO4 as Cathode Material Using Impedance Spectroscopy. *J. Power Sources* **2011**, *196* (12), 5342–5348. https://doi.org/10.1016/j.jpowsour.2010.09.121.

(168) Han, S.; Park, J.; Lu, W.; Sastry, A. M. Numerical Study of Grain Boundary Effect on Li+ Effective Diffusivity and Intercalation-Induced Stresses in Li-Ion Battery Active Materials. *J. Power Sources* **2013**, *240*, 155–167. https://doi.org/10.1016/j.jpowsour.2013.03.135.

(169) Dash, U.; Sahoo, S.; Parashar, S. K. S.; Chaudhuri, P. Effect of Li+ Ion Mobility on the Grain Boundary Conductivity of Li2TiO3 Nanoceramics. *J. Adv. Ceram.* **2014**, *3* (2), 98–108. https://doi.org/10.1007/s40145-014-0098-9.

(170) Morgan, D.; Van der Ven, A.; Ceder, G. Li Conductivity in LixMPO4 (M= Mn, Fe, Co, Ni) Olivine Materials. *Electrochem. Solid-State Lett.* **2004**, *7* (7), A(30)-A(32).

(171) Massey, F. J. The Kolmogorov-Smirnov Test for Goodness of Fit. *J. Am. Stat. Assoc.* **1951**, *46* (253), 68–78. https://doi.org/10.1080/01621459.1951.10500769.

(172) Zhu, J.; Lu, L.; Zeng, K. Nanoscale Mapping of Lithium-Ion Diffusion in a Cathode within an All-Solid-State Lithium-Ion Battery by Advanced Scanning Probe Microscopy Techniques. *ACS Nano* **2013**, *7* (2), 1666–1675. https://doi.org/10.1021/nn305648j.

(173) Kalinin, S.; Balke, N.; Jesse, S.; Tselev, A.; Kumar, A.; Arruda, T. M.; Guo, S.; Proksch, R. Li-Ion Dynamics and Reactivity on the Nanoscale. *Mater. Today* **2011**, *14* (11), 548–558.

(174) Jesse, S.; Baddorf, A. P.; Kalinin, S. V. Dynamic Behaviour in Piezoresponse Force Microscopy. *Nanotechnology* **2006**, *17* (6), 1615–1628. https://doi.org/10.1088/0957-4484/17/6/014.

(175) Gruverman, A.; Auciello, O.; Tokumoto, H. IMAGING AND CONTROL OF DOMAIN STRUCTURES IN FERROELECTRIC THIN FILMS VIA SCANNING FORCE MICROSCOPY. *Annu. Rev. Mater. Sci.* **1998**, *28* (1), 101–123. https://doi.org/10.1146/annurev.matsci.28.1.101.

(176) Jesse, S.; Mirman, B.; Kalinin, S. V. Resonance Enhancement in Piezoresponse Force Microscopy: Mapping Electromechanical Activity, Contact Stiffness, and Q Factor. *Appl. Phys. Lett.* **2006**, *89* (2), 022906. https://doi.org/10.1063/1.2221496.

(177) Pietsch, P.; Westhoff, D.; Feinauer, J.; Eller, J.; Marone, F.; Stampanoni, M.; Schmidt, V.; Wood, V. Quantifying Microstructural Dynamics and Electrochemical Activity of Graphite and Silicon-Graphite Lithium Ion Battery Anodes. *Nat. Commun.* **2016**, *7* (1), 12909. https://doi.org/10.1038/ncomms12909.

(178) Finegan, D. P.; Tudisco, E.; Scheel, M.; Robinson, J. B.; Taiwo, O. O.; Eastwood, D. S.; Lee, P. D.; Michiel, M. D.; Bay, B.; Hall, S. A.; Hinds, G.; Brett, D. J. L.; Shearing,

P. R. Quantifying Bulk Electrode Strain and Material Displacement within Lithium Batteries via High-Speed Operando Tomography and Digital Volume Correlation. *Adv. Sci.* **2016**, *3* (3), 1500332. https://doi.org/10.1002/advs.201500332.

(179) Malik, R.; Abdellahi, A.; Ceder, G. A Critical Review of the Li Insertion Mechanisms in LiFePO [Subscript 4] Electrodes; Electrochemical Society, 2013.

(180) Dreyer, W.; Jamnik, J.; Guhlke, C.; Huth, R.; Moškon, J.; Gaberšček, M. The Thermodynamic Origin of Hysteresis in Insertion Batteries. *Nat. Mater.* **2010**, *9* (5), 448–453. https://doi.org/10.1038/nmat2730.

(181) Sun, S.; Guan, T.; Shen, B.; Leng, K.; Gao, Y.; Cheng, X.; Yin, G. Changes of Degradation Mechanisms of LiFePO 4 /Graphite Batteries Cycled at Different Ambient Temperatures. *Electrochimica Acta* **2017**, *237*, 248–258. https://doi.org/10.1016/j.electacta.2017.03.158.

(182) Lewerenz, M.; Warnecke, A.; Sauer, D. U. Post-Mortem Analysis on LiFePO4|Graphite Cells Describing the Evolution & Composition of Covering Layer on Anode and Their Impact on Cell Performance. *J. Power Sources* **2017**, *369*, 122–132. https://doi.org/10.1016/j.jpowsour.2017.10.003.

(183) Amine, K.; Liu, J.; Belharouak, I. High-Temperature Storage and Cycling of C-LiFePO4/Graphite Li-Ion Cells. *Electrochem. Commun.* **2005**, *7* (7), 669–673. https://doi.org/10.1016/j.elecom.2005.04.018.

(184) Wu, B.; Yonghuan, R.; Li, N. LiFePO4 Cathode Material. In *Electric Vehicles - The Benefits and Barriers*; Soylu, S., Ed.; IntechOpen: London; Vol. IntechOpen.

(185) Wang, J.; Yang, J.; Tang, Y.; Li, R.; Liang, G.; Sham, T.-K.; Sun, X. Surface Aging at Olivine LiFePO $_4$: A Direct Visual Observation of Iron Dissolution and the Protection Role of Nano-Carbon Coating. *J Mater Chem A* **2013**, *1* (5), 1579–1586. https://doi.org/10.1039/C2TA00521B.

(186) Prosini, P.; Lisi, M.; Zane, D.; Pasquali, M. Determination of the Chemical Diffusion Coefficient of Lithium in LiFePO4. *Solid State Ion.* **2002**, *148* (1–2), 45–51. https://doi.org/10.1016/S0167-2738(02)00134-0.

(187) Satyavani, T. V. S. L.; Ramya Kiran, B.; Rajesh Kumar, V.; Srinivas Kumar, A.; Naidu, S. V. Effect of Particle Size on Dc Conductivity, Activation Energy and Diffusion Coefficient of Lithium Iron Phosphate in Li-Ion Cells. *Eng. Sci. Technol. Int. J.* **2016**, *19* (1), 40–44. https://doi.org/10.1016/j.jestch.2015.05.011.

(188) Di Lecce, D.; Hassoun, J. Lithium Transport Properties in LiMn $_{1-\alpha}$ Fe $_\alpha$ PO $_4$ Olivine Cathodes. *J. Phys. Chem. C* **2015**, *119* (36), 20855–20863. https://doi.org/10.1021/acs.jpcc.5b06727.

(189) Malik, R.; Burch, D.; Bazant, M.; Ceder, G. Particle Size Dependence of the Ionic Diffusivity. *Nano Lett.* **2010**, *10* (10), 4123–4127. https://doi.org/10.1021/nl1023595.

(190) Delmas, C.; Maccario, M.; Croguennec, L.; Le Cras, F.; Weill, F. Lithium Deintercalation in LiFePO4 Nanoparticles via a Domino-Cascade Model. *Nat. Mater.* **2008**, *7* (8), 665–671. https://doi.org/10.1038/nmat2230.

(191) Jiang, F.; Peng, P. Elucidating the Performance Limitations of Lithium-Ion Batteries Due to Species and Charge Transport through Five Characteristic Parameters. *Sci. Rep.* **2016**, *6* (1). https://doi.org/10.1038/srep32639.

(192) Jow, T. R.; Delp, S. A.; Allen, J. L.; Jones, J.-P.; Smart, M. C. Factors Limiting Li+ Charge Transfer Kinetics in Li-Ion Batteries. *J. Electrochem. Soc.* **2018**, *165* (2), A361–A367. https://doi.org/10.1149/2.1221802jes.

(193) Lee, Y.-S.; Ryu, K.-S. Study of the Lithium Diffusion Properties and High Rate Performance of TiNb6O17 as an Anode in Lithium Secondary Battery. *Sci. Rep.* **2017**, *7* (1). https://doi.org/10.1038/s41598-017-16711-9.

(194) Sawai, K.; Ohzuku, T. Factors Affecting Rate Capability of Graphite Electrodes for Lithium-Ion Batteries. *J. Electrochem. Soc.* **2003**, *150* (6), A674–A678. https://doi.org/10.1149/1.1568107.
(195) Newman, J.; Thomas-Alyea, K. *Electrochemical Systems*; John Wiley & Sons, Ltd, 2004; Vol. 3rd Edition.
(196) A123 Systems Inc. Safety Data Sheet - Product Name: High Power Lithium Ion Cell, Phosphate-Based. *Saf. Data Sheet - Prod. Name High Power Lithium Ion Cell Phosphate-Based* **2011**.
(197) Marongiu, A.; Sauer, D. U. On-Board Aging Estimation Using Half-Cell Voltage Curves for LiFePO4 Cathode-Based Lithium-Ion Batteries for EV Applications. *Int. J. Automot. Technol.* **2016**, *17* (3), 465–472. https://doi.org/10.1007/s12239-016-0048-3.
(198) Omenya, F.; Chernova, N. A.; Upreti, S.; Zavalij, P. Y.; Nam, K.-W.; Yang, X.-Q.; Whittingham, M. S. Can Vanadium Be Substituted into LiFePO $_4$? *Chem. Mater.* **2011**, *23* (21), 4733–4740. https://doi.org/10.1021/cm2017032.
(199) Spingler, F. B.; Naumann, M.; Jossen, A. Capacity Recovery Effect in Commercial LiFePO4 / Graphite Cells. *J. Electrochem. Soc.* **2020**, *167* (4), 040526. https://doi.org/10.1149/1945-7111/ab7900.
(200) Lewerenz, M.; Marongiu, A.; Warnecke, A.; Sauer, D. U. Differential Voltage Analysis as a Tool for Analyzing Inhomogeneous Aging: A Case Study for LiFePO4|Graphite Cylindrical Cells. *J. Power Sources* **2017**, *368*, 57–67. https://doi.org/10.1016/j.jpowsour.2017.09.059.
(201) Li, D.; Danilov, D. L.; Gao, L.; Yang, Y.; Notten, P. H. L. Degradation Mechanisms of the Graphite Electrode in C6/LiFePO4 Batteries Unraveled by a Non-Destructive Approach. *J. Electrochem. Soc.* **2016**, *163* (14), A3016–A3021. https://doi.org/10.1149/2.0821614jes.
(202) Lavigne, L.; Sabatier, J.; Francisco, J. M.; Guillemard, F.; Noury, A. Lithium-Ion Batteries Aging Motinoring Througth Open Circuit Voltage (OCV) Curve Modelling and Adjustment: In *Proceedings of the 13th International Conference on Informatics in Control, Automation and Robotics*; SCITEPRESS - Science and and Technology Publications: Lisbon, Portugal, 2016; pp 57–67. https://doi.org/10.5220/0005961400570067.
(203) Farmann, A.; Sauer, D. U. A Study on the Dependency of the Open-Circuit Voltage on Temperature and Actual Aging State of Lithium-Ion Batteries. *J. Power Sources* **2017**, *347*, 1–13. https://doi.org/10.1016/j.jpowsour.2017.01.098.
(204) Anseán, D.; Dubarry, M.; Devie, A.; Liaw, B. Y.; García, V. M.; Viera, J. C.; González, M. Operando Lithium Plating Quantification and Early Detection of a Commercial LiFePO4 Cell Cycled under Dynamic Driving Schedule. *J. Power Sources* **2017**, *356*, 36–46. https://doi.org/10.1016/j.jpowsour.2017.04.072.
(205) Petzl, M.; Danzer, M. A. Nondestructive Detection, Characterization, and Quantification of Lithium Plating in Commercial Lithium-Ion Batteries. *J. Power Sources* **2014**, *254*, 80–87. https://doi.org/10.1016/j.jpowsour.2013.12.060.
(206) Jiang, J.; Shi, W.; Zheng, J.; Zuo, P.; Xiao, J.; Chen, X.; Xu, W.; Zhang, J.-G. Optimized Operating Range for Large-Format LiFePO4/Graphite Batteries. *J. Electrochem. Soc.* **2014**, *161* (3), A336–A341. https://doi.org/10.1149/2.052403jes.
(207) Lewerenz, M.; Münnix, J.; Schmalstieg, J.; Käbitz, S.; Knips, M.; Sauer, D. U. Systematic Aging of Commercial LiFePO 4 |Graphite Cylindrical Cells Including a Theory Explaining Rise of Capacity during Aging. *J. Power Sources* **2017**, *345*, 254–263. https://doi.org/10.1016/j.jpowsour.2017.01.133.
(208) Lewerenz, M. Dissection and Quantitative Description of Aging of Lithium-Ion Batteries Using Non-Destructive Methods Validated by Post-Mortem-Analyses, RWTH Aachen, Aachen, 2018.

(209) Lavigne, L.; Sabatier, J.; Francisco, J. M.; Guillemard, F.; Noury, A. Lithium-Ion Open Circuit Voltage (OCV) Curve Modelling and Its Ageing Adjustment. *J. Power Sources* **2016**, *324*, 694–703. https://doi.org/10.1016/j.jpowsour.2016.05.121.

(210) Birkl, C. R.; Roberts, M. R.; McTurk, E.; Bruce, P. G.; Howey, D. A. Degradation Diagnostics for Lithium Ion Cells. *J. Power Sources* **2017**, *341*, 373–386. https://doi.org/10.1016/j.jpowsour.2016.12.011.

(211) Van der Ven, A.; Wagemaker, M. Effect of Surface Energies and Nano-Particle Size Distribution on Open Circuit Voltage of Li-Electrodes. *Electrochem. Commun.* **2009**, *11* (4), 881–884. https://doi.org/10.1016/j.elecom.2009.02.015.

(212) Wang, C.; Appleby, A. J.; Little, F. E. Electrochemical Impedance Study of Initial Lithium Ion Intercalation into Graphite Powders. *Electrochimica Acta* **2001**, *46* (12), 1793–1813. https://doi.org/10.1016/S0013-4686(00)00782-9.

(213) Dubarry, M.; Berecibar, M.; Devie, A.; Anseán, D.; Omar, N.; Villarreal, I. State of Health Battery Estimator Enabling Degradation Diagnosis: Model and Algorithm Description. *J. Power Sources* **2017**, *360*, 59–69. https://doi.org/10.1016/j.jpowsour.2017.05.121.

(214) Smart, M. C.; Ratnakumar, B. V. Effects of Electrolyte Composition on Lithium Plating in Lithium-Ion Cells. *J. Electrochem. Soc.* **2011**, *158* (4), A379. https://doi.org/10.1149/1.3544439.

(215) Hein, S.; Latz, A. Influence of Local Lithium Metal Deposition in 3D Microstructures on Local and Global Behavior of Lithium-Ion Batteries. *Electrochimica Acta* **2016**, *201*, 354–365. https://doi.org/10.1016/j.electacta.2016.01.220.

(216) Feng, X.; Li, J.; Ouyang, M.; Lu, L.; Li, J.; He, X. Using Probability Density Function to Evaluate the State of Health of Lithium-Ion Batteries. *J. Power Sources* **2013**, *232*, 209–218. https://doi.org/10.1016/j.jpowsour.2013.01.018.

(217) Waldmann, T.; Wilka, M.; Kasper, M.; Fleischhammer, M.; Wohlfahrt-Mehrens, M. Temperature Dependent Ageing Mechanisms in Lithium-Ion Batteries – A Post-Mortem Study. *J. Power Sources* **2014**, *262*, 129–135. https://doi.org/10.1016/j.jpowsour.2014.03.112.

(218) Ansean, D.; Gonzalez, M.; Blanco, C.; Viera, J. C.; Fernandez, Y.; Garcia, V. M. Lithium-Ion Battery Degradation Indicators via Incremental Capacity Analysis. In *2017 IEEE International Conference on Environment and Electrical Engineering and 2017 IEEE Industrial and Commercial Power Systems Europe (EEEIC / I&CPS Europe)*; IEEE: Milan, Italy, 2017; pp 1–6. https://doi.org/10.1109/EEEIC.2017.7977776.

(219) Stroe, D.; Swierczynski, M.; Stroe, A.; Kaer, S. K.; Teodorescu, R. Lithium-Ion Battery Power Degradation Modelling by Electrochemical Impedance Spectroscopy. *IET Renew. Power Gener.* **2017**, *11* (9), 1136–1141. https://doi.org/10.1049/iet-rpg.2016.0958.

(220) Liao, X.-Z.; Ma, Z.-F.; Gong, Q.; He, Y.-S.; Pei, L.; Zeng, L.-J. Low-Temperature Performance of LiFePO4/C Cathode in a Quaternary Carbonate-Based Electrolyte. *Electrochem. Commun.* **2008**, *10* (5), 691–694. https://doi.org/10.1016/j.elecom.2008.02.017.

(221) Osaka, T.; Momma, T.; Mukoyama, D.; Nara, H. Proposal of Novel Equivalent Circuit for Electrochemical Impedance Analysis of Commercially Available Lithium Ion Battery. *J. Power Sources* **2012**, *205*, 483–486. https://doi.org/10.1016/j.jpowsour.2012.01.070.

(222) Liu, P.; Wang, J.; Hicks-Garner, J.; Sherman, E.; Soukiazian, S.; Verbrugge, M.; Tataria, H.; Musser, J.; Finamore, P. Aging Mechanisms of LiFePO[Sub 4] Batteries Deduced by Electrochemical and Structural Analyses. *J. Electrochem. Soc.* **2010**, *157* (4), A499. https://doi.org/10.1149/1.3294790.

(223) Liu, P.; Zhang, W.; Liu, X.; Zhang, Y.; Wu, F. Electrochemical Impedance Analysis of C/LiFePO 4 Batteries in Cycling Process. *IOP Conf. Ser. Mater. Sci. Eng.* **2018**, *452*, 032088. https://doi.org/10.1088/1757-899X/452/3/032088.

(224) Scipioni, R.; Jørgensen, P. S.; Graves, C.; Hjelm, J.; Jensen, S. H. A Physically-Based Equivalent Circuit Model for the Impedance of a LiFePO 4 /Graphite 26650 Cylindrical Cell. *J. Electrochem. Soc.* **2017**, *164* (9), A2017–A2030. https://doi.org/10.1149/2.1071709jes.

(225) Prada, E.; Di Domenico, D.; Creff, Y.; Bernard, J.; Sauvant-Moynot, V.; Huet, F. A Simplified Electrochemical and Thermal Aging Model of LiFePO 4 -Graphite Li-Ion Batteries: Power and Capacity Fade Simulations. *J. Electrochem. Soc.* **2013**, *160* (4), A616–A628. https://doi.org/10.1149/2.053304jes.

(226) Steinhauer, M.; Risse, S.; Wagner, N.; Friedrich, K. A. Investigation of the Solid Electrolyte Interphase Formation at Graphite Anodes in Lithium-Ion Batteries with Electrochemical Impedance Spectroscopy. *Electrochimica Acta* **2017**, *228*, 652–658. https://doi.org/10.1016/j.electacta.2017.01.128.

(227) Illig, J.; Ender, M.; Chrobak, T.; Schmidt, J. P.; Klotz, D.; Ivers-Tiffée, E. Separation of Charge Transfer and Contact Resistance in LiFePO 4 -Cathodes by Impedance Modeling. *J. Electrochem. Soc.* **2012**, *159* (7), A952–A960. https://doi.org/10.1149/2.030207jes.

(228) Bach, T. C.; Schuster, S. F.; Fleder, E.; Müller, J.; Brand, M. J.; Lorrmann, H.; Jossen, A.; Sextl, G. Nonlinear Aging of Cylindrical Lithium-Ion Cells Linked to Heterogeneous Compression. *J. Energy Storage* **2016**, *5*, 212–223. https://doi.org/10.1016/j.est.2016.01.003.

(229) Guo, Z.; Chen, Z. High-Temperature Capacity Fading Mechanism for LiFePO4/Graphite Soft-Packed Cell without Fe Dissolution. *J. Electroanal. Chem.* **2015**, *754*, 148–153. https://doi.org/10.1016/j.jelechem.2015.07.009.

(230) Andersson, A. M.; Edström, K.; Rao, N.; Wendsjö, Å. Temperature Dependence of the Passivation Layer on Graphite. *J. Power Sources* **1999**, *81–82*, 286–290. https://doi.org/10.1016/S0378-7753(99)00202-5.

(231) Andersson, A. M.; Edström, K. Chemical Composition and Morphology of the Elevated Temperature SEI on Graphite. *J. Electrochem. Soc.* **2001**, *148* (10), A1100–A1109. https://doi.org/10.1149/1.1397771.

(232) Lu, P.; Li, C.; Schneider, E. W.; Harris, S. J. Chemistry, Impedance, and Morphology Evolution in Solid Electrolyte Interphase Films during Formation in Lithium Ion Batteries. *J. Phys. Chem. C* **2014**, *118* (2), 896–903. https://doi.org/10.1021/jp4111019.

(233) Bhattacharya, S.; Riahi, A. R.; Alpas, A. T. Thermal Cycling Induced Capacity Enhancement of Graphite Anodes in Lithium-Ion Cells. *Carbon* **2014**, *67*, 592–606. https://doi.org/10.1016/j.carbon.2013.10.032.

(234) Liu, L.; Park, J.; Lin, X.; Sastry, A. M.; Lu, W. A Thermal-Electrochemical Model That Gives Spatial-Dependent Growth of Solid Electrolyte Interphase in a Li-Ion Battery. *J. Power Sources* **2014**, *268*, 482–490. https://doi.org/10.1016/j.jpowsour.2014.06.050.

(235) Lee, S.-B.; Pyun, S.-I. The Effect of Electrolyte Temperature on the Passivity of Solid Electrolyte Interphase Formed on a Graphite Electrode. *Carbon* **2002**, *40* (13), 2333–2339. https://doi.org/10.1016/S0008-6223(02)00144-6.

(236) Anseán, D.; Dubarry, M.; Devie, A.; Liaw, B. Y.; García, V. M.; Viera, J. C.; González, M. Fast Charging Technique for High Power LiFePO 4 Batteries: A Mechanistic Analysis of Aging. *J. Power Sources* **2016**, *321*, 201–209. https://doi.org/10.1016/j.jpowsour.2016.04.140.

(237) Chen, M.; Shao, L.-L.; Yang, H.-B.; Ren, T.-Z.; Du, G.; Yuan, Z.-Y. Vanadium-Doping of LiFePO4/Carbon Composite Cathode Materials Synthesized with Organophosphorus

Source. *Electrochimica Acta* **2015**, *167*, 278–286. https://doi.org/10.1016/j.electacta.2015.03.185.

(238) Wandt, J.; Freiberg, A.; Thomas, R.; Gorlin, Y.; Siebel, A.; Jung, R.; Gasteiger, H. A.; Tromp, M. Transition Metal Dissolution and Deposition in Li-Ion Batteries Investigated by Operando X-Ray Absorption Spectroscopy. *J. Mater. Chem. A* **2016**, *4* (47), 18300–18305. https://doi.org/10.1039/C6TA08865A.

(239) Talyosef, Y.; Markovsky, B.; Salitra, G.; Aurbach, D.; Kim, H.-J.; Choi, S. The Study of LiNi0.5Mn1.5O4 5-V Cathodes for Li-Ion Batteries. *J. Power Sources* **2005**, *146* (1–2), 664–669. https://doi.org/10.1016/j.jpowsour.2005.03.064.

(240) Li, D.; L. Danilov, D.; Gao, L.; Yang, Y.; Notten, P. H. L. Degradation Mechanisms of C6/LiFePO4 Batteries: Experimental Analyses of Cycling-Induced Aging. *Electrochimica Acta* **2016**, *210*, 445–455. https://doi.org/10.1016/j.electacta.2016.05.091.

(241) Lai, Y.; Cao, Z.; Song, H.; Zhang, Z.; Chen, X.; Lu, H.; Jia, M.; Li, J. Influence of Fe (II) Species in Electrolyte on Performance of Graphite Anode for Lithium-Ion Batteries. *J. Electrochem. Soc.* **2012**, *159* (12), A1961–A1966. https://doi.org/10.1149/2.044212jes.

(242) Simolka, M.; Heger, J.-F.; Traub, N.; Kaess, H.; Friedrich, K. A. Influence of Cycling Profile, Depth of Discharge and Temperature on Commercial LFP/C Cell Ageing: Cell Level Analysis with ICA, DVA and OCV Measurements. *J. Electrochem. Soc.* **2020**, *167* (11), 110502. https://doi.org/10.1149/1945-7111/ab9cd1.

(243) Xiao, Y.; Hao, D.; Chen, H.; Gong, Z.; Yang, Y. Economical Synthesis and Promotion of the Electrochemical Performance of Silicon Nanowires as Anode Material in Li-Ion Batteries. *ACS Appl. Mater. Interfaces* **2013**, *5* (5), 1681–1687. https://doi.org/10.1021/am302731y.

(244) Sun, H.-H.; Dolocan, A.; Weeks, J. A.; Rodriguez, R.; Heller, A.; Mullins, C. B. *In Situ* Formation of a Multicomponent Inorganic-Rich SEI Layer Provides a Fast Charging and High Specific Energy Li-Metal Battery. *J. Mater. Chem. A* **2019**, *7* (30), 17782–17789. https://doi.org/10.1039/C9TA05063A.

(245) Zhu, J.; Zeng, K.; Lu, L. Cycling Effects on Surface Morphology, Nanomechanical and Interfacial Reliability of LiMn2O4 Cathode in Thin Film Lithium Ion Batteries. *Electrochimica Acta* **2012**, *68*, 52–59. https://doi.org/10.1016/j.electacta.2012.02.032.

(246) Wu, J.; Yang, S.; Cai, W.; Bi, Z.; Shang, G.; Yao, J. Multi-Characterization of LiCoO2 Cathode Films Using Advanced AFM-Based Techniques with High Resolution. *Sci. Rep.* **2017**, *7* (1), 11164. https://doi.org/10.1038/s41598-017-11623-0.

(247) Kostecki, R.; Zhang, X.; Ross Jr., P. N.; Kong, F.; Sloop, S.; Kerr, J. B.; Striebel, K.; Cairns, E.; McLarnon, F. *Failure Modes in High-Power Lithium-Ion Batteries for Use Inhybrid Electric Vehicles*; LBNL--48359, 861953; 2001. https://doi.org/10.2172/861953.

(248) Demirocak, D. E.; Bhushan, B. Probing the Aging Effects on Nanomechanical Properties of a LiFePO4 Cathode in a Large Format Prismatic Cell. *J. Power Sources* **2015**, *280*, 256–262. https://doi.org/10.1016/j.jpowsour.2015.01.114.

(249) Herstedt, M.; Stjerndahl, M.; Nytén, A.; Gustafsson, T.; Rensmo, H.; Siegbahn, H.; Ravet, N.; Armand, M.; Thomas, J. O.; Edström, K. Surface Chemistry of Carbon-Treated LiFePO[Sub 4] Particles for Li-Ion Battery Cathodes Studied by PES. *Electrochem. Solid-State Lett.* **2003**, *6* (9), A202. https://doi.org/10.1149/1.1594413.

(250) Aurbach, D. A Comparative Study of Synthetic Graphite and Li Electrodes in Electrolyte Solutions Based on Ethylene Carbonate-Dimethyl Carbonate Mixtures. *J. Electrochem. Soc.* **1996**, *143* (12), 3809. https://doi.org/10.1149/1.1837300.

(251) Wang, Y.-S.; Huang, C.-M.; Hsieh, H.-W.; Lin, Y.-F.; Lin, C.-Y.; Lee, J.-T. Effect of Temperature on the Dissolution of Solid Electrolyte Interface on Mesocarbon

Microbeads Electrodes in Propylene Carbonate-Based Electrolytes. *Electrochimica Acta* **2014**, *142*, 34–42. https://doi.org/10.1016/j.electacta.2014.07.091.

(252) Klett, M.; Eriksson, R.; Groot, J.; Svens, P.; Ciosek Högström, K.; Lindström, R. W.; Berg, H.; Gustafson, T.; Lindbergh, G.; Edström, K. Non-Uniform Aging of Cycled Commercial LiFePO4//Graphite Cylindrical Cells Revealed by Post-Mortem Analysis. *J. Power Sources* **2014**, *257*, 126–137. https://doi.org/10.1016/j.jpowsour.2014.01.105.

(253) Hovington, P.; Lagacé, M.; Guerfi, A.; Bouchard, P.; Mauger, A.; Julien, C. M.; Armand, M.; Zaghib, K. New Lithium Metal Polymer Solid State Battery for an Ultrahigh Energy: Nano C-LiFePO $_4$ versus Nano Li $_{1.2}$ V $_3$ O $_8$. *Nano Lett.* **2015**, *15* (4), 2671–2678. https://doi.org/10.1021/acs.nanolett.5b00326.

(254) Dubarry, M.; Baure, G.; Pastor-Fernández, C.; Yu, T. F.; Widanage, W. D.; Marco, J. Battery Energy Storage System Modeling: A Combined Comprehensive Approach. *J. Energy Storage* **2019**, *21*, 172–185. https://doi.org/10.1016/j.est.2018.11.012.

A. Appendix

I. Composition of commercial LFP cathode and graphite anode, extracted from the commercial full cell

The samples were analyzed using SEM-EDX (Jeol JSM-7200F equipped with a Bruker Quantax EDX system). We used 15 kV acceleration voltage to guarantee the detection of any trace iron on the anode. The samples were prepared within an argon filled glovebox (H_2O and O_2 < 1 ppm) and quickly transferred into the vacuum chamber of the SEM system. They were in contact with air for approximately 30 seconds. The detection limit is around 0.03 %.

Cathode:

	Norm. mass %	Deviation %
Oxygen	33.89108	0.52609
Iron	32.1628	0.58066
Phosphor	17.88036	0.17198
Carbon	11.8598	1.40395
Fluor	2.4756	0.16523
Vanadium	0.9795	0.00352
Nitrogen	0.66282	0.04876
Silicon	0.05129	0.01671
Aluminum	0.03676	0.00538

Anode:

	Norm. mass %	Deviation %
Carbon	90.03733	0.63809
Oxygen	2.52145	0.14697
Fluor	5.96388	0.44248
Copper	1.00804	0.03361
Phosphor	0.41711	0.03299
Iron	0.03261	0.01053

II. *ICA and DVA curves for cell aged at 100% DOD with AP2 at 55°C*

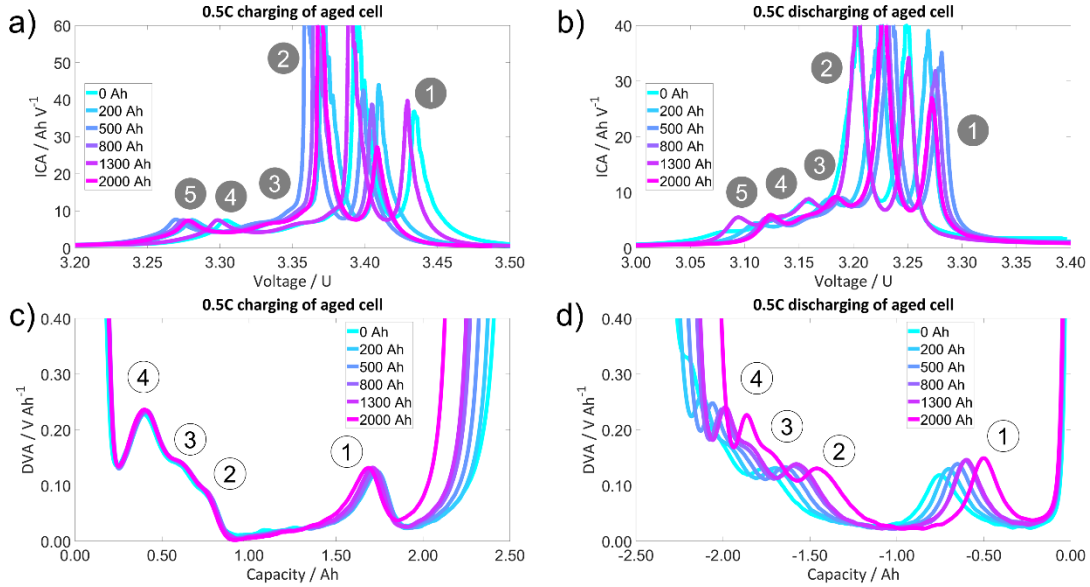

Figure A1: ICA (a and b) and DVA (c and d) analysis of a commercial LFP cell, cycled at 55°C with 100% DOD and AP2 at different aging steps. Charging in a) and c) and discharging in b) and d).

III. *Evolution of the ICA peak 5 intensity and the width of the ICA peak 1 and DVA peak 1 over aging at 55°C*

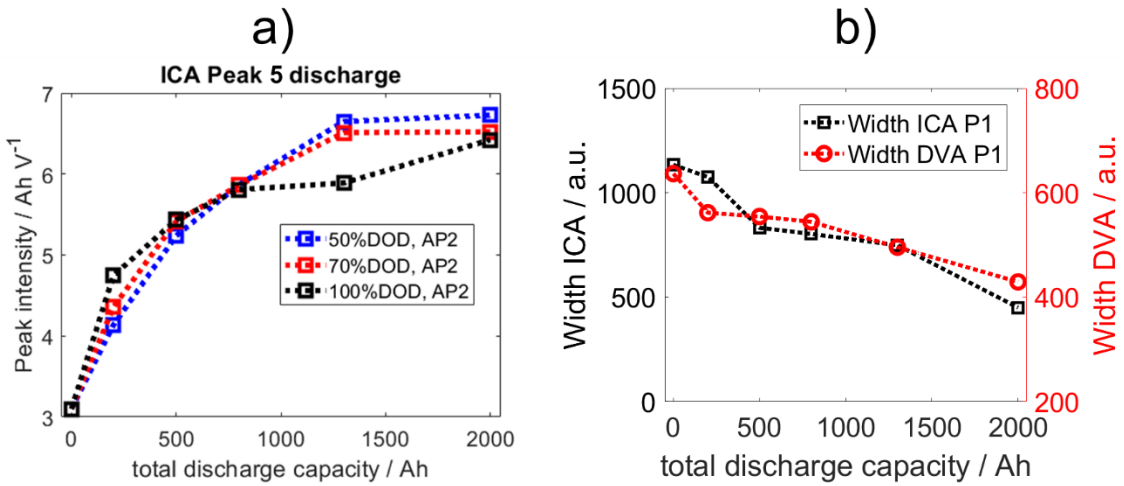

Figure A2: Evolution of the ICA peak 5 intensity over aging of different ageing profiles in a) and reduction of the ICA peak 1 and DVA peak 1 peak widths during ageing of the cell aged with 50% DOD with AP2 in b); both at 55°C aging

IV. ICA and DVA curves for cell aged at 100% DOD with AP2 at -20°C

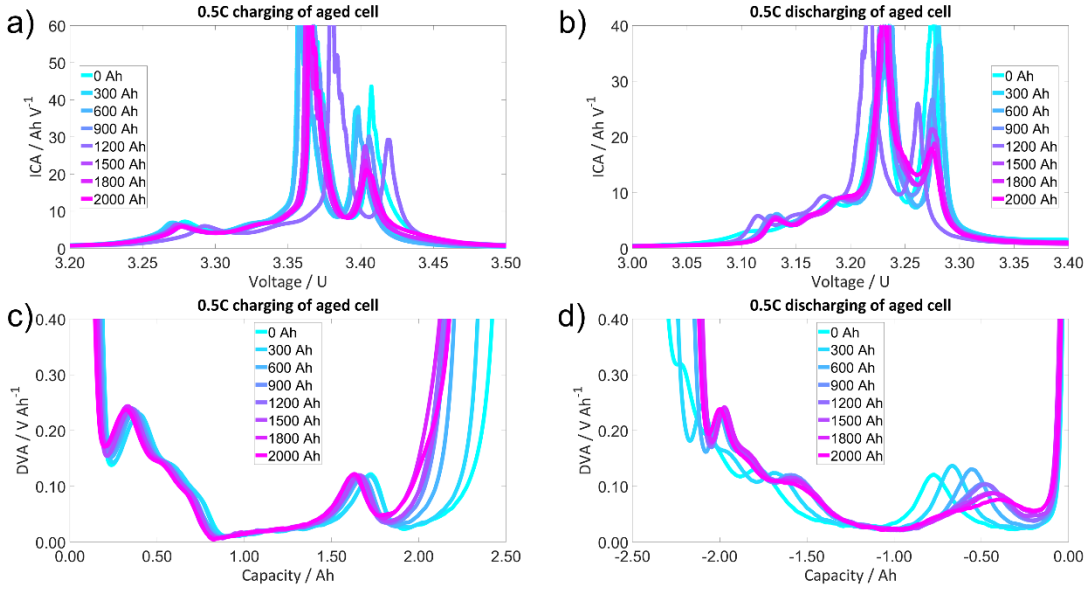

Figure A3: ICA (a and b) and DVA (c and d) analysis of a commercial LFP cell, cycled at -20°C with 100% DOD and AP2 at different aging steps. Charging in a) and c) and discharging in b) and d).

V. Evolution of parameter ΔMinMax over aging of the cells aged at 55°C and -20°C

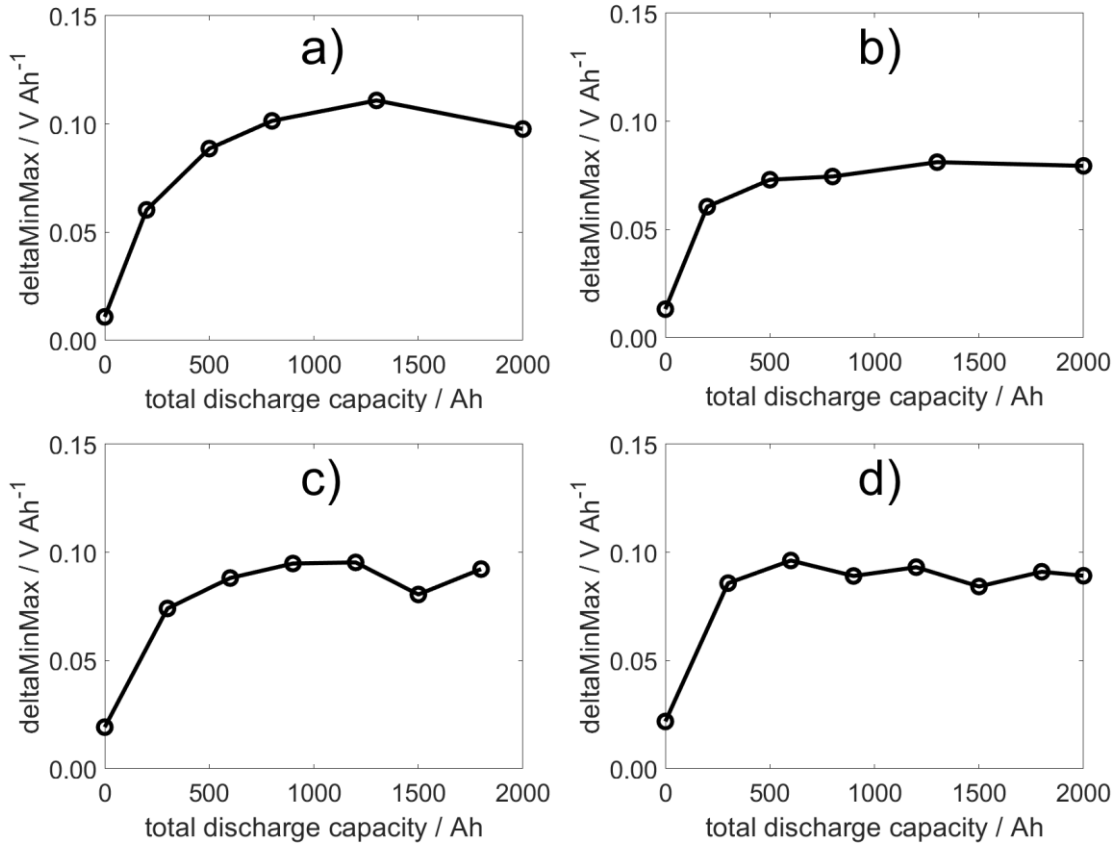

Figure A4: Evolution of ΔMinMax over aging for cell aged at a) 50% DOD, AP2, 55°C, b) 100% DOD, AP2, 55°C, c) 50% DOD, AP2, -20°C and d) 100% DOD, AP2, -20°C

VI. Characterization at 0.5C during checkups of the cells aged at -20°C to visualize the plating and stripping plateau

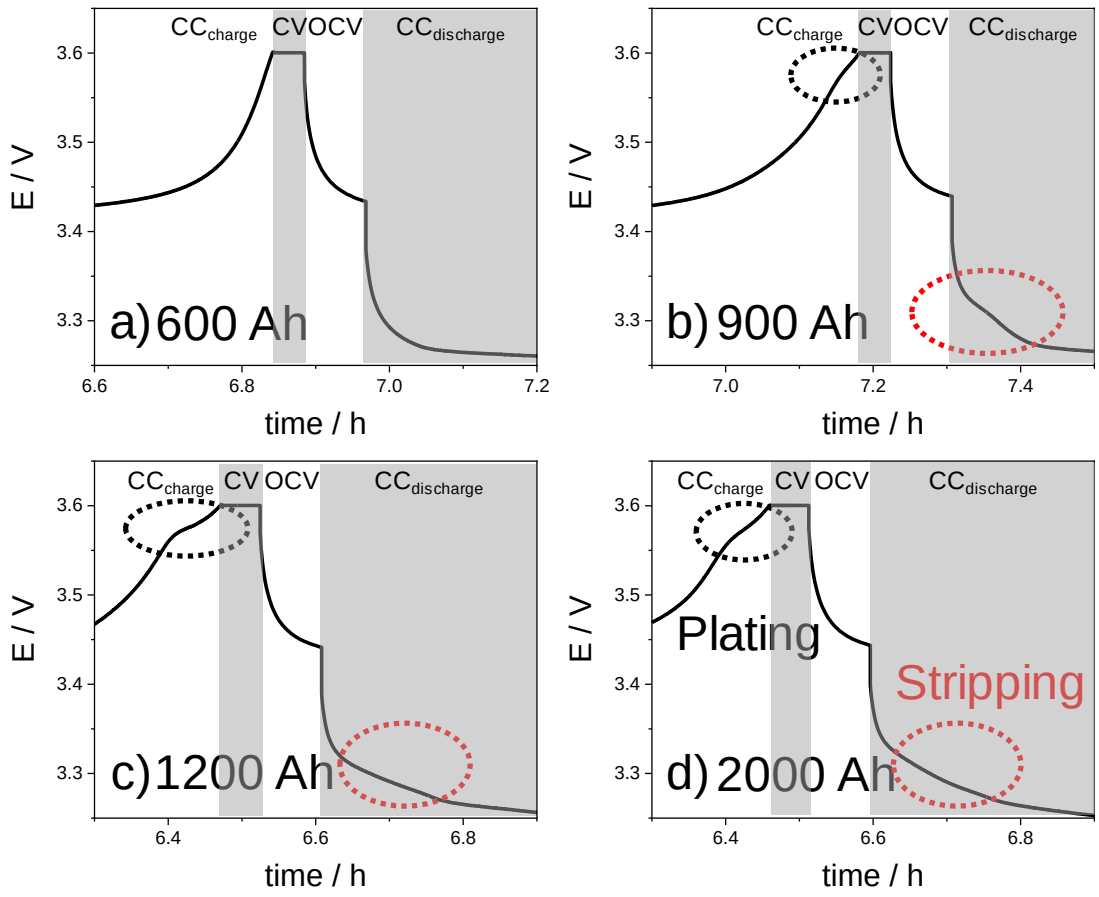

Figure A5: Comparison of 0.5C charge and discharge process during characterization at 25°C for cell aged at 50% DOD, AP2 (a = 600 Ah, b = 900 Ah, c = 1200 Ah and d = 2000 Ah). CC = constant current, CV = constant voltage.

VII. Evolution of the ICA peak 5 intensity and the width of the ICA peak 1 and DVA peak 1 over aging at 55°C

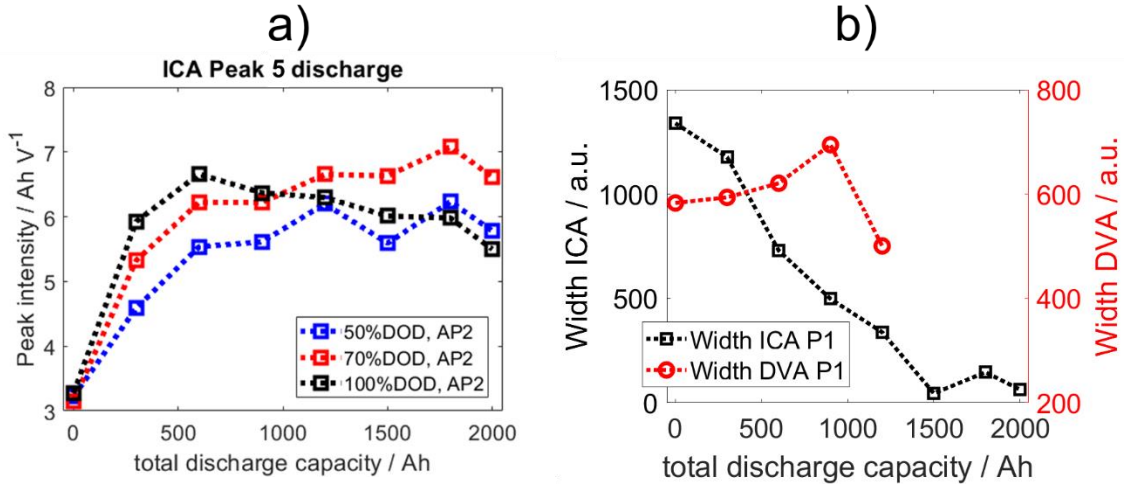

Figure A6: Evolution of the ICA peak 5 intensity over aging of different ageing profiles in a) and reduction of the ICA peak 1 and DVA peak 1 peak widths during ageing of the cell aged with 50% DOD with AP2 in b); both at -20°C aging

VIII. Decrease of normalized ICA peak 1intensity over aging for one cell from each DOD group at 55°C and -20°C with the corresponding normalized cell capacity

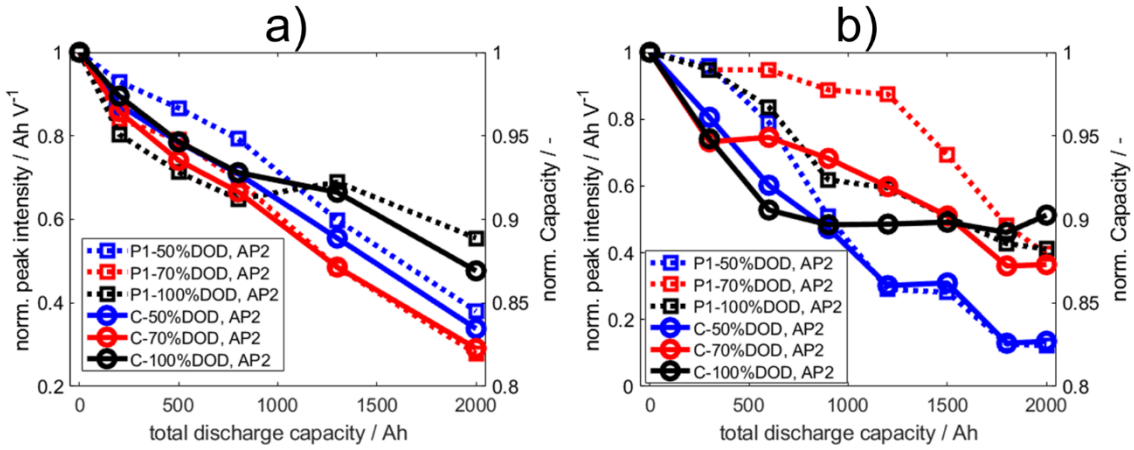

Figure A7: Comparison of the discharge ICA peak 1 decline and the capacity loss of cells aged at 55°c (a) and -20°C (b). "P1" represents the peak intensity of ICA peak 1 and "C" the capacity of the cell.

IX. Evolution of resistance R_1 and R_{total} for the cells aged at 55°C and -20°C in 7.1.4 and Fehler! Verweisquelle konnte nicht gefunden werden.

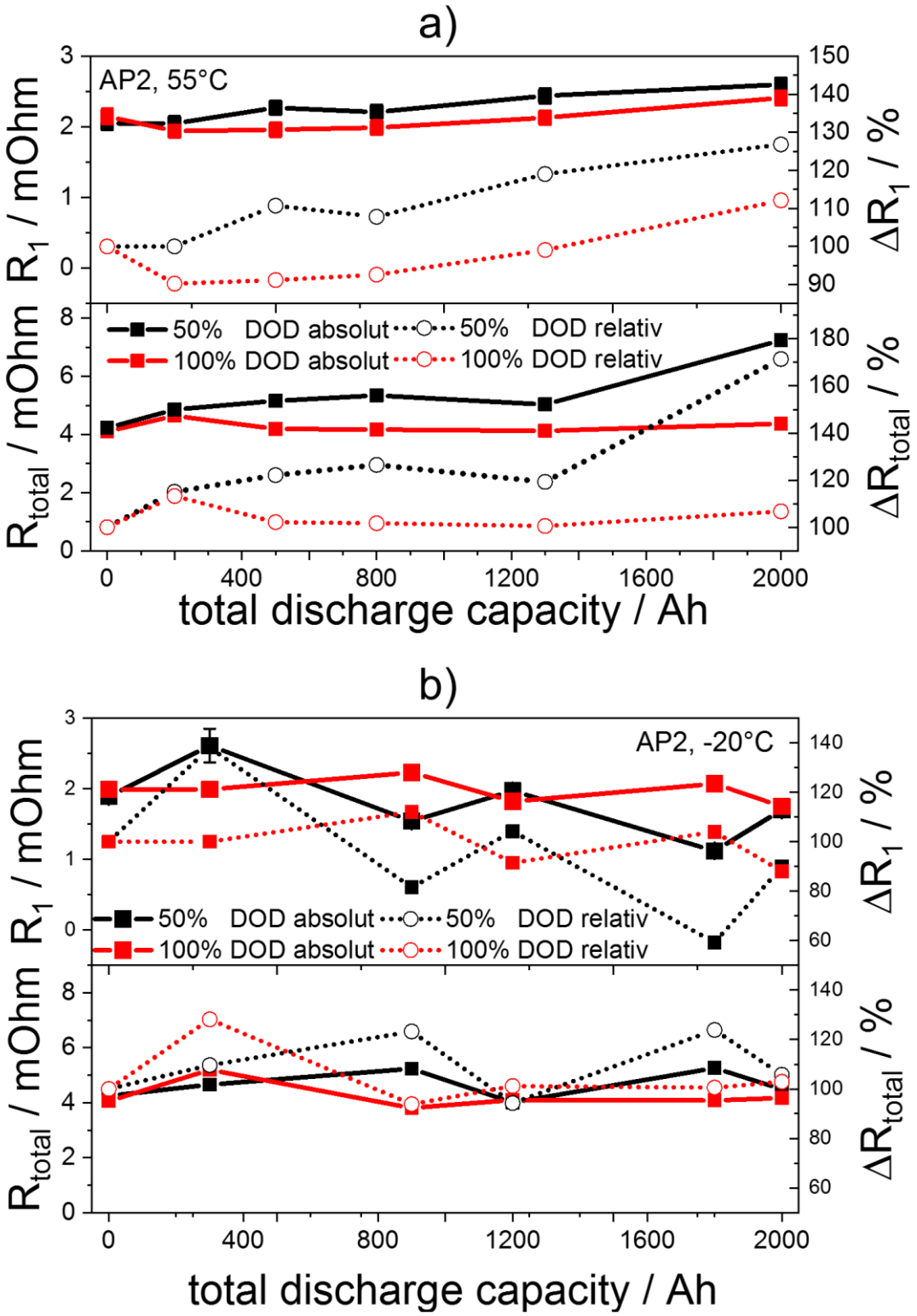

Figure A8: Evolution of R_1 and R_{total} for the cell aged with 50% and 100% DOD, AP2 at 55°C (a) and -20°C (b).

X. SEM images of anode surfaces before and after aging at 55°C and -20°C with additional lower magnification

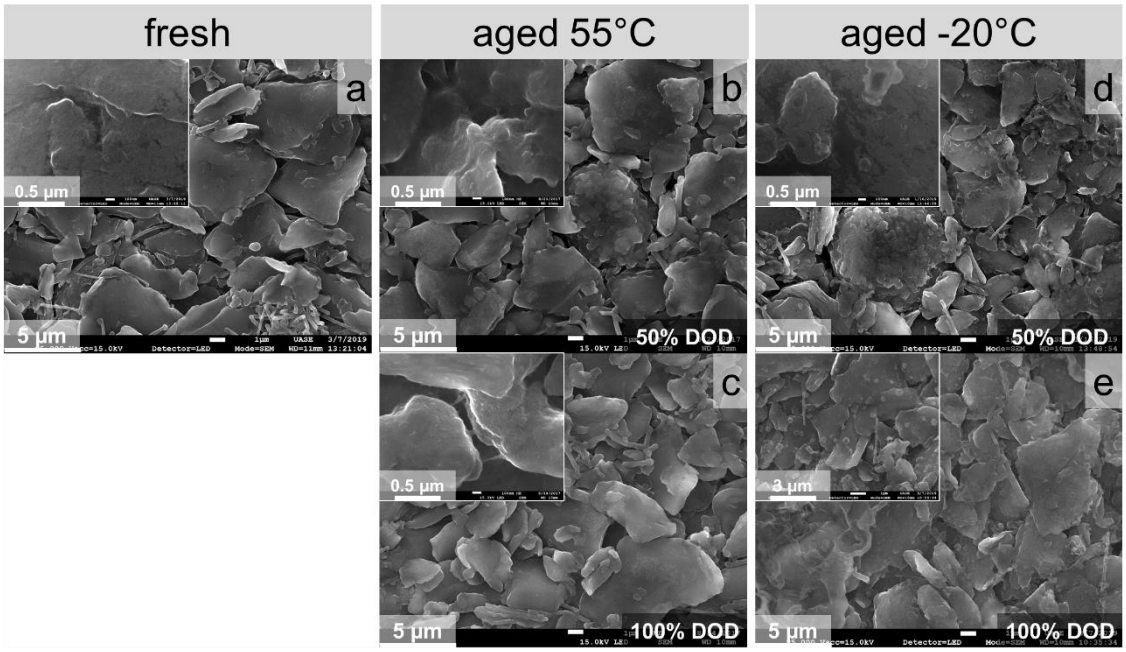

Figure A9: SEM images of the fresh anode in (a), anodes aged at 55°C in (b) and (c) and aged at -20°C in (d) and (e).

XI. AFM surface measurements of anodes in fresh state and aged at 55°C

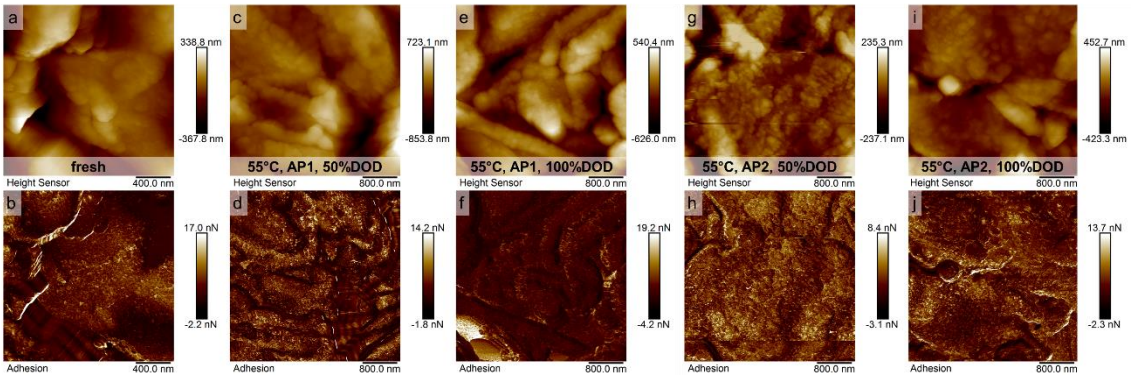

Figure A10: AFM measurements of anode surfaces fresh (a, b), aged at 55°C using 50% DOD with AP1 (c, d), 100% DOD with AP1 (e, f), 50% DOD with AP2 (g, h) and 100% DOD with AP2 (i, j).

XII. AFM surface measurements of anodes in fresh state and aged at -20°C

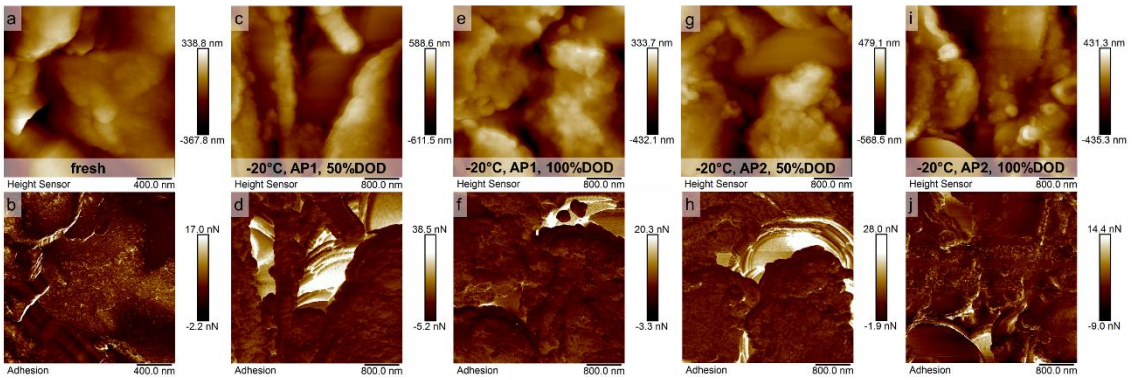

Figure A11: AFM measurements of anode surfaces fresh (a, b), aged at -20°C using 50% DOD with AP1 (c, d), 100% DOD with AP1 (e, f), 50% DOD with AP2 (g, h) and 100% DOD with AP2 (i, j).

XIII. Focus on a surface agglomerate consisting of nano-particle on the cathode surface aged at 55°C showing the differences in adhesion and conductivity

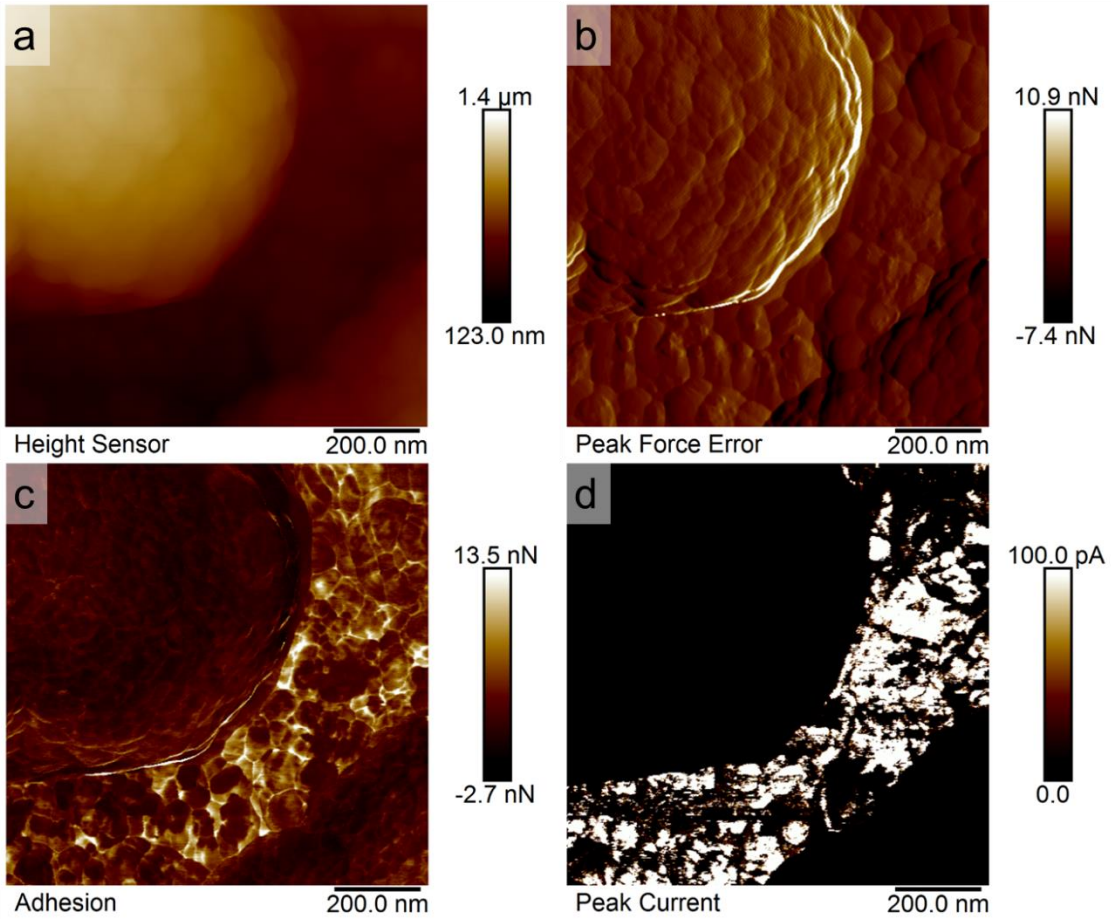

Figure A12: AFM measurements of cathode surface particle showing the topography (a), Peak Force Error (b), Adhesion (c) and Peak Current (d).

XIV. Comparing the results at end of life of the share of the conductive area with the remaining cell capacity of the cells shows no direct correlation between these parameters

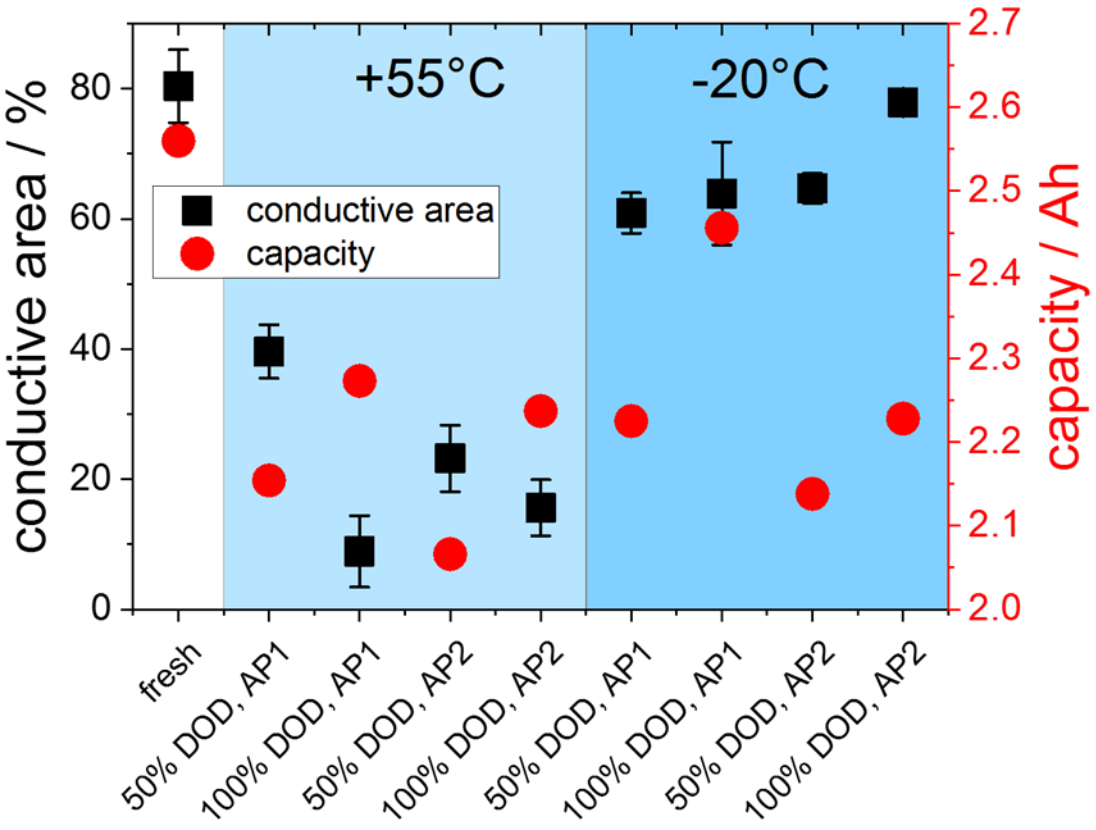

Figure A13: Comparison of the trends of surface conductive area and remaining cell capacity at end of life of the differently aged cells.

Publications

Part of this work has already been published in or submitted to peer-review for referenced journals or as posters on conferences:

Paper

- Simolka, M.; Heim, C.; Friedrich, K. A.; Hiesgen, R. Visualization of Local Ionic Concentration and Diffusion Constants Using a Tailored Electrochemical Strain Microscopy Method. *J. Electrochem. Soc.* **2019**, *166* (3), A5496–A5502. https://doi.org/10.1149/2.0711903jes.
- Simolka, M.; Kaess, H.; Friedrich, K. A. Comparison of Fresh and Aged Lithium Iron Phosphate Cathodes Using a Tailored Electrochemical Strain Microscopy Technique. *Beilstein Journal of Nanotechnology* **2020**, *11*, 583–596. https://doi.org/10.3762/bjnano.11.46.
- Simolka, M.; Heger, J.-F.; Traub, N.; Kaess, H.; Friedrich, K. A. Influence of Cycling Profile, Depth of Discharge and Temperature on Commercial LFP/C Cell Ageing: Cell Level Analysis with ICA, DVA and OCV Measurements. *Journal of The Electrochemical Society* **2020**, *167* (11), 110502. https://doi.org/10.1149/1945-7111/ab9cd1.
- Simolka, M.; Heger, J.-F.; Kaess, H.; Biswas, I.; Friedrich, K. A. Influence of Cycling Profile, Depth of Discharge and Temperature on Commercial LFP/C Cell Ageing: Post-Mortem Material Analysis of Structure, Morphology and Chemical Composition. *J Appl Electrochem* **2020**, *50* (11), 1101–1117. https://doi.org/10.1007/s10800-020-01465-6.

Presentation

- "Local Analysis of Li-ion Concentration and Diffusion-Migration Coefficients in Lithium-Silicon Electrodes", M. Simolka, C. Heim K. A. Friedrich and R. Hiesgen, nanoGe Fall Meeting 2018, Torremolinos, Spain

Poster

- "Resolving Li-Ion concentration hot spots in silicon anodes using a modified electrochemical strain microscopy technique", M. Simolka, C. Heim, K. A. Friedrich, R. Hiesgen, ElecNano 8, Nancy, France
- "Visualization of Li-ion Concentration and Diffusion in Si Anodes Using an Adapted Electrochemical Strain Microscopy Method", M. Simolka, C. Heim, K. A. Friedrich, R. Hiesgen, IMLB 2018, Kyoto, Japan